

38307?
2170823
TR diss 2257

~~12155~~

Stelling van de commissie

**TR diss
2257**

FINITE ELEMENT METHODS IN RESISTIVITY LOGGING

PROEFSCHRIFT

ter verkrijging van de graad van doctor aan
de Technische Universiteit Delft, op gezag van
de Rector Magnificus, prof.ir. K.F. Wakker
in het openbaar te verdedigen ten overstaan van
een commissie aangewezen door het College van Dekanen
op 14 september 1993 te 10.00 uur

door

John Richard Lovell

geboren te
Cardiff, Wales

B.A., M.A. (Oxon)
M.A. (Cornell)



Dit proefschrift is goedgekeurd door de promotor
Prof.dr.ir. H. Blok

Library of Congress Catalogue Card Number: 93-093655

ISBN-90-5326-008-0

Copyright ©1993 by Schlumberger Technology Corporation.

All rights reserved. No parts of this publication may be reproduced, stored in a retrieval system, or transmitted in any form or by any means, electronic, mechanical, photocopying, recording or otherwise without permission of Schlumberger-Doll Research, Ridgefield, CT 06877-4108, USA.

The cover figure is a plot of the initial error when solving for the potential due to a monopole source in a formation with a 45 degree dipping half space. The error is shown projected onto cylinders and planes in the computational domain, together with a 3D isosurface viewed with light sources. The initial guess is the potential field from a lower source position. The error is concentrated along the bed boundary and the position of the bed boundary relative to the previous tool position.

The author is employed by Schlumberger-Doll Research, Ridgefield, CT 06877-4108, USA, and gratefully acknowledges their sponsorship of the research reported here and their permission and support to publish this monograph. In particular, he would like to thank Dr Kambiz Safinya for his encouragement to begin this thesis, Alison Fazio and Ralph Giuliano for cheerful and reliable graphics support, and Dr Michael L. Oristaglio both for his many constructive suggestions and for his stewardship of the text through to publication. Lastly, he would like to express his debt and gratitude to Drs Tarek M. Habashy and Weng C. Chew for their patience and enthusiasm in teaching him electromagnetics.

Cyflwynaf y llawysgrif hon gyda diolch i mam a dad

Abstract

Resistivity measurements are used in geophysical logging to help determine hydrocarbon reserves. The derivation of formation parameters from resistivity measurements is a complicated nonlinear procedure often requiring additional geological information. It is important that the tool measurements be accurate with as few misleading artifacts as possible. This requires an excellent understanding of tool physics, both to design new tools and interpret the measurements of existing tools. The Laterolog measurements in particular are difficult to interpret because the response is very nonlinear as a function of electrical conductivity, unlike Induction measurements. Forward modelling of the Laterolog is almost invariably done with finite element codes which require the inversion of large sparse matrices. Modern techniques can be used to accelerate this inversion. Moreover, an understanding of the tool physics can help refine these numerical techniques.

In axisymmetric formations, the best way to model the Laterolog is to cast the finite element problem in terms of the azimuthal magnetic field H_ϕ rather than the classical electric potential Φ . The use of H_ϕ allows one to model such frequency effects on the Laterolog as the Groningen effect: an anomalous indication of hydrocarbon beneath highly resistive layers. Moreover, unlike the Φ formulation, the H_ϕ formulation does not exhibit a numerical singularity as the contact impedance on electrodes tends to zero.

In fully three-dimensional problems, e.g., with highly deviated or horizontal wells, the H_ϕ formulation is not appropriate nor is a complete solution in terms of Maxwell's equations practical. To obtain a rapid solution in terms of Φ requires a discretization that matches dipping bed boundaries and fractures while still retaining sufficient structure for modern iterative methods to be applicable. Decompositions of the approximation space tie directly back to the meshing and discretization strategy as well as giving insight into preconditioning techniques for conjugate gradient methods.

Contents

Abstract	vii
1 Introduction	1
1.1 Overview	1
1.2 Mathematical formulations	7
1.3 Sparse matrices	19
1.3.1 Stencil formulations	21
1.4 Maxwell's equations of electromagnetics	22
1.4.1 Perfect conductors and insulators	24
1.4.2 Reciprocity	26
1.4.3 Weak formulation of Maxwell's equations	27
1.4.4 Existence of a solution	28
1.4.5 Maxwell's equations at DC	29
1.4.6 Low frequency solutions to Maxwell's equations	30
1.4.7 TE and TM fields	33
1.4.8 General solutions	34

2 Resistivity Modelling	39
2.1 Introduction	39
2.2 Overview of resistivity tools	41
2.2.1 Solenoids	43
2.2.2 Toroids	45
2.2.3 Electrodes	47
2.3 Finite element solutions for Laterologs	49
2.3.1 Potential formulation at DC	49
2.3.2 Assembly of stiffness matrix and Dirichlet constraints	52
2.3.3 Computation of electrode currents	55
2.3.4 Reciprocity and solutions for focussed tools	56
2.3.5 Solution in the presence of focussing constraints	57
2.3.6 Electrode impedance	60
2.4 Iterative solution techniques	61
2.4.1 Incomplete LU Preconditioning	65
2.5 Adaptive meshing	67
2.6 Lanczos methods	70
2.7 Conclusions	72
3 Solutions at Non-Zero Frequencies	79
3.1 Introduction	79
3.2 Mathematical formulation	81
3.3 Finite element formulation	91

CONTENTS

xi

3.4	Matrix inversion	96
3.5	Resistivity tools in heterogeneous media	98
3.5.1	Influence of casing in homogeneous and layered media	101
3.6	Conclusions	108
3.A	Stiffness matrix expansions	108
3.B	Boundary condition for armoured cable	111
3.C	Linear resistance for coaxial currents	113
4	Contact Impedance Modelling	119
4.1	Introduction	119
4.2	Contact impedance modelling	120
4.3	Contact impedance modelling with H_ϕ	123
4.4	Verification	126
4.5	Conclusions	134
4.A	CWNLAT and ALAT3D sample input files	139
5	Hierarchical Discretization	151
5.1	Introduction	151
5.2	Tensor product discretization	152
5.2.1	Isoparametric elements	153
5.2.2	Cartesian elements	159
5.3	Eccentricity	161
5.4	Bed boundaries	164

5.5	Decomposition of pentahedra	172
5.6	Fractures	175
5.6.1	Finite element formulation	177
5.6.2	Local stiffness matrices	179
5.7	Implementation details	180
5.8	Conclusions	182
6	Conclusions	187
6.1	Overview	187
	Glossary of Codes	189
	Glossary of Tools	191
	Samenvatting	193
	Biographical Sketch	197
	Index	199

Abstract. This chapter presents an overview of the thesis and describes the new finite element applications that are examined in the thesis. We introduce Maxwell's equations and demonstrate the existence and uniqueness of the solution. We also give a rapid survey of some of the ideas from linear algebra and functional analysis that are the underpinnings of the finite element formulation.

1.1 Overview

This thesis describes finite element algorithms for resistivity modelling in geophysics. Its emphasis is the interaction between discretization and solution techniques. Both traditional and novel discretizations are considered for time harmonic Maxwell's equations in 2D and 3D with emphasis on the low frequency and DC excitation in 3D. Structure in the discretization leads to streamlined matrix inversion. For example, relaxation methods can take advantage of tensor product decompositions of the approximation space and hierarchical methods can take advantage of direct sum decompositions. Decompositions of the approximation space tie directly back to the meshing and discretization and give insight into preconditioning conjugate gradient methods.

The major new developments presented in this thesis involve the application of modern finite element methods to difficult modelling problems in geophysics, specifically: Groningen effect in axisymmetric formations and focussed electrode modelling in highly deviated and horizontal wells.

What is new in this thesis:

- Laterolog modelling in terms of the azimuthal component of magnetic field, H_ϕ .
- Superconvergent formulations for apparent resistivity.
- A method of modelling Groningen effect.
- Contact impedance modelling for non-zero frequency ω .

- Solution for 3D fields across horizontal beds.
- Unifying view of relationship between mesh discretization and solution strategy: the importance of discretizations which preserve 'structure.'

The motivation behind the thesis is a need for robust and accurate modelling of electromagnetic tool configurations used to probe rock formations. Such tools are lowered down boreholes and used in oil exploration and production to measure the electrical properties of rocks. From these measurements an interpretation can be made as to the hydrocarbon bearing potential of the formation. The two most important families of such tools are the Induction and Laterolog configurations.

The Induction tool, [16], [32], [45], generates an azimuthal current around a metallic sonde which induces current loops in the rock formation as shown in Figure 1.1. These current loops in turn set up a secondary magnetic field which induces a voltage across the receiver coil. We shall see in Chapter 2 that this voltage is roughly proportional to formation conductivity. There is also much larger direct coupling term, however, and this must first be removed from the voltage measurement by subtracting the response from a third 'bucking' coil (not shown in Figure 1.1). In a layered formation, the resistivities of adjacent beds will also affect the tool response, a phenomenon known as shoulder effect. Rather than an exact value in each bed one obtains a log of *apparent resistivity* which must be further postprocessed to estimate true bed resistivities. Multiple arrays of weighted transmitter and receiver coils are used to simplify this postprocessing, a procedure known as *focussing* and this is discussed further in [45].

Laterolog tools, [17], [44], [45], rely on a different principle whereby current is injected directly into the formation from metallic electrodes. In an azimuthally symmetric formation, the electric field will lie purely in the azimuthal plane (i.e., $E_\phi = 0$). In a homogeneous formation, the amount of voltage required to drive unit current between two electrodes will be proportional to the resistance of the formation. The presence of neighbouring beds again degrades the response and Laterolog produces a log of 'apparent resistivity' which is postprocessed to estimate the true resistivity of each bed. An array of electrodes is again used to focus the current in such a way that the shoulder effects are minimized as shown in Figure 1.2. Figure 1.3 shows the more sophisticated focussing arrangements used in the Dual Laterolog (DLL).[†] Two separate focussing systems are combined onto the same tool by operating them at different frequencies (35 Hz for the LLd mode and 280 Hz for the LLs). As can be seen from Figure 1.3, the current paths in the LLd mode penetrate deeply into the formation whereas the LLs mode is more sensitive to the region near the borehole, [44].

[†]Mark of Schlumberger

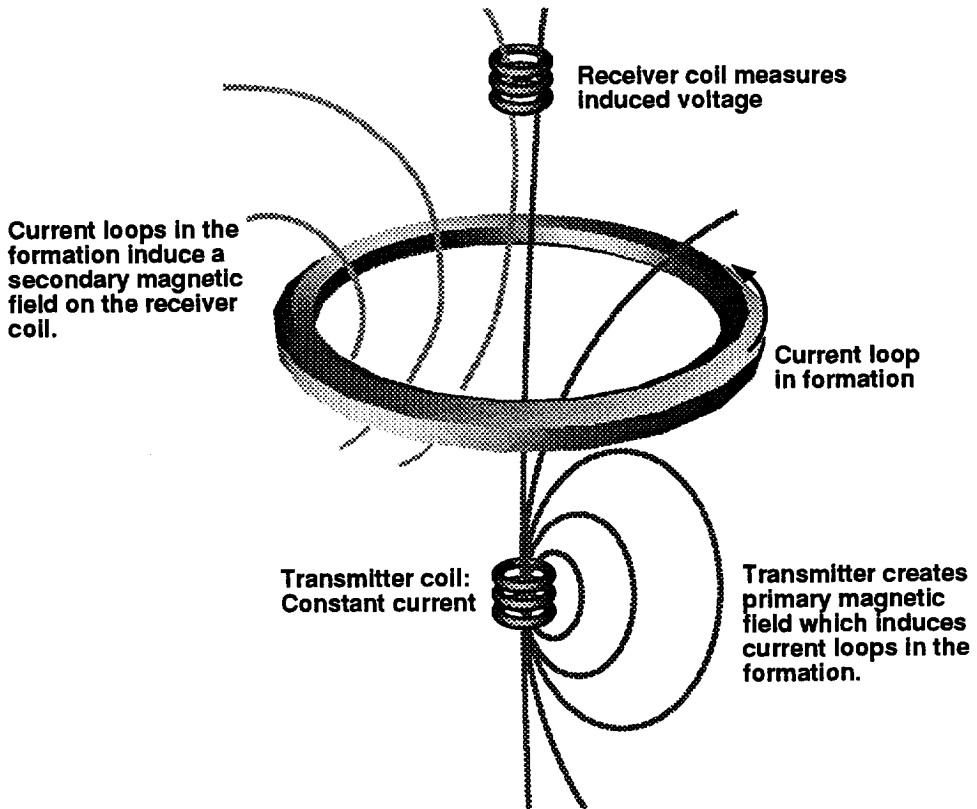


Figure 1.1: Schematic representation of an Induction coil. The transmitter coil creates a primary magnetic field which induces current loops in the formation. These current loops induce a voltage on the receiver coil which is proportional to formation conductivity. However, there is also direct coupling from transmitter to receiver which must first be subtracted from the measured voltage. (Reproduced courtesy of Schlumberger Technical Review)

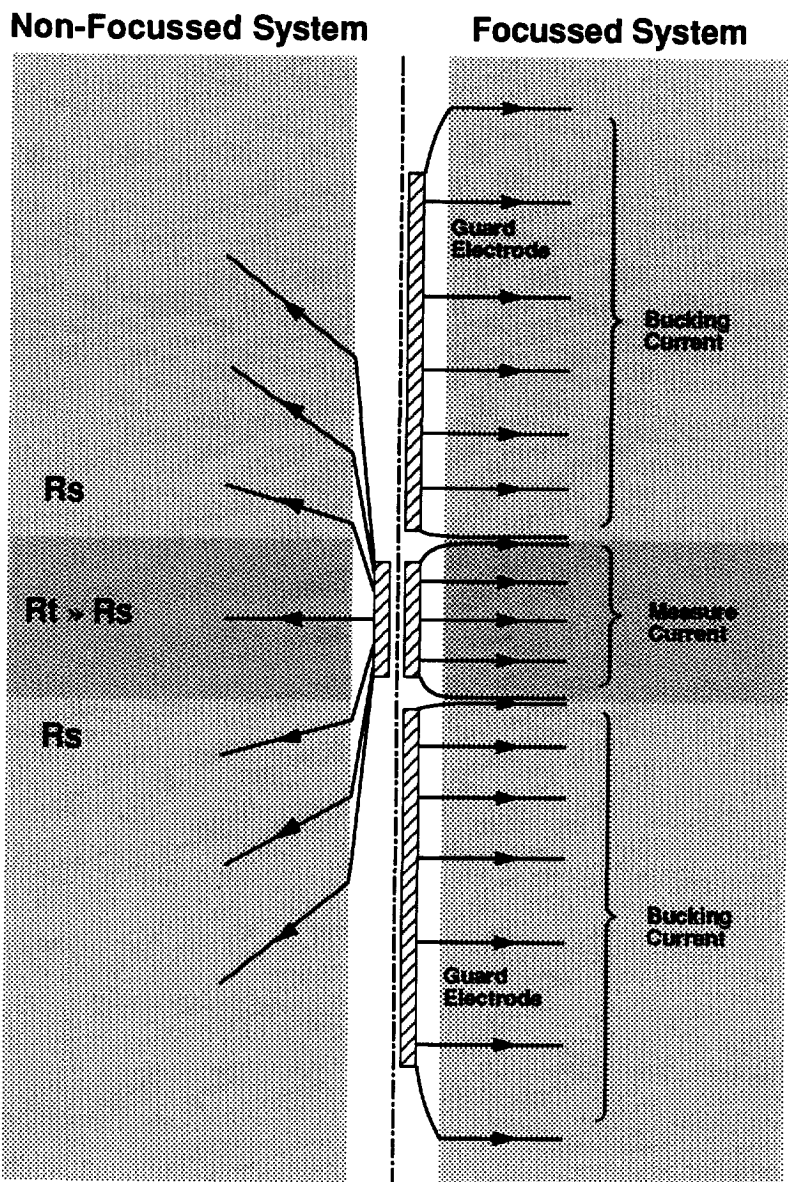


Figure 1.2: Focussing with large guard electrodes reduces shoulder effects from adjacent beds.
(Reproduced courtesy of Schlumberger Technical Review.)

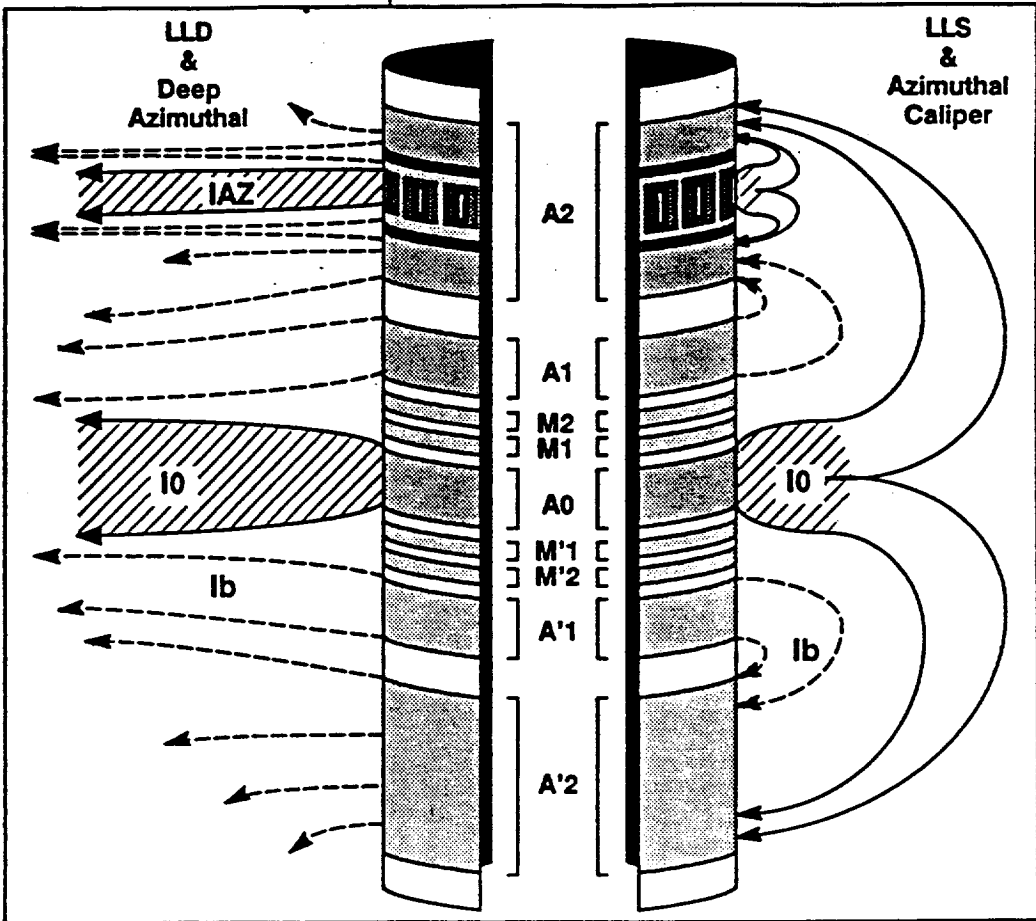


Figure 1.3: Focussing conditions used for the Dual Laterolog. (Reproduced courtesy of Schlumberger Technical Review.) The Azimuthal Resistivity Imager has the same configuration as the Dual Laterolog except that the A2 electrode is segmented azimuthally as shown in the top of the figure. For both tools, the voltage monitors at M1 and M2 (and M'1 and M'2) are maintained at the same potential by varying the current from the guard electrodes A1 and A2 (and A'1 and A'2). The effect is to minimize shoulder effects on the A0 measure electrode.

In addition to shoulder effect, the presence of the borehole will also influence the apparent resistivity, and if the borehole is not aligned perpendicularly to the bed boundaries there will also be a dip effect. The goal of modern tool designs of both Induction and Laterolog tools is to obtain accurate apparent resistivities and develop new postprocessing schemes so that true formation resistivities can be estimated with confidence. This requires an in-depth understanding of the physics of the measurement and an ability to predict the tool response in a give configuration, which in turn is dependent on the availability of high-speed and accurate modelling codes. For Induction tools (e.g., the DIT[†]) a wide range of such codes has recently become available, e.g., [3], but fewer codes are available for Laterologs, mainly because the Induction tool can often be well-modelled using idealized point-sources whereas the Laterolog cannot, [45]. The thrust of this thesis is to show how to solve for the response of a Laterolog in previously unobtainable configurations and also how to improve the accuracy and speed of finite element codes in 2D configurations that have been previously solved.

For example, Groningen effect is a finite frequency phenomenon on Laterologs that can generate anomalously high readings of resistivity and lead to the erroneous supposition of hydrocarbon beneath massive anhydrite or halite layers, (e.g., [10], [29], [47]). Our modelling of Groningen effect uses a finite element formulation for the azimuthal magnetic field component, H_ϕ . The only previous technique suggested in the literature, [4], assumes a low frequency approximation to Maxwell's equation. Using H_ϕ allows full modelling of Maxwell's equation in axisymmetric media.

Moreover, the use of H_ϕ instead of the classical electrostatic potential Φ provides a straightforward method of computing current lines as contour plots of ρH_ϕ . Deriving current lines from Φ can become numerically unstable if Φ is not very accurate. We discuss H_ϕ modelling in Chapter 3. The use of H_ϕ does raises an interesting problem, namely how to model electrodes subject to contact impedance. We present the solution to this problem in Chapter 4.

We also show how to use finite elements to derive a tool response without any loss of accuracy present in traditional methods such as presented in [19]. This method is called superconvergence and, while popular in mathematics journals, has rarely been applied to geophysical problems. It is closely related to the idea of using variational principles [11] to derive the desired quantity (the apparent resistivity) instead of using the variational technique to compute field distributions, with apparent resistivity obtained by postprocessing. We have not found references in the geophysics literature using this technique. This technique does not require that the FEM expansion be in terms of H_ϕ ; the method works as well for traditional FEM solutions of Laplace's equation in Φ . We discuss this in Chapter 2.

In 3D, we give a new approach to mesh discretization for Laplace's equation in Φ which

[†]Mark of Schlumberger

allows convenient tensor product formulations (like finite difference or FEM on a uniform mesh) but retains the flexibility of FEM methods to be conformal with bed boundaries and complicated tool geometries. We apply this technique to models of highly deviated wells where beds intersect at angles of 80-90 degrees. Traditional 3D finite element packages can have problems because the mesh generators lead to globally skewed systems of tetrahedra. Our method presented in Chapter 5 shows how to avoid this.

The remainder of this chapter provides a rapid overview of mathematical ideas and conventions used within this thesis. The purpose is to fix notation and provide references to standard texts rather than didactic exposition. Lastly, as an example of these techniques we demonstrate that the weak form of Maxwell's equations has a unique solution.

1.2 Mathematical formulations

We very briefly overview mathematical ideas and notation needed for subsequent computations on function spaces, convergence, etc. We have deliberately chosen a sloppy approach to any topological subtleties; these issues have been well-covered in the literature (e.g., [37], [38]). Instead, we stress the important ideas behind the mathematical terminology.

Notational conventions

We use the standard notation for the arithmetic fields, writing in blackboard bold: \mathbb{Z} for all integers, \mathbb{R} for the reals and \mathbb{C} for the complex domain. E.g., if Ω is some three dimensional domain we have $\Omega \subset \mathbb{R}^3$. The closure of Ω , denoted $\bar{\Omega}$, is the union of the boundary $\partial\Omega$ and interior $\overset{\circ}{\Omega}$. We shall always assume Ω to be a bounded subdomain with polygonal or smoothly varying boundary. If Ω_1 and Ω_2 are two spaces, we write $\Omega_1 \times \Omega_2$ for the space¹ of ordered pairs (u, v) , $u \in \Omega_1$, $v \in \Omega_2$ and similarly write $\Omega^2 = \Omega \times \Omega$, etc. If a space V is not normally considered a subspace of W but there is an exact copy of V inside W then rather than writing $V \subset W$ we may also write $V \hookrightarrow W$. This map is called the inclusion map and by definition it is one-to-one.

Bold faced symbols in lower case represent vectors in the domain, e.g., \mathbf{r} or \mathbf{r}' , and bold faced terms in capital letters represent vector fields on the domain, e.g., $\mathbf{E}(\mathbf{r})$. The unit vectors in \mathbb{R}^3 are denoted $\mathbf{i}, \mathbf{j}, \mathbf{k}$ or else as $\hat{\mathbf{x}}, \hat{\mathbf{y}}, \hat{\mathbf{z}}$. Cylindrical coordinate vectors are given as $\hat{\rho}, \hat{\phi}$ and $\hat{\mathbf{z}}$. ($\hat{\theta}$ is reserved for latitudinal spherical coordinates.) The terminology \hat{u} , etc, may also be

¹Also called the *Cartesian product* of Ω_1 and Ω_2 .

used to represent an approximation to u . $\hat{\nu}$ will always denote the outward pointing normal from the boundary $\partial\Omega$.

Tensors are denoted $\hat{\mathbf{A}}$ etc, and in dyadic notation \mathbf{ii} , etc. For example, the identity tensor is given by

$$(1.1) \quad \hat{\mathbf{I}} = \hat{\mathbf{x}}\hat{\mathbf{x}} + \hat{\mathbf{y}}\hat{\mathbf{y}} + \hat{\mathbf{z}}\hat{\mathbf{z}}.$$

Vectors in abstract vector spaces, however, are *not* flagged in bold case, e.g., we write $v \in V_h$ to indicate that v is some element of the vector space V_h . v may actually be a function on Ω and V_h will then have been provided with additional topological structure (e.g., it is a Banach or Hilbert space). All vector spaces will be assumed to be complex valued, and vector space constructs will be defined over \mathbb{C} . In \mathbb{C}^n , we shall always use the notation that $\langle x, y \rangle$ denotes the bilinear form

$$(1.2) \quad \langle x, y \rangle = \sum_i x_i y_i$$

without complex conjugation. $\langle x, y \rangle$ is thus not an inner product because it is not positive definite.² The inner product over \mathbb{C}^n is given by $\langle x, \bar{y} \rangle$ which we term sesquilinear, [38], because it is linear in the first component but $\langle x, \overline{a_1 y_1 + a_2 y_2} \rangle = \bar{a}_1 \langle x, \bar{y}_1 \rangle + \bar{a}_2 \langle x, \bar{y}_2 \rangle$ is conjugate linear. We write

$$\|u\| = \sqrt{\langle u, \bar{u} \rangle}$$

for the norm. If u is a complex-valued vector, $|u|$ is used to denote a seminorm³, e.g., $\sqrt{|\langle u, u \rangle|}$.

The space of infinitely continuous, complex valued functions defined on Ω is denoted $\mathcal{C}^\infty(\Omega)$. $\mathcal{C}_0^\infty(\Omega)$ denotes the space of smooth functions which are zero in a neighbourhood of $\partial\Omega$. An abstract, complex-valued bilinear form $b(u, v)$ is termed continuous if there exists a real positive M such that $|b(u, v)| \leq M \|u\| \|v\|$ for all u and v . In addition, if there exists a $\gamma > 0$ such that $|b(u, \bar{u})| \geq \gamma \|u\|^2$ for all u then $b(u, v)$ is termed *coercive*. We term a complex valued bilinear form symmetric if $b(u, v) = b(v, u)$.

Upper case is used both for vector spaces and matrix representation of operators on that space. Operators from one vector space to another may also be written in *Euler fonts*. E.g., if v_1, \dots, v_n is a basis for an n -dimensional space V and w_1, \dots, w_m is a basis for an m -dimensional space W then a linear operator $\mathfrak{R}: V \rightarrow W$ is represented by a matrix R ,

²[9] and [21] refer to this bilinear form as a *formal* inner product

³A seminorm satisfies all of the properties of a norm save that $|u|$ can be zero for non-zero u .

where

$$(1.3) \quad \Re(v_i) = \sum_j R_{ij} w_j.$$

Courier font (e.g., this) is used for computer symbols and algorithms, e.g., \Re might represent a particular storage scheme for the components of the matrix R , or operator \Re . We also use Courier font for fragments of computer codes.

Integration

Integration may be written in mathematical or engineering notation according to convenience. E.g., if Ω is the 3D domain $[x_1, x_2] \times [y_1, y_2] \times [z_1, z_2]$ then we may write

$$(1.4) \quad \int_{\Omega} f \quad \text{or} \quad \iiint_{\Omega} f \quad \text{or} \quad \int_{x_1}^{x_2} \int_{y_1}^{y_2} \int_{z_1}^{z_2} f(x, y, z) dx dy dz.$$

Boundary integrals may similarly be denoted $\oint_{\partial\Omega}$ regardless of whether Ω is 2D or 3D. We will typically use S to denote a 2D subset of Ω and V for 3D.

In many cases, we need only approximate values of integrals and use numerical quadrature rules of the form

$$(1.5) \quad \int_{\Omega} f \approx \sum_p w_p f(x_p)$$

where the x_p are suitable selected points in Ω called 'stations' and the w_p are weights. Gaussian quadrature rules for $\Omega = [0, 1]$ are well known (e.g., [2]). More complicated formulae for more general domains (such as triangles and tetrahedra) are given in [43].

The simplest quadrature rules are based on the trapezoid rule, for example, if $C = \{c(t) : t \in [0, 1]\}$ denotes a curve in \mathbb{C} then we numerically evaluate a contour integral as

$$(1.6) \quad \oint_C f(z) dz = \sum_{i=1}^N \frac{f(c(t_i)) + f(c(t_{i-1}))}{2} (c(t_i) - c(t_{i-1}))$$

where t_0, \dots, t_N is a partition of $[0, 1]$.

Contour integrals in the complex plane are often more easily evaluated by deforming the contour. By Cauchy's theorem if c_1 and c_2 begin and end at the same points in \mathbb{C} with c_1 homotopic to c_2 then

$$(1.7) \quad \oint_{c_1} f(z) dz = \oint_{c_2} f(z) dz + \sum_r \text{Res}[f; z_r]$$

where z_r is the list of poles between c_1 and c_2 . Ideally, one can find a curve c_2 along which the integral is more easily integrated numerically.

It is important to take into account branch cuts when deforming contours. For example, the following routines compute $f(z) = \sqrt{z(z-1)}$ with two different branch cuts

```
COMPLEX FUNCTION F1(Z)
COMPLEX Z
F1 = SQRT(Z*(Z-1))
RETURN
END
```

```
COMPLEX FUNCTION F2(Z)
COMPLEX Z
F2 = SQRT(Z) * SQRT(Z-1)
RETURN
END
```

Delta functions δ are defined by their action on functions in $C_0^\infty(\Omega)$, namely that

$$(1.8) \quad \delta(f) = f(0)$$

and, more generally, given $x \in \Omega$

$$(1.9) \quad \delta(x)(f) = f(x).$$

The derivative of the delta function is the map $\delta'(x)$ defined by

$$(1.10) \quad \delta'(x)(f) = -f'(x).$$

In cylindrical coordinates, the 3D delta function is defined as $\delta(\mathbf{r}) = \delta(x)\delta(y)\delta(z) = \delta(\rho)\delta(z)/(2\pi\rho)$.

Delta functions can also be defined heuristically as the derivative of characteristic or Haar functions. We define the characteristic function on an interval, $\chi_{[a,b]}$, to be the function which is "1" on the interval $[a, b]$ and zero elsewhere. Characteristic functions on arbitrary domains are similarly defined. If f is a function defined on Ω then we define its 'support' to be the set of points x where $f(x) \neq 0$. The set of points for which $f(x) = 0$ is called the 'kernel' of f denoted $\ker(f)$. The set of points $f(x)$ is called the 'image' of f and denoted $\text{im}(f)$.

Linear algebra and Sobolev spaces

As the equations describing electromagnetic fields are linear in nature (a phenomenon known as 'superposition'), the natural mathematical language to describe solution algorithms is that of linear algebra and functional analysis. Electromagnetic fields will be viewed as points in abstract linear spaces and an understanding of the properties of these spaces can guide us in algorithm development. In this subsection, we fix the notation for the linear spaces that we will be using through this monograph.

Given two vector spaces, V and W , their direct sum, $V \oplus W$, is the space of dimension $n + m$ with basis $v_1, \dots, v_n, w_1, \dots, w_m$. If V and W are two vector spaces, $V \times W$ is not a vector space, but becomes one, namely $V \oplus W$, by enforcing the identification of ordered pairs $(v, \alpha_1 w_1 + \alpha_2 w_2) = \alpha_1(v, w_1) + \alpha_2(v, w_2)$ for $\alpha_1, \alpha_2 \in \mathbb{C}$. In fact, for infinite dimensional spaces, this is the usual definition of $V \oplus W$, (e.g., [31]).

A potentially larger space of dimension mn is the tensor product $V \otimes W$. It has basis vectors $v_i \otimes w_j$ where an appropriate meaning is given to the tensor product of individual vectors. For example, the dyads live in $\mathbb{R}^3 \otimes \mathbb{R}^3$ and we could also write equation (1.1) as

$$(1.11) \quad \hat{\mathbf{I}} = \hat{\mathbf{x}} \otimes \hat{\mathbf{x}} + \hat{\mathbf{y}} \otimes \hat{\mathbf{y}} + \hat{\mathbf{z}} \otimes \hat{\mathbf{z}}.$$

As an example, for finite dimensional spaces, $V \otimes W$ can be thought of as the space of matrix representations of bilinear functions from $V \times W$ to \mathbb{C} .⁴ (This is the usual analogy of dyads being 'the same thing' as matrices.) For infinite dimensional spaces, [13], [31], the space $V \otimes W$ is defined to be that unique space such that any bilinear function f from $V \times W$ to \mathbb{C} corresponds to the composition of the map of the ordered pair $(v, w) \mapsto v \otimes w$ followed by a linear map from $V \otimes W$ to \mathbb{C} .⁵

The dual of a vector space V , denoted V' , consists of the continuous linear maps from V to \mathbb{C} . We shall usually assume that our vector spaces V come equipped with a norm $\|v\|_V$ and the corresponding norm on V' is then

$$(1.12) \quad \|f\|_{V'} = \max_{v \neq 0} \frac{f(v)}{\|v\|} = \max_{\|v\|=1} f(v).$$

Note that a linear function f is continuous if and only if $\|f\|_{V'} < \infty$. If V is finite dimensional and the linear operator f is represented as a matrix F as shown in equation (1.3) then $\|f\|$ is the largest eigenvalue of F .

⁴Not sesquilinear!

⁵[1] gives a good exposition of tensor products for both contravariant and covariant tensors, but only for finite dimensional spaces.

Some normed spaces are actually inner product spaces in that there is a bilinear map $V \times V \rightarrow \mathbb{C}$, $(v, w) \mapsto \langle v, w \rangle$, such that $\langle v, \bar{v} \rangle = \|v\|^2$. An inner product space V is termed a Hilbert space if it is *complete*, i.e., if the limit point of any convergent sequence always lies in that space. This is not true, for example, of the rational numbers (fractions), the sequence $1, 1 + 1/1!, 1 + 1/1! + 1/2!, 1 + 1/1! + 1/2! + 1/3!, \dots$ is a convergent sequence of rational numbers but the limit e is not a rational number. Nor is $\mathcal{C}^0(\Omega)$, the space of continuous functions, complete because it is easy to take a limit of continuous functions and have the limit be discontinuous (think of adding Fourier harmonics to form a square-wave).

Standard examples of Hilbert spaces are $L^2(\Omega)$ and $H^1(\Omega)$, the spaces of complex valued functions f on Ω such that $\langle f, \bar{f} \rangle_0 < \infty$ and $\langle f, \bar{f} \rangle_1 < \infty$ respectively, where

$$(1.13) \quad \langle f, g \rangle_0 = \int_{\Omega} f g \quad \text{and} \quad \langle f, g \rangle_1 = \int_{\Omega} f g + (\nabla f) \cdot (\nabla g).$$

We write L^2 as H^0 and generalize to write $H^n(\Omega)$ for the space of functions whose n th partial derivatives have finite L^2 -norm. The spaces H^n are often called Sobolev spaces. The inner product on H^n is

$$(1.14) \quad \langle f, g \rangle_n = \sum_{\#(\alpha) \leq n} \int_{\Omega} (D^{\alpha} f)(D^{\alpha} g).$$

where (in 2D) $\alpha = (\alpha_1, \alpha_2)$, $\#(\alpha) = \alpha_1 + \alpha_2$ and $D^{\alpha} = \partial^{\alpha_1}/\partial x^{\alpha_1} \partial^{\alpha_2}/\partial y^{\alpha_2}$ with a similar definition in 3D.

In $H^1(\Omega)$, we define the semi-norm

$$(1.15) \quad |f|_1^2 = \int_{\Omega} \nabla f \cdot \nabla \bar{f},$$

and in $H^n(\Omega)$

$$(1.16) \quad |f|_n^2 = \sum_{|\alpha|=n} \int_{\Omega} D^{\alpha} f \cdot D^{\alpha} \bar{f}.$$

For any $H^n(\Omega)$,

$$(1.17) \quad \|f\|^2 = \sum_{i=0}^n |f|_i^2 = \langle f, \bar{f} \rangle_n.$$

Fractional spaces $H^{n+\epsilon}(\Omega)$, $n \geq 0$, $\epsilon \in [0, 1)$ are defined in terms of the norm

$$(1.18) \quad \|v\|_{H^{n+\epsilon}(\Omega)}^2 = \|v\|_n^2 + |v|_{H^{n+\epsilon}(\Omega)}^2$$

where (e.g., [7])

$$(1.19) \quad |v|_{H^{n+\epsilon}(\Omega)}^2 = \sum_{|\alpha|=n} \int_{\Omega} \frac{|D^{\alpha}v(x) - D^{\alpha}v(y)|}{|x-y|^{d+2\epsilon}}$$

where d is the dimension of Ω .

If $r > 0$ then we define $H^{-r}(\Omega)$ as the dual space $(H_0^r(\Omega))'$ where $H_0^r(\Omega)$ denotes the space of functions $u \in H^r(\Omega)$ with $u = 0$ on $\partial\Omega$. Because $H_0^r(\Omega) \subset H^r(\Omega)$ then $(H^r(\Omega))' \subset (H_0^r(\Omega))' = H^{-r}(\Omega)$. Compared to $(H^r(\Omega))'$, $H^{-r}(\Omega)$ contains some additional boundary operators (given in [35], p. 110) that can only be defined if $u \rightarrow 0$ near $\partial\Omega$ and which involve derivatives of order less than r .

Some of the above statements about Sobolev spaces become a lot harder to visualize when one recalls the glossed over notion of *completeness*. For example, one cannot strictly speaking define $H_0^r(\Omega)$ as the space of functions $u \in H^r(\Omega)$ with $u|_{\partial\Omega} = 0$ on $\partial\Omega$ because u need not be continuous and its value on $\partial\Omega$ need not be defined. All of the spaces $H^r(\Omega)$ are Hilbert spaces so (tucked away in the definition) they are necessarily complete. Each of these spaces is built by defining a "point" in $H^r(\Omega)$ to be the limit of a sequence of smooth functions. The only difference between the H^r 's lies in the definition of the limit. For example, we define $H_0^r(\Omega)$ as the completion of $C_0^\infty(\Omega)$ in the $\|\cdot\|_r$ norm.

In addition to the inclusion $C^\infty(\Omega) \hookrightarrow H^r(\Omega)$ for $r \geq 0$, there is a natural inclusion of $C_0^\infty(\Omega) \hookrightarrow (H_0^r(\Omega))'$ defined by

$$(1.20) \quad g: f \mapsto \langle f, g \rangle = \int_{\Omega} fg \quad \forall f \in H_0^r(\Omega)$$

for $g \in C_0^\infty(\Omega)$ and so we can also define $H^{-r}(\Omega)$ as a limit of smooth functions, provided we take the $\|\cdot\|_{-r}$ norm. This was the historical approach to defining delta functions (e.g., [5]). Even if $g \in H^{-r}(\Omega)$ is not a smooth function, we shall still write $\langle f, g \rangle$ for $g(f)$.

Examining the structure of the Sobolev spaces, there is an apparent singularity at $r = 0$. For $r = 0^+$, the Sobolev space places no restriction on the function values on $\partial\Omega$. For $r = 0^-$, the Sobolev space is defined as a dual space. In fact there is no singularity. When $r = 0$, $H_0^r(\Omega) = H^r(\Omega)$ because there is no restriction on continuity in $L^2(\Omega)$, and when $r = 0$ there are no lower order boundary operators left to be defined in $(H_0^r(\Omega))' = (H^r(\Omega))'$. Lastly, $L^2(\Omega)$ is known to be self-dual, [38].

The lack of completeness of C^n and the existence of a continuous scale of spaces H^r for any $r \in \mathbb{R}$ are strong reasons to use the Sobolev spaces. In particular, in the context of differential equations we have that⁶

⁶ [38] gives the proof if L has constant coefficients, [24] gives the more general case.

Theorem 1 *If L is an elliptic 2nd order operator with smooth coefficients and $Lu = f$ with $f \in H^r(\Omega)$ and $r \in \mathbb{R}$ then $u \in H^{r+2}(\Omega)$.*

This theorem would *not* be true if we replaced, for example, $H^r(\Omega)$ with $C^r(\Omega)$. Even if f were in C^r then $L^{-1}f$ need not lie in C^{r+2} . It will, however, lie in some slightly large space. That space is precisely the space given by completing C^{r+2} under the $\|\cdot\|_{r+2}$ norm.

Fractional spaces arise because data which has, say, r derivatives in the interior of Ω can actually be a little less smooth on the boundary $\partial\Omega$, in fact, by exactly ‘half a derivative’. Suppose that $u \in H^1(\Omega)$ so that $\nabla u \in (H^0(\Omega))^d$ (recall that the superscript d means d separate copies). On the boundary, we will have that $u \in H^{1/2}(\partial\Omega)$ and $\nabla u \cdot \hat{\nu} \in H^{-1/2}(\partial\Omega)$. Heuristically speaking, the potential distribution, u , along a boundary is going to be ‘more smooth’ than the corresponding current distribution $\nabla u \cdot \hat{\nu}$.

We have seen that if $r > s$ then $H^r \subset H^s$, but in addition, by the Riesz representation theorem, [38], there is also defined an isomorphism between $H^{-r}(\Omega)$ and $H^r(\Omega)$. I.e., given any $g \in H^{-r}$ we can always find $g \in H^r(\Omega)$ such that $g(f) = \langle g, f \rangle_r$ for all $f \in H^r(\Omega)$. Using the notation defined above, this says that $\langle g, f \rangle = \langle g, f \rangle_r$ for some $g \in H^r$. If $r > 0$, this does *not* imply, of course, that there exists a g with $\langle g, f \rangle = \langle g, f \rangle_0$. For example, if $\Omega = (-1, 1) \subset \mathbb{R}$ then all functions in $H_0^1(\Omega)$ are actually continuous, so the delta function, δ is a well defined ‘point’ of $H^{-1}(\Omega)$. This means that there is a well-defined continuous function d such that $\langle d, f \rangle_1 = f(0)$ for all $f \in H^1(\Omega)$.⁷ But there does not exist a function $\hat{d} \in H^1(\Omega)$ such that $\langle \hat{d}, f \rangle_0 = f(0)$ (if there were then we would have that $\delta = \hat{d} \in H^1(\Omega)$ which is clearly false).

The fact (used in the previous paragraph) that functions in $H_0^1((-a, a))$ are actually continuous may not seem surprising, but this result does *not* extend to higher dimensions. For example, in 2D the function $\log \log(\rho)$ is in $H^1(\mathbb{R}^2)$ but is *not* continuous at the origin. The relationship between continuity and the Sobolev index r is a little subtle. Specifically, if Ω is a bounded, polygonal open subset of \mathbb{R}^d , then

Theorem 2 (Sobolev Embedding) $H^{n+d/2}(\Omega) \subset C^n(\Omega) \subset H^n(\Omega)$.

For example, in 1D, functions are continuous if they have a derivative with finite energy, whereas in 3D having a second derivatives with finite energy is needed to guarantee continuity. A relatively simple proof of this result is given in [38].

When $\Omega = \mathbb{R}^d$ is unbounded, we can use a simpler definition for Sobolev spaces based on the

⁷ $d(x)$ takes on a surprisingly simple form!

Fourier transform. Specifically, for any $r, u \in H^r(\mathbb{R}^d)$ if

$$(1.21) \quad \|u\|_{H^r(\mathbb{R}^d)}^2 = \int_{\mathbf{k} \in \mathbb{R}^d} |\hat{u}|^2 (1 + |\mathbf{k}|^2)^r d\mathbf{k} < \infty.$$

From this definition, for example, [35] shows that the statement in 2D that “derivative with finite energy implies continuity” only *just* fails: for $\Omega \subset \mathbb{R}^2$, $H^{1+\epsilon}(\Omega) \subset C^1(\Omega)$ for any $\epsilon > 0$. The 2D delta function lies in $H^{-1-\epsilon}(\Omega)$ for any $\epsilon > 0$, but not in $H^{-1}(\Omega)$. Similarly, in 1D, $\delta \in H^{-1/2-\epsilon}(\mathbb{R})$ for any $\epsilon > 0$.

Galerkin formulations

We say that an equation $Lu = f$ is valid in the weak or distributional sense if $\langle Lu, v \rangle = \langle f, v \rangle$ for all v . v is termed a test function. The space of test functions must be chosen sufficiently smooth that the inner product $\langle Lu, v \rangle$ exists in the ‘classical’ sense (after integration by parts if necessary). E.g., if L is a second order differential operator and u is in $H^1(\Omega)$ then $Lu \in H^{-1}(\Omega)$ and we could take $v \in H^n(\Omega)$, ($n \geq 1$). Alternatively, if $u \in H^4(\Omega)$, then $Lu \in H^2(\Omega)$ would be continuous and we could take v to be a delta function, in which case $Lu = f$ would be enforced at every point – the ‘strong’ sense of the differential equation. In the finite dimensional case, we know that an operator will be invertible if its smallest eigenvalue is bounded away from the origin. In the more general case, we have the result

Theorem 3 (Lax-Milgram) *If A is a coercive, symmetric bilinear form defined over V , i.e., $\gamma \|v\|^2 \leq |A(v, \bar{v})| \leq C \|v\|^2$ for all $v \in V$, then for any $f \in V$ there exists a unique solution, u , to the system of equations*

$$A(u, v) = \langle f, v \rangle \quad \forall v \in V,$$

and $\|u\| \leq C/\gamma \|f\|$.

Note that $|A(u, \bar{u})|$ is not the same as $A(u, \bar{u})$ because the latter need not be real valued. Also, it is not a restriction to think of the right-hand side as an inner product because by the Riesz representation theorem any continuous linear operator on V can be so represented. Lastly, note that $A(u, v) = \langle f, v \rangle$ for all $v \in V$ is the same system of equations as $A(u, \bar{v}) = \langle f, \bar{v} \rangle$ for all $v \in V$.

If W is a closed subspace of a Hilbert space V , then we can define W^\perp to be the space of functions u such that $\langle u, w \rangle = 0$ for all $w \in W$. We will then have a direct sum decomposition $V = W \oplus W^\perp$. Any point $v \in V$ can be written uniquely as $w_1 + w_2$ with $w_1 \in W$ and

$w_2 \in W^\perp$. This in turn defines a natural map called the projection operator $P : V \rightarrow W$ given by $P(v) = P(w_1 + w_2) = w_1$. $P(v)$ will be the closest point in W to v .

The combination of these two ideas is used repeatedly in the so-called method of moments, [23], or Galerkin method: Given a symmetric, invertible linear operator $L : V \rightarrow V'$ we solve the system $Lu = f$ restricted to some finite dimensional subspace $W \subset V$ with \hat{u} the image of u under the natural projection $P : V = W \oplus W^\perp \rightarrow W$. Thus we wish to find $\hat{u} \in W$ such that $\langle L\hat{u}, \hat{v} \rangle = \langle f, \hat{v} \rangle$ for all $\hat{v} \in W$. By the Lax-Milgram theorem, such a \hat{u} will exist provided L is coercive over the subspace W , i.e., provided the smallest eigenvalue of L is bounded away from 0.

A concrete example of this is given in the Section 1.4 where we show that there must exist a solution to the time-harmonic representation of Maxwell's equations in a lossy media.

If we are given a basis w_1, \dots, w_n for W then $\hat{u} = u_1 w_1 + \dots u_n w_n$ and we are thus required to solve the finite dimensional system

$$(1.22) \quad \sum_{i=1}^n u_j \langle L\hat{w}_j, \hat{w}_i \rangle = \langle f, \hat{w}_i \rangle$$

for $i = 1, \dots, n$. $\langle L\hat{w}_j, \hat{w}_i \rangle$ clearly constitutes an $n \times n$ matrix which we term the *stiffness matrix*.

Sometimes, the test functions v are required to satisfy a linear constraint $Pv = 0$, say, so that W is the kernel of P and a basis for W may not be obvious or easy to implement on the computer. In this case we can appeal to the theory of Lagrange multipliers for a solution. We know that for any bounded linear operator $P : X \rightarrow Y$ then $X = \ker(P) \oplus \text{im}(P^t)$ where P^t is the adjoint operator (i.e., transpose) defined by $\langle Px, y \rangle = \langle x, P^t y \rangle$, [38]. So $\langle L\hat{u}, \hat{v} \rangle = 0$ for all $\hat{v} \in \ker(P)$ is exactly the statement that $Lu \in \text{im}(P^t)$, i.e., that $Lu = P^t \lambda$ for some $\lambda \in Y$. λ is known as a Lagrange multiplier. This formulation can be used to impose divergence conditions on the solution of Maxwell's equations in 3D. In Chapter 2, we shall use Lagrange multipliers to help examine constraint equations for focussed Laterologs.

Connectivity and calculus

We have seen that notion of completeness is important to the study of differential equations. A second topological concept intimately related to calculus is connectivity. The domain Ω is called simply connected (written $\pi_1(\Omega) = 0$) if the image of any circle in Ω extends to the image of a disc lying wholly within Ω (e.g., not the case for a circle around the borehole if Ω consists of the formation minus the borehole). Graphically, if $\pi_1(\Omega) = 0$ then one can

"shrink" any circle to a point. Similarly, we write that $\pi_2(\Omega) = 0$ if any sphere can be shrunk to a point in the domain (e.g., not the case for \mathbb{R}^3 minus a point). We have the well known results that

Theorem 4 If $\pi_1(\Omega) = 0$ then $\nabla \times \mathbf{A} = 0$ if and only if $\mathbf{A} = -\nabla \Phi$ for some scalar field Φ .

Theorem 5 If $\pi_2(\Omega) = 0$ then $\nabla \cdot \mathbf{A} = 0$ if and only if $\mathbf{A} = \nabla \times \mathbf{B}$ for some vector field \mathbf{B} .

Other important links between geometry and calculus are Stokes' and Gauss' theorems

$$(1.23) \quad \int_S \nabla \times \mathbf{A} \cdot d\mathbf{v} = \oint_{\partial S} \mathbf{A} \cdot d\mathbf{l},$$

$$(1.24) \quad \int_V \nabla \cdot \mathbf{A} = \oint_{\partial V} \mathbf{A} \cdot d\mathbf{v}$$

for surfaces, S , and volumes, V , respectively, from which we can derive the classical 3D formulae

$$(1.25) \quad \int_{\Omega} \mathbf{f} \cdot \nabla \times \mathbf{g} = \int_{\Omega} \mathbf{g} \cdot \nabla \times \mathbf{f} + \int_{\partial\Omega} \mathbf{f} \times \mathbf{g} \cdot d\mathbf{v}$$

and

$$(1.26) \quad \int_{\Omega} \psi \nabla \cdot \mathbf{f} = - \int_{\Omega} \nabla \psi \cdot \mathbf{f} + \int_{\partial\Omega} \psi \mathbf{f} \cdot d\mathbf{v}.$$

In cylindrical coordinates, the gradient, curl and divergence are given by

$$(1.27) \quad \nabla \Phi = \hat{\rho} \frac{\partial \Phi}{\partial \rho} + \hat{\phi} \frac{1}{\rho} \frac{\partial \Phi}{\partial \phi} + \hat{z} \frac{\partial \Phi}{\partial z},$$

$$(1.28) \quad \nabla \times \mathbf{A} = \hat{\rho} \left[\frac{1}{\rho} \frac{\partial A_z}{\partial \phi} - \frac{\partial A_{\phi}}{\partial z} \right] + \hat{\phi} \left[\frac{\partial A_{\rho}}{\partial z} - \frac{\partial A_z}{\partial \rho} \right] + \hat{z} \left[\frac{1}{\rho} \frac{\partial}{\partial \rho} (\rho A_{\phi}) - \frac{1}{\rho} \frac{\partial A_{\rho}}{\partial \phi} \right],$$

$$(1.29) \quad \nabla \cdot \mathbf{A} = \frac{1}{\rho} \frac{\partial}{\partial \rho} (\rho A_{\rho}) + \frac{1}{\rho} \frac{\partial A_{\phi}}{\partial \phi} + \frac{\partial A_z}{\partial z}.$$

Direct sum decompositions

For a simple application of Sobolev spaces, we can consider the space $H^{curl}(\Omega)$ which is the completion of $(C^\infty(\Omega))^3$ under the norm

$$(1.30) \quad \|u\|_{curl}^2 = \int_{\Omega} u \cdot \bar{u} + \nabla \times u \cdot \nabla \times \bar{u}$$

and the subspace

$$(1.31) \quad X_0 = \{\nabla \chi \text{ such that } \chi \in H^1(\Omega) \text{ and } \chi|_{\partial\Omega} = 0\}.$$

X_0 is complete under the $\|\cdot\|_{curl}$ norm and is a closed subspace of H^{curl} so has a well-defined orthogonal space X_0^\perp :

$$(1.32) \quad X_0^\perp = \{u \in H^{curl} \text{ such that } \int_{\Omega} u \cdot \bar{v} + \nabla \times u \cdot \nabla \times \bar{v} = 0 \text{ for all } v \in X_0\}$$

i.e.,

$$(1.33) \quad X_0^\perp = \{u \in H^{curl} \text{ such that } \int_{\Omega} u \cdot \nabla \bar{\chi} = 0 \forall \chi \in H_0^1(\Omega)\}$$

$$(1.34) \quad = \{u \in H^{curl} \text{ such that } \int_{\Omega} (\nabla \cdot u) \bar{\chi} = 0 \forall \chi \in H_0^1(\Omega)\}$$

where we have used equation (1.26) and the fact that $\chi = 0$ on $\partial\Omega$. In general, $u \in H^{curl}$ need only be tangentially continuous, so that $\nabla \cdot u \in H^{-1}(\Omega)$, but $H_0^1(\Omega)$ is the dual space of $H^{-1}(\Omega)$ so the only way for $\langle \nabla \cdot u, \bar{\chi} \rangle$ to be zero for all χ is if $\nabla \cdot u \equiv 0$. As $H^{curl} = X_0 \oplus X_0^\perp$, we have thus proved

Theorem 6 Every element $u \in H^{curl}(\Omega)$ can be written uniquely as $u = \nabla \chi + v$ where $\nabla \cdot v = 0$ and $\chi = 0$ on $\partial\Omega$.

In particular, $v \in H^1(\Omega)^3$ even though u itself can be discontinuous.

If we remove the boundary restriction on χ , we increase X_0 slightly to

$$(1.35) \quad X = \{\nabla \chi \text{ such that } \chi \in H^1(\Omega)\}.$$

By applying the same reasoning as above to this subspace we get that

Theorem 7 Every element $u \in H^{curl}(\Omega)$ can be written uniquely as $u = \nabla \chi + v$ where $\nabla \cdot v = 0$ and $v \cdot \hat{\nu} = 0$ on $\partial\Omega$.

Lastly, we can write

$$(1.36) \quad \hat{X} = \{\mathbf{u} \in H^{curl} \text{ such that } \nabla \times \mathbf{u} = 0\},$$

which is a larger space than X if Ω is not simply connected. We obtain the decomposition

Theorem 8 *Every element $\mathbf{u} \in H^{curl}(\Omega)$ can be written uniquely as $\mathbf{u} = \mathbf{w} + \mathbf{v}$ where $\nabla \times \mathbf{w} = 0$, $\nabla \cdot \mathbf{v} = 0$, $\mathbf{v} \cdot \hat{\nu} = 0$ on $\partial\Omega$ and moreover $\langle \mathbf{v}, \mathbf{f} \rangle = 0$ for any \mathbf{f} with $\nabla \times \mathbf{f} = 0$ even if \mathbf{f} is not the gradient of a scalar.*

In each case, note that uniqueness of the decomposition can also be established directly, for example, if $\nabla \chi \in X_0^\perp$ then $\nabla \cdot \nabla \chi = 0$ with $\chi = 0$ on $\partial\Omega$ which has the unique solution $\chi \equiv 0$.

1.3 Sparse matrices

Sparse matrices arise naturally in the study of finite element problems because of the inherently local nature of the differential operators. We give a brief overview of some standard techniques used to manipulate sparse matrices. Non-local behaviour may be observed on the boundaries, for example representations of the boundary conditions "at infinity" may be non-local and conditions on the tool can also be non-local, especially when dealing with focussed electrode devices. Such boundary conditions will not significantly decrease the sparsity of A .

The most fundamental question is how to store the matrix A . We define the profile of the $N \times N$ matrix A to be the smallest number $p(i) \geq 0$, $i = 1, \dots, N$ such that $A_{ij} = 0$ if $|i - j| > p(i)$. The maximum value of $p(i)$ is termed the bandwidth (or more precisely the half-bandwidth). If A is symmetric, profile or skyline storage for A is A where

$$A_{ij} = A[D[I] + J - I] \quad \text{and} \quad D(i) = 1 + \sum_{k=1}^{i-1} (p(k) + 1).$$

The zero elements of A beyond the profile are not stored. $D[I]$ gives the location in A of the diagonal of the I th row. We can use a similar profile storage scheme if A is not symmetric. An advantage of this formulation is that if $A = LU$ is a factorization of A as a product of lower and upper triangular matrices, then L and U can lie in the same storage structure as A . If A is symmetric then $U = DL^t$ for some diagonal matrix D . We can always choose L to have unit diagonals. The following algorithm known as row-wise Gaussian elimination, [5],

computes U and L from A

$$(1.37) \quad \begin{aligned} U_{ij} &= A_{ij} - \sum_{r=1}^{i-1} L_{ir} U_{rj} && \text{for } i \leq j, \\ L_{ij} &= \left(A_{ij} - \sum_{r=1}^{j-1} L_{ir} U_{rj} \right) / U_{jj} && \text{for } i > j, \end{aligned}$$

where we proceed in the row-wise fashion

$$(1.38) \quad (i, j) = (1, 1), (1, 2), \dots, (1, n), (2, 1), \dots, (N, N).$$

If we do not store the diagonal of L then in fact we can overlay L and U into the *same* storage as A . If A is symmetric then we do not need to store L at all.

The major disadvantage of the profile storage scheme is that it can be very large. In a typical finite element problem on, say, a $n \times n \times n$ mesh the profile of A will be $O(n^2)$ even though most of the entries within that profile are zero. The corresponding entries in L and U , however, will not be zero, a phenomenon known as fill-in, [22]. Moreover, it is strongly oriented towards Gaussian elimination, which can be an expensive solution strategy. An alternative approach is to only store the non-zeros of A .

RS/CS storage system

This method of storing a matrix requires two pointer (integer) arrays in addition to a packed array containing the non-zero data (which we shall assume to be complex valued). The first pointer array $RS(I)$ indicates the location in $A(*)$ of the first nonzero element of each row. I.e., the storage locations $A[J]$, $J=RS[I], \dots, RS[I+1]-1$ contain the non-zero elements on the I th row. We set $RS[N+1]-1$ to point to the last element of A . We should stress that $RS(I)$ refers to a storage location within $A(*)$ and not within $A(*, *)$. The second array $CS(*)$ lists the corresponding column numbers. An example may make this clearer. Consider the matrix

$$(1.39) \quad A = \begin{pmatrix} 1 & 0 & 0 & -1 \\ 0 & 8 & -3 & 4 \\ 0 & -3 & 5 & 0 \\ -1 & 4 & 0 & 6 \end{pmatrix}.$$

The corresponding data storage is:

$$\begin{aligned} A &= 1 \ -1 \ 8 \ -3 \ 4 \ -3 \ 5 \ -1 \ 4 \ 6 \\ CS &= 1 \ 4 \ 2 \ 3 \ 4 \ 2 \ 3 \ 1 \ 2 \ 4 \\ RS &= 1 \ 3 \ 6 \ 8 \ 11 \end{aligned}$$

E.g., the data for the third row lies in $A(*)$ and $CS(*)$ starting from location $RS(3) = 6$ to $RS(4)-1 = 7$, i.e., the elements of $A(3, *)$ are -3, 5, with corresponding columns 2, 3.

Other storage schemes

For symmetric matrices, there is clearly redundant information in the above system and an obvious contraction is to, say, not include lower triangular components in $A(*)$:

$$\begin{array}{rcl} A & = & 1 \ -1 \ 8 \ -3 \ 4 \ 5 \ 6 \\ CS & = & 1 \ 4 \ 2 \ 3 \ 4 \ 3 \ 4 \\ RS & = & 1 \ 3 \ 6 \ 7 \ 8 \end{array}$$

The first scheme has the disadvantages that it is slightly awkward to locate diagonal entries of A , whilst in the symmetric scheme traversing columns (as will be required in the ILU preconditioning step, for example) is inconvenient. Other popular choices include storing the diagonal entry *first* on each row (e.g., [36]) and storing the symmetric matrix in column oriented storage (recommended by [5]). The simplicity of the RS/CS scheme tends to outweigh its disadvantages, however, and will be the method used exclusively in this text.

Given the RS/CS storage scheme, multiplication $y = Ax$ is quite straightforward:

```
DO I = 1, N
  Y[I] = 0
END DO
DO I = 1, N
  DO J = RS[I], RS[I+1] - 1
    Y[I] = Y[I] + A[J]*X[CS[J]]
  END DO
END DO
```

1.3.1 Stencil formulations

An alternative approach is possible if the matrix A arises from a uniform mesh. For example supposing Ω to be a rectangular domain in the ρ, z plane, we can construct a mesh of rectangles given partitions $\rho_0, \dots, \rho_N, z_0, \dots, z_M$ along $\partial\Omega$. We do not number the nodes from $1, \dots, N_\rho N_z$ but retain the 2D structure. The discretization space, $V_h^\rho \otimes V_h^z$, is the tensor product of the 1D discretizations in ρ and z .

Matrix assembly is simplified because we know a priori that ij will be a neighbour of pq if and only if $|i - p| \leq 1$ and $|j - q| \leq 1$. The global stiffness matrix of equation (1.22) will have a nine-point stencil at each node and is most easily coded in FORTRAN as

$A[-1:1, -1:1, 0:NRHO, 0:NZ]$. There is no need for an RS/CS data structure. For example, if A is symmetric, multiplication of $y = Ax$ becomes:

```
DO I = 0, NRHO
  DO J = 0, NZ
    Y[I,J] = A[-1,-1,I,J]*X[I-1,J-1] + A[ 0,-1,I,J]*X[I  ,J-1]
            + A[ 1,-1,I,J]*X[I+1,J-1] + A[-1, 0,I,J]*X[I-1,J  ]
            + A[ 0, 0,I,J]*X[I  ,J  ] + A[ 1, 0,I,J]*X[I+1,J  ]
            + A[-1, 1,I,J]*X[I-1,J+1] + A[ 0, 1,I,J]*X[I  ,J+1]
            + A[ 1, 1,I,J]*X[I+1,J+1]
  END DO
END DO
```

Pointer arithmetic is avoided and the compiler can generate gather-scatter operations at compile-time if needed. Appropriate care needs to be taken, however, to ensure that $A[P, Q, I, J]$ is zero if $X[I+P, J+Q]$ is exterior to the domain.

1.4 Maxwell's equations of electromagnetics

In this section, we present an overview of Maxwell's equations, boundary conditions, generic sources and material properties. We shall assume a time harmonic excitation of the form $e^{-i\omega t}$ and suppose that a current source \mathbf{J} excites an electric field \mathbf{E} and magnetic field \mathbf{H} within some domain $\Omega \subset \mathbb{R}^3$. Here \mathbf{J} , \mathbf{E} , and \mathbf{H} are three dimensional, complex valued vector fields. Maxwell's equations describe the relationships between these fields in terms of the constitutive properties of the medium:

$$(1.40a) \quad \nabla \times \mathbf{H} = (\sigma - i\omega\epsilon)\mathbf{E} + \mathbf{J},$$

$$(1.40b) \quad \nabla \times \mathbf{E} = i\omega\mu\mathbf{H},$$

$$(1.40c) \quad \nabla \cdot \epsilon\mathbf{E} = \rho_T,$$

$$(1.40d) \quad \nabla \cdot \mu\mathbf{H} = 0,$$

where σ is the electrical conductivity, ϵ is the electrical permittivity, and μ the magnetic permeability. In general, we shall suppose that each of these constitutive parameters is real valued and strictly positive within Ω . $\sigma\mathbf{E}$ is termed the induced ohmic current, $-i\omega\epsilon\mathbf{E}$ the induced displacement current and \mathbf{J} the impressed current.

In equation (1.40c), ρ_T denotes the total electric charge density in the domain. If we take the

divergence of equation (1.40a) we obtain

$$(1.41) \quad i\omega\rho_T = \nabla \cdot (\mathbf{J} + \sigma\mathbf{E}),$$

so that ρ_T has contributions from both the divergence of the impressed current and also from $\nabla \cdot \sigma\mathbf{E}$. We will obtain charge accumulation at points of discontinuity of $\sigma\mathbf{E}$. These accumulated charges contribute to ρ_T . Only in the special case that $\sigma = 0$ can we know ρ_T a priori. As this occurs rarely in geophysical problems (essentially only within the interior of resistivity tools!) we shall not use ρ_T in the remainder of this dissertation. (In very low resistivity anhydrites and halites, we shall always assume that there is *some* nonzero conductivity σ .)

We do not suppose that the material properties are smoothly varying and so equations (1.40a) – (1.40d) must be understood in the weak or distributional sense. In particular, if we choose constant test functions, we obtain the global integral formulations of Maxwell's equations:

Ampère's Law

$$(1.42) \quad \int_S \nabla \times \mathbf{H} \cdot d\boldsymbol{\nu} = \oint_{\partial S} \mathbf{H} \cdot d\mathbf{l} = \int_S \sigma\mathbf{E} \cdot d\boldsymbol{\nu} - i\omega \int_S \epsilon\mathbf{E} \cdot d\boldsymbol{\nu} + \int_S \mathbf{J} \cdot d\boldsymbol{\nu},$$

Faraday's Law

$$(1.43) \quad \int_S \nabla \times \mathbf{E} \cdot d\boldsymbol{\nu} = \oint_{\partial S} \mathbf{E} \cdot d\mathbf{l} = i\omega \int_S \mu\mathbf{H} \cdot d\boldsymbol{\nu},$$

Gauss' Law of Electricity

$$(1.44) \quad \oint_{\partial V} \epsilon\mathbf{E} \cdot d\boldsymbol{\nu} = \int_V \rho_T dV,$$

Gauss' Law of Magnetism

$$(1.45) \quad \oint_{\partial V} \mu\mathbf{H} \cdot d\boldsymbol{\nu} = 0,$$

for a 2D surface, S , or 3D volume, V , in Ω and $d\boldsymbol{\nu} = \hat{\boldsymbol{\nu}}dS$, etc.

From these equations, we can derive the standard boundary conditions across domains of discontinuity in the material properties (e.g., [11], [25], [26]) which we do not repeat here, save to note that the tangential electric and magnetic fields must always be continuous across an interface if the conductivities are finite. In a well posed finite element formulation, boundary conditions interior to the domain (e.g., at formation bed boundaries) will be natural with respect to the Galerkin operator, [42].

Implementation of approximate boundary conditions at infinity have typically played an important role in FEM, but in geophysical applications the fields will decay rapidly (exponentially in many cases) from the sources and homogeneous Neumann or Dirichlet conditions are not inappropriate provided the boundaries are taken sufficiently far from the sources. In Chapters 3 and 4, we discuss boundary conditions on tool surfaces and electrodes. Boundary conditions on cable armour are given in Chapter 3 and boundary conditions across imperfect electrodes are given in Chapter 4. Here we shall limit ourselves to a discussion of boundary conditions across perfect conductors and insulators.

1.4.1 Perfect conductors and insulators

For almost all situations in resistivity modelling, the ohmic current is non-zero. However, for some tool configurations, we also need to postulate the existence of a 'perfect insulator' where σ and $i\omega\epsilon$ are *both* so small that we can take $\sigma \equiv i\omega\epsilon \equiv 0$. We suppose that $\mu = \mu_0$, the permeability of free space, inside a 'perfect insulator.' The electromagnetic field inside a perfect insulator need not be zero. The opposite case of extremely large conductivity, termed a 'perfect conductor' is less problematical because the electromagnetic field therein must be zero.⁸ We shall typically suppose that perfect conductors have been removed from Ω and replaced with suitable boundary conditions on \mathbf{E} and \mathbf{H} . More specifically, we have:

Theorem 9 *On the boundary of a perfect conductor, the tangential component of \mathbf{E} and the normal component of \mathbf{H} are both zero.*

The normal component of \mathbf{E} and tangential component of \mathbf{H} need not be zero. We define the surface current to be

$$(1.46) \quad \mathbf{J}_s = \hat{\nu} \times \mathbf{H}.$$

Across the boundary of a perfect insulator the tangential components of \mathbf{E} and \mathbf{H} are both continuous. This is clearly *not* necessarily the case for perfect conductors. The normal components of $\mu\mathbf{H}$ and $(\sigma - i\omega\epsilon)\mathbf{E}$ are, however, continuous for both cases.

Unlike 'perfect' electrical conductors, perfect electrical insulators do not exist in nature, but their use simplifies some mathematical formulations. In practice, a 'perfect' insulator is one in which $\sigma \approx 0$ and the dimensions of which are so small that displacement currents can be

⁸If $\omega = 0$ and $\sigma = \infty$, there could also exist a so-called magnetostatic field $\mathbf{H} = \nabla\chi$ with $\nabla \cdot \mu\nabla\chi = 0$. We can always ignore this magnetostatic component in resistivity modelling.

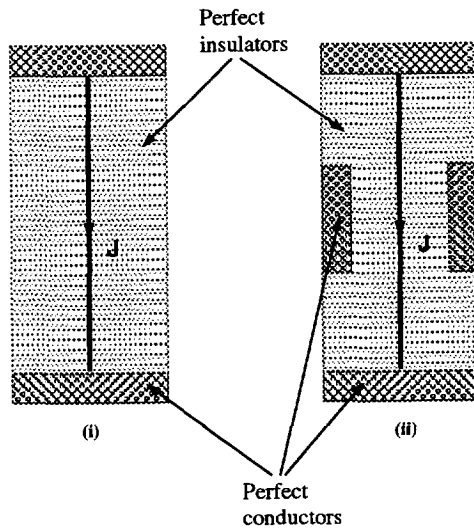


Figure 1.4: Formulation purely in terms of tangential \mathbf{H} on the insulating boundaries of the axisymmetric cylinder will be valid for (i) and invalid for (ii). J denotes a possible current source along a wire at the centre of the cylinders.

assumed negligible. For example, we will suppose that the certain sections of the Laterolog consist of perfect insulators with a current carrying wire down the centre of the insulator.

The field within a perfect insulator is not zero but if we are given all three components of either the electric or magnetic field on the boundary then the field inside is unique. The following (admittedly perverse) example shows that it is not sufficient to be only given the tangential magnetic field on the boundary of a perfect insulator. Figure 1.4 shows two cylindrical domains with perfectly conducting caps at $z = 0$ and $z = L$ connected by a current carrying wire at the centre of the cylinder. In the second case, there is also an annular conducting ring around the middle of the domain. In this case, one can construct a function ψ which is "1" above the conducting ring and "0" below and such that $\nabla^2 \psi = 0$. On the metallic boundaries we can choose $\nabla \psi \cdot \hat{\nu} = 0$. The magnetic field $\mathbf{H} = \nabla \psi$ will have zero tangential component on the insulators but be non-zero inside the domain. Such a ψ cannot be constructed in case (i). For this geometry, specifying tangential magnetic field on the insulating sections *will* give a unique solution on the interior of the domain.

Such problems of non-uniqueness are not restricted to perfect insulators. [27] and [28] show how non-uniqueness can arise in magnetic scalar potentials in multiply connected regions and

Kotiuga relates this non-uniqueness to elements of relative cohomology groups [6], [41].

We shall see in Section 1.4.4 that if $|\sigma - i\omega\epsilon|$ is bounded away from zero then specifying tangential EM fields will give rise to a unique solution. In Section 1.4.6 we also examine the case when Ω contains perfect insulators.

1.4.2 Reciprocity

Following [23] and [26], we consider two time-harmonic sources \mathbf{J}_a and \mathbf{J}_b in a domain Ω subject to appropriate boundary conditions. These sources generate electromagnetic fields $\mathbf{E}_a, \mathbf{H}_a$ and $\mathbf{E}_b, \mathbf{H}_b$ respectively. The *reaction* between the two fields is defined in [39] as

$$(1.47) \quad [a, b] = \int_{\Omega} \mathbf{J}_a \cdot \mathbf{E}_b$$

and it is clear that

$$(1.48) \quad [a, b] - [b, a] = \int_{\Omega} \nabla \cdot (\mathbf{E}_b \times \mathbf{H}_a - \mathbf{E}_a \times \mathbf{H}_b) = \int_{\partial\Omega} (\mathbf{E}_b \times \mathbf{H}_a - \mathbf{E}_a \times \mathbf{H}_b) \cdot d\boldsymbol{\nu},$$

which [14], [15] and [20] cite as a special case of the Lorenz reciprocity theorem. Depending upon the boundary conditions imposed on $\partial\Omega$, we may have that $[a, b] = [b, a]$ in which case we describe the system as *reciprocal*. In particular, any boundary condition of the form

$$\alpha \hat{\boldsymbol{\nu}} \times \mathbf{E} + \beta \hat{\boldsymbol{\nu}} \times \hat{\boldsymbol{\nu}} \times \mathbf{H} = 0$$

(where α and β are arbitrary) will give rise to a reciprocal system. Boundary conditions involving tangential derivatives and those corresponding to focussed Laterologs can give rise to non-reciprocal systems as we shall see in Chapter 2. An unbounded (isotropic) domain will always be reciprocal as the fields will decay to zero at infinity. In an anisotropic domain, the material properties σ , ϵ and μ are tensors, not scalars, with

$$(1.49) \quad \nabla \times \mathbf{E} = i\omega \bar{\bar{\mu}} \mathbf{H}, \quad \text{and} \quad \nabla \times \mathbf{H} = (\bar{\bar{\sigma}} - i\omega \bar{\bar{\epsilon}}) \mathbf{E} + \mathbf{J}.$$

For the anisotropic case, we can only have a reciprocal system if, in addition to the appropriate conditions on $\partial\Omega$, we have that the material property tensors are *symmetric* (e.g., $\bar{\bar{\sigma}} = \bar{\bar{\sigma}}^t$), [14], [15].

We shall see in Chapter 2 that in a finite element context reciprocity corresponds to symmetric (or complex symmetric) matrices, for which sophisticated inversion methods exist. If we introduce feedback circuits on electrodes to enforce focussing conditions then the resulting finite element matrices need not be symmetric and so harder to invert. Solution techniques which avoid this problem are also presented in Chapter 2.

1.4.3 Weak formulation of Maxwell's equations

In general, to solve for \mathbf{E} and \mathbf{H} , we will remove perfect conductors and perfect insulators from Ω and replace them with boundary conditions on $\partial\Omega$. We can suppose that the tangential \mathbf{E} field is zero across the perfect conductors and let us suppose that we have been able to solve for the \mathbf{H} field within the perfect insulators ($= \overline{\mathbf{H}}$, say). In this case, following [40], p. 48, we can write $\partial\Omega = \partial\Omega_0 \cup \partial\Omega_\nu$ where $\mathbf{H} \times \nu = \overline{\mathbf{H}} \times \nu$ on $\partial\Omega_0$ and $\mathbf{E} \times \nu = 0$ on $\partial\Omega_\nu$. From (1.40a) and (1.40b) we have

$$(1.50) \quad \nabla \times \frac{1}{\sigma - i\omega\epsilon} \nabla \times \mathbf{H} - i\omega\mu\mathbf{H} = \nabla \times \frac{\mathbf{J}}{\sigma - i\omega\epsilon},$$

which we interpret in the weak form

$$(1.51) \quad \int_{\Omega} \mathbf{h} \cdot \nabla \times \frac{1}{\sigma - i\omega\epsilon} \nabla \times \mathbf{H} - i\omega\mu \mathbf{h} \cdot \mathbf{H} = \int_{\Omega} \mathbf{h} \cdot \nabla \times \frac{\mathbf{J}}{\sigma - i\omega\epsilon} \quad \forall \mathbf{h} \in H_0^{curl}(\Omega).$$

Here $H_0^{curl}(\Omega)$ is the Sobolev space containing those fields, $\mathbf{h} \in H^{curl}(\Omega)$, such that $\mathbf{h} \times \hat{\nu} = 0$ on $\partial\Omega_0$. [34]. We do not suppose \mathbf{h} to be continuous. The integrals in Equation (1.51) will exist in the classical sense after integration by parts (equation (1.25))

$$(1.52) \quad \int_{\Omega} \frac{1}{\sigma - i\omega\epsilon} \nabla \times \mathbf{h} \cdot \nabla \times \mathbf{H} - i\omega\mu \mathbf{h} \cdot \mathbf{H} + \oint_{\partial\Omega} \frac{1}{\sigma - i\omega\epsilon} \mathbf{h} \cdot (\nabla \times \mathbf{H}) \times \hat{\nu} \\ = \int_{\Omega} \mathbf{h} \cdot \nabla \times \frac{\mathbf{J}}{\sigma - i\omega\epsilon}.$$

Because $\mathbf{H} \times \hat{\nu}$ is prescribed on $\partial\Omega_0$ we have set to zero the tangential component of \mathbf{h} on $\partial\Omega_0$ to avoid an overdetermined system. On the remainder of $\partial\Omega$, $(\nabla \times \mathbf{H}) \times \hat{\nu} = \hat{\nu} \times (\sigma - i\omega\epsilon)\mathbf{E}$ is zero by hypothesis so the boundary integral vanishes from (1.52) to give

$$(1.53) \quad A_{\omega}(\mathbf{H}, \mathbf{h}) = \int_{\Omega} \mathbf{h} \cdot \nabla \times \frac{\mathbf{J}}{\sigma - i\omega\epsilon} = \langle \mathbf{M}, \mathbf{h} \rangle \quad \forall \mathbf{h} \in H_0^{curl}(\Omega)$$

where the bilinear form

$$(1.54) \quad A_{\omega}(\mathbf{f}, \mathbf{g}) = \int_{\Omega} \frac{\nabla \times \mathbf{f} \cdot \nabla \times \mathbf{g}}{\sigma - i\omega\epsilon} - i\omega\mu \mathbf{f} \cdot \mathbf{g}$$

and

$$(1.55) \quad \mathbf{M} = \nabla \times \frac{\mathbf{J}}{\sigma - i\omega\epsilon}.$$

In the next section, we show that A_ω is coercive and hence can use the Lax-Milgram theorem to guarantee existence of a solution to (1.53) within a bounded domain where $0 < |\sigma - i\omega\epsilon| < \infty$. Note that standard texts do *not* discuss the question of existence, only uniqueness, which is simpler.

1.4.4 Existence of a solution

Assume that $\partial\Omega$ is divided into two regions $\partial\Omega_0$ where the tangential \mathbf{H} field is zero and $\partial\Omega_\nu$ where the tangential \mathbf{E} field is zero. We can think of $\partial\Omega_0$ as bounding a source free perfect insulator and $\partial\Omega_\nu$ as bounding a perfect conductor. Let $H_0^{curl}(\Omega)$ be the subset of $H^{curl}(\Omega)$ consisting of those functions which are tangentially zero on $\partial\Omega_0$. We shall show that the bilinear form $A_\omega(\mathbf{f}, \mathbf{g})$ is coercive over $H_0^{curl}(\Omega)$ if σ, ϵ and μ are all real and bounded away from zero and ω is strictly positive. As an immediate corollary of the Lax-Milgram lemma, a solution to

$$A_\omega(\mathbf{H}, \mathbf{h}) = \langle \mathbf{M}, \mathbf{h} \rangle \quad \forall \mathbf{h} \in H_0^{curl}(\Omega)$$

must exist and be unique. Moreover the bounds on A_ω will give a relationship between $\|\mathbf{H}\|_{curl}$ and $\|\mathbf{M}\|_{curl}$, where

$$(1.56) \quad \|\mathbf{H}\|_{curl}^2 = \int_{\Omega} |\mathbf{H}|^2 + |\nabla \times \mathbf{H}|^2$$

is the norm on $H^{curl}(\Omega)$.

Let us write $1/(\sigma - i\omega\epsilon)$ as $\rho' + i\rho''$ and by hypothesis $0 < \rho'_{min} \leq \rho' \leq \rho'_{max} < \infty$ over Ω and similarly for ρ'' . For notational simplicity, we assume that μ is constant.

We have that

$$(1.57) \quad |A_\omega(\mathbf{f}, \bar{\mathbf{f}})|^2 = \left\{ \int_{\Omega} \rho' \|\nabla \times \mathbf{f}\|^2 \right\}^2 + \left\{ \int_{\Omega} \rho'' \|\nabla \times \mathbf{f}\|^2 - \omega\mu \|\mathbf{f}\|^2 \right\}^2,$$

so

$$(1.58) \quad \frac{|A_\omega(\mathbf{f}, \bar{\mathbf{f}})|^2}{\|\mathbf{f}\|_0^4} \geq \lambda \left\{ \frac{\int \|\nabla \times \mathbf{f}\| \rho''}{\int \|\mathbf{f}\|^2} \right\}^2 + \left\{ \frac{\int \|\nabla \times \mathbf{f}\| \rho''}{\int \|\mathbf{f}\|^2} - \omega\mu \right\}^2,$$

where $\lambda = \rho'_{min}/\rho'_{max}$. Now if $f(x) = \lambda x^2 + (x - \omega\mu)^2$ then $f(x)$ has a minimum when $x = \omega\mu/(\lambda + 1)$, namely $f = \omega^2\mu^2\lambda/(\lambda + 1)$ so for any $x \in \mathbb{R}$, $\lambda x^2 + (x - \omega\mu)^2 \geq \omega^2\mu^2\lambda/(\lambda + 1)$ and hence

$$(1.59) \quad \frac{|A_\omega(\mathbf{f}, \bar{\mathbf{f}})|^2}{\|\mathbf{f}\|_0^4} \geq \frac{\omega^2\mu^2\lambda}{\lambda + 1} = \gamma^2$$

and

$$(1.60) \quad |A_\omega(\mathbf{f}, \bar{\mathbf{f}})| \geq \gamma \|\mathbf{f}\|_0^2.$$

Certainly,

$$(1.61) \quad |A_\omega(\mathbf{f}, \bar{\mathbf{f}})| \geq \rho'_{min} \int_{\Omega} \|\nabla \times \mathbf{f}\|^2$$

and so (possibly with a different value of γ)

$$(1.62) \quad |A(\mathbf{f}, \bar{\mathbf{f}})| \geq \gamma \|\mathbf{f}\|_{curl}^2.$$

Note that in particular that $\gamma \rightarrow 0$ as $\omega \rightarrow 0$, $\rho'_{min} \rightarrow 0$ or $\rho''_{max} \rightarrow \infty$.

Boundedness is easier to prove as $(a - b)^2 \leq 2a^2 + 2b^2$ and so

$$(1.63) \quad |A_\omega(\mathbf{f}, \bar{\mathbf{f}})|^2 \leq \left\{ \rho'_{max} \int_{\Omega} \|\nabla \times \mathbf{f}\|^2 \right\}^2 + 2 \left\{ \rho''_{max} \int_{\Omega} \|\nabla \times \mathbf{f}\|^2 \right\}^2 + 2 \left\{ \omega \mu \int_{\Omega} \|\mathbf{f}\|^2 \right\}^2$$

and

$$(1.64) \quad |A_\omega(\mathbf{f}, \bar{\mathbf{f}})| \leq C \int_{\Omega} \|\mathbf{f}\|^2 + \|\nabla \times \mathbf{f}\|^2$$

for a suitable choice of C .

Thus by the Lax-Milgram lemma provided ω is bounded away from zero A_ω is coercive and a solution to Maxwell's equation will exist in $H^{curl}(\Omega)$ (at least in a distributional sense) and be unique. Also note that as the frequency tends to zero, the bound C/γ on $\|\mathbf{H}\|$ will tend to infinity and the solution will become more and more unstable. In fact, equation (1.53) has a weak singularity at $\omega = 0$. To obtain uniqueness and existence at $\omega = 0$, it is necessary to impose equation (1.40d). In the next section, we discuss the formulation of Maxwell's equations at zero frequency.

1.4.5 Maxwell's equations at DC

When $\omega = 0$, Maxwell's equations for the magnetic field are

$$(1.65) \quad \nabla \times \mathbf{H} = \sigma \mathbf{E} + \mathbf{J},$$

$$(1.66) \quad \nabla \times \mathbf{E} = 0$$

and

$$(1.67) \quad \nabla \cdot \mu \mathbf{H} = 0,$$

whence

$$(1.68) \quad \nabla \times \frac{1}{\sigma} \nabla \times \mathbf{H} = \nabla \times \frac{\mathbf{J}}{\sigma} \quad \text{and} \quad \nabla \cdot \mu \mathbf{H} = 0$$

which we term the \mathbf{H} -formulation.

Alternatively, if $\pi_1(\Omega) = 0$ then from Theorem 4, $\mathbf{E} = -\nabla\Phi$ for some scalar field Φ and we obtain Poisson's equation

$$(1.69) \quad \nabla \cdot \sigma \nabla \Phi = \nabla \cdot \mathbf{J},$$

which we term the Φ -formulation.

Boundary conditions are different from the CW (non-DC) case considered in the previous section. For the Φ formulation, we must prescribe either Φ or $\partial\Phi/\partial\nu$ on the boundary. For the \mathbf{H} formulation, we must prescribe either $\mathbf{H} \times \hat{\nu}$ on the boundary or $\mathbf{H} \cdot \hat{\nu}$.

Existence and uniqueness proofs for the DC case follow familiar arguments (e.g., [5], [12], [42]). The only hard part is to prove coercivity and for this one uses the Poincaré inequality that for any bounded Ω , there exists a $C_\Omega > 0$, such that

$$(1.70) \quad \int_{\Omega} (\nabla \Phi)^2 \geq C_\Omega \int_{\Omega} \Phi^2$$

for all Φ which are constrained to zero on some part of $\partial\Omega$.⁹

1.4.6 Low frequency solutions to Maxwell's equations

We have seen in section 1.4.4 that Maxwell's equations lead to a coercive formulation but that at low frequencies the smallest eigenvalue of the operator A_ω tends to zero. Druskin, [18], has recently shown that if a divergence condition is enforced then coercivity is maintained

⁹e.g., see [12], [35]. [42] gives a simple proof of this inequality for the case $\Omega = (a, b) \subset \mathbb{R}$. It is important that some part of the domain be held to zero otherwise a $\Phi = \chi_\Omega$ would be a counterexample.

regardless of frequency. Specifically, there exists a constant $\gamma > 0$ independent of ω and \mathbf{f} , but depending on the material parameters σ , μ and ϵ such that

$$(1.71) \quad |A_\omega(\mathbf{f}, \bar{\mathbf{f}})| \geq \gamma \|\mathbf{f}\|_{curl}^2 \quad \text{for all } \mathbf{f} \text{ such that } \nabla \cdot \mu \mathbf{f} = 0.$$

An immediate, and important, corollary is that if V_h is a subspace of $H^{curl}(\Omega)$ which has the property that every element of V_h is divergence free then the solution $\hat{\mathbf{H}}_h \in V_h$ to

$$(1.72) \quad A_\omega(\mathbf{H}_h, \mathbf{h}_h) = \langle \mathbf{M}, \mathbf{h}_h \rangle \quad \forall \mathbf{h}_h \in V_h$$

satisfies

$$(1.73) \quad \|\mathbf{H} - \hat{\mathbf{H}}_h\|_{curl}^2 \leq \frac{C}{\gamma} \min_{\mathbf{H}_h \in V_h} \|\mathbf{H} - \mathbf{H}_h\|_{curl}^2$$

where \mathbf{H} is the true solution in H^{curl} , i.e., up to a constant that does not vary with ω , then the finite element solution over V_h is "as close" to \mathbf{H} as the best possible \mathbf{H}_h in V_h . We repeat Druskin's proof here for the convenience of the reader.

Let $\partial\Omega_\nu$ be a subset of the boundary which has the property that there are points where \mathbf{i} , \mathbf{j} and \mathbf{k} are tangent vectors, i.e., $\partial\Omega_\nu$ is such that the constraint $\mathbf{u} \times \boldsymbol{\nu} = 0$ on $\partial\Omega_\nu$ implies that $u_x = 0$ somewhere on $\partial\Omega_\nu$, $u_y = 0$ somewhere on $\partial\Omega_\nu$ and $u_z = 0$ somewhere on $\partial\Omega_\nu$. In that case, the Poincaré inequality, (1.70), applied separately to each component of \mathbf{u} gives that for some $\gamma > 0$

$$(1.74) \quad \int_\Omega \nabla \mathbf{u} : \nabla \bar{\mathbf{u}} \geq \gamma \int_\Omega \mathbf{u} \cdot \bar{\mathbf{u}}$$

for all \mathbf{u} satisfying $\mathbf{u} \times \boldsymbol{\nu} = 0$ on $\partial\Omega_\nu$. From this it is immediately clear that

$$(1.75) \quad \int_\Omega \nabla \times \mathbf{E} \cdot \nabla \times \bar{\mathbf{E}} \geq \gamma \int_\Omega \mathbf{E} \cdot \bar{\mathbf{E}}$$

for all \mathbf{E} satisfying $\mathbf{E} \times \boldsymbol{\nu} = 0$ on $\partial\Omega_\nu$ with $\nabla \cdot \mathbf{E} = 0$. We shall write $\partial\Omega_0$ for $\partial\Omega - \partial\Omega_\nu$ and suppose that $(\nabla \times \mathbf{E}) \times \boldsymbol{\nu} = 0$ on $\partial\Omega_0$.

As μ is real, we thus have

$$(1.76) \quad \int_\Omega \frac{1}{\mu} |\nabla \times \mathbf{E}|^2 \geq \frac{\gamma}{\mu_{max}} \int_\Omega |\mathbf{E}|^2$$

$$(1.77) \quad = \alpha \int_\Omega |\mathbf{E}|^2,$$

say. Let α_0 be the largest such value of α for which the bound holds.

Druskin's proof relies on the observation that for a bounded linear functional A , then if λ is the maximum value such that $\bar{\mathbf{x}}^t A \mathbf{x} \geq \lambda \bar{\mathbf{x}}^t \mathbf{x}$ then λ is also the *minimum* value such that $\bar{\mathbf{x}}^t A \mathbf{x} = \lambda \bar{\mathbf{x}}^t \mathbf{x}$ has a non-zero solution.

So for the case here, α_0 is the smallest value of α such that

$$(1.78) \quad \int_{\Omega} \frac{1}{\mu} |\nabla \times \mathbf{E}|^2 = \alpha \int_{\Omega} |\mathbf{E}|^2$$

has a non-zero solution. Let \mathbf{E}_0 be that solution. As α_0 is non-zero it is also easy to show that $\nabla \cdot \mathbf{E}_0 = 0$. Let $\mathbf{H}_0 = 1/\mu \nabla \times \mathbf{E}_0$, then \mathbf{H}_0 is non-zero and

$$(1.79) \quad \nabla \times \nabla \times \mathbf{H}_0 = \alpha_0 \mu \mathbf{H}_0$$

with $\mathbf{H}_0 \times \hat{\nu} = 0$ on $\partial\Omega_{\nu}$ and $(\nabla \times \mathbf{H}_0) \times \hat{\nu} = 0$ on $\partial\Omega_0$. It is also clear from equation (1.79) that $\nabla \cdot \mu \mathbf{H} = 0$. Moreover, α_0 is the smallest value of α such that

$$\nabla \times \nabla \times \mathbf{H} = \alpha \mu \mathbf{H}$$

has a non-zero solution \mathbf{H} satisfying the divergence and boundary conditions. Finally, assuming σ is real,

$$(1.80) \quad \int_{\Omega} \frac{1}{\sigma} |\nabla \times \mathbf{H}|^2 \geq \alpha_0 \int_{\Omega} \mu |\mathbf{H}|^2 \geq \alpha_0 \mu_{\min} \int_{\Omega} |\mathbf{H}|^2$$

for all \mathbf{H} with $\nabla \cdot \mu \mathbf{H} = 0$, $\mathbf{H} \times \hat{\nu} = 0$ on $\partial\Omega_{\nu}$ and $(\nabla \times \mathbf{H}) \times \hat{\nu} = 0$ on $\partial\Omega_{\nu}$. Note that this bound does not require any smoothness for μ or σ .

[18] also points out that this is a special case of the fact that the set of points λ such that the pencil

$$\nabla \times \frac{1}{\mu} \nabla \times \mathbf{E} = \lambda \sigma \mathbf{E},$$

$$\mathbf{E} \times \hat{\nu} = 0 \quad \text{on } \partial\Omega_{\nu} \quad (\nabla \times \mathbf{E}) \times \hat{\nu} = 0 \quad \text{on } \partial\Omega_0,$$

has a non-zero solution is the same as that set for the pencil

$$\nabla \times \frac{1}{\sigma} \nabla \times \mathbf{H} = \lambda \mu \mathbf{H},$$

$$\mathbf{H} \times \hat{\nu} = 0 \quad \text{on } \partial\Omega_0 \quad (\nabla \times \mathbf{H}) \times \hat{\nu} = 0 \quad \text{on } \partial\Omega_{\nu}.$$

Given equation (1.80) then equation (1.71) follows by applying the result to the real and imaginary parts of $A_{\omega}(\mathbf{f}, \bar{\mathbf{f}})$. From a finite element perspective, this result is a little disatisfying

in that in general it may be highly non-trivial to build approximation spaces in $V_h \subset H^{curl}$ which satisfy $\nabla \cdot \mu \mathbf{H}_h = 0$ for all $\mathbf{H}_h \in V_h$. For this reason, in this thesis, we shall concentrate on two cases for which the construction of V_h is essentially trivial, namely DC solutions in terms of Φ and azimuthally symmetric solutions in terms of H_ϕ . [18] has shown how the divergence condition *can* fit naturally with the Yee-Lebedev finite difference formulation, however.

The imposition of a divergence constraint also allows us to discuss existence and uniqueness over domains Ω which contain perfect insulators. If $\sigma - i\omega\epsilon \equiv 0$ in the closed subdomain $\Omega_0 \subset \Omega$ and $|\sigma - i\omega\epsilon| \geq s > 0$ in $\Omega - \Omega_0$ then define the space

$$(1.81) \quad \mathcal{H} = \{\mathbf{h} \in H^{curl}(\Omega) \text{ such that } \nabla \cdot \mu \mathbf{h} = 0 \text{ and } \nabla \times \mathbf{h} = 0 \text{ on } \Omega_0\},$$

so that, for example, if Ω_0 is simply connected then $\mathbf{h} = \nabla \chi$ on Ω_0 . We redefine A_ω as

$$(1.82) \quad A_\omega(\mathbf{f}, \mathbf{g}) = \int_{\Omega - \Omega_0} \frac{1}{\sigma - i\omega\epsilon} \nabla \times \mathbf{f} \cdot \nabla \times \mathbf{g} - i\omega \int_{\Omega} \mu \mathbf{f} \cdot \mathbf{g},$$

so that A_ω will be bounded over \mathcal{H} . Coercivity follows because for suitable $\gamma > 0$ and $\tilde{\gamma} > 0$

$$(1.83) \quad \begin{aligned} |A_\omega(\mathbf{f}, \bar{\mathbf{f}})| &\geq \gamma \int_{\Omega - \Omega_0} |\nabla \times \mathbf{f}|^2 \\ &= \gamma \int_{\Omega} |\nabla \times \mathbf{f}|^2 \\ &\geq \tilde{\gamma} \int_{\Omega} |\mathbf{f}|^2 \end{aligned}$$

where we have used equation (1.71) and $\tilde{\gamma}$ is independent of ω . A_ω is thus bounded and coercive over \mathcal{H} , so existence and uniqueness (over \mathcal{H}) follows from the Lax-Milgram theorem. If the divergence condition were not imposed, but we still insisted that $\nabla \times \mathbf{h} = 0$ for all $\mathbf{h} \in \mathcal{H}$, then coercivity would still be satisfied but with a constant that tended to zero as $\omega \rightarrow 0$.

1.4.7 TE and TM fields

In 3D, the \mathbf{H} formulation will be more complicated because of the vector nature of the problem and the need to enforce the divergence condition. For DC problems, the Φ formulation is thus much simpler. In some 2D cases, however, the Φ formulation no longer has this advantage. For example, consider an axisymmetric geometry. Maxwell's equations will decouple into two modes "transverse magnetic" (TM) and "transverse electric" (TE) [11], [26]. The first has zero $\hat{\phi}$ component of electric field and the second a zero $\hat{\phi}$ component of magnetic field. The non-zero components of a TM mode are H_ϕ , E_ρ and E_z . The non-zero components of a TE mode are E_ϕ , H_ρ and H_z .

These azimuthal fields can be used as scalar potentials. For example, for the axisymmetric TM case, we have

$$(1.84) \quad \hat{\phi} \cdot \nabla \times \frac{1}{\sigma} \nabla \times (H_\phi \hat{\phi}) = \hat{\phi} \cdot \nabla \times \frac{\mathbf{J}}{\sigma},$$

which is a coercive formulation. Because $\partial/\partial\phi = 0$, the divergence condition is automatically satisfied. Moreover equation (1.84) extends very simply to the CW case:

$$(1.85) \quad \hat{\phi} \cdot \nabla \times \frac{1}{\sigma - i\omega\epsilon} \nabla \times (H_\phi \hat{\phi}) - i\omega\mu H_\phi = \hat{\phi} \cdot \nabla \times \frac{\mathbf{J}}{\sigma - i\omega\epsilon},$$

whereas the Φ formulation is only valid at DC. In Chapters 3 and 4, we discuss other advantages of the H_ϕ formulation.

In Chapter 2, we shall see that resistivity tools on a mandrel divide naturally into those which generate TE fields and those which generate TM. Solenoids generate TE field and while toroids and electrodes generate TM.

1.4.8 General solutions

The simplest solutions arise when the material properties are homogeneous in which case Maxwell's equations reduce to the simpler vector Helmholtz equation

$$(1.86) \quad \nabla \times \nabla \times \mathbf{E} - k^2 \mathbf{E} = i\omega\mu \mathbf{J},$$

where $k^2 = i\omega\mu(\sigma - i\omega\epsilon)$. k is termed the wavenumber of the medium. We can always choose k such that $Re(k) \geq 0$ and $Im(k) \geq 0$. Electromagnetic fields in the medium will propagate as waves with wavenumber k , for example we have plane wave solutions

$$(1.87) \quad \mathbf{E}(\mathbf{r}) = \omega\mu \mathbf{E}_0 e^{i\mathbf{k} \cdot \mathbf{r}} \quad \mathbf{H}(\mathbf{r}) = \mathbf{k} \times \mathbf{E}_0 e^{i\mathbf{k} \cdot \mathbf{r}},$$

where \mathbf{E}_0 is an arbitrary vector (in \mathbb{C}^3) and $\mathbf{k} \cdot \mathbf{r} = k_x x + k_y y + k_z z$ with $k_x^2 + k_y^2 + k_z^2 = k^2$. Some or all of the components of \mathbf{k} will be imaginary. In addition to plane waves, cylindrical waves are often appropriate representations of EM fields in borehole logging. Such waves are most conveniently written in terms of the \hat{z} components of the electric and magnetic field vectors. Waves which are outgoing in the radial direction take the form

$$(1.88) \quad \begin{bmatrix} E_z \\ H_z \end{bmatrix} = e^{ik_z z} e^{\pm i\nu\phi} H_\nu^{(1)}(k_\rho \rho) \begin{bmatrix} e \\ h \end{bmatrix},$$

where e and h are arbitrary constants and $k_\rho^2 + k_z^2 = k^2$. Here $H_\nu^{(1)}$ denotes the ν th order Hankel function of the first kind (e.g., [2], [46]) and we have chosen a branch cut such that

$Im(k_\rho) \geq 0$ for all k_z . These outgoing waves have a singularity at $\rho = 0$. Waves which are nonsingular on the axis take the form

$$(1.89) \quad \begin{bmatrix} E_z \\ H_z \end{bmatrix} = e^{ik_z z} e^{\pm i\nu\phi} J_\nu(k_\rho \rho) \begin{bmatrix} e \\ h \end{bmatrix},$$

where J_n is the n th order Bessel function (e.g., [2], [46]).

If the material properties are constant, but \mathbf{J} is complicated, then (e.g., see [26], p. 229) we can write the general solution to equation (1.86) as

$$(1.90) \quad \mathbf{E}(\mathbf{r}) = i\omega\mu \left[\hat{\mathbf{I}} + \frac{1}{k^2} \nabla \nabla \right] \cdot \int_{\Omega} \frac{e^{ik|\mathbf{r}-\mathbf{r}'|}}{4\pi|\mathbf{r}-\mathbf{r}'|} \mathbf{J}(\mathbf{r}') dV',$$

so that by Faraday's law

$$(1.91) \quad \mathbf{H}(\mathbf{r}) = \nabla \times \int_{\Omega} \frac{e^{ik|\mathbf{r}-\mathbf{r}'|}}{4\pi|\mathbf{r}-\mathbf{r}'|} \mathbf{J}(\mathbf{r}') dV'.$$

Equations (1.90) and (1.91) can be viewed as an analytic representation of Green's principle, [14], [26], [33], which decomposes an EM field into a sum of spherical waves emanating from different positions \mathbf{r}' with strengths $\mathbf{J}(\mathbf{r}')$. The Sommerfeld-Weyl integrals

$$(1.92) \quad \frac{e^{ikr}}{r} = \frac{i}{2} \int_{-\infty}^{\infty} dk_z \int_{-\infty}^{\infty} dk_y \frac{e^{ik_z z} e^{ik_y y} e^{ik_x |x|}}{k_x}$$

$$(1.93) \quad = \frac{i}{2} \int_{-\infty}^{\infty} dk_z H_0^{(1)}(k_\rho \rho) e^{ik_z z},$$

can be used to give alternate representations in terms of plane or cylindrical waves. In the above integrals, $k_x^2 + k_y^2 = k_\rho^2$, $k_\rho^2 + k_z^2 = k^2$ and the Fourier integral is taken along the Sommerfeld contour, [26]. Such representations are very convenient when solving for EM fields in layered media, e.g., [8], [11], [26], [30].

In Chapter 2, we present an overview of computational methods as they apply to modelling resistivity tools. The main emphasis is on Laterolog and Induction modelling. We shall examine solutions to Maxwell's equations for some simple cases and also review traditional finite element solutions to equation (1.69). Chapters 3 and 4 examine FEM solutions to equation (1.85) in more detail and discuss how the presence of the finite frequency affects matrix inversion. In Chapter 3, we also give examples of the Groningen effect on Laterologs. In Chapter 5, we examine more sophisticated techniques for solving equation (1.69) in complicated geometries arising in highly deviated wells.

References

- [1] Abraham, R., J. E. Marsden, and T. S. Raitu, *Manifolds, Tensor Analysis and Applications*, Addison Wesley, Reading, MA, 1983.
- [2] Abramowitz, M. and I. A. Stegun, *Handbook of Mathematical Functions*, Dover, New York, 1972.
- [3] Anderson, B., T. D. Barber, J. Singer, and T. Broussard, "ELMOD – putting electromagnetic modeling to work to improve resistivity log interpretation", in Transactions of the 30th SPWLA Symposium, Denver, CO, 1989. Paper M.
- [4] Anderson, B. and W. C. Chew, "SFL interpretation using high speed synthetic computer generated logs", in Transactions of the 26th SPWLA Symposium, Dallas, TX, 1985. Paper K.
- [5] Axelsson, O. and V. A. Barker, *Finite Element Solution of Boundary Value Problems*, Academic Press, New York, 1984.
- [6] Bott, R. and L. W. Tu, *Differential Forms in Algebraic Topology*, Springer-Verlag, New York, 1982.
- [7] Bramble, J., J. Pasciak, and J. Xu, "The analysis of multigrid algorithms with non-embedded spaces or non-inherited quadratic forms", *Math. Comp.*, **55**, 1991, pp. 1–34.
- [8] Brekhovskikh, L. M., *Waves in Layered Media*, Academic Press, New York, 1960.
- [9] Brezinski, C., *Padé-type approximation and general orthogonal polynomials*, Birkhäuser, Basel, 1980.
- [10] Chaba, A., *Os efeitos Delaware e Groningen: Um estudo quantitativo por elementos finitos*, Master's thesis, Universidade Federal do Pará, Belém, Brazil, 1993.
- [11] Chew, W. C., *Waves and Fields in Inhomogeneous Media*, Van Nostrand Reinhold, New York, 1990.
- [12] Ciarlet, P. G., *Finite Element Method for Elliptic Problems*, North-Holland, Amsterdam, 1978.
- [13] Cohn, P. M., *Algebra, Vol. 2*, John Wiley, London, 1977.
- [14] de Hoop, A. T., *Radiation and Scattering of Electromagnetic Waves*, Delft University of Technology, 1990.

- [15] ———, *Reciprocity, causality and Huygens' principle in electromagnetic wave theory*, in *Huygens' Principle 1690 – 1990: Theory and Applications*, H. Blok, H. A. Ferwerda, and H. K. Kuiken, eds., Elsevier Science, Amsterdam, 1992, pp. 171 – 192.
- [16] Doll, H., “*Introduction to induction logging*”, *Jour. Pet. Tech.*, 1949.
- [17] ———, “*The Laterolog*”, *Jour. Pet. Tech.*, 1951.
- [18] Druskin, V. L., *Coercivity of Maxwell's equations at low frequencies*, 1993. Personal communication.
- [19] Edmundson, H. and S. Gianzero, “*The mathematics of resistivity and induction logging*”, *Schlumberger Technical Review*, **29**, no. 1, 1981, pp. 4–32. To be reprinted in *SPWLA Reprint Series on Resistivity Logging*, 1992.
- [20] Fokkema, J. T. and P. M. van den Berg, *Seismic Applications of Acoustic Reciprocity*, Elsevier, Amsterdam, 1993.
- [21] Freund, R. W., M. H. Gutknecht, and N. M. Nachtigal, “*An implementation of the look-ahead Lanczos algorithm*”, *SIAM J. Sci. Comput.*, **14**, no. 1, 1993, pp. 137–158.
- [22] George, A. and J. W. H. Liu, *Computer Solution of Large Sparse Positive Definite Systems*, Prentice Hall, Englewood Cliffs, NJ, 1981.
- [23] Harrington, R., *Field Computation by Moment Methods*, Kreiger, Malabar, FL, 1983.
- [24] Hörmander, L., *Linear Partial Differential Operators*, Springer-Verlag, Berlin, 1963.
- [25] Jackson, J. D., *Classical Electrodynamics*, John Wiley, New York, 1962.
- [26] Kong, J. A., *Theory of Electromagnetic Waves*, John Wiley, New York, 1975.
- [27] Kotiuga, P. R., “*On making cuts for magnetic scalar potentials in multiply connected regions*”, *J. Appl. Phys.*, **61**, no. 8, 1990, pp. 3916–3918.
- [28] ———, “*Topological duality in three-dimensional eddy-current problems and its role in computer-aided formulation*”, *J. Appl. Phys.*, **67**, no. 9, 1990, pp. 4717–4719.
- [29] Lacour-Gayet, P., “*The Groningen effect . . . causes and a partial remedy*”, *Schlumberger Technical Review*, **29**, no. 1, 1981, pp. 37–47.
- [30] Lovell, J. R. and W. C. Chew, “*Effect of tool eccentricity on some electrical well logging tools*”, *IEEE Trans. Geoscience Remote Sensing*, **28**, no. 1, 1990, pp. 127–136.
- [31] MacLane, S. and G. Birkhoff, *Algebra*, MacMillan, New York, 1967.

- [32] Moran, J. H. and K. S. Kunz, "Basic theory of induction logging", *Geophysics*, **27**, no. 6, 1962, pp. 829–858.
- [33] Morse, P. M. and H. Feshbach, *Methods of Theoretical Physics*, McGraw-Hill, New York, 1953.
- [34] Nedelec, J. C., "Mixed finite elements in \mathbb{R}^3 ", *Numer. Math.*, **35**, 1990, pp. 315–341.
- [35] Oden, J. T. and J. N. Reddy, *An Introduction to the Mathematical Theory of Finite Elements*, Wiley, New York, 1976.
- [36] Perronet, A., *The club MODULEF: a library of subroutines for finite element analysis*, in *Computing Methods in Applied Sciences and Engineering*, vol. 704 of *Lecture Notes in Mathematics*, Springer-Verlag, Berlin, 1979, pp. 127–153.
- [37] Riesz, F. and B. Sz.-Nagy, *Functional Analysis*, Frederick Ungar Publishing, New York, 1955.
- [38] Rudin, W., *Functional Analysis*, McGraw-Hill, New York, 1973.
- [39] Rumsey, V. H., "Reaction concepts in electromagnetic theory", *Phys. Rev.*, **94**, no. 95, 1954, pp. 1483–91.
- [40] Silvester, R. P. and R. L. Ferrari, *Finite Element Methods for Electrical Engineers*, Cambridge University Press, Cambridge, 1983.
- [41] Spanier, E., *Algebraic Topology*, Springer-Verlag, New York, 1966.
- [42] Strang, G. and G. J. Fix, *An Analysis of the Finite Element Method*, Prentice-Hall, Inc., Englewood Cliffs, NJ, 1973.
- [43] Stroud, A. H., *Approximate Calculation of Multiple Integrals*, Prentice-Hall, Englewood Cliffs, NJ, 1971.
- [44] Suau, J., P. Grimaldi, A. Poupon, and P. Souhaite, "The Dual Laterolog R_{xo} tool", in *SPE 47th Annual Technical Conference*, San Antonio, TX, 1972. Paper SPE 4018.
- [45] Titman, J., *Physics of Well Logging*, Dover, New York, 1984.
- [46] Watson, G. N., *A Treatise on the Theory of Bessel Functions*, Pergamon Press, New York, 1944. 2nd Ed.
- [47] Woodehouse, R., "The Laterolog Groningen phantom can cost you money", in *Transactions of the 19th SPWLA Symposium*, 1978, pp. 1–17. Paper R.

Computational Methods in Resistivity Modelling

Abstract. Resistivity tools can be divided into two classes: one with TE sources and primary field components E_ϕ , H_ρ , H_z and one with TM sources and primary field components H_ϕ , E_ρ , E_z . Induction tools are TE sources, Laterologs are TM. TE modelling in layered media is readily amenable to analytic or semianalytic methods. Because of different boundary conditions, TM modelling can be more complicated. Iterative finite element techniques can be applicable in such cases. We review some of the traditional iterative methods and show how they can be applied to focussed resistivity tools.

2.1 Introduction¹

Resistivity devices are used to probe rock formations and provide estimates of hydrocarbon potential, usually in combination with other measurements, such as dielectric, [63], nuclear, [10], [20], or sonic porosity measurement, [64]. The interpretation of such measurements has been extensively discussed in the literature (e.g., [17], [20], [64]). We shall only give sufficient description of the logging process to motivate the mathematical developments in the rest of this text.

All of the resistivity tools that we shall consider consist of electromagnetic sensors lowered down a borehole drilled into a potentially hydrocarbon bearing rock formation. The most readily producible oil will be that which over geological time has settled within pores and fractures in sandstones or carbonates and been trapped beneath an impermeable layer such as shale.

The borehole is drilled with a rugged drill-bit secured on a metal pipe through which mud is pumped. The mud flushes cuttings from the face of the bit and acts as a lubricant. The flow of the mud can be used to drive mud downhole turbines which in turn drive the drill-bit.

¹ This chapter constitutes condensed course notes from a graduate level course taught by the author in January – March 1992 at the Federal University of Pará, Belem, Brasil and sponsored by Petrobras.

Alternatively, on a rotary assembly, the torque for the drill-bit is provided by turning the drill-pipe. The mud used must also be sufficiently dense to resist pressure from overpressured zones which might otherwise force the drilling mud uphole.

Because of the many demands placed on the drilling mud, its composition is not straightforward, but for electromagnetic modelling only its electrical conductivity is important, [52]. Muds which are made as emulsions of water drops in oil can be assumed to have an extremely low conductivity. Non-oil based muds can have varying degrees of conductivity depending on their salinity. For example, muds made from sea-water are common in the Middle East and these are very conductive ($0.005 - 0.05\Omega m$ at downhole temperatures) as are muds which are used to drill through salt domes (a high degree of salinity helps prevent washouts of the halite), [12]. Muds made from fresh water will be less conductive ($0.01 - 5.0\Omega m$) depending on the range of additives added to the mud.

Measurements of formation resistivity and porosity may be made while drilling or else after drilling by lowering on a reinforced cable a sonde containing the sensors. There are advantages and disadvantages to both methods. The latter method, known as wireline logging, has the advantage that sophisticated measurements can be made with sensors that do not have to withstand the rigours of drilling and whose data can be transmitted to the surface along transmission lines within the armoured cable. Logging while drilling (LWD) has the big advantage that the measurement is not corrupted by drilling mud penetrating into the rock formation. LWD has the disadvantage that the telemetry rate to the surface is very low because of the absence of a wireline cable – instead, data is sent to the surface by pulses in the mud flow or stored within the tool for later downloading when the bit is pulled back to the surface.

The angle through which the borehole penetrates the rock formation can be more or less arbitrary. Vertical wells are cheaper but have a smaller intersection with the hydrocarbon pay zone. Horizontal wells are recently proving popular as engineering difficulties are being conquered and the costs of drilling decrease. Horizontal and highly deviated wells offer the promise of increased production due to the longer interval of pay zone through which the borehole passes. The modelling of modern resistivity tools through such highly deviated wells is one of the main developments of this dissertation.

Modern resistivity tool designs for both wireline and LWD configurations have drastically improved the ability to determine the true resistivity of a bed with minimum distortions in the measurement from nearby beds. To perform such measurements the sensors now typically consist of some kind of focussed array of transmitters and/or receivers. Each of these can mathematically be modelled as a weighted sum of the individual components where the weighting is determined by the focussing. The response of the individual sensors in turn can be derived from Maxwell's equations applied to the pertinent source and boundary conditions. These sensors can often be represented in an idealized fashion as point sources which can

greatly simplify numerical modelling. Some tool configurations, such as the Laterologs, however, cannot be modelled with point sources, and there is a need for robust and accurate codes. We emphasize finite element formulations for Laterologs and review a simple finite element algorithm appropriate for simple electrode devices in axisymmetric media. We pay particular attention to iterative solutions and also discuss how focussing techniques can complicate the finite element formulation.

2.2 Overview of resistivity tools

Maxwell's equations in the context of resistivity logging were presented in Chapter 1:

$$(2.1a) \quad \nabla \times \mathbf{H} = (\sigma - i\omega\epsilon)\mathbf{E} + \mathbf{J},$$

$$(2.1b) \quad \nabla \times \mathbf{E} = i\omega\mu\mathbf{H}.$$

The electromagnetic source, \mathbf{J} , is either divergence free or not. The former case, termed *inductive*, relies on electromagnetic coupling to generate the field. In the latter case, termed *galvanic*, current will enter the domain directly from the points of non-zero divergence although there may be additional coupling effects from \mathbf{J} when ω is non-zero. The first category can be grouped together as "coils" and the latter category as "electrodes." Coils in turn can be divided into those which, roughly, drive their current in the same direction as the coil and those which drive their current in a perpendicular direction. We refer to these coils as solenoidal or toroidal, respectively. Typical representations of the three different excitations are given in Figure 2.1.

In wireline resistivity logging, the coils will usually be wrapped around a cylindrical mandrel, which may or may not be metallic depending on the tool design. The purpose of the mandrel is to provide structural stability to the sonde and also insulate the sensors from measurement and telemetry circuits inside the mandrel. Smaller sensors can alternatively be located on metallic pads which are forced against the borehole wall by powerful springs, e.g., [33], [43]. In logging while drilling, the coils or electrodes will be embedded in the drill-string.

The first source electrode configurations used in resistivity logging were the Normal and Lateral devices, [64], shown in Figure 2.1c. In both cases, the points of non-zero divergence are the ends of a current carrying wire, with one end at the surface and the other downhole. The ends of the wire are electrically connected to highly conductive metallic electrodes to improve the electrical connection between the source and the formation. The current return at the surface, called the fish, was usually in a small pool of conductive mud, also to improve the electrical connection. The source configuration is shown schematically in Figure 2.1c. The downhole source is invariably termed the 'A' electrode and 'B' is the current return. In some

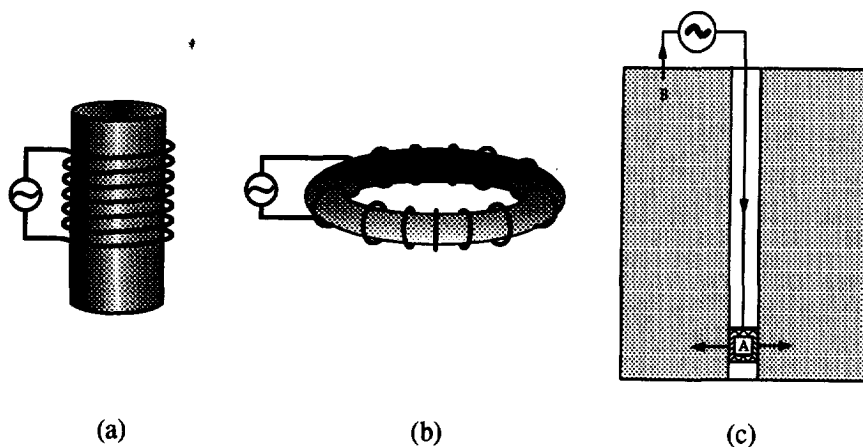


Figure 2.1: (a) Solenoidal coil, (b) toroidal coil, and (c) Normal/Lateral electrode excitation.

tool designs the B electrode is also downhole. The difference between the Normal and Lateral designs lies not in the source assembly but in the resistivity measurement itself. For the Normal design the potential difference $V_M - V_N$ was measured where M was a downhole measure electrode and N was uphole. For the Lateral design, both M and N measure electrodes were downhole. Modern tool designs have many measure electrodes downhole and the apparent resistivity is a complicated combination of all measure electrodes. We shall always assume that the potential, Φ , decays to zero at 'infinity' (e.g., the surface) and V_N is the value of Φ at whatever point N is located.

The electrode configuration will clearly only pass a non-zero current if the formation has a finite resistivity, which will always be assumed even though in some halites and anhydrites that resistivity may be very high. More of a problem is that the electrode tools are usually not in direct electrical contact with the formation but rely on the ability of the borehole mud to carry the electrical current from the source electrode A into the formation. For this reason electrode devices are only practical in conductive, salty muds. As the muds become fresher (i.e., less salt) they will become less conductive. Oil-based mud can be assumed to have such low conductance that electrode measurements will only carry current if there is a breakdown in the oil/water emulsion allowing current to pass [4].

In addition to the galvanic currents leaving A , at non-zero frequencies the flow of current from B to A could conceivably also cause inductive coupling. Before examining this coupling, we need to examine the electromagnetic properties of solenoids and toroids.

2.2.1 Solenoids

Solenoidal coils provide the building blocks for Induction devices such as shown in Figure 1.1. Mostly used in oil-based or fresh muds, they generate a field which primarily contains E_ϕ , H_ρ , H_z components, i.e., it is TE. Inhomogeneities in material properties, e.g., across dipping beds, can also excite TM modes, as can eccentricity of the sonde, (e.g., [40], [41]). The idealized representation is a thin loop of current of radius a and centred at $z = 0$:

$$(2.2) \quad \mathbf{J}(\mathbf{r}) = \hat{\phi} I \delta(\rho - a) \delta(z).$$

In a homogeneous formation, we can use the integral formulae of section 1.4.8 to derive the expression for electric field

$$(2.3) \quad \mathbf{E}(\mathbf{r}) = i\omega\mu \left[\hat{\mathbf{I}} + \frac{1}{k^2} \nabla \nabla \right] \cdot \int_0^{2\pi} d\phi' \int_0^a \rho' d\rho' \int_{-\infty}^{\infty} dz' \frac{e^{ik|\mathbf{r}-\mathbf{r}'|}}{4\pi|\mathbf{r}-\mathbf{r}'|} \hat{\phi}' I \delta(\rho' - a) \delta(z'),$$

We can evaluate equation (2.3) explicitly if the radius a is small. The only tricky parts are to remember that $\hat{\phi}'$ varies as a function of ϕ' :

$$(2.4) \quad \hat{\phi}' = -\hat{\rho} \sin(\phi' - \phi) + \hat{\phi} \cos(\phi' - \phi)$$

and to derive the small argument expansion

$$(2.5) \quad \frac{e^{ik|\mathbf{r}-\mathbf{r}'|}}{4\pi|\mathbf{r}-\mathbf{r}'|} \approx \frac{e^{ikr}}{4\pi r} \left[1 + \frac{a\rho}{r^2} (1 - ikr) \cos(\phi' - \phi) \right]$$

valid for $a \ll r$. We obtain

$$(2.6) \quad \mathbf{E}(\mathbf{r}) = \hat{\phi} E_\phi = -\hat{\phi} i\omega\mu ik I \pi a^2 \frac{e^{ikr}}{4\pi r} \left[1 + \frac{i}{kr} \right] \frac{\rho}{r}.$$

The source obtained as the limit as a tends to zero but $I\pi a^2$ remains constant is termed the vertical magnetic dipole (VMD). If we place another thin coil, Γ , of radius a at $z = L$ with $L \gg a$ then the voltage induced across the coil will be

$$(2.7) \quad V = \oint_{\Gamma} E_\phi = 2\pi a (-i\omega\mu) ik I \pi a^2 \frac{e^{ikL}}{4\pi L} \left[1 + \frac{i}{kL} \right] \frac{a}{L}.$$

If the source coil has N_T turns and the receiver coil N_R turns then for low frequency excitation

$\sigma \gg \omega\epsilon$ and $|kL| \ll 1$ so we can expand equation (2.7) in powers of kL to give

$$\begin{aligned}
 V &= -i\omega\mu N_T N_R \frac{I(\pi a^2)^2}{2\pi L^3} (ikL - 1)(1 + ikL - k^2 L^2/2 + \dots) \\
 &\approx i\omega\mu N_T N_R \frac{I(\pi a^2)^2}{2\pi L^3} (1 + k^2 L^2/2) \\
 (2.8) \quad &\approx N_T N_R \frac{I(\pi a^2)^2}{2\pi L^3} (i\omega\mu - \omega^2 \mu^2 \sigma L^2/2)
 \end{aligned}$$

which is the fundamental formula for Induction modelling. In particular, we see that the real (in-phase) component is proportional to σ and that the out-of-phase component, the so-called 'direct mutual signal,' is much larger. In practical tools such as the Dual Induction Tool, the direct mutual signal is removed by subtracting off the voltage on a third bucking coil situated at $z = \tilde{L} < L$ whose location and number of turns are computed so that the out-of-phase components exactly cancel (in air).

If a is not small, equation (2.3) can be evaluated in terms of elliptic integrals [1], [28], but it is also instructive to write the field in terms of cylindrical waves as indicated in section 1.4.8. In terms of the \hat{z} component, we have (e.g., [28], [34])

$$(2.9) \quad H_z = \frac{iIa}{4} \int_{-\infty}^{\infty} dk_z k_\rho J_1(k_\rho a) H_0^{(1)}(k_\rho \rho) e^{ik_z z} \quad \text{for } \rho > a$$

and

$$(2.10) \quad H_z = \frac{iIa}{4} \int_{-\infty}^{\infty} dk_z k_\rho J_0(k_\rho \rho) H_1^{(1)}(k_\rho a) e^{ik_z z} \quad \text{for } \rho < a$$

where $k_\rho^2 + k_z^2 = k^2 = i\omega\mu(\sigma - i\omega\epsilon)$, $Im(k_\rho) \geq 0$ as before and the Fourier integral is understood in the Sommerfeld sense.

The presence of an infinitely long metallic or insulating mandrel down the centre of the tool does not hugely complicate modelling. We must take into account the reflection of the electromagnetic fields from that mandrel. For $\rho > a$, we obtain

(2.11a)

$$H_z = \frac{iIa}{4} \int_{-\infty}^{\infty} dk_z k_\rho \{ J_1(k_\rho a) + \Gamma H_1^{(1)}(k_\rho a) \} H_0^{(1)}(k_\rho \rho) e^{ik_z z}$$

(2.11b)

$$E_\phi = -\frac{\omega\mu Ia}{4} \int_{-\infty}^{\infty} dk_z \{ J_1(k_\rho a) + \Gamma H_1^{(1)}(k_\rho a) \} H_1^{(1)}(k_\rho \rho) e^{ik_z z}$$

where $\Gamma = -J_1(k_\rho b)/H_1^{(1)}(k_\rho b)$ if $E_\phi = 0$ on $\rho = b$ (perfectly conducting mandrel) and $\Gamma = -J_0(k_\rho b)/H_0^{(1)}(k_\rho b)$ if $H_z = 0$ on $\rho = b$ (perfectly insulating mandrel) and we are assuming the mandrel to have infinite extent. As discussed in Chapter 1, by perfectly insulating mandrel we mean an insulating mandrel (with zero conductivity) and small enough that displacement currents can be ignored.

If the mandrel is conducting and we take the limit as $a \rightarrow 0$ (so that $b \rightarrow 0$ also) then

(2.12)

$$\begin{aligned} E_\phi &= i\omega\mu\frac{i}{4}Ia \int_{-\infty}^{\infty} dk_z \{J_1(k_\rho a) + \Gamma H_1^{(1)}(k_\rho a)\} H_1^{(1)}(k_\rho \rho) e^{ik_z z} \\ &\rightarrow i\omega\mu\frac{i}{8}I(a^2 - b^2) \int_{-\infty}^{\infty} dk_z k_\rho H_1^{(1)}(k_\rho \rho) e^{ik_z z} \\ &= \frac{\omega\mu I(a^2 - b^2)}{8} \frac{\partial}{\partial \rho} \int_{-\infty}^{\infty} dk_z H_0^{(1)}(k_\rho \rho) e^{ik_z z} \\ &= -i\omega\mu \frac{I\pi(a^2 - b^2)}{4\pi} \frac{\partial}{\partial \rho} \frac{e^{ikr}}{r} = -i\omega\mu I\pi(a^2 - b^2) \frac{e^{ikr}}{4\pi r} \left[1 + \frac{i}{kr}\right] \frac{ik\rho}{r} \end{aligned}$$

which, apart from a scaling factor, is the same as equation (2.6). Equation (2.8) can thus be viewed as the response of a 2-coil sonde on an insulating mandrel with $L \gg a$. Indeed, a fundamental design consideration when building induction tools is to ensure that the effects of mandrel and finite size coil do not significantly change the response of the tool from that of a pure magnetic dipole, e.g., see [28].

Moreover, not only can induction tools be modelled as combinations of point dipoles but the tool response in heterogeneous media is fairly well approximated by a convolution of the bed conductivities against certain readily computable geometric functions of ρ and z : [3], [25], [50], [64]. Inversion of the tool response follows by deconvolution, [8], [61]. To make the deconvolution as accurate as possible, arrays of transmitter and receiver coils are used with different predetermined weightings, [7], [9]. The corresponding situation for Laterologs is quite different and focussing issues are a lot more important.

2.2.2 Toroids

Toroids are the dual of solenoids. Instead of an azimuthally directed electric current running along the coil, toroids in effect produce a azimuthal 'magnetic current,' I_M . We can determine this magnetic current from simple geometric arguments. Suppose that the azimuthal cross-section of the toroid is $z^2 + (\rho - a)^2 \leq r_s^2$ then from Ampère's Law we have that for small

r_s

$$(2.13) \quad 2\pi\rho H_\phi = \begin{cases} 0 & |\rho - a| > r_s \\ N_T I & |\rho - a| < r_s \end{cases}$$

where N_T is the number of turns of the coil and I the current. Since $\nabla \times \mathbf{E} = i\omega\mu\hat{\phi}H_\phi$, we can write $\nabla \times \mathbf{E} = -\mathbf{M} = -I_M\hat{\phi}\delta(z)\delta(\rho - a)$ if

$$(2.14) \quad I_M = -i\omega\mu \int H_\phi d\rho dz = -i\omega\mu\pi r_s^2 N_T I / (2\pi a).$$

Similar expressions have been given in [13], [26] and [42].

If the geometry is axisymmetric, the field components generated by the toroid are H_ϕ , E_ρ , E_z , i.e., the field is TM, and H_ϕ satisfies the differential equation

$$(2.15) \quad \hat{\phi} \cdot \nabla \times \frac{1}{\sigma - i\omega\epsilon} \nabla \times (H_\phi \hat{\phi}) - i\omega\mu H_\phi = -M_\phi = i\omega\mu\pi r_s^2 N_T I \frac{\delta(\rho - a)\delta(z)}{2\pi a}.$$

If the formation is homogeneous

$$(2.16) \quad \hat{\phi} \cdot \nabla \times \nabla \times (H_\phi \hat{\phi}) - k^2 H_\phi = (\sigma - i\omega\epsilon) I_M \delta(\rho - a)\delta(z),$$

and we can derive an expression for H_ϕ analogous to that for E_ϕ in the previous section

$$(2.17) \quad \mathbf{H} = (\sigma - i\omega\epsilon) \left[\hat{\mathbf{I}} + \frac{1}{k^2} \nabla \nabla \right] \cdot \int_{\Omega} \frac{e^{ik|\mathbf{r} - \mathbf{r}'|}}{4\pi|\mathbf{r} - \mathbf{r}'|} \mathbf{M}(\mathbf{r}') dV'$$

$$(2.18) \quad = -\hat{\phi}(\sigma - i\omega\epsilon)\pi a^2 I_M i k \frac{e^{ikr}}{4\pi r} \left[1 + \frac{i}{kr} \right] \frac{\rho}{r}$$

for small a .

As in the previous section, to solve for the presence of a mandrel inside the coil we write the field in cylindrical waves and add an additional field component to represent reflected field from the mandrel. We obtain

$$(2.19) \quad E_z = \frac{iI_M a}{4} \int_{-\infty}^{\infty} dk_z k_\rho \{ J_1(k_\rho a) + \Gamma H_1^{(1)}(k_\rho a) \} H_0^{(1)}(k_\rho \rho) e^{ik_z z}$$

where now $\Gamma = -J_0(k_\rho b)/H_0^{(1)}(k_\rho b)$ if $E_z = 0$ on $\rho = b$ (perfectly conducting mandrel) and $\Gamma = -J_1(k_\rho b)/H_1^{(1)}(k_\rho b)$ if $H_\phi = 0$ on $\rho = b$ (perfectly insulating mandrel).

This expression assumes the mandrel to have infinite extent. If the mandrel is insulating the length of the mandrel is not a major influence on the induced fields. If the toroid is wrapped around a metallic mandrel, however, the situation is quite different. In particular the length of the mandrel above and below the coil significantly influences the response of the tool. Essentially, the problem is that with a metallic mandrel the toroid induces electric fields along the mandrel and the mandrel itself acts as an antenna. For an insulating mandrel this problem does not arise.

These results indicate a key difference between TE and TM modelling in borehole logging. While TE and TM are duals, because of differences in material properties, tool strings consisting of TM coils on a conductive mandrel are poorly approximated by point sources. In the next section, we will examine the TM fields generated by electrodes.

2.2.3 Electrodes

The simplest representation of the Normal/Lateral source configuration is a small sphere emitting DC current I in a homogeneous medium of conductivity σ . The electric field excited is (e.g., [30])

$$(2.20) \quad \mathbf{E}(\mathbf{r}) = \frac{I}{\sigma} \frac{\hat{\mathbf{r}}}{4\pi|\mathbf{r}|^2}.$$

Here in fact, $\mathbf{E} = -\nabla\Phi$, where the potential is given by

$$(2.21) \quad \Phi = \frac{I}{\sigma} \frac{1}{4\pi|\mathbf{r}|}.$$

The field due to two such monopoles with current I leaving the first (at $z = 0$, say) and returning to the second (at $z = l$, say) is given by,

$$(2.22) \quad \mathbf{E}(\mathbf{r}) = \frac{I}{\sigma} \left\{ \frac{\hat{\mathbf{r}}}{4\pi|\mathbf{r}|^2} - \frac{\hat{\mathbf{r}}'}{4\pi|\mathbf{r}'|^2} \right\},$$

where \mathbf{r} denotes coordinates relative to the first monopole and \mathbf{r}' denotes coordinates relative to the second. As l tends to zero, so does \mathbf{E} , but we can also consider the limit where l tends to zero but Il remains finite, called a Hertzian dipole or vertical electric dipole (VED), which gives rise to the electric field

$$(2.23) \quad \mathbf{E} = \frac{Il}{4\pi r^3 \sigma} \left\{ 2\hat{\mathbf{r}} \cos \theta + \hat{\boldsymbol{\theta}} \sin \theta \right\}$$

and magnetic field

$$(2.24) \quad \mathbf{H} = \hat{\phi} \frac{Il}{4\pi r^2} \sin \theta = \hat{\phi} \frac{Il}{4\pi r^2} \frac{\rho}{r}.$$

Galvanic sources which radiate at non-zero frequencies cannot be written by inspection, but we can again use the integral formulae of section 1.4.8 for some simple cases. For example, for the VED introduced above, the time harmonic current source is

$$(2.25) \quad \mathbf{J}(\mathbf{r}) = \hat{\mathbf{z}} Il \delta(\mathbf{r})$$

whence

$$(2.26) \quad \begin{aligned} \mathbf{E}(\mathbf{r}) &= i\omega\mu \left[\hat{\mathbf{I}} + \frac{1}{k^2} \nabla \nabla \right] \cdot \iiint d\mathbf{r}' \frac{e^{ik|\mathbf{r}-\mathbf{r}'|}}{4\pi|\mathbf{r}-\mathbf{r}'|} \hat{\mathbf{z}} Il \delta(\mathbf{r}) \\ &= i\omega\mu Il \left[\hat{\mathbf{z}} + \frac{1}{k^2} \nabla \frac{\partial}{\partial z} \right] \frac{e^{ikr}}{4\pi r} \end{aligned}$$

and

$$(2.27) \quad \mathbf{H}(\mathbf{r}) = -\hat{\phi} ik Il \frac{e^{ikr}}{4\pi r} \left[1 + \frac{i}{kr} \right] \frac{\rho}{r}.$$

which is seen to be the dual of equation (2.6).

Simple electrode tools in resistivity logging such as the Lateral and Normal configurations can be modelled as point sources. The depth of investigation is determined by the separation between the source electrode, A , and measure electrode M . The 'Short Normal' had a 16 inch separation, the 'Long Normal' had a 64 inch separation. The main difficulty interpreting resistivity logs from a Normal or Lateral was that the apparent resistivity at one tool position was quite sensitive to the resistivities in adjacent (and further) beds, a phenomenon known as shoulder effect. The simplest way to decrease this was to extend the length of A and measure only the current from the centre of the electrode. This arrangement is shown in the LL3[†] of Figure 1.2 where the A electrode is divided into three separate electrodes maintained at equipotentials. The outer electrodes are called guard electrodes and the inner A_0 electrode is the 'measure' electrode. The Dual Laterolog (DLL)[†] shown in Figure 1.3 has a much more sophisticated arrangement with a large number of sources and receivers at different potentials, and governed by a set of linear focussing constraints, [62]. In addition to the different electrode potentials, the regions in between the electrodes are covered with insulating material and modelled as perfect electric insulators. The effect is that the boundary condition on the tool is a complicated mix of Dirichlet and Neumann boundary conditions, for which finite element solutions are the most appropriate.

[†]Mark of Schlumberger

2.3 Finite element solutions for Laterologs

In the remainder of this chapter, we show how to solve for Laterolog excitation in two dimensional axisymmetric formations using finite elements and iterative inversion. We assume DC excitation and solve for the electric potential Φ . Three dimensional formulations in Φ are deferred to Chapters 4 and 5. In Chapter 3, we present an alternative formulation for axisymmetric formations in terms of H_ϕ .

2.3.1 Potential formulation at DC

We have seen in section 1.4.5 that at DC, Maxwell's equations decouple into two separate equations for \mathbf{E} and \mathbf{H} with $\mathbf{E} = -\nabla\Phi$ and $\nabla \cdot \sigma \nabla\Phi = \nabla \cdot \mathbf{J}$. For Laterolog modelling, $\mathbf{J} = 0$. All of the source conditions are represented by boundary terms on $\rho = a$, the surface of the tool. If the formation is axisymmetric, we can suppose that Φ is only a function of ρ and z . From Equations (1.27) and (1.29) we have

$$(2.28) \quad L(\Phi) = \frac{1}{\rho} \frac{\partial}{\partial \rho} \left(\sigma \rho \frac{\partial \Phi}{\partial \rho} \right) + \frac{\partial}{\partial z} \left(\sigma \frac{\partial \Phi}{\partial z} \right) = 0.$$

We suppose the Laterolog to consist of electrodes Γ_i at fixed potentials V_i and separated from one another by insulating sections. We write $\partial\Omega_0 = \bigcup_i \Gamma_i$ and $\partial\Omega = \partial\Omega_0 \cup \partial\Omega_\nu$ and so

$$(2.29) \quad \Phi = V_i \quad \text{on} \quad \Gamma_i \quad \text{and} \quad \frac{\partial \Phi}{\partial \nu} = 0 \quad \text{on} \quad \partial\Omega_\nu.$$

In the terminology of Chapter 1, we have removed the perfect insulators and perfect conductors from the domain and replaced them with boundary conditions. Current emanates only from the Γ_i electrodes. We shall suppose that Γ_0 is the current return at infinity with $V_0 = 0$. To avoid problems near $\rho = 0$, we shall also suppose that $\rho \geq a$ throughout Ω . A typical configuration is shown in Figure 2.2.

We solve equation (2.28) using the Galerkin method presented in Chapter 1. Given $V = (V_1, \dots, V_n)$, let $H_V^1(\Omega)$ be the subspace of $H^1(\Omega)$ with $\Phi = V_i$ on Γ_i and $\Phi = 0$ on Γ_0 . The Galerkin method enables us to find a solution of equation (2.28) projected onto some subspace W of $H^1(\Omega)$. We choose W to be a finite dimensional space built from local 'pyramid' functions defined on a triangulation of Ω .

More specifically, we shall suppose that we are given a mesh of triangles $\Delta \in \mathcal{T}_h$ where the h denotes the diameter of the largest triangle in \mathcal{T}_h . Each node $(\rho_i, z_i) = 1, \dots, N$ may lie on any number of triangles. We choose W_h to be the space generated from a basis

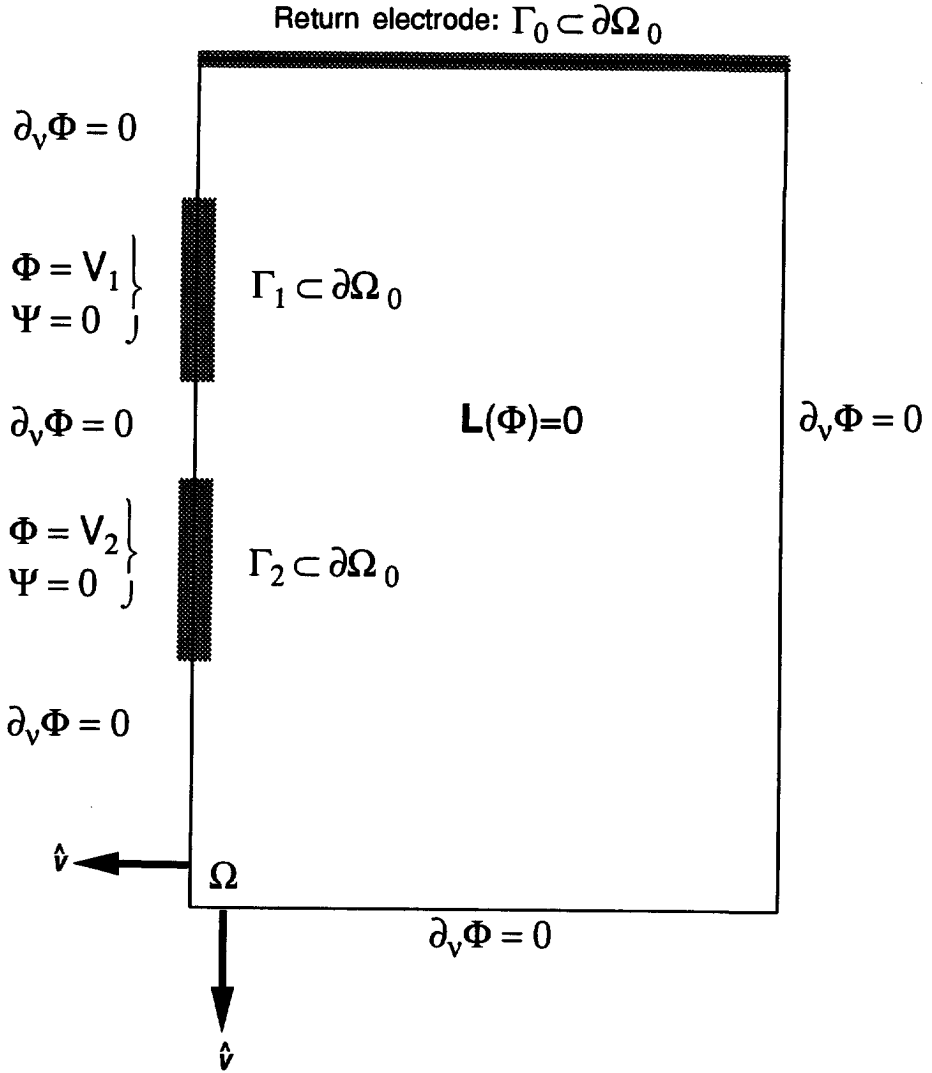


Figure 2.2: Typical finite element configuration. The domain Ω is partially bounded by electrodes Γ_i . Γ_0 is taken to be the current return 'at infinity' with $\Phi = \Psi = 0$. On the other electrodes Φ is set to the given voltage V_i with $\Psi = 0$. The remainder of the boundary is denoted $\partial\Omega_\nu$. In the limit as the mesh is refined, $\partial\Phi/\partial\nu = 0$ on $\partial\Omega_\nu$. There is no constraint on Ψ on $\partial\Omega_\nu$. $\hat{\nu}$ denotes the outward pointing normal from the domain Ω .

$B_i(\rho, z)$, $i = 1, \dots, N$ consisting of piecewise linear functions with $B_i(\rho_j, z_j) = \delta_{ij}$ where δ_{ij} denotes the Kröner delta function. If a triangle Δ has node numbers n_r , $r = 1, 2, 3$ then within Δ

$$(2.30a) \quad B_{n_1}(\rho, z) = \frac{(z_2 - z_3)(\rho - \rho_3) - (\rho_2 - \rho_3)(z - z_3)}{(z_2 - z_3)(\rho_1 - \rho_3) - (\rho_2 - \rho_3)(z_1 - z_3)},$$

$$(2.30b) \quad B_{n_2}(\rho, z) = \frac{(z_3 - z_1)(\rho - \rho_1) - (\rho_3 - \rho_1)(z - z_1)}{(z_3 - z_1)(\rho_2 - \rho_1) - (\rho_3 - \rho_1)(z_2 - z_1)},$$

$$(2.30c) \quad B_{n_3}(\rho, z) = \frac{(z_1 - z_2)(\rho - \rho_2) - (\rho_1 - \rho_2)(z - z_2)}{(z_1 - z_2)(\rho_3 - \rho_2) - (\rho_1 - \rho_2)(z_3 - z_2)}.$$

This discretization is termed P1. A similar discretization using bilinear functions on rectangles is termed Q1.

We define the finite element solution Φ_h to be that real-valued function in $V_h = H_V^1(\Omega) \cap W_h$ such that

$$(2.31) \quad \langle \Psi_h, L(\Phi_h) \rangle = 0 \quad \forall \Psi \in H_0^1(\Omega) \cap W_h.$$

Note that $L(\Phi_h) \in H^{-1}(\Omega)$ so the bilinear form $\langle \Psi_h, L(\Phi_h) \rangle$ is defined, at least in the distributional sense. In practice, we will use integration by parts to obtain

$$(2.32) \quad \langle \Psi, L(\Phi) \rangle = \iint_{\Omega} d\rho dz \sigma \rho \left(\frac{\partial \Psi}{\partial \rho} \frac{\partial \Phi}{\partial \rho} + \frac{\partial \Psi}{\partial z} \frac{\partial \Phi}{\partial z} \right)$$

which is clearly a symmetric bilinear form. Provided that $\sigma \rho \geq \sigma_{\min} \rho_{\min} > 0$, then from equation (1.70) we see that there exist $\gamma > 0$ and $C > 0$ such that (for real-valued functions Φ)

$$(2.33) \quad \gamma \|\Phi\|_1^2 \leq \langle \Phi, L(\Phi) \rangle \leq C \|\Phi\|_1^2$$

provided that we insist that $\Phi = 0$ on Γ_0 . If we do not impose any Dirichlet constraints on Φ then the constant function would have $\langle \Phi, L(\Phi) \rangle$ zero with $\|\Phi\|_1$ non-zero thereby violating the lower inequality. By the Lax-Milgram lemma, a solution Φ exists in $H^1(\Omega)$. As L is also coercive over the subspace W_h , we can also be sure that Φ_h exists.

We can successively subdivide the triangles in \mathcal{T}_h to give a sequence of finite dimensional spaces $W_h \supset W_{h/2} \supset W_{h/4} \supset \dots$. We can obtain a finite element solution for each of these spaces and can show² that for some constant C independent of h and Φ

$$(2.34) \quad \|\Phi - \Phi_h\|_0 \leq Ch^2 \|\Phi\|_2.$$

²This result depends on sufficient smoothness of σ and $\partial\Omega$, e.g., [60]. [35] proves a similar result for the case of σ an arbitrary bounded function of Ω .

(Note that Φ will be in $H^2(\Omega)$ if the source term is in $H^0(\Omega)$.)

Thus, as the mesh is refined the finite element answer approaches the true solution Φ . In fact, it is not always necessary to subdivide the mesh uniformly. Rather one needs to have a fine mesh in regions of Ω where Φ varies rapidly (e.g., near the ends of electrodes). The subject of how to adaptively change T_h based on knowledge of Φ_h is discussed in section 2.5.

2.3.2 Assembly of stiffness matrix and Dirichlet constraints

As the basis functions $B_i(\rho, z)$ span the space W_h , it is necessarily the case that

$$(2.35) \quad \Phi_h = \sum_{j=1}^N u_j B_j(\rho, z)$$

for some $u_j \in \mathbb{R}$ and we set $\Psi = B_i(\rho, z)$ for $i = 1, \dots, N$ so that equation (2.31) becomes

$$(2.36) \quad \sum_{j=1}^N \langle B_i, L(B_j) \rangle u_j = 0 \quad \forall B_i \in H_0^1(\Omega) \cap W_h.$$

As noted in Section 1.2, $\langle B_i, L(B_j) \rangle$ constitutes an $N \times N$ matrix, A , called the stiffness matrix.

u denotes the coordinates of the function Φ_h projected onto the space W_h and we similarly write v for the components of Ψ_h . In matrix notation, $\langle \Psi_h, L(\Phi_h) \rangle = v^t A u$. If $\Psi_h = B_i$ then $v^t A u = 0$ is the i th row of the matrix equation $A u = 0$. Φ_h and Ψ_h are functions in $H^1(\Omega)$, whereas u and v are vectors in \mathbb{R}^N (or \mathbb{C}^N) where N is the dimension of W_h .

The Dirichlet constraints require a modification of the stiffness matrix, A . As $\Psi_h \in H_0^1(\Omega)$, then the i th component of v must be zero if the i th node is Dirichlet. Suppose for convenience that we have listed the M Dirichlet nodes last with $\mathbb{R}^N = \mathbb{R}^{N-M} \oplus \mathbb{R}^M$. We write corresponding decompositions as $u = u_1 + u_2$ and $v = v_1 + v_2$ where $u_1, v_1 \in \mathbb{R}^{N-M}$ and $u_2, v_2 \in \mathbb{R}^M$. We can also write

$$(2.37) \quad v^t A u = (v_1^t + v_2^t) A (u_1 + u_2) = \begin{pmatrix} v_1^t & v_2^t \end{pmatrix} \begin{pmatrix} A_{11} & A_{12} \\ A_{21} & A_{22} \end{pmatrix} \begin{pmatrix} u_1^t \\ u_2^t \end{pmatrix}.$$

Here A_{11} is an $(N - M) \times (N - M)$ matrix and A_{22} is $M \times M$.

By supposition, u_2 is to be set to some known Dirichlet value \bar{u}_2 . We must have that $v_2 = 0$ but there are no restriction on v_1 so the only way for $v^t A u = 0$ is to have that

$$(2.38) \quad (A_{11} \quad A_{12}) \begin{pmatrix} u_1^t \\ u_2^t \end{pmatrix} = 0.$$

If we combine this equation with the known equation for u_2 , we obtain

$$(2.39) \quad \begin{pmatrix} A_{11} & A_{12} \\ 0 & I \end{pmatrix} \begin{pmatrix} u_1 \\ u_2 \end{pmatrix} = \begin{pmatrix} 0 \\ \bar{u}_2 \end{pmatrix}.$$

Physically, the i th row of Au represents a computation of net current divergence at the i th node. At interior nodes and those on $\partial\Omega_\nu$, we know that this net current must be zero. At Dirichlet nodes, however, we do not know what this net current is, so we must set the test functions Ψ_h to be zero at those nodes, i.e., we must *delete* those nodes from the stiffness matrix A . To maintain a well-defined system, in place of each deleted row, we can insert the known Dirichlet value for that node. This is precisely equation (2.39).

We can maintain symmetry by writing $A_{11}u_1 = -A_{12}u_2 = -A_{12}\bar{u}_2$, i.e.,

$$(2.40) \quad \begin{pmatrix} A_{11} & 0 \\ 0 & I \end{pmatrix} \begin{pmatrix} u_1 \\ u_2 \end{pmatrix} = \begin{pmatrix} -A_{12}\bar{u}_2 \\ \bar{u}_2 \end{pmatrix}.$$

A key difference between finite element and finite difference programs is that in the former the stiffness matrix may have considerably less structure and the programs must be able to deal with more or less arbitrary mesh topologies. As described in Chapter 1, we can store only the non-zero entries of A using an RS/CS sparse matrix method. The RS/CS structure can be readily obtained from the mesh topology. We shall suppose that we are using the P1 piecewise linear elements introduced above, so that a matrix element A_{ij} will only be non-zero if i and j are nodes of a common triangle. We can suppose that the finite element mesh is described by given the list of nodes n_{ik} , $k = 1, \dots, N_i$ associated with each node i . Ignoring the fact that A is symmetric we can take an RS/CS storage scheme defined by

$$(2.41) \quad RS[i] = \sum_{j=1}^i N_j; \quad \text{and} \quad CS[RS[i] + k - 1] = n_{ik} \quad k = 1, \dots, N_i.$$

If we wish to only store the upper triangle of a symmetric matrix then we perform the same operation but on the subset of nodes n_{ik} with $k \geq i$.

If the mesh is rectangular with nodes (ρ_i, z_j) , $i = 1, \dots, N_\rho$, $j = 1, \dots, N_z$ we can choose a stencil formulation, as A_{ijpq} will be zero if $|i - p| > 1$ or $|j - q| > 1$. For such a mesh, there

is very little difference between finite elements and finite differences, at least from a coding perspective.

The simplest way to perform the operation implied by equation (2.40) (and which does not involve renumbering the nodes so that the Dirichlet nodes are last) is to set $P(i)$ to be a mask which is 'true' for Dirichlet nodes and 'false' for non-Dirichlet nodes. Then set

if $P(i)$ **then** $u_i := \bar{u}_i$ **else** $u_i := 0$;

$f := Au$;

if $P(i)$ **then** $f_i := -f_i$ **else** $f_i := 0$;

if $P(i)$ **then** $B_{ij} := A_{ij}$;

if $P(i).or.P(j)$ **then** $A_{ij} := 0$;

if $P(i)$ **then** $A_{ii} := 1$;

This operation is essentially modular in that it does not require any knowledge of the storage scheme for A , only that there be a subroutine to perform $f \leftarrow Au$. At the end of the operation we have stored $(A_{21} \ A_{22})$ in the matrix B and replaced the corresponding rows in A with $(0 \ 1)$. We have also replaced the columns A_{12} in A with 0 as required in equation (2.40).

We have seen in Chapter 1, that if $\partial\Omega_0$ is a closed subset of the boundary and $H_0^1(\Omega)$ contains those functions in $H^1(\Omega)$ which are zero on $\partial\Omega_0$, then there is a natural direct sum decomposition

$$(2.42) \quad H^1(\Omega) = H_0^1(\Omega) \oplus H^{1/2}(\partial\Omega_0)$$

where $H^{1/2}(\partial\Omega_0)$ represents the possible range of Dirichlet functions, \bar{u} , on $\partial\Omega_0$. Equation (2.40) is precisely the decomposition of A in terms of this direct sum with

$$(2.43) \quad A_{11} : H_0^1(\Omega) \rightarrow H^{-1}(\Omega) \quad \text{and} \quad A_{12} : H^{1/2}(\partial\Omega_0) \rightarrow H^{-1}(\Omega).$$

$B : H_0^1(\Omega) \oplus H^{1/2}(\partial\Omega_0) \rightarrow H^{-1/2}(\partial\Omega_0)$ provides the dual map from the potential data into the space of current distributions on $\partial\Omega_0$. Indeed, we shall see in the next section that multiplying the potential (U_1, U_2) by B is precisely the operation needed to compute electrode currents on $\partial\Omega$.

2.3.3 Computation of electrode currents

An important technique which is not common in geophysical modelling is the use of superconvergent or variational methods to compute apparent resistivity, [37], [39]. We have seen that the approximate potential Φ_h is accurate to $O(h^2)$. On the electrodes themselves, in fact, Φ is exact because the Dirichlet boundary conditions were imposed strongly by requiring that $\Phi_h \in H_V^1(\Omega)$. To arrive at an apparent resistivity, however (either for focussed or unfocussed tools) we also need to be able to compute the current emanating from each electrode

$$(2.44) \quad I_i = \oint_{\Gamma_i} \sigma \frac{\partial \Phi}{\partial \nu},$$

where ν is as usual the normal pointing outward from Ω , i.e., into the electrode (and hence the *lack of* minus sign).

Standard methods (e.g., differentiating Φ_h) will bring about a loss of accuracy in the computation of I_i . Better is to see that if $L(\Phi) = 0$ then equation (2.44) follows by applying equation (1.26) to

$$(2.45) \quad I_i = \int_{\Omega} \sigma \rho \left(\frac{\partial \Phi}{\partial \rho} \frac{\partial \chi}{\partial \rho} + \frac{\partial \Phi}{\partial z} \frac{\partial \chi}{\partial z} \right) = \langle \chi, L(\Phi) \rangle,$$

where $\chi = \chi_{\Gamma_i}$ is 1 on the electrode and zero elsewhere on $\partial\Omega$ (it's value inside Ω will not affect the value of I_i). In fact, because $\partial\Phi/\partial\nu = 0$ on $\partial\Omega - \Gamma$, we can choose arbitrary $\chi \in H^{1/2}(\partial\Omega)$ provided $\chi|_{\Gamma_j} = \delta_{ij}$. (I.e., χ is 1 on the i th electrode, zero on all other electrodes and χ is the restriction of some H^1 function to the boundary $\partial\Omega$.) In particular, we could even choose χ to be a multiple of Φ !

Our approximate formula for I_i using the finite element solution is then

$$(2.46) \quad I_i \approx (I_h)_i = \langle \chi_h, L(\Phi_h) \rangle,$$

where $\chi_h \in W_h$ is 1 on the nodes of Γ_i and zero on the other boundary (and interior) nodes. We shall show that as the mesh is refined

$$(2.47) \quad \|I_i - (I_h)_i\| = O(h^2).$$

Such a result is termed superconvergent because

$$(2.48) \quad \|\Phi - \Phi_h\|_0 = O(h^2) \quad \text{and} \quad \|\nabla\Phi - \nabla\Phi_h\|_0 = O(h)$$

so we have gained an order of accuracy greater than we could have obtained from $\nabla\Phi_h$.

We can give a simple proof of this result based upon the following observations:

- Clearly it suffices to show the result when $\Phi = 1$ on Γ_1 and $\Phi = 0$ on the remaining electrodes. We can lump all of these electrodes together and call them Γ_0 .
- The functional $\langle \Phi, L(\Phi) \rangle$ is real and coercive so its stationary point is a minimum.
- Equation (2.45) is actually valid when $\chi = \Phi$, the stationary point of $\langle \Phi, L(\Phi) \rangle$ because as we discussed above the value of χ on $\partial\Omega - \Gamma$ is irrelevant.
- I.e., I_i is actually the minimum value of $\langle \Phi, L(\Phi) \rangle$ with Φ constrained to be 1 on Γ_1 and 0 on Γ_0 . This can also be seen, [15], as an application of Gauss' principle whereby a knowledge of the energy stored in the medium translates directly back to the apparent resistivity.
- $\langle \Psi, L(\Phi) \rangle$ is variational and L is symmetric so by the usual argument, e.g., [14]

$$\begin{aligned} \langle \Phi, L(\Phi) \rangle - \langle \Phi_h, L(\Phi_h) \rangle &= \langle \Phi - \Phi_h, L(\Phi - \Phi_h) \rangle + 2\langle \Phi_h, L(\Phi - \Phi_h) \rangle \\ &= \langle \Phi - \Phi_h, L(\Phi - \Phi_h) \rangle \end{aligned}$$

because $\langle \Psi_h, L(\Phi - \Phi_h) \rangle = 0$ for all Ψ_h by construction. Because L is continuous, for some C we have

$$\langle \Phi - \Phi_h, L(\Phi - \Phi_h) \rangle \leq C \|\nabla \Phi - \nabla \Phi_h\|_0^2 = O(h^2),$$

where we have used equation (2.48).

We see that the computation of I_i is thus accurate to $O(h^2)$. In fact, it is not just along electrodes that we can use this superconvergence result. The formulation in terms of stiffness matrices actually gives accurate values for the internal current flow too. Not the current flow at a point, or through a node of the mesh, but a value for the integrated current flow through any line segment of the mesh. This ties in with the notion of staggered meshes. Given the mesh of nodal points we can construct a 'dual' mesh with a node at the midpoint of each line. At that point we let the unknown be the net current flux through that line. The finite element formulation for Φ_h gives automatically the result for the unknown currents on the staggered mesh.

Similar results have been reported in the finite difference literature where improved accuracy can be obtained if the electric and magnetic fields are stored on staggered meshes, [48], [49].

2.3.4 Reciprocity and solutions for focussed tools

For focussed tools we are given a system of N constraints on the voltage or currents on the N tool electrodes (together with a constraint of zero potential on some reference Γ_0 at infinity).

To arrive at the apparent resistivity for focussed tools one solves for N linearly independent excitations. The focussed solution must be a linear combination of these N solutions and can be arrived at by inverting an $N \times N$ matrix. For example, we can solve for the fields Φ_j , $j = 1, \dots, N$ satisfying

$$(2.49) \quad L(\Phi_j) = 0, \quad \Phi_j = \delta_{ij} \quad \text{on} \quad \Gamma_i.$$

By the previous comments, the current on the i th electrode given unit voltage excitation on the j th electrode is

$$(2.50) \quad Z_{ij} = \langle \Phi_i, L(\Phi_j) \rangle.$$

We refer to this matrix as the transfer impedance matrix. Using the variational formula to compute currents shows that the transfer impedance matrix will be symmetric even for the finite element solution over a coarse mesh. However, if the solution to the finite element system of equations is only approximate then symmetry will be lost. If we obtain an exact solution to the finite element system of equations, e.g., by Gaussian elimination, then we will retain symmetry. From a physical perspective, the transfer impedance matrix is symmetric because the Dirichlet conditions on the electrodes give rise to a reciprocal system in the sense of Section 1.4.2.

In Chapter 4, we show how to solve for focussing constraints using the current excitations as a 'basis' instead of the voltage excitation shown above which produces the inverse matrix Z^{-1} which can provide better numerical accuracy in some cases.

2.3.5 Solution in the presence of focussing constraints

Some focussing conditions on Laterologs such as those shown in Figure 1.3 require active tool electronics which violate reciprocity. Such boundary conditions cannot be introduced into the global stiffness matrix without losing symmetry. The purpose of this section is to demonstrate how the focussing constraints violate symmetry and to give an example which partially illustrates the problem. Suppose that we have two tool electrodes Γ_i with boundary conditions $V_1 = 1$, $I_1 = 0$. We have no a priori information about the potential on Γ_2 and we suppose that the current returns to some electrode Γ_0 with $V_0 = 0$ as shown in Figure 2.2. In terms of voltage excitation, the voltage V_2 is adjusted so as to maintain a zero net current on I_1 . Electronically this would be done with some kind of feedback loop.

We can suppose that each electrode is represented by just one node and that our superconvergent formula for I_1 is

$$(2.51) \quad I_1 = A_{11}\Phi_1 + \dots + A_{1n}\Phi_n$$

The correct solution is given by applying the Dirichlet constraints to give the system

$$(2.52) \quad \begin{pmatrix} 1 & 0 & \dots & 0 \\ 0 & 1 & \dots & 0 \\ a_{31} & a_{32} & \dots & a_{3n} \\ \vdots & \vdots & \ddots & \vdots \\ a_{n1} & a_{n2} & \dots & a_{nn} \end{pmatrix} \begin{pmatrix} \Phi_1 \\ \Phi_2 \\ \Phi_3 \\ \vdots \\ \Phi_n \end{pmatrix} = \begin{pmatrix} V_1 \\ V_2 \\ 0 \\ \vdots \\ 0 \end{pmatrix}$$

which we can write in block form

$$(2.53) \quad \begin{pmatrix} I & 0 & 0 \\ 0 & I & 0 \\ A_{31} & A_{32} & A_{33} \end{pmatrix} \begin{pmatrix} \Phi_1 \\ \Phi_2 \\ \Phi_3 \end{pmatrix} = \begin{pmatrix} V_1 \\ V_2 \\ 0 \end{pmatrix}$$

whence $\Phi_3 = -A_{33}^{-1}(A_{31}V_1 + A_{32}V_2)$ and

$$(2.54) \quad I_1 = A_{11}V_1 + A_{12}V_2 - A_{13}A_{33}^{-1}(A_{31}V_1 + A_{32}V_2)$$

which with $I_1 = 0$ and $V_1 = 1$ gives

$$(2.55) \quad V_2 = -\frac{A_{11} - A_{13}A_{33}^{-1}A_{31}}{A_{12} - A_{13}A_{33}^{-1}A_{32}}.$$

Note that A_{33} will be invertible because it contains the Dirichlet nodes on the current return Γ_0 : the stiffness matrix for Laplace's equation has a zero eigenvalue (corresponding to the constant functions) unless part of the boundary is constrained to a Dirichlet value.

We can obtain the same result by solving the non-symmetric system

$$(2.56) \quad \begin{pmatrix} A_{11} & A_{12} & A_{13} \\ I & 0 & 0 \\ A_{31} & A_{32} & A_{33} \end{pmatrix} \begin{pmatrix} \Phi_1 \\ \Phi_2 \\ \Phi_3 \end{pmatrix} = \begin{pmatrix} 0 \\ 1 \\ 0 \end{pmatrix},$$

where the first row is the equation $I_1 = 0$ and we have obtained the second row by replacing the original condition on I_2 by $\Phi_1 = 1$.

The important thing is that the boundary conditions on the electrodes are

$$(2.57) \quad \Phi_1 = 1 \quad \text{and} \quad A_{11}\Phi_1 + A_{12}\Phi_2 + A_{13}\Phi_3 = 0,$$

which we will write $P\Phi = R$. The conditions on the test functions are different, namely

$$(2.58) \quad \Psi_1 = 0 \quad \text{and} \quad \Psi_2 = 0,$$

which we will write $Q\Psi = 0$. We are imposing the potential constraints P and in exchange *not* imposing known currents on the two electrodes. We are trying to find a $\Phi \in H^1(\Omega)$ satisfying $P\Phi = R$ such that

$$\Psi^t A \Phi = 0 \quad \forall \Psi \in \ker(Q).$$

(Recall from Chapter 1 that $\ker(Q)$, the kernel of Q , is the space of functions Ψ for which $Q\Psi = 0$.) From the theory of Lagrange multipliers, we know that this constrained problem is equivalent to

$$(2.59) \quad \begin{pmatrix} A & Q^t \\ P & 0 \end{pmatrix} \begin{pmatrix} \Phi \\ \lambda \end{pmatrix} = \begin{pmatrix} 0 \\ R \end{pmatrix}.$$

For our particular example we obtain

$$(2.60) \quad \begin{pmatrix} A_{11} & A_{12} & A_{13} & 1 & 0 \\ A_{21} & A_{22} & A_{23} & 0 & 1 \\ A_{31} & A_{32} & A_{33} & 0 & 0 \\ A_{11} & A_{12} & A_{13} & 0 & 0 \\ 1 & 0 & 0 & 0 & 0 \end{pmatrix} \begin{pmatrix} \Phi_1 \\ \Phi_2 \\ \Phi_3 \\ \lambda_1 \\ \lambda_2 \end{pmatrix} = \begin{pmatrix} 0 \\ 0 \\ 0 \\ 0 \\ 1 \end{pmatrix},$$

which leads to the same system nonsymmetric system as equations (2.56).

We can obtain a different (and incorrect!) solution if we try to maintain symmetry by choosing Ψ to lie in $\ker(P)$ and not $\ker(Q)$, i.e., we restrict the *test* functions to lie in the space

$$(2.61) \quad \Psi_1 = 0 \quad \text{and} \quad A_{11}\Psi_1 + A_{12}\Psi_2 + A_{13}\Psi_3 = 0.$$

In this case we would have to solve the Lagrangian system

$$(2.62) \quad \begin{pmatrix} A_{11} & A_{12} & A_{13} & A_{11} & 1 \\ A_{21} & A_{22} & A_{23} & A_{21} & 0 \\ A_{31} & A_{32} & A_{33} & A_{31} & 0 \\ A_{11} & A_{12} & A_{13} & 0 & 0 \\ 1 & 0 & 0 & 0 & 0 \end{pmatrix} \begin{pmatrix} \Phi_1 \\ \Phi_2 \\ \Phi_3 \\ \lambda_1 \\ \lambda_2 \end{pmatrix} = \begin{pmatrix} 0 \\ 0 \\ 0 \\ 0 \\ 1 \end{pmatrix}$$

whence $\lambda_2 = -A_{11}\lambda_1$, $\Phi_1 = 1$ and

$$(2.63) \quad \begin{pmatrix} 0 & A_{12} & A_{13} \\ A_{21} & A_{22} & A_{23} \\ A_{31} & A_{32} & A_{33} \end{pmatrix} \begin{pmatrix} \lambda_1 \\ \Phi_2 \\ \Phi_3 \end{pmatrix} = - \begin{pmatrix} A_{11} \\ A_{21} \\ A_{31} \end{pmatrix} \Phi_1.$$

We shall show that this system of equations is *inconsistent* with the correct solution for Φ .

We know from the true solution that $A_{31}\Phi_1 + A_{32}\Phi_2 + A_{33}\Phi_3 = 0$ so we must have that $A_{31}\lambda_1 = 0$ which can only be true if either *all* of the elements in A_{31} are zero or $\lambda_1 = 0$. So $\lambda_1 = 0$ and we obtain

$$(2.64) \quad \begin{pmatrix} A_{11} & A_{12} & A_{13} \\ A_{21} & A_{22} & A_{23} \\ A_{31} & A_{32} & A_{33} \end{pmatrix} \begin{pmatrix} \Phi_1 \\ \Phi_2 \\ \Phi_3 \end{pmatrix} = \begin{pmatrix} 0 \\ 0 \\ 0 \end{pmatrix}$$

which is clearly false. In other words, the *only* way that we can obtain a valid symmetric formulation is if $A_{31} = 0$. This is clearly consistent because then the conditions on the test functions are that $\Psi_1 = 0$ and $A_{11}\Psi_1 + A_{12}\Psi_2 = 0$ which decouple into Dirichlet constraints on Φ_1 and (if A_{12} is non-zero) Φ_2 (i.e., $\ker(P) = \ker(Q)$ if $A_{13} = 0$).

In conclusion, care must be taken when entering focussing conditions into stiffness matrices.³ If the focussing conditions are also applied to the test functions then (a) the resulting stiffness matrix will be symmetric and (b) the answer could be wrong!

2.3.6 Electrode impedance

At low frequencies, in fact, it is not possible to ensure that $\Phi = V$ on a current carrying electrode. Instead, an electrochemical reaction will take place which will cause a potential drop across the electrode, [45], [65]. This drop can be characterized by a material constant called the contact impedance Z_c with units Ω^2 and defined as the potential drop across the electrode for unit current density. Its formulation at DC thus corresponds to the mixed Neumann condition

$$(2.65) \quad \sigma \frac{\partial \Phi}{\partial \nu} = \frac{V - \Phi}{Z_c}$$

where ν is again the outward pointing normal from Ω (i.e., into the electrode). Z_c will vary with frequency, mud salinity and the electrochemical composition of the electrode. [45] and [51] show that most of the voltage drop takes place across a very thin capacitive zone in front of the electrode with additional contributions from electrolyte diffusion into and out of this zone. Typical values of Z_c in the low frequency (1Hz - 100Hz) range from $10^{-5}\Omega m^2$ to $10^{-3}\Omega m^2$. At higher frequencies Z_c becomes less important [36], [44], [51]. In Chapter 4, we discuss the impact that Z_c has on finite element modelling using both the Φ formulation presented here and the H_ϕ formulation developed in Chapter 3.

³For example, the MODULEF finite element package insists that linear boundary conditions apply equally to the test and trial functions, [55].

2.4 Iterative solution techniques

When A is a symmetric operator, the idea behind many iterative methods of solving $Ax = b$ is to recast the problem into finding a stationary point of the functional

$$(2.66) \quad f(x) = \frac{x^t Ax}{2} - b^t x$$

because

$$(2.67) \quad \frac{df(x)}{dx} = Ax - b$$

so $x = A^{-1}b$ is a stationary point of f . When A is not symmetric then

$$(2.68) \quad \frac{df(x)}{dx} = \frac{1}{2}(A + A^t)x - b$$

so this method cannot be used to invert A , except for the important case that A is *Hermitian* (that is $A = \overline{A}^t$). In this case, $x = A^{-1}b$ is the stationary point of the slightly different functional

$$(2.69) \quad f(x) = \overline{x}^t Ax - \overline{b}^t x - \overline{x}^t b.$$

The methods described here for (complex) symmetric matrices will go through for Hermitian matrices if we use the inner product $\langle x, \overline{y} \rangle$ instead of the complex-valued bilinear form $\langle x, y \rangle$. We will not discuss Hermitian matrices further in this text, however, because they occur infrequently in FEM discretizations of lossy media.

Recall that a *real valued* matrix A is positive definite if $\overline{d}^t A d > 0$ for any d , in which case we write $A > 0$. If $A > 0$ then the stationary point of $f(x)$ will actually be a minimum. For more general (e.g., complex) symmetric matrices we cannot assume $x = A^{-1}b$ to be a minimum.

Our strategy to find the stationary point of $f(x)$ is to use a sequence of search vectors $d_k, k = 1, 2, \dots$ and define x_{k+1} to be the stationary point of the one-dimensional function $f(x_k + \tau d_k)$. The only difference between the iterative schemes we propose here is the choice of d_k . McCormick, [46], has shown that more sophisticated methods such as multigrid and domain decomposition also come under the same formulation. We need the following definitions: let e_1, \dots, e_n be the standard basis for \mathbb{R}^N (i.e., e_i is the i th column of the $N \times N$ identity matrix) and let A_0 be some symmetric matrix which is 'close' to A and such that A_0^{-1} can be computed more rapidly than A^{-1} . We will always write $g_k = Ax_k - f$ for the residual error after k iterations. Let x_1 be some initial guess and set $d_0 = 0$. We define the following iterative methods:

Gauss-Seidel $d_k = e_{\text{mod}(k, N)}$

Steepest Descent $d_k = -g_k$

Biconjugate Gradient $d_k = -g_k + \frac{g_k^t g_k}{g_{k-1}^t g_{k-1}} d_{k-1}$

Preconditioned Biconjugate Gradient $d_k = -A_0^{-1} g_k + \frac{g_k^t A_0^{-1} g_k}{g_{k-1}^t A_0^{-1} g_{k-1}} d_{k-1}$

for $k = 1, 2, \dots$

Depending upon the properties of A (and A_0), these algorithms may or may not converge. In particular, they are all guaranteed to converge if A is real valued and $A > 0$, [66], [67]. Some will converge under more general circumstances. For a trivial example, if A has purely negative eigenvalues then steepest descent will converge, although it should then be more properly called steepest ascent! For general complex symmetric matrices the steepest descent algorithm will diverge (rapidly). Gauss-Seidel will also diverge. The convergence behaviour of the biconjugate gradient algorithm is more tricky, as is the nomenclature⁴. If A is purely real and symmetric (regardless of whether or not it is positive definite) the biconjugate gradient algorithm is called the conjugate gradient algorithm, [5]. For the conjugate gradient algorithm (ignoring effects of machine roundoff) then there is only one possible point of failure, the computation of τ .

At each iteration, we are given a search direction d_k and need to find the stationary point of $f(x_k + \tau d_k)$. We have

$$(2.70) \quad \frac{df(x_k + \tau d_k)}{d\tau} = \frac{d}{d\tau} \{ (x_k + \tau d_k)^t A (x_k + \tau d_k) / 2 - b^t (x_k + \tau d_k) \}$$

$$(2.71) \quad = (x_k + \tau d_k)^t A d_k - b^t d_k = 0$$

whence,

$$(2.72) \quad \tau = -\frac{d_k^t g_k}{d_k^t A d_k}.$$

If A is *not* positive definite then conceivably $d_k^t A d_k = 0$ for non-zero d_k and the conjugate gradient algorithm will fail. If, however, $A > 0$ (so that A is real) and we are solving $Ax = b$ where b is real then all the d_k will be real-valued so $d_k^t A d_k = 0$ only for $d_k = 0$ and, by construction, this can only happen if $g_k = 0$ (e.g., [6]) in which case x_k is the desired solution.

⁴ This nomenclature is unfortunately now standard, e.g. [22], [57], [59].

When $A > 0$, the conjugate gradient algorithm also has the property, [6], that the (real-valued) g_k are orthogonal to one another in the absence of machine round-off error. There certainly cannot exist more than N orthogonal vectors in \mathbb{R}^N , so we must also have that $g_k = 0$ for $k > N$. I.e., the conjugate gradient algorithm is guaranteed to converge in at least N steps provided that there is no machine round-off and no division by zero in the computation of τ , [29], [57]. For $A > 0$, [16] and [54] have the even stronger result that the algorithm will converge to machine precision (albeit not necessarily in N steps) even in the presence of machine round-off.⁵ For the non-positive definite case, consider the problem of solving $Ax = b$ with zero initial guess and

$$A = \begin{pmatrix} 1 & 0 \\ 0 & -1 \end{pmatrix}.$$

We have

$$d_1 = -g_1 = \begin{pmatrix} b_1 \\ b_2 \end{pmatrix} \quad Ad_1 = \begin{pmatrix} b_1 \\ -b_2 \end{pmatrix}$$

so

$$\tau_1 = -d_1^t g_1 / d_1^t A d_1 = \frac{b_1^2 + b_2^2}{b_1^2 - b_2^2} \quad \text{and} \quad x_2 = \frac{b_1^2 + b_2^2}{b_1^2 - b_2^2} \begin{pmatrix} b_1 \\ b_2 \end{pmatrix}.$$

$$g_2 = \frac{b_1^2 + b_2^2}{b_1^2 - b_2^2} \begin{pmatrix} b_1 \\ -b_2 \end{pmatrix} - \begin{pmatrix} b_1 \\ b_2 \end{pmatrix} = \frac{2b_1 b_2}{b_1^2 - b_2^2} \begin{pmatrix} b_2 \\ -b_1 \end{pmatrix} =$$

$$d_2 = -g_2 + \frac{g_2^t g_2}{g_1^t g_1} d_1 = \frac{b_2^2 - b_1^2}{b_1^2 + b_2^2} d_1$$

so that

$$\tau_2 = \frac{b_2^2 - b_1^2}{b_1^2 + b_2^2}$$

and

$$x_3 = \begin{pmatrix} b_1 \\ -b_2 \end{pmatrix}$$

so we have obtained the solution after two multiplications by A , provided $b_1 \neq b_2$. Different initial guesses would give rise to different conditions needed to avoid division by zero, but it will always be the case, [16], that such conditions will form a subset of measure zero. In the presence of machine round-off, this means that there is no upper bound on τ , although the likelihood of actually dividing by zero is small.

While the conjugate gradient algorithm has only one potential point of failure, the biconjugate gradient algorithm has three.⁶ In addition to the fact that τ need not be defined for some

⁵ In the presence of machine round-off, the g_k rapidly lose their orthogonality, [27], [54].

⁶ Of course, the algorithms themselves are the same! For symmetric matrices, the attribute 'bi' only refers to the types of matrix to which the algorithm is applied.

d_k , it is conceivable that g_k could be non-zero but $g_k^t g_k = 0$. A more subtle problem is that complex symmetric matrices need not have N linearly independent eigenvectors. Such matrices are termed defective. For example,

$$(2.73) \quad A = \begin{pmatrix} a & b \\ b & a \pm 2ib \end{pmatrix}$$

has only one eigenvector. [16] shows that if the biconjugate gradient algorithm runs to completion *and* the matrix A is non-defective, then the algorithm will have converged to $x = A^{-1}b$. In the absence of machine error, the residual errors g_k satisfy the 'formal' orthogonality relationship $g_k^t g_l = 0$ for $k \neq l$, [11], [23], and as A is non-defective we also have that $g_k^t g_k \neq 0$. There cannot be more than N such vectors in \mathbb{C}^N , so if the algorithm converges then it must do so in N or fewer iterations.

It is well known, e.g., [6], that the preconditioned biconjugate gradient algorithm defined above is equivalent to biconjugate gradient applied to $A_0^{-1/2} A A_0^{-1/2}$, so the convergence analysis for the preconditioned biconjugate gradient algorithm is essentially that of the conjugate gradient algorithm. The only difference is that A could be positive definite and A_0 indefinite, in which case preconditioning could introduce a possibility of failure that was not present in the non-preconditioned algorithm. Also, the 'closer' A_0 is to A then the closer $A_0^{-1/2} A A_0^{-1/2}$ is to the identity matrix and if this is so then it seems reasonable to expect a more robust and rapidly converging algorithm.

This has been quantified by [54]. The convergence of the biconjugate gradient algorithm is intimately related to the eigenvalue distribution or spectrum $\sigma(A)$ ⁷, [6], [31], namely that if $A > 0$ and $\hat{x} = A^{-1}b$ is the desired solution then

$$(2.74) \quad (\hat{x} - x_k)^t A (\hat{x} - x_k) \leq \max_{\lambda \in \sigma(A)} |p_k(\lambda)| (\hat{x} - x_0)^t A (\hat{x} - x_0)$$

for any k th degree polynomial $p_k(x)$ with $p(0) = 1$. Here x_k is the solution after the k th iteration and x_0 is the initial guess.

For example, if $S = [\lambda_1, \lambda_N]$ contains all of the (necessarily real and positive) eigenvalues of the positive definite matrix A , then for any p_k with $p_k(0) = 1$,

$$(2.75) \quad \max_{\lambda \in \sigma(A)} |p_k(\lambda)| \leq \max_{\lambda \in S} |p_k(\lambda)|$$

and the polynomial we use will give a bound on the error $\hat{x} - x_k$. Obviously, we want to find

⁷More precisely, the spectrum of a bounded operator is the (necessarily compact) set of points λ such that $A - \lambda$ is not invertible.

p_k to give as tight a bound as possible, and [6] shows that this is bound is

(2.76)

$$\min_{p_k} \max_{\lambda \in S} |p_k(\lambda)| = T_k \left[\frac{\lambda_N + \lambda_1}{\lambda_N - \lambda_1} \right]^{-1} < 2 \left(\frac{\sqrt{\lambda_N} - \sqrt{\lambda_1}}{\sqrt{\lambda_N} + \sqrt{\lambda_1}} \right)^k < 2e^{-2k/\sqrt{\kappa(A)}}$$

where T_k is the Chebyshev polynomial of degree k , [1], and $\kappa(A) = \lambda_N/\lambda_1$ is the condition number of A . This is a somewhat pessimistic estimate because it assumes the eigenvalues are evenly spaced within $[\lambda_1, \lambda_N]$. [6] and [31] give tighter bounds when more information about $\sigma(A)$ is known. Clustering near the smallest eigenvalues is particularly significant. Nonetheless, this bound does show us that if we choose A_0 such that $\kappa(A_0^{-1/2} A A_0^{-1/2}) < \kappa(A)$ then convergence will improve.

In fact, the ‘downside’ of the (bi)conjugate gradient applied to indefinite matrices is not that the algorithm will, or will not, converge in N steps (which for large sparse systems would be prohibitive anyway) but rather that the *asymptotic* rate of convergence will be much poorer than indicated by equation (2.76) if there are many eigenvalues λ with $\text{Re}(\lambda) < 0$, [18]. Moreover, [21] and [53] give numerical examples which show that if a large number of eigenvalues straddle the origin of the complex plane then methods based on Krylov approximations generally offer no significant advantage over solving the normal equations by ‘standard’ conjugate gradient.⁸

Biconjugate gradient iteration (i.e., complex symmetric A) without preconditioning is not very robust, especially for high frequencies, ω . Not only can the asymptotic rate of convergence be poor but also near-divisions by zero can make τ very large causing wild oscillations and loss of accuracy in $|g_k|$. In addition to reducing the condition number, a good preconditioner will be one which reduces such oscillations, presumably by bringing $A_0^{-1/2} A A_0^{-1/2}$ closer to a positive definite matrix.

Even at DC, however, preconditioning is a necessary step because of the ill-conditioning caused by (i) conductivity contrasts and (ii) mesh refinement, [6]. A method was developed in [47], which partially alleviates these two problems, namely incomplete LU preconditioning: traditional LU factorization as developed in Chapter 1 but with fill-in excluded.

2.4.1 Incomplete LU Preconditioning

The closer that A_0 approximates A , then the closer $A_0^{-1} A$ will be to the identity, giving rise to a more convergent algorithm. However, while A has a sparse storage, A^{-1} requires a very

⁸The *normal* equation corresponding to $Ax = b$ is $\bar{A}^t A x = \bar{A}^t b$.

large amount and it could be very computationally expensive to choose A_0 too close to A . The trick is to find a good preconditioner A_0 which accelerates convergence without requiring large storage requirements.

The idea behind ILU preconditioning, [6], [24] is to compute matrices L and U such that $A_0 = LU$ is close to A , but such that L and U retain the sparse storage of A . The matrix $C = LU - A$ is termed the ILU defect and is hopefully 'small' relative to A . The following algorithm shows how to overwrite A with L and U and at the same time compute C .

```

do r = 1 to N - 1
  do r = 1 to N - 1
    d = A(r, r)
    do i = r + 1 to N
      if A(i, r) ≠ 0 then
        e = A(i, r)/d
        A(i, r) = e
        do j = r + 1 to N
          if A(r, j) ≠ 0 then
            if A(i, j) ≠ 0 then
              A(i, j) = A(i, j) - e × A(r, j)
            else
              C(i, j) = C(i, j) + e × A(r, j)
              C(i, i) = C(i, i) - e × A(r, j)           : optional
              A(i, i) = A(i, i) - e × A(r, j)           : optional
            end if
          end if
        end do
      end if
    end do
  end if
end do
end do
end do
end do

```

At the end of this algorithm A has been overwritten by L and U with L having unit diagonals which are not stored, i.e., the diagonal elements that are stored in A after the ILU algorithm are the diagonal elements of U . Note that as A is complex symmetric, so is C and $U = DL^t$ for some diagonal matrix D .

As written, this is the so-called modified ILU whereby fill is actually transferred to the diagonal of A (the lines flagged as 'optional' in the above code). This has the effect that C is necessarily the weighted sum of positive semi-definite matrices which simplifies a number

of mathematical proofs and has occasionally been shown to improve convergence, [6]. Our numerical experiments have not determined conclusively whether there is an advantage or not in adding this term to the diagonal of A . Adding additional terms to the diagonal can also ensure that the product LU is positive definite at DC, [32].

A thorough examination of ILU preconditioning is given in [6] where it is shown that the effect of ILU preconditioning is a decrease in iteration count from $O(N^{1/d})$ to $O(N^{1/(2d)})$ where d is the dimension of the problem. For example, as each iteration requires $O(N)$ operations, the total cpu count for an ILU preconditioned conjugate gradient solution to the 2D equation (2.31) is $O(N^{5/4})$. We shall return to this point in Chapter 3 when we look at some practical examples of the biconjugate gradient algorithm to Maxwell's equations.

2.5 Adaptive meshing

We have seen that given piecewise linear approximation functions, the finite element solution converges quadratically as the mesh is refined. This result is pessimistic in that it supposes the whole mesh to be refined uniformly. In practice, there will be areas where the solution is already well approximated by piecewise linear functions and in such regions there is little advantage to subdividing the mesh. We examine criteria that can be used to decide where to subdivide the mesh and still retain quadratic convergence.

There are two essentially different ways of refining meshes, the first compares the mesh against some approximate solution which captures the physics, typically some information about the second derivative is needed, then, say, the areas of each triangle can be adjusted so that the net "weight" of each function is the same on each element. This is the approach used in TWODEPEP, [58]. An alternative method looks at the finite element on the coarse mesh and applies some functional to that mesh, "hot spots" of which will then be candidates for refinement. The functionals used are again usually related to the norm of the second derivative.

Consider a P1 discretization on a quasi-uniform mesh Ω_h of triangles and suppose we have computed the corresponding Galerkin solution u_h . Conceivably, Ω_h will be sufficiently fine in some places and not fine enough in others. We would like to be able to analyze u_h to determine refinement points in Ω_h . Let $\Omega_{h/2}$ be the mesh obtained by subdividing each triangle of Ω_h into 4 as shown dotted in Figure 2.3. We can assume that the node numbers of those Ω_h nodes in $\Omega_{h/2}$ have not changed.

We demonstrate a procedure which will determine whether mesh around the u_0 node is a candidate for refinement. (We shall use u_0 , etc., both for the value of the solution at that point

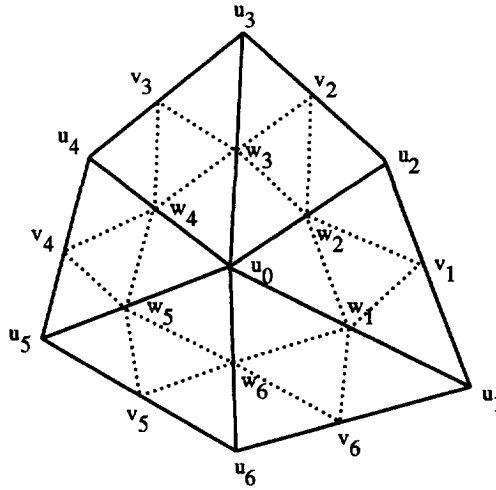


Figure 2.3: Refinement patch (shown dotted) on triangular mesh.

and the node number.)

Examining Figure 2.3, we see that if there are N_0 triangles in Ω_h which contain node u_0 then there are N_0 radial spurs from u_0 and so an additional N_0 interior nodes on $\Omega_{h/2}$ mesh as well as an additional N_0 new ‘boundary’ nodes. We order the triangles anti-clockwise and use the notation u_j for the original node on the triangle, w_j for the node on the j th spur and v_j for the j th boundary node. By abuse of notation, we shall also write u_1 as u_{N_0+1} , etc.

We use the RS/CS data structure to compute the v_i and w_i . Suppose that RS1,CS1 is the data structure for Ω_h and RS2,CS2 for $\Omega_{h/2}$. If I denotes the u_0 node number, then u_i are given by CS1[RS1[I] : RS1[I+1] - 1] and the w_i are the values CS2[RS2[I] : RS2[I+1] - 1] (the diagonal term u_0 is also in both of these lists). The only tricky point is that with the subdivision of Figure 2.3 then v_i is the *unique* node in the $h/2$ mesh which is a neighbour of both u_i and u_{i+1} . (This would not be true for some alternate subdivision schemes.) So v_i is obtained as the intersection of CS2[RS2[J] : RS2[J+1] - 1] and CS2[RS2[K] : RS2[K+1] - 1] where $J = u_i$ and $K = u_{i+1}$.

Note that when considering Laplace’s equation in the plane, if the material properties are constant within each element of size h , then we do not have to recompute the stiffness matrices for any of the $h/2$ elements (regardless of dimension) because the material properties

and Jacobian are constant within the h element. E.g., consider the local stiffness matrix from the element 045.

$$(2.77) \quad (u_0 \quad u_4 \quad u_5) \begin{pmatrix} A_{00} & A_{04} & A_{05} \\ A_{40} & A_{44} & A_{45} \\ A_{50} & A_{54} & A_{55} \end{pmatrix} \begin{pmatrix} u_0 \\ u_4 \\ u_5 \end{pmatrix}$$

(our notation deliberately ignores symmetry). Then as the $h/2$ triangles are similar, the contribution from element 045 to the global stiffness matrix for the $h/2$ elements is

$$\begin{pmatrix} u_0 \\ w_4 \\ u_4 \\ v_4 \\ u_5 \\ w_5 \end{pmatrix}^t \begin{pmatrix} A_{00} & A_{04} & 0 & 0 & 0 & A_{05} \\ A_{40} & A_{00} + A_{44} + A_{55} & A_{04} & A_{50} + A_{05} & 0 & A_{45} + A_{54} \\ 0 & A_{40} & A_{44} & A_{45} & 0 & 0 \\ 0 & A_{50} + A_{05} & A_{54} & A_{00} + A_{44} + A_{55} & A_{54} & A_{40} + A_{04} \\ 0 & 0 & 0 & A_{54} & A_{55} & A_{50} \\ A_{50} & A_{45} + A_{54} & 0 & A_{04} + A_{40} & A_{05} & A_{00} + A_{44} + A_{55} \end{pmatrix} \begin{pmatrix} u_0 \\ w_4 \\ u_4 \\ v_4 \\ u_5 \\ w_5 \end{pmatrix}$$

If Dirichlet conditions are not imposed on the stiffness matrix then we have noted earlier that constant functions are then eigenvectors corresponding to the zero eigenvalue. The columns (and by symmetry the rows) will necessarily sum to zero. As a check on the above equation, we can see that as the rows and columns of the local h stiffness matrix sum to zero so do the rows and columns of the $h/2$ matrix. Symmetry properties in the h mesh will also be conferred onto $\Omega_{h/2}$.

However, when solving Laplace's equation in axisymmetric coordinates or when solving for H_ϕ either with, or without frequency, the formula for the $h/2$ stiffness matrix is not correct. For axisymmetric coordinates, we have seen that the material property term enters the stiffness matrix as $\sigma\rho$. In Chapter 3, we shall see that with an alternative formulation based on H_ϕ , the material properties enter as $1/(\sigma\rho)$. When solving for frequency problems the stiffness matrix and mass matrix do not scale together. For 2D problems in the plane with lumped mass approximation then scale invariance does hold.

For these more general problems, we have two choices: compute the true stiffness matrix on the $h/2$ mesh, or not! If not, then one can argue that all that is important is that some 'fairly close' second order operator is well approximated by the mesh: if the original mesh was fine enough then this assumption is valid. Note that here we are only looking for a heuristic as to which nodes should be refined, not to use the $h/2$ stiffness matrix to update u_h directly.

Once we have the $h/2$ global matrix for the patch, we suppose that we know the boundary values u_i and interpolate the v_i with

$$v_i = \frac{u_{i+1} + u_i}{2}$$

and then use an iterative method (a small number of Gauss-Seidel steps suffices) method to update u_0 and check for a significant change. If there is a significant change then that node is a candidate for mesh refinement.

2.6 Lanczos methods and focussing⁹

We have seen that the focussed Laterolog problem can be cast formally into solving the non-symmetric block system

$$(2.78) \quad \begin{pmatrix} A_{11} & A_{12} & 0 \\ A_{21} & A_{22} & -I \\ 0 & P & Q \end{pmatrix} \begin{pmatrix} \Phi \\ V \\ E \end{pmatrix} = \begin{pmatrix} 0 \\ 0 \\ R \end{pmatrix}$$

where V is denotes the N electrode voltages, E the corresponding electrode currents and $PV + QE = R$ is the focussing constraint. We have divided the nodes up into 'interior' nodes with subscript 1 and use subscript 2 for electrode nodes. If E were known in advance then we could solve the first two rows, whereas if V were known in advance then we would solve the constrained system

$$(2.79) \quad \begin{pmatrix} A_{11} & A_{12} \\ 0 & I \end{pmatrix} \begin{pmatrix} \Phi_1 \\ \Phi_2 \end{pmatrix} = \begin{pmatrix} 0 \\ V \end{pmatrix}$$

It is the non-reciprocal nature of the $PV + QE = R$ focussing that causes the problem.

In Section 2.3.3, we proposed solving N separate equations with each equation having unit current emanating from just one electrode, i.e., solving the block system

$$(2.80) \quad \begin{pmatrix} A_{11} & A_{12} \\ A_{21} & A_{22} \end{pmatrix} \begin{pmatrix} \Phi_1 \\ Z \end{pmatrix} = \begin{pmatrix} 0 \\ I \end{pmatrix}$$

where I is the $N \times N$ identity matrix and $\Phi_1 = (\phi_{11}, \phi_{12}, \dots, \phi_{1N})$ is the collection of solutions for each excitation. Z is the symmetric transfer impedance matrix. Then we can use Gaussian elimination to solve

$$(2.81) \quad (PZ + Q)E = R.$$

From an iterative perspective, we can of course stop after, say, k iterations so that Z_k is the approximate (and probably not quite symmetric) transfer impedance matrix. Substituting into

⁹Presented in [38].

equation (2.81) gives the approximate currents

$$(2.82) \quad (PZ_k + Q)E_k = R.$$

and $E_k \rightarrow E$ as the conjugate gradient iteration count increases. Unfortunately, this method is not very numerically convenient because the computation of $(PZ_k + Q)^{-1}$ typically involves the subtraction of very similar numbers so Z_k must be obtained to high accuracy (better than 6-7 significant figures). It would be better if we could find a way of solving $(PZ_k + Q)E_k = R$ without ever computing Z . (E.g., $A^{-1}f - A^{-1}g$ might require $A^{-1}f$ and $A^{-1}g$ to high accuracy whereas $A^{-1}(f - g)$ need not.)

Two approaches come to mind. This first is to solve $(PZ_k + Q)E_k = R$ itself iteratively. This would only require the (approximate) action of A^{-1} on another vector, not require the values of Z_k themselves. Because $(PZ_k + Q)$ is non-symmetric we cannot use conjugate gradient directly. Possible choices are conjugate gradient applied to the normal equations $(Z_k^t P^t + Q^t)(PZ_k + Q)E_k = (Z_k^t P^t + Q^t)R$ or a generalized minimum residual method such as [56] applied to the non-symmetric equations directly.

The second approach is to use a connection between conjugate gradient iteration and tridiagonalization. We have mentioned that, by construction, the residual errors g_k are orthogonal (at least in the absence of machine error), so that with $x_j = g_j / \|g_j\|$ for $j = 1, \dots, k$ then $X_k^t X_k = I_k$, the $k \times k$ identity matrix. Moreover, [16] shows that for suitable α_j and β_j defined in terms of τ_j and $\|g_j\|$ then we have the Lanczos three-term recurrence relation

$$(2.83) \quad Ax_j = \beta_{j+1}x_{j+1} + \alpha_j x_j + \beta_{j-1}x_{j-1},$$

i.e., $AX_k = X_k T_k$ for some tridiagonal matrix T_k . Because of the orthogonality of the x_j , T_k represents the projection of A onto the space generated by x_1, \dots, x_k . In the presence of machine error, orthogonality cannot be assumed, but nonetheless one can show, [2], [19], that for an analytic function f then

$$(2.84) \quad f(A)X_k = X_k f(T_k).$$

Note that if we assume a zero initial guess then the first column of X_k is $b/\|b\|$ where b is the right-hand vector so that, for example,

$$(2.85) \quad A^{-1}b \approx X_k T_k^{-1}(\|b\| \ 0 \ 0 \ \dots \ 0).$$

Applying N independent conjugate gradient iterations, with k steps in each, and right-hand vectors $b = e_j$, $j = 1, \dots, N$ thus corresponds to a block decomposition

$$(2.86) \quad AX_k = X_k T_k \quad \text{and} \quad X_k^t X_k = I_k$$

with the first 'block' vector being $(0 \ I_N)^t$ so that

$$(2.87) \quad A^{-1} \begin{pmatrix} 0 \\ I_N \end{pmatrix} = X_k T_k^{-1} (I_N, \ 0, \dots, 0),$$

and we can write the focussed system as

$$(2.88) \quad T_k V - \begin{pmatrix} I_N \\ 0 \end{pmatrix} E = 0,$$

$$(2.89) \quad P(0, I_N) X_k V + Q E = R.$$

The advantages of this formulation are that we do not need to compute $A^{-1}f$ exactly for any vector f in order to continue the iteration. With the GMRES approach, [56], we need to have an initial guess for the E 's. That initial guess gets better as k increases because we have the solution for the E of the previous k , but the operator Z_k will have to be started again "from scratch" and applied to many different vectors. A disadvantage of the Lanczos formulation is that we are always in effect solving $A^{-1}I_N$ and using the conjugate gradient information gained in the solution of that system to drive the matrix inversion.

2.7 Conclusions

We have presented some of the state of the art methods used in finite element modelling, many of which have not appeared in the geophysical literature. In the subsequent chapters, we shall expand and enhance these methods and develop new applications to electrode (TM) modelling in 2D and 3D formations.

References

- [1] Abramowitz, M. and I. A. Stegun, *Handbook of Mathematical Functions*, Dover, New York, 1972.
- [2] Allers, A., A. Sezginer, and V. Druskin, "Solution of 2 1/2-dimensional problems using the Lanczos decomposition", Submitted to Radio Science, 1993.
- [3] Anderson, B., "Induction sonde response in stratified media", The Log Analyst, **24**, no. 1, 1983, pp. 25-31.

- [4] ———, “*The analysis of some unsolved induction interpretation problems using computer modelling*”, *The Log Analyst*, **27**, no. 5, 1986, pp. 60–73.
- [5] Asby, S. F., T. A. Manteuffel, and P. E. Saylor, “*A taxonomy for conjugate gradient methods*”, *SIAM J. Numer. Anal.*, **27**, 1990, pp. 1542–1568.
- [6] Axelsson, O. and V. A. Barker, *Finite Element Solution of Boundary Value Problems*, Academic Press, New York, 1984.
- [7] Barber, T. D., “*Induction log vertical resolution enhancement – physics and limitations*”, in *Transactions of the 28th SPWLA Symposium*, San Antonio, TX, 1985.
- [8] ———, “*Real time environmental corrections for the phasor induction tool*”, in *Transactions of the 26th SPWLA Symposium*, Dallas, TX, 1985. Paper EE.
- [9] Barber, T. D. and R. Rosthal, “*Using a multiarray induction tool to achieve logs with minimum environmental effects*”, in *SPE 66th Annual Technical Conference*, Dallas, TX, 1991. Paper SPE 22725.
- [10] Boyce, J., G. King, W. Diamond, A. Becker, J. Doucet, and R. Bramblett, “*An electron Linac as an x-ray source for measuring geological density*”, *Nucl. Inst. and Meth.*, **A242**, no. 507, 1986.
- [11] Brezinski, C., *Padé-type approximation and general orthogonal polynomials*, Birkhäuser, Basel, 1980.
- [12] Chaba, A., *Os efeitos Delaware e Groningen: Um estudo quantitativo por elementos finitos*, Master's thesis, Universidade Federal do Pará, Belém, Brazil, 1993.
- [13] Chew, W. C., *Equivalence of a toroid and a voltage gap*, 1990. Personal communication.
- [14] ———, *Waves and Fields in Inhomogeneous Media*, Van Nostrand Reinhold, New York, 1990.
- [15] ———, *Superconvergence and Gauss' principle*, 1992. Personal communication.
- [16] Cullum, J. K. and R. A. Willoughby, *Lanczos Algorithms for Large Symmetric Eigenvalue Calculations, Vol. 1 Theory*, vol. 3 of *Progress in Scientific Computing*, Birkhäuser, Boston, 1985.
- [17] Dewan, J. T., *Essentials of Modern Open-hole Log Interpretation*, PennWell, Tulsa, 1983.
- [18] Druskin, V. L., *On the convergence of conjugate gradient method for indefinite matrices*, 1992. Personal communication.

- [19] Druskin, V. L. and L. Knizhnerman, "Two polynomial methods of calculating functions of symmetric matrices", *Journal of Computational Mathematics and Mathematical Physics*, **29**, no. 6, 1989, pp. 112–121.
- [20] Ellis, D., *Fundamentals of Well Logging Interpretation*, Dover, New York, 1984.
- [21] Freund, R. W., *Pseudo Ritz values for indefinite Hermitian matrices*, tech. rep., NASA Ames, CA, 1989. RIACS Technical Report 89.33.
- [22] ———, "Conjugate gradient-type methods for linear systems with complex symmetric coefficient matrices", *SIAM J. Sci. Stat. Comput.*, **13**, no. 1, 1992, pp. 425–448.
- [23] Freund, R. W., M. H. Gutknecht, and N. M. Nachtigal, "An implementation of the look-ahead Lanczos algorithm", *SIAM J. Sci. Comput.*, **14**, no. 1, 1993, pp. 137–158.
- [24] George, A. and J. W. H. Liu, *Computer Solution of Large Sparse Positive Definite Systems*, Prentice Hall, Englewood Cliffs, NJ, 1981.
- [25] Gianzero, S. and B. Anderson, "A new look at skin effect", in *Transactions of the 22nd SPWLA Symposium*, Mexico, 1981. Paper I.
- [26] Gianzero, S., R. Chemali, Y. Lin, S. Su, and M. Foster, "A new resistivity tool for measurements while drilling", in *26th SPWLA Symposium*, Dallas, TX, 1985. Paper A.
- [27] Golub, G. H. and C. van Loan, *Matrix Computations*, Johns Hopkins University Press, Baltimore, MD, 1983.
- [28] Habashy, T. M., J. Xia, and M. G. Lüling, *A model for the compensated dual resistivity (CDR) tool in a cylindrically stratified medium*, tech. rep., Schlumberger-Doll Research, Ridgefield, CT, 1991.
- [29] Hestenes, M. R. and E. Stiefel, "Method of conjugate gradients for solving linear systems", *J. Res. Nat. Bur. Stand.*, **49**, 1952, pp. 409–435.
- [30] Jackson, J. D., *Classical Electrodynamics*, John Wiley, New York, 1962.
- [31] Jennings, A., "Influence of the eigenvalue spectrum on the convergence rate of the conjugate gradient method", *J. Inst. Math. Appl.*, **20**, 1977, pp. 61–72.
- [32] Kershaw, D. S., "The incomplete Cholesky-conjugate gradient method for the iterative solution of systems of linear equations", *J. Comp. Phys.*, **26**, 1977, pp. 43 – 65.
- [33] Kleinberg, R. L., W. C. Chew, E. Y. Chow, B. Clark, and D. D. Griffin, "Microinduction sensor for the oil-based mud dipmeter", *SPE Formation Evaluation*, **12**, 1988, pp. 733–742.

- [34] Kong, J. A., *Theory of Electromagnetic Waves*, John Wiley, New York, 1975.
- [35] Křížek, M. and P. Neittaanmäki, *Finite Element Approximation of Variational Problems and Applications*, Longman Scientific and Technical, Harlow, UK, 1990.
- [36] Lorenz, W. J. and F. Mansfield, "Determination of corrosion rates by electrochemical DC and AC methods", *Corrosion Science*, **21**, no. 9, 1981, pp. 647–672.
- [37] Lovell, J. R., *Modelling frequency effects on Laterologs*, tech. rep., Schlumberger-Doll Research, Ridgefield, CT, 1990. Report EMG-90-34.
- [38] ———, "Iterative methods for focussed Laterologs", in SIAM Conference on Mathematical and Computational Issues in the Geosciences, Houston, TX, 1993.
- [39] ———, "Superconvergent and hierarchical methods in 3D finite elements", in Progress in Electromagnetic Research Symposium, Pasadena, CA, 1993.
- [40] Lovell, J. R. and W. C. Chew, "Response of a point source in a multicylindrical layered medium", *IEEE Trans. Geoscience Remote Sensing*, **25**, no. 6, 1987, pp. 850–858.
- [41] ———, "Effect of tool eccentricity on some electrical well logging tools", *IEEE Trans. Geoscience Remote Sensing*, **28**, no. 1, 1990, pp. 127–136.
- [42] Lüling, M. G., *The electromagnetics of a toroidal coil*, 1991. Personal communication.
- [43] Luthi, S. M. and P. Souhaite, "Fracture apertures from electrical borehole scans", *Geophysics*, **55**, 1990, pp. 821–833.
- [44] Macdonald, D. D., "Theoretical analysis of electrochemical impedance", in Corrosion 87, NACE, Houston, TX, 1987. Paper 479.
- [45] Madden, T. R., *Electrode polarization and its influence on the electrical properties of mineralized rocks*, PhD thesis, Dept of Earth and Planetary Science, MIT, 1961.
- [46] McCormick, S., *Equivalence of iterative schemes*, 1992. Personal communication, Copper Mountain Multigrid Conference.
- [47] Meijerink, J. A. and H. A. van der Vorst, "An iterative solution method for linear systems of which the coefficient matrix is a symmetric M-matrix", *Math. Comp.*, **31**, 1977, pp. 148–162.
- [48] Monk, P. B., *An analysis of Nédélec's method for the spatial discretization of Maxwell's equations*, tech. rep., University of Delaware, Newark, DE, 1991.
- [49] ———, "A mixed method for approximating Maxwell's equations", *Siam J. Numer. Anal.*, **28**, no. 6, 1991, pp. 1610 – 1634.

- [50] Moran, J. H., "Induction logging – geometrical factors with skin effect", *The Log Analyst*, **23**, no. 2, 1982, pp. 4–10.
- [51] Morgan, D., T. R. Madden, and Y. Angoran, *Mineralogical and chemical contributions to spectral ip*, 1988. Personal communication.
- [52] Mowat, G., A. McKee, and T. Geehan, "Drilling mud properties and formation evaluation", in *Transactions of the 15th Annual Symposium of the Indonesian Petroleum Association*, Jakarta, 1980.
- [53] Nachtigal, N. M., S. C. Reddy, and L. N. Trefethen, *How fast are non-symmetric iterations?*, tech. rep., MIT, 1990. Numerical Analysis Report 90-2.
- [54] Paige, C. C. and M. A. Saunders, "Solution of sparse indefinite systems of linear equations", *SIAM J. Numer. Anal.*, **12**, 1975, pp. 617–629.
- [55] Perronet, A., *The club MODULEF: a library of subroutines for finite element analysis*, in *Computing Methods in Applied Sciences and Engineering*, vol. 704 of *Lecture Notes in Mathematics*, Springer-Verlag, Berlin, 1979, pp. 127–153.
- [56] Saad, Y. and M. H. Schultz, "GMRES, a generalized minimum residual algorithm for solving non-symmetric linear systems", *SIAM J. Sci. Stat. Comput.*, **7**, 1986, pp. 856–859.
- [57] Sarkar, T. K., "On the application of the generalized biconjugate gradient method", *J. Elect. Waves and Applications*, **1**, no. 4, 1987, pp. 325–345.
- [58] Sewell, G., *Analysis of a Finite Element Method: PDE/PROTRAN*, Springer-Verlag, New York, 1985.
- [59] Smith, C. F., A. F. Peterson, and R. Mittra, "The biconjugate gradient method for electromagnetic scattering", *IEEE Trans. Antennas and Propagation*, **38**, 1990, pp. 938–940.
- [60] Strang, G. and G. J. Fix, *An Analysis of the Finite Element Method*, Prentice-Hall, Inc., Englewood Cliffs, NJ, 1973.
- [61] Strickland, R., P. Sinclair, and J. de Brecht, "Introduction to the high resolution induction tool", in *Transactions of the 28th SPWLA Symposium*, London, England, 1987. Paper E.
- [62] Suau, J., P. Grimaldi, A. Poupon, and P. Souhaite, "The Dual Laterolog R_{xo} tool", in *SPE 47th Annual Technical Conference*, San Antonio, TX, 1972. Paper SPE 4018.

- [63] Taherian, M. R., W. E. Kenyon, and K. A. Safinya, "*Measurement of dielectric response of water-saturated rocks*", *Geophysics*, **55**, no. 12, 1990, pp. 1530–1541.
- [64] Titman, J., *Physics of Well Logging*, Dover, New York, 1984.
- [65] Wait, J. R., *Geo-electromagnetism*, Academic Press, New York, 1982.
- [66] Xu, J., "*Iterative methods by space decomposition and subspace correction*", *SIAM Review*, **34**, no. 4, 1992, pp. 581–613.
- [67] Young, D. M., *Iterative Solution of Large Linear Systems*, Academic Press, New York, 1971.

Laterolog Modelling at Non-Zero Frequencies

Abstract. Focussed electrode tools such as Laterologs operate at low frequencies and have been historically modelled as though they operated at DC. While capturing much of the tool physics, this prohibits modelling some important phenomenon such as the Groningen effect, an anomalous indication of hydrocarbon beneath large highly resistive anhydrite blocks. For applications in axisymmetric configurations (e.g., where the tool is centred and the beds are perpendicular to the borehole) we have developed a finite element formulation which solves for tool response regardless of excitation frequency. We show how the resulting stiffness matrix can be rapidly inverted and present a post-processing scheme which computes apparent resistivity without a loss in accuracy due to mesh discretization. From an interpretative view point, our formulation produces the current lines instead of equipotential surfaces and as such has been found to be more useful in understanding tool physics.

3.1 Introduction

Electrode tools operating over a wide range of frequencies are used in borehole logging to estimate formation resistivities. These resistivities are used to evaluate the amount of hydrocarbon in the rock. The simplest electrode configuration is termed the Schlumberger Array or electrical survey (ES) is shown in Figure 2.1c and involves a current source emanating from an electrode A returning to electrode B with two voltage electrodes M and N , [2], [33]. In a homogeneous formation, the resistivity is proportional to the potential difference between M and N divided by the current from A . The proportionality constant is termed the 'K-factor' and depends on electrode spacings and the like. In an inhomogeneous environment, this proportionality relationship is no longer valid and the tool instead reads an 'apparent' resistivity R_a , which must be further processed to arrive at formation resistivity. As discussed in Chapter 2, we refer to the configuration as Normal when N and B are at the surface, as Lateral if B is at the surface with N downhole, and as Shallow ES if both M and B are downhole.

Newer electrode tools are typically combinations of these configurations subject to focussing

conditions which maintain desired equipotential surfaces independent of the formation conductivity, [13]. Prime examples of such focussed tools are the Laterologs, typically run in one of two modes: a 'Shallow Mode' which is primarily sensitive to resistivity near the borehole and the 'Deep Mode' which probes a few metres into the formation. By running the two modes at different frequencies they can be combined to a single tool, as has been done with the Dual Laterolog (DLL)[†] shown in Figure 1.3. To minimize some anomalous effects, the voltage reference N for the DLL is always downhole, separated from the tool housing by a long (50m) insulated cable known as the bridle, [37].

Most of the mathematical and physical properties of Dual Laterologs are well understood [28], [35]. In particular, the separation between the Deep and Shallow readings can be shown to be dependent on the invaded zone around the borehole. So-called 'tornado charts' are then used to back out such parameters as depth of invasion, resistivity of invaded zone (R_{xo}) and formation resistivity (R_t), [11], [13], [40]. Layered environments complicate the interpretation but the usual assumption is that the operating frequencies are low enough to be able to predict the tool response by DC modelling of the layered media [4], [14]. This modelling has shown that for an unfocussed tool, currents will readily deviate away from resistive layers to penetrate neighbouring beds which are more conductive, as shown in the left-hand side of Figure 1.2. By using focussing techniques such as shown for the LL3 in the right-hand side of Figure 1.2 and for the DLL in Figure 1.3, however, shoulder effects can be reduced. They can not always be eliminated however.

In particular, if the DLL is logging beneath a highly resistive bed then one can show that the deep reading of apparent resistivity will increase as the voltage reference N enters the resistive zone. This has been termed the Delaware effect and has been minimized by putting the current return B at the surface. Under certain circumstances involving partially cased holes, however, separations have been observed which are both larger than the calculated Delaware effect and unrelated to invasion [41]. Lacour-Gayet, [21], [22], has shown that these separations vary with frequency. This phenomenon has come to be known as the Groningen effect after the eponymous oil field in the Netherlands where the phenomenon was first observed.

We present a new finite element formulation, [23], which can model the Groningen effect and has led to new strategies to remove it, [12]. Our formulation also lends itself to modelling the toroidal antennae recently proposed by for logging while drilling.

A commonality between these sources is that in an axisymmetric formation (e.g., in a vertical borehole penetrating horizontal layered beds) the only field components generated are H_ϕ , E_ρ and E_z . Because the magnetic field in the \hat{z} direction is zero such fields are termed Transverse Magnetic (TM). Induction tools excite the dual fields E_ϕ , H_ρ and H_z and are

[†]Mark of Schlumberger

termed Transverse Electric (TE). Without azimuthal symmetry either tool can generate all six components of electromagnetic field. For example, [25] shows how eccentricing an induction tool causes the formation to couple TE and TM modes. A non-perpendicular angle between borehole and beds will also cause coupling, [18].

In layered media, one can solve for tool response using spectral FFT techniques, e.g., [3], [8] but in more complicated geometries involving, say, a borehole, multiple beds and invaded zones where borehole fluid has penetrated the beds, semi-analytic or finite-element techniques become the method of choice, [9], [10]. This is especially true for the study of the Groningen effect as it involves armoured cable, highly conductive casing, and beds of widely varying resistivities. Low frequency TM excitation is often assumed to be DC, in which case Maxwell's equations collapse to the familiar Laplace's equation for which FEM codes abound, [5], [27], [42], [43]. In this chapter, we concentrate on finite element formulations for TM excitation at non-zero frequencies. In fact, our formulation is also valid at DC, and a trivial extension thereof covers TE excitation.

Whilst our finite element decomposition is essentially classical (e.g., [36], [43]) and can be viewed as a TM version of the TE code in [6], we do take advantage of the novel features introduced in the previous chapter, specifically (a) the use of an incomplete LU preconditioner combined with biconjugate iteration to solve the complex symmetric stiffness matrices, and (b) the use of a 'superconvergent' technique to compute normal derivatives along the boundary. The resulting code, called CWNLAT, is both faster and more accurate than other codes presented in the geophysics literature (e.g., [4], [42]).

In the next two sections, we present the mathematical and finite element formulation, concentrating on sources pertinent to borehole geophysics and leaving explicit details to Appendix 3.A. Subsequent sections deal with the matrix inversion and the Groningen effect.

3.2 Mathematical formulation

Assuming a time harmonic excitation of the form $e^{-i\omega t}$, Maxwell's equations in an axisymmetric, anisotropic domain Ω take the form

$$(3.1a) \quad \nabla \times \mathbf{E} = i\omega\mu\mathbf{H},$$

$$(3.1b) \quad \nabla \times \mathbf{H} = \bar{\sigma}\mathbf{E} + \mathbf{J}$$

where μ is the magnetic permeability and $\bar{\sigma}$ denotes a complex-valued anisotropic conductivity. \mathbf{J} is the impressed current density and $\bar{\sigma}\mathbf{E}$ the induced current density. The units of \mathbf{E} are V/m, the units of \mathbf{H} are A/m. We allow $\bar{\sigma}$ to be transverse isotropic with $\bar{\sigma} = \sigma_\rho \hat{\rho}\hat{\rho} + \sigma_\phi \hat{\phi}\hat{\phi} + \sigma_z \hat{z}\hat{z}$

[7],[29]. We do not consider a nonvertical symmetry axis for the anisotropy because this would couple the TE and TM modes. A non-zero term in $\hat{\rho}\hat{z}$ would not couple the modes but would imply an unusual anisotropy caused by grains or fractures oriented conically around the borehole and is also excluded from consideration. As in the previous chapters, in an isotropic formation we write σ instead of $\bar{\sigma}$. Compared to our earlier terminology, for notational convenience we have absorbed the dielectric term $i\omega\bar{\epsilon}$ into the expression for conductivity. For the frequencies under consideration in this chapter, dielectric effects will be negligible but we do not need this assumption for our modelling. We suppose σ_ρ and σ_z to be complex valued with positive real components which ensures that the fields will decay away from the source(s). If ω is nonzero, this decay will be exponential. We also suppose the imaginary components of σ_ρ and σ_z to be non-negative.

Assuming TM excitation, so that $\mathbf{J} = J_\rho\hat{\rho} + J_z\hat{z}$, we write $u = 2\pi\rho H_\phi$ and Maxwell's equations reduce to the second order equations

$$(3.2) \quad L(u) = \frac{\partial}{\partial\rho} \frac{1}{\rho\sigma_z} \frac{\partial u}{\partial\rho} + \frac{\partial}{\partial z} \frac{1}{\rho\sigma_\rho} \frac{\partial u}{\partial z} + \frac{i\omega\mu}{\rho} u = 2\pi M_\phi$$

where we have written

$$(3.3) \quad M_\phi \equiv -\hat{\phi} \cdot \nabla \times \bar{\sigma}^{-1} \cdot \mathbf{J} = \frac{\partial}{\partial\rho} \left(\frac{J_z}{\sigma_z} \right) - \frac{\partial}{\partial z} \left(\frac{J_\rho}{\sigma_\rho} \right).$$

The units of M_ϕ are V/m². Physically, $u = 2\pi\rho H_\phi$ is equal to the total amount of current¹ passing vertically through a disk of radius ρ . Moreover, contour lines of u are exactly the current lines in the formation, which is convenient for visualization of the fields.

As shown in Figure 3.1, we exclude the axis $\rho = 0$ from the domain Ω and set $\rho = a$ for the inner radius of Ω . $\hat{\nu}$ points outward from the boundary $\partial\Omega$, and $\hat{\tau} = \hat{\nu} \times \hat{\phi}$ denotes the tangent vector. We define dl to be the variable of integration $\tau_\rho d\rho + \tau_z dz$ along the boundary. If u and v are complex-valued scalar functions on Ω , we introduced in Chapter 1 the notations

$$(3.4) \quad \langle v, u \rangle_{L^2(\Omega)} = \iint_{\Omega} v u \, d\rho dz, \quad \langle v, u \rangle_{L^2(\partial\Omega)} = \oint_{\partial\Omega} v u \, dl.$$

Note that the element of integration here is $d\rho dz$ and not $\rho d\rho dz$, and that we are *not* taking any complex conjugates.

The boundary of Ω is divided into $\partial\Omega_0$: regions bounded by 'perfect' insulators (where $\sigma \equiv 0$ and displacement currents are negligible) and $\partial\Omega_\nu$ for the remainder. Boundary conditions along $\partial\Omega_0$ are called Dirichlet and correspond to insulated wires carrying known currents:

¹ Including displacement current.

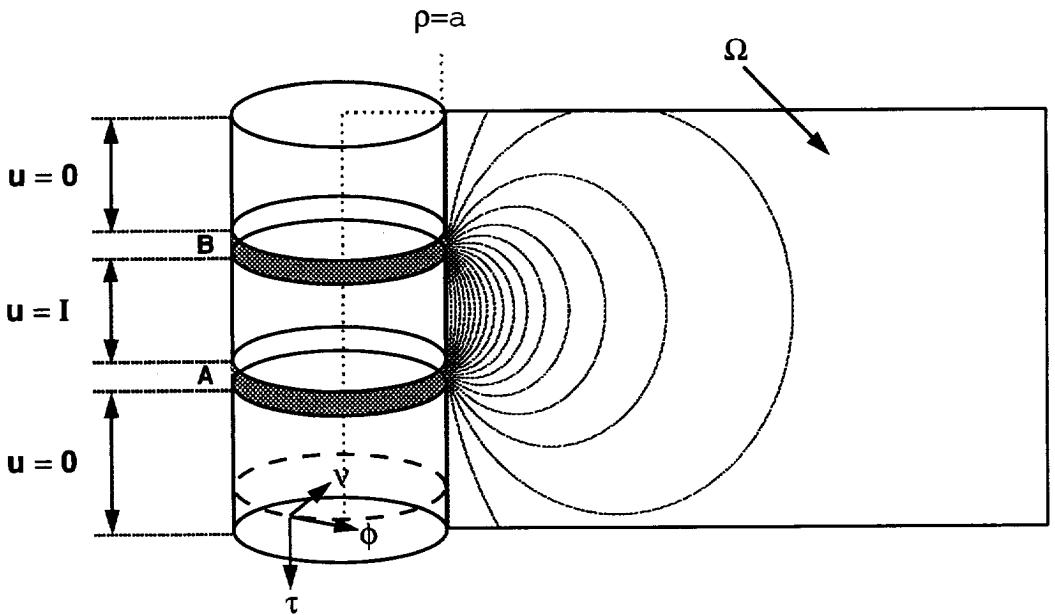


Figure 3.1: Configuration for a Shallow ES. Electrodes A and B have Neumann condition $E_\tau = Z_s H_\phi$. The boundary between electrodes has a Dirichlet constraint on $u = 2\pi\rho H_\phi$. ν denotes the unit normal vector pointing out of Ω and τ is the unit tangent vector to $\partial\Omega$. The electrodes at A and B are solid, $0 \leq \rho \leq a$.

applying Stokes theorem to a disk of radius a in the $\rho\phi$ plane, gives $u = 2\pi a H_\phi = I$, where I is the sum of impressed and induced currents passing perpendicularly through that disk. In general, across an imperfect conductor only the former will be known a priori but, by taking a to be sufficiently small (relative to ω), then the contribution from induced displacement currents along the borehole can be assumed negligible. Because the field decays exponentially from the source, boundary conditions 'at infinity' can be replaced by a zero Dirichlet condition boundary sufficiently far from the tool. In particular, $H_\phi = 0$ is a good approximation at an air/earth interface. In general, we write \bar{u} for the boundary conditions along $\partial\Omega_0$ with $\bar{u} \in H^{1/2}(\partial\Omega_0)$ as discussed in Chapter 1. We write $H_0^1(\Omega)$ for those functions in $H^1(\Omega)$ which are zero on $\partial\Omega_0$.

In this chapter, the source free boundary conditions along $\partial\Omega_\nu$ take the form $E_\tau - Z_s H_\phi = 0$ where Z_s represents the surface impedance in Ω . In general, we can always suppose that $Z_s = -z'_s - i\omega z''_s$ where z'_s and z''_s are both non-negative. Such boundary conditions can arise, for example, on electrodes or cable armour. We take $Z_s = 0$ if the electrodes are perfectly conducting. If the electrodes have radius a and a linear resistance per unit length R (in Ω/m) then we take $Z_s = -2\pi a R$. (The negative sign arises because $\hat{\tau} = -\hat{z}$ on $\rho = a$.)

For example, Figure 3.1 shows a Shallow ES with current I leaving electrode A and returning to electrode B : we set $u = I$ on that part of $\partial\Omega_0$ between A and B , and set $u = 0$ elsewhere on $\partial\Omega_0$. On the electrodes we set $E_\tau = 0$. The frequency here was 35Hz with skin effects negligible because of the short spacing between electrodes. Figure 3.1 shows only part of the computational domain Ω and the boundary segments 'at infinity' are not shown.

Our finite element formalism allows for the more general possibility of $E_\tau - Z_s H_\phi = T_\phi$, called an inhomogeneous mixed Neumann or Robin boundary condition. This is appropriate for modelling voltage gaps, for example, where $T_\phi \in H^{-1/2}(\partial\Omega_\nu)$ can be prescribed a priori. In Chapter 4, we shall develop a still more general boundary condition on $\partial\Omega_\nu$ which allows one to model electrodes with contact impedance. It is important to note that in this chapter when we refer to an electrode impedance we are referring to the ratio E_τ/H_ϕ on that electrode and *not* a contact impedance.

We show in Appendix 3.B that a Robin boundary condition is also a natural representation of a current carrying wireline cable. E.g., to model a Long Normal and bridle suspended from an armoured cable, we use the boundary conditions shown in Figure 3.2 where the unmarked sections of the boundary have the Dirichlet condition $H_\phi = 0$. Figure 3.2 shows the corresponding current lines computed by CWNLAT for the case of DC excitation when the cable armour is perfectly conducting (so that $T_\phi = Z_s = 0$). Figure 3.3 also assumes DC excitation but now T_ϕ and Z_s are large. We see that the fields along the cable armour have moved closer to the constant $2\pi H_\phi = I$ that would correspond to a perfectly insulating cable and that relatively more current returns to electrode B. These two examples are unrealistic

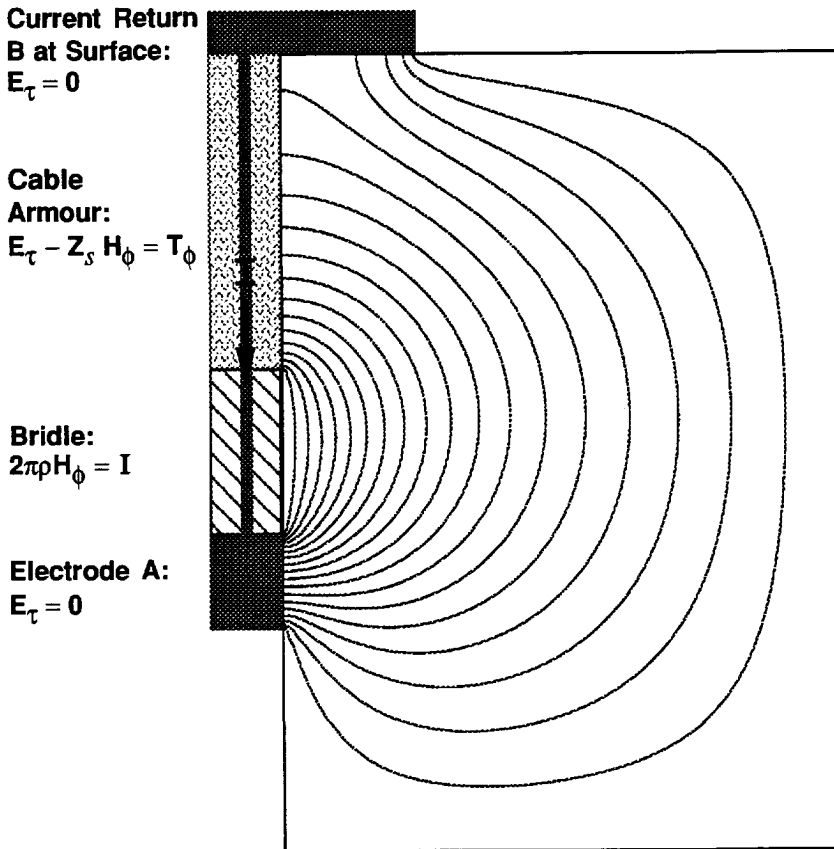


Figure 3.2: Boundary conditions for an electrode A suspended on an armoured cable. Electrode A is separated from the cable armour by an insulating bridge. The electric field lines were computed for the DC case with perfectly conducting cable armour, $Z_s = T_\phi = 0$.

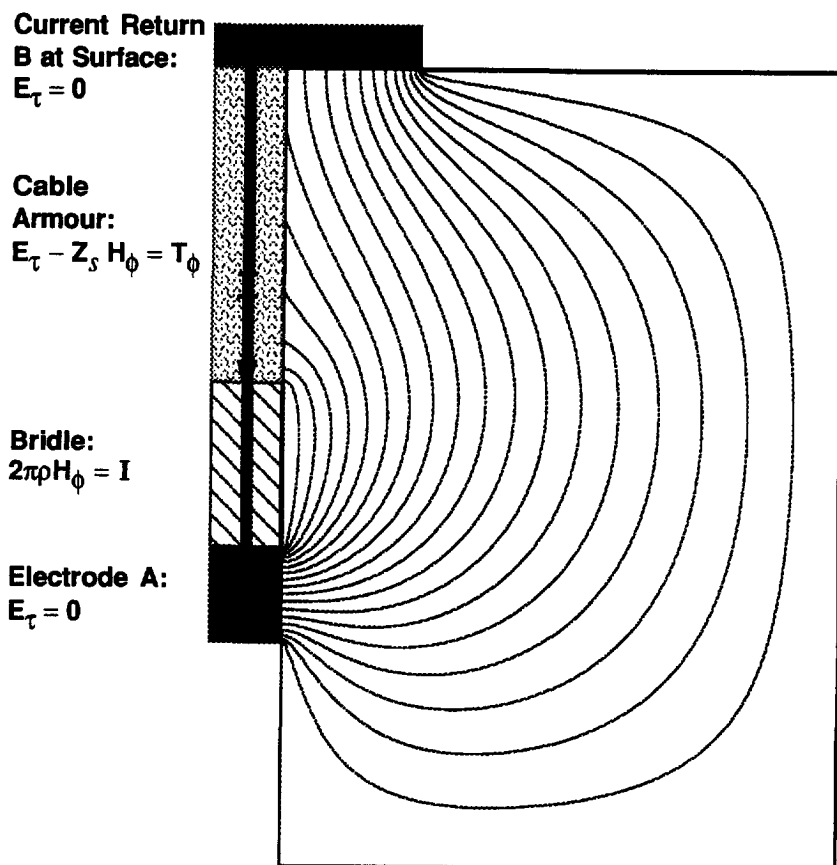


Figure 3.3: Boundary conditions for an electrode A suspended on an armoured cable. Electrode A is separated from the cable armour by an insulating bridle. The electrical field lines were computed for the DC case with imperfectly conducting cable armour so that both Z_s and T_ϕ are non-zero.

because of the small size of Ω . When modelling the DLL, we will take the boundaries of Ω to be far from the tool. We will examine the fields due to the DLL in more detail in section 3.5.

Certain tool configurations have sources inside Ω . Distributed source fields (i.e., those without any delta functions) arise naturally if one first solves for an associated 'primary' field and use the finite element formalism to solve for the remaining 'secondary' field (e.g., [6]). Delta function sources arise in the representation of toroidal antenna: as we have seen in section 2.2.2, a toroid at (ρ_0, z_0) is represented by the source term

$$(3.5) \quad M_\phi = -i\omega\mu I N_T \pi r_s^2 \frac{\delta(\rho - \rho_0)}{2\pi\rho} \delta(z - z_0)$$

where I is the current, N_T is the number of turns and r_s the radius of the toroidal coils in the ρz plane (assumed small). Such sources are used on recent logging while drilling (LWD) tools where the toroids are wrapped around a drill pipe to measure the formation resistivity while drilling.

Figure 3.4 shows the current lines induced by such an assembly operating at 1 Hz. We have assumed that the drill bit is wider than the rest of the pipe and has cut a mud-filled borehole shown by the dotted lines. In Figure 3.5, which shows the current lines induced by the same assembly at 1 kHz, we see that skin effect in the metal pipe changes the current pattern: e.g., the field decreases more rapidly away from the toroid and the fields no longer penetrate into the interior of the drill-pipe. Similar results to Figure 3.4 have been described by [16], but our formulation allows us to simultaneously take into account the finite length of the tool and the finite operating frequency.

For a Normal tool or Laterolog, once we have solved equation (3.2), we obtain the apparent resistivity from the electric boundary potential

$$(3.6) \quad \Phi(\mathbf{x}) = - \int_{\mathbf{x}_*}^{\mathbf{x}} \mathbf{E} \cdot \hat{\tau} \, dl$$

where the integration is counter-clockwise along $\partial\Omega$ from some 'reference potential' at \mathbf{x}_* . Note that for non-zero ω , we cannot define a unique potential across Ω nor need the potential at \mathbf{x}_* be single valued. Clearly

$$(3.7) \quad \begin{aligned} 2\pi \mathbf{E} \cdot \hat{\tau} &= \frac{1}{\rho\sigma_z} \frac{\partial u}{\partial \rho} \hat{\mathbf{z}} \cdot \hat{\tau} - \frac{1}{\rho\sigma_\rho} \frac{\partial u}{\partial z} \hat{\rho} \cdot \hat{\tau} \\ &= \frac{1}{\rho\sigma_z} \frac{\partial u}{\partial \rho} \hat{\rho} \cdot \hat{\nu} + \frac{1}{\rho\sigma_\rho} \frac{\partial u}{\partial z} \hat{\mathbf{z}} \cdot \hat{\nu} \end{aligned}$$

which we write as $1/(\rho\bar{\sigma})\partial u/\partial\nu$. The boundary condition along $\partial\Omega_\nu$ thus becomes

$$(3.8) \quad \frac{1}{\rho\bar{\sigma}} \frac{\partial u}{\partial \nu} - \frac{Z_s}{\rho} u = 2\pi T_\phi$$

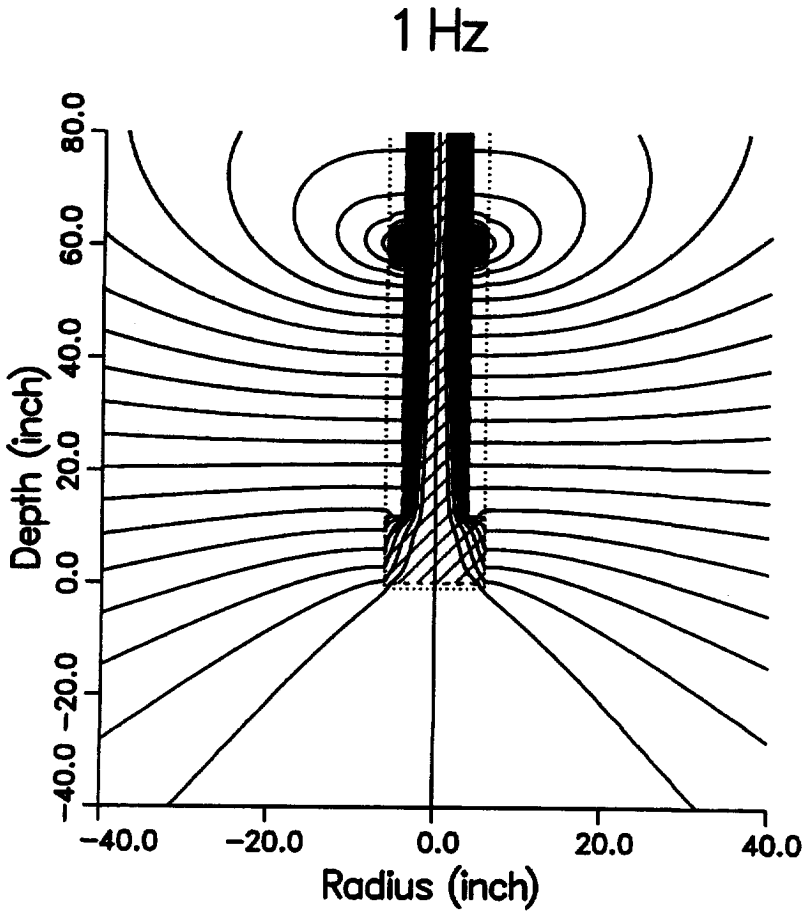


Figure 3.4: Electric field induced by toroidal coil on a drill-stem at 1 Hz. The borehole wall is denoted with a dotted line and the drill string itself is shown hatched.

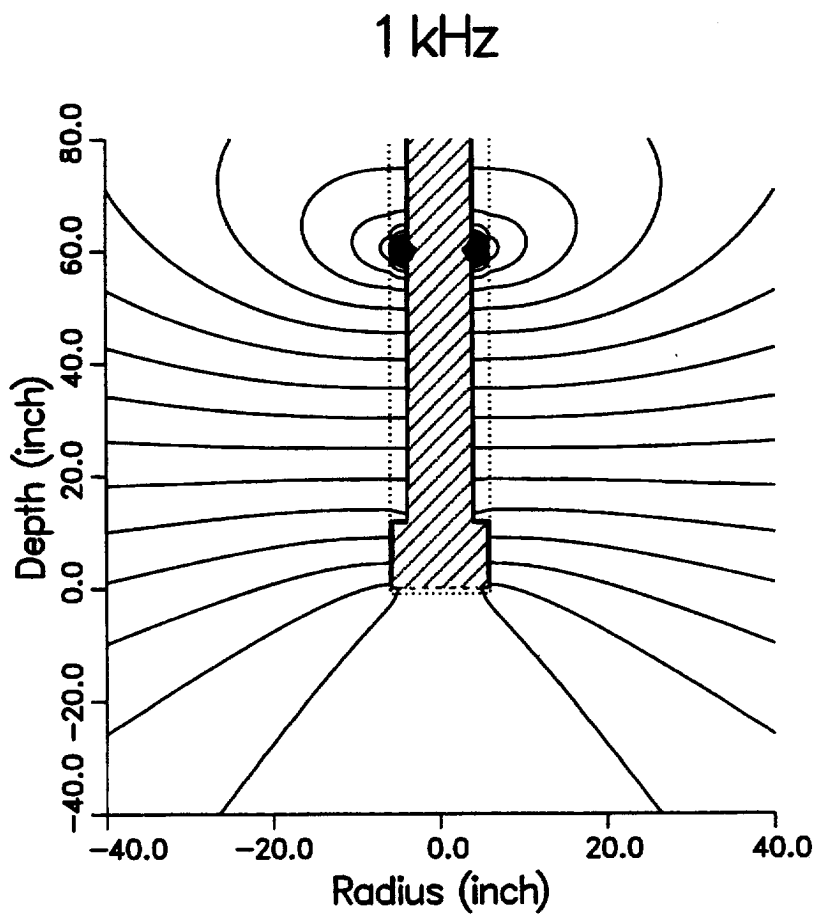


Figure 3.5: Electric field induced by toroidal coil on a drill-stem at 1 kHz. The borehole wall is denoted with a dotted line and the drill string itself is shown hatched.

and we generalize Φ to the function $H^{1/2}(\partial\Omega) \times H^{1/2}(\partial\Omega) \rightarrow \mathbb{C}$

$$(3.9) \quad \Phi(v, u) = -\frac{1}{2\pi} \oint_{\partial\Omega} \frac{1}{\rho \bar{\sigma}} \frac{\partial u}{\partial \nu} v \, dl.$$

If v is 1 along some section of $\partial\Omega$ from A to B and zero elsewhere then $\Phi(v, u)$ is the potential difference between A and B . As any element of $H^{1/2}(\partial\Omega)$ extends to a H^1 function defined on Ω , we can also view Φ as a bilinear form on $H^1(\Omega)$.

To arrive at a finite element system of equations, we first cast equations (3.2) and (3.8) into a weak form by integrating against a test function v . We are thus required to find $u \in H^1(\Omega)$ such that $u = \bar{u}$ on $\partial\Omega_0$ and

$$(3.10a) \quad \left\langle v, \frac{\partial}{\partial \rho} \frac{1}{\rho \sigma_z} \frac{\partial u}{\partial \rho} + \frac{\partial}{\partial z} \frac{1}{\rho \sigma_\rho} \frac{\partial u}{\partial z} \right\rangle_{L^2(\Omega)} + \left\langle v, \frac{i\omega\mu}{\rho} u \right\rangle_{L^2(\Omega)} = 2\pi \langle v, M_\phi \rangle_{L^2(\Omega)},$$

$$(3.10b) \quad -2\pi\Phi(v, u) - \left\langle v, \frac{Z_s}{\rho} u \right\rangle_{L^2(\partial\Omega_\nu)} = 2\pi \langle v, T_\phi \rangle_{L^2(\partial\Omega_\nu)},$$

for all test functions $v \in H_0^1(\partial\Omega)$. We would obtain an overdetermined system if we ‘tested’ u with non-zero v on $\partial\Omega_0$ while at the same time insisting that $u = \bar{u}$ there. Integrating by parts and combining the two equations, we obtain

$$(3.11) \quad P(v, u) - \left\langle v, \frac{Z_s}{\rho} u \right\rangle_{L^2(\partial\Omega_\nu)} = -2\pi \langle v, M_\phi \rangle_{L^2(\Omega)} + 2\pi \langle v, T_\phi \rangle_{L^2(\partial\Omega_\nu)}$$

for all $v \in H_0^1(\Omega)$ where P is the bilinear form

$$(3.12) \quad P(v, u) = \left\langle \frac{1}{\rho \sigma_z} \frac{\partial v}{\partial \rho}, \frac{\partial u}{\partial \rho} \right\rangle_{L^2(\Omega)} + \left\langle \frac{1}{\rho \sigma_\rho} \frac{\partial v}{\partial z}, \frac{\partial u}{\partial z} \right\rangle_{L^2(\Omega)} - \left\langle v, \frac{i\omega\mu}{\rho} u \right\rangle_{L^2(\Omega)}.$$

The Dirichlet conditions are satisfied in the strong sense in that, for any mesh, the approximate solution u_h will necessarily satisfy $u_h = \bar{u}$ on $\partial\Omega$. The Neumann terms are only satisfied in the weak sense, i.e., only when integrated with respect to the test function v .

Applying Green’s formula to equation (3.11), we see that when u is a solution to (3.2) and v is zero over the support of M_ϕ (i.e., $\langle v, M_\phi \rangle_{L^2(\Omega)} = 0$) then

$$(3.13) \quad \Phi(v, u) = -\frac{1}{2\pi} P(v, u).$$

This gives us a second algorithm for computing Φ . We refer to (3.8) as the 'classical' formulation and (3.13) as the 'superconvergent' formulation. We show in the next section that when u is an approximate finite element solution, the second formulation is much more accurate. Essentially the same result was derived in section 2.3.3.

3.3 Finite element formulation

The finite element solution proceeds by first dividing Ω into a series of rectangles (the 'elements') bounded by mesh lines $z = z_1, \dots, z_{N_z}$ and $\rho = \rho_1, \dots, \rho_{N_\rho}$ (with $\rho_1 = a$). Finer meshes have extra ρ and z lines. This subdivision is done in a 'quasi-uniform' fashion so that the mesh diameter h , (i.e., the largest diagonal value of any of the elements) remains roughly proportional to $1/\sqrt{N}$ with $N = N_\rho N_z$ the number of nodes. Separate levels of refinement are labelled by their mesh diameter.

Given a subdivision with diameter h , we write $V_h \subset H^1(\Omega)$ for the (finite dimensional) space of piecewise-bilinear functions over that mesh. In Appendix 3.A, we construct a set of basis functions for V_h such that for each node ij of the mesh, the basis function $\mathcal{B}_{ij}(\rho, z)$ satisfies $\mathcal{B}_{ij}(\rho_p, z_q) = \delta_{ip} \delta_{jq}$ where δ denotes the Kronecker delta. \mathcal{B}_{ij} give a representation of V_h as the tensor product $V_h^\rho \otimes V_h^z$ of one-dimensional basis functions in ρ and z , respectively. We replace equation (3.11) with the discrete problem: Find $u_h \in V_h$ such that $u_h = \bar{u}$ on $\partial\Omega_0$ and

(3.14)

$$P(v_h, u_h) - \left\langle \frac{Z_s}{\rho} v_h, u_h \right\rangle_{L^2(\partial\Omega_\nu)} = -2\pi \langle v_h, M_\phi \rangle_{L^2(\Omega)} + 2\pi \langle v_h, T_\phi \rangle_{L^2(\partial\Omega_\nu)}$$

for all test functions $v_h \in V_h \cap H_0^1(\Omega)$. The constraints on $\partial\Omega_0$ are imposed on both u and v_h whereas the constraints on $\partial\Omega_\nu$ will only be satisfied 'on average' over each boundary element. We shall write $ij \in \partial\Omega_0$ if the ij th node lies on $\partial\Omega_0$ so the test functions v_h consist of any \mathcal{B}_{ij} such that $ij \notin \partial\Omega_0$. We write

$$(3.15a) \quad A_{ijpq} = P(\mathcal{B}_{ij}, \mathcal{B}_{pq}) - \left\langle \mathcal{B}_{ij}, \frac{Z_s}{\rho} \mathcal{B}_{pq} \right\rangle_{L^2(\partial\Omega_\nu)}$$

$$(3.15b) \quad f_{ij} = -2\pi \langle \mathcal{B}_{ij}, M_\phi \rangle_{L^2(\Omega)} + 2\pi \langle \mathcal{B}_{ij}, T_\phi \rangle_{L^2(\partial\Omega_\nu)}$$

so that with

$$(3.16) \quad u_h(\rho, z) = \sum_{pq} B_{pq}(\rho, z) u_{pq}$$

then

$$(3.17) \quad \sum_{pq} A_{ij\ pq} u_{pq} = f_{ij} \quad \text{for all } ij \notin \partial\Omega_0.$$

Explicit formulae for A are given in Appendix 3.A. These equations, together with the constraints $u_h = \bar{u}$ on $\partial\Omega_0$, define a large sparse system of equations for u_{pq} . The complex symmetric matrix A is termed the global stiffness matrix.

As we have seen in section 2.3.2, the Dirichlet nodes in the finite element calculation require special attention. Suppose we number the Dirichlet nodes last so that $A(v, u)$ decouples into blocks

$$(3.18) \quad A(v, u) = \begin{pmatrix} v_1^t & v_2^t \end{pmatrix} \begin{pmatrix} A_{11} & A_{12} \\ A_{21} & A_{22} \end{pmatrix} \begin{pmatrix} u_1 \\ u_2 \end{pmatrix}$$

where $v_2 = 0$ and $u_2 = \bar{u}_2$, i.e., A_{12} and A_{22} correspond to nodes where $v_h \in \partial\Omega_0$. For these rows we do not test with v_h , but rather insert the known values of \bar{u} to give

$$(3.19) \quad \begin{pmatrix} A_{11} & A_{12} \\ 0 & I \end{pmatrix} \begin{pmatrix} u_1 \\ u_2 \end{pmatrix} = \begin{pmatrix} f_1 \\ \bar{u}_2 \end{pmatrix}$$

Our solution technique is tailored to complex symmetric matrices, so we premultiply by

$$\begin{pmatrix} I & -A_{12} \\ 0 & I \end{pmatrix}$$

to give the symmetric system

$$(3.20) \quad \begin{pmatrix} A_{11} & 0 \\ 0 & I \end{pmatrix} \begin{pmatrix} u_1 \\ u_2 \end{pmatrix} = \begin{pmatrix} f_1 - A_{12}\bar{u}_2 \\ \bar{u}_2 \end{pmatrix}.$$

In the subsequent section, we show how to invert equation (3.20) using the preconditioned ILU biconjugate gradient scheme developed in Chapter 2.

There remain the questions as to how well does u_h approximate u and how to compute boundary potentials and apparent resistivities. For example, u_h need not satisfy equation (3.10b) pointwise on $\partial\Omega_\nu$, although u_h will clearly agree with u at each node on $\partial\Omega_0$. In fact, one can show, e.g., [5], that u_h converges to u throughout $\bar{\Omega}$ and does so at least quadratically – which we write as $\|u - u_h\| = O(h^2)$, (e.g., a three times finer mesh gives an answer which is nine times more accurate). Under certain quite restrictive hypotheses, one can also show that the error in u_h evaluated at special points within each rectangle is $O(h^3)$, a phenomenon known as ‘superconvergence’ – for essentially no extra effort one obtains an order of magnitude

improvement, [34]. Unfortunately, for practical problems with discontinuous conductivities and varying mesh diameters, this $O(h^3)$ superconvergence does not appear to exist.

As alluded to in the previous section, we do have a superconvergent method for computing apparent resistivity. Specifically, if $v_h = \chi_{AB}$ is 1 for the nodes along a boundary section AB and zero everywhere in $\bar{\Omega}$ then

$$(3.21) \quad \left| P(v_h, u_h) - \int_{A-h/2}^{B+h/2} \frac{1}{\rho \bar{\sigma}} \frac{\partial u}{\partial \nu} dl \right| = O(h^2)$$

e.g., if $A = B$ then $-2\pi P(v_h, u_h)$ represents the jump in potential across A. (From equation (3.15a), P is the same matrix as A less the impedance contributions.) A formal proof of this result is identical to that of section 2.3.3 and is not repeated here. Algorithmically, the result is extremely useful: after solving for u , the "potential jumps" across each node are given by one extra matrix multiplication by P .

In coding, it is simplest to have two separate matrices: One first builds the matrix P then adds impedance terms to form A . The rows of A are overwritten at each Dirichlet node according to equation (3.20) and $Au_h = f_h$ is solved. The subsequent computation of potentials is very inexpensive. With bilinear elements, Pu_h could certainly be computed in $9N$ operations. In fact, as we only need Pu_h along the boundary, the computation is $O(\sqrt{N})$. Finally, the potential difference between two electrodes 'A' and 'B' is given by adding together the values of $-2\pi Pu_h$ at the boundary nodes between 'A' and 'B.'

Physically, setting the i th row of Pu to zero corresponds to a numerical statement of Faraday's law in a loop, Γ_i , surrounding the i th node (with $O(h^2)$ error). On boundary nodes, this loop cannot be closed: Pu contains only the contributions from that part of Γ_i in Ω . To complete the statement of Faraday's law requires the contribution, f , from $\mathbf{E} \cdot \hat{\tau} dl / 2\pi$ over the missing section. Faraday's law becomes the i th row of $Pu = f$. E.g., at DC, given u (and assuming $M_\phi \equiv 0$) then (to $O(h^2)$) Pu gives the electromotive force around each of the Γ_i : zero at all interior nodes and equal to the jump in potential across each boundary node.

We demonstrate superconvergence numerically using the example of a Shallow ES operating at 1kHz in a 10 Ω m homogeneous formation with 0.1 Ω m borehole (and 8" diameter). Figure 3.6 shows the real component of the potential computed the two ways and for different mesh sizes. One set of curves has been displaced by a distance of 10 volts for clarity. In Figure 3.7, we show the difference between the two convergence rates at an arbitrary point 'A' on the upper electrode. We used Richardson extrapolation, [38], to estimate the true potential at A (required to define 'error' as no analytic expression exists). The curve obtained from $P(v_h, u_h)$ is clearly converging much faster than that obtained from equation (3.8). Moreover, the expected convergence rates (given by the slopes of the curves on the log-log plot) confirm

Computation of Potentials
for different mesh sizes

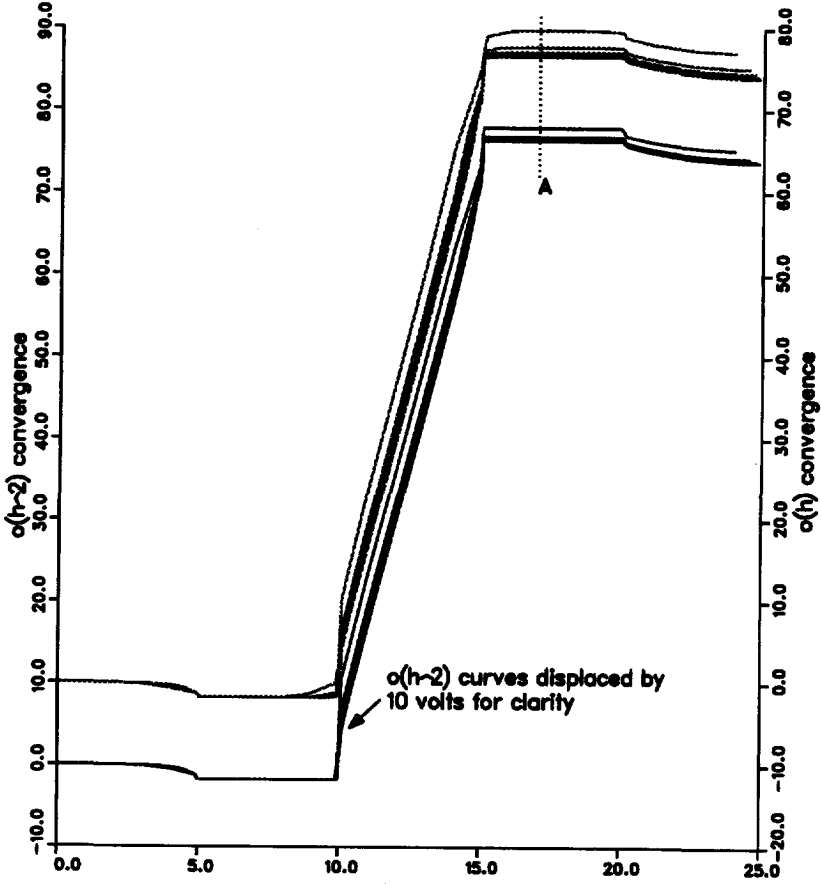


Figure 3.6: Superconvergence results for a Shallow ES at 1 kHz. The figure shows the potential along $p = a$ as a function of z , with electrodes at $[5, 10]$ and $[15, 20]$. The results from different mesh sizes are shown overlaid and we also do this computation using a non-superconvergent $O(h)$ method and the superconvergent $O(h^2)$ method. The latter set of curves are displaced 10 volts for clarity. The potentials at point A are also replotted in Figure 3.7.

Superconvergence of Potential at A

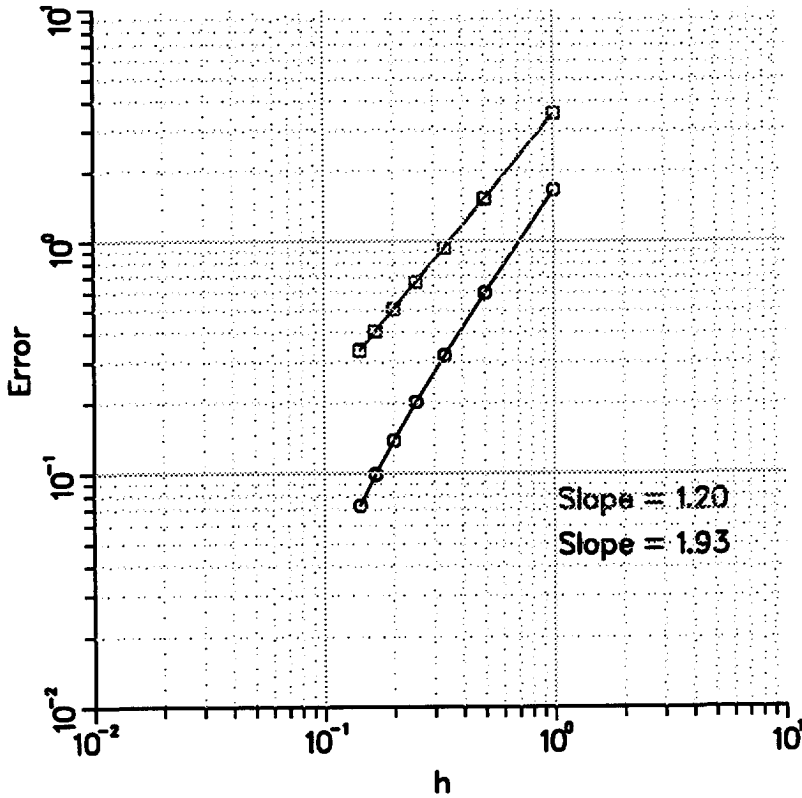


Figure 3.7: Superconvergence results for a Shallow ES at 1 kHz. The figure shows the error in the computation of potential at the point A of Figure 3.6 when the potential is computed by two different methods. The slope of the curves on the log-log scale indicate the rate of convergence, namely 1.20 and 1.93. The asymptotic rates predicted theoretically are $O(h)$ and $O(h^2)$, respectively.

the theoretical results. We have plotted the *real* value of the potential, but similar results were also observed for the imaginary component.

3.4 Matrix inversion

In this section, we show how to solve the system $Au_h = f_h$ arising from the finite element discretization. We shall drop the subscript h as we consider a fixed mesh diameter. For any non-singular $N \times N$ system of equations $Au = f$ then u must lie in the space generated by successively applying A to f : the vectors f, Af, A^2f, \dots cannot all continue to be linearly independent and so for some $\beta_i, i = 1, \dots, n$ with $\beta_0 \neq 0$

$$(3.22) \quad \beta_0 f + \beta_1 Af + \dots + \beta_n A^n f = 0$$

implying that $u = -(\beta_1 f + \dots + \beta_n A^{n-1} f)/\beta_0$ with $n \leq N$. The problem, of course, lies in generating the β_i . The spaces generated by $\{f\}, \{f, Af\}, \{f, Af, A^2f\}$, etc, are called Krylov spaces. If A is positive definite and symmetric then the conjugate gradient method chooses from each Krylov space the vector closest to the true solution (in the energy norm) and we have seen in Section 2.4 that a solution with a given accuracy can be obtained after $O(\sqrt{\kappa(A)})$ iterations, where $\kappa(A)$ is the condition number of A . When A is arrived at via finite element discretization, this number of iterations can still be prohibitively large and we accelerate the convergence by preconditioning with a matrix A_0 having a similar spectrum to A but which is readily inverted. Our method of choice is incomplete LU factorization. As presented in Chapter 2, we set $A_0 = LU$ where $A = LU + C$ and L (resp. U) lower (resp. upper) triangular matrices with the same sparse structure as A . We compute L, U and C with the ILU algorithm of [5] presented in Chapter 2.

As shown by [5], on a uniform mesh of diameter h , if A is the stiffness matrix corresponding to a second order elliptic operator then $\kappa(A) = O(h^{-2}) = O(N^{2/d})$ where N is the total number of unknowns and d is the dimension. This can be seen physically because (e.g. in 3D) the lowest order eigenmode will be, roughly, a piecewise linear discretization of $\sin(x/L)\sin(y/L)\sin(z/L)$ where L is the linear dimension of Ω whereas the highest order mode will be, roughly, $\sin(hx/L)\sin(hy/L)\sin(hz/L)$. For a second order operator the corresponding eigenvalues will be $1/L^2$ and h^2/L^2 so the ratio between them is h^2 . As the mesh is refined, $\kappa(A)$ will increase and so the number of iterations required for convergence will also increase. [5] shows that large variations in material properties also increase the condition number. Under certain fairly restrictive conditions, [26] showed that the condition number of the ILU preconditioned system was $O(N^{1/d})$.

Unfortunately, even at DC, the hypotheses in [26] will not usually be valid but in practice we

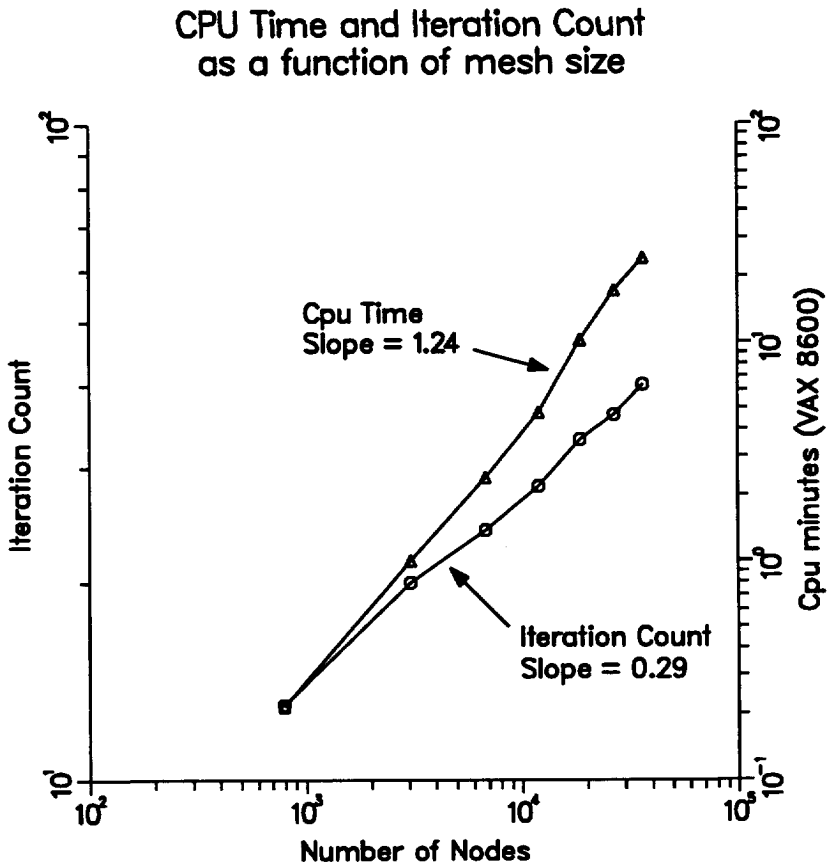


Figure 3.8: Convergence of the CWNLAT code as a function of mesh size. The configuration was a 64 inch Shallow ES at 1 kHz in a 10 ohm-m formation with 0.1 ohm-m, 8 inch borehole.

observe the predicted convergence rate of $O(N^{1/(2d)})$ regardless of frequency. Figure 3.8 shows a typical example of convergence for a Shallow ES operating at 1 kHz in a formation with borehole. In general, the iteration count will depend on the eigenvalue distribution of A , [19], [30].

From Appendix 3.A, we know that $A = S + i\omega T$ with S and T both real symmetric. S is spectrally equivalent to the stiffness matrix for Laplace's equation and, by the Poincaré inequality (i.e., equation 1.70) will be coercive provided that Dirichlet constraints have been applied to A . In general T can have both positive and negative eigenvalues.

If $\lambda + i\mu$ is an eigenvalue of A with eigenvector $u + iv$ then

$$(3.23) \quad (\lambda + i\mu)(\|u\|^2 + \|v\|^2) = (u^t - iv^t)(\lambda + i\mu)(u + iv)$$

$$(3.24) \quad = (u^t - iv^t)(S + i\omega T)(u + iv)$$

$$(3.25) \quad = (u^t Su + v^t Sv) + i\omega(u^t Tu + v^t Tv)$$

so that if $\gamma_S \|u\|^2 \leq u^t Su \leq C_S \|u\|^2$ and $|v^t Tv| \leq C_T \|v\|^2$ then $\gamma_S \leq \lambda \leq C_S$ and $|\mu| \leq \omega C_T$, i.e., the eigenvalues of A lie in a rectangular box parallel to the real and imaginary axes and bounded away from zero.²

Moreover, when $\omega \neq 0$, the ILU factorization appears to cluster the eigenvalues nearer the real axis which further helps stabilize the biconjugate gradient routine, [15], [24]. Eigenvalue distributions and the convergence rates for complex symmetric matrices arising in EM moment method solutions have also been discussed in [31] and [32].

3.5 Resistivity tools in heterogeneous media

Consider first the response of a Normal tool with a 9.14m (360 inch) electrode in a homogeneous formation and a return at the surface. We applied the CWNLAT code to re-confirm the observations of Lacour-Gayet, [21]. At DC, the current lines will emanate radially from the source. At non-zero frequencies, however, because of skin effect the returning currents in the formation will be constrained to lie in a cylinder around the borehole with radius proportional to the skin depth: $\delta = \sqrt{2/\sigma\omega\mu}$. For example, Figure 3.9 shows the current paths induced when the electrode operates at 35 and is suspended on a cable without armour in a $1\Omega m$ formation ($\delta = 85m$).

²In 3D this statement is not true in general, but one can show that there must exist a α such that the eigenvalues of A lie in a parallel strip which has been rotated by $e^{i\alpha}$ and which is bounded away from the origin.

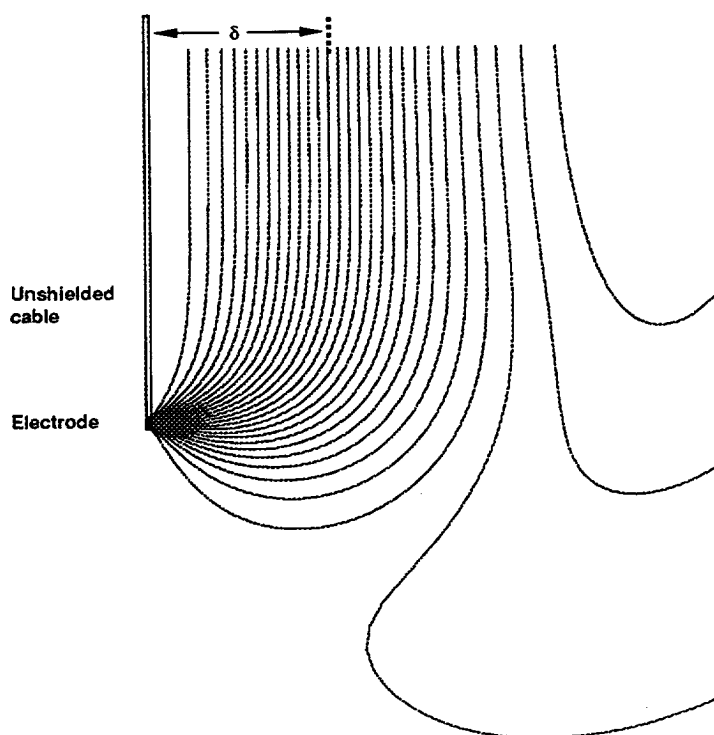


Figure 3.9: Current lines induced by a 35Hz electrode on a cable without armour in a 1 ohm-m formation. We show the current lines in just one azimuthal plane. The electrode length is 9.14m and the skin depth δ is 85m.

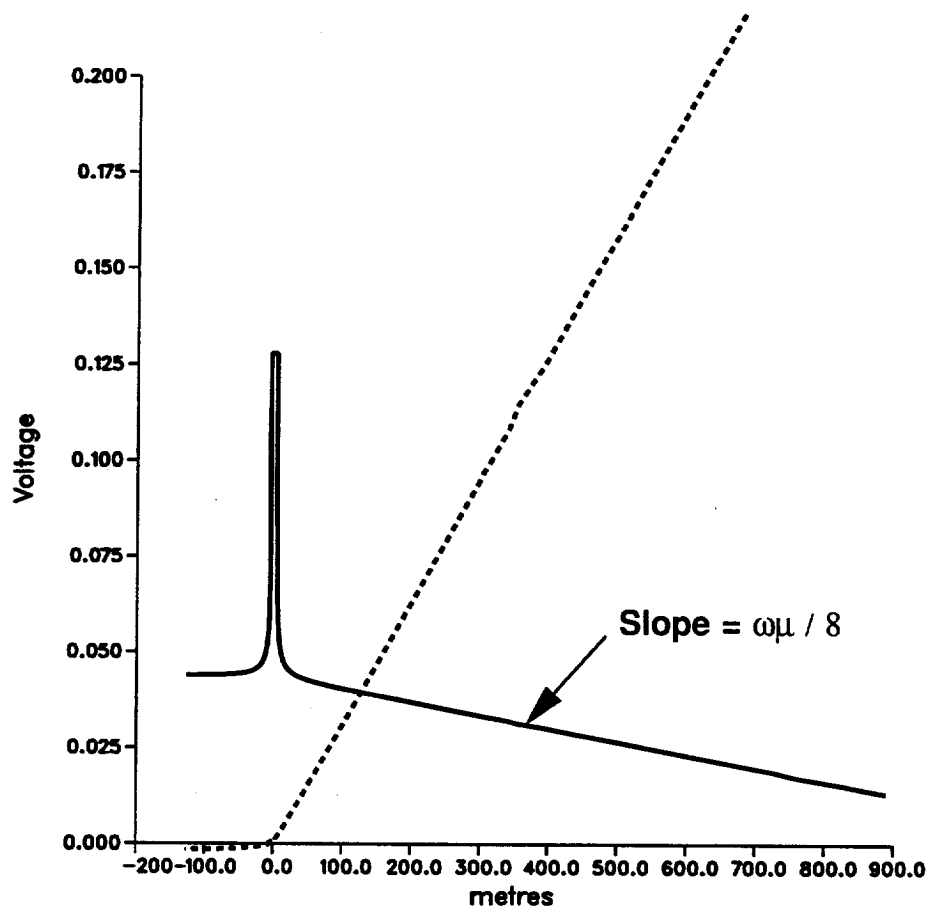


Figure 3.10: Potential along borehole axis induced by a 35Hz electrode on a cable without armour in a 1 ohm-m formation. The units on the x-axis are metres. The out-of-phase voltage is shown dotted, the in-phase solid. The electrode is emitting unit current.

Figure 3.10 shows the potential along the borehole axis. Unlike the DC case, at a finite frequency the potential decreases linearly along the cable. The linear resistance can be roughly approximated as the formation resistivity divided by the area of a circle of radius δ

$$(3.26) \quad R_{coax} = \frac{1/\sigma}{\pi\delta^2} = \frac{\omega\mu}{2\pi}$$

but a more exact expression derived in Appendix 3.C which takes into account percentage of currents flowing outside the circle of radius δ is shown to be $\omega\mu/8$. In particular, the slope is independent of formation resistivity. Near the electrode the potential decrease is exponential. The out-of-phase potential is shown dotted and is also linear along the cable (its slope is dependent on formation conductivity). Note that if the voltage reference is placed 50m from the source electrode, the change in apparent resistivity due to the 35Hz frequency will be quite small.

The presence of cable armour does not significantly change the current lines when the formation is sufficiently conductive. Essentially, the cable provides an alternative current return. Although the cable conductivity is high, the cross-sectional area will be quite small. Typical values for Z_s are $-1 \times 10^{-4}\Omega$ to $-1 \times 10^{-3}\Omega$. Figure 3.11 shows the current lines in a $1\Omega m$ formation when the tool assembly now consists of a 9.14m (360 inch) electrode with radius (1.8 inch), an insulating bridle with radius 12.7mm (0.5 inch) and a conducting cable armour with conductivity $10^{-6}\Omega m$, interior radius 2.54mm (0.1 inch) and exterior radius 6.35mm (0.25 inch). Note that the interior of the cable is set to a perfect insulator through which the 35 Hz current passes to the electrode. We would get quite different response if we took the interior of the cable armour to be a perfect conductor because then there would be a very efficient path to the surface by just crossing radially through the cable and up the conducting core to the surface. Figure 3.12 shows the same configuration but now in a $10^4\Omega m$ formation. The cable now offers a less resistive path to the surface and there is less skin effect.

3.5.1 Influence of casing in homogeneous and layered media

In this section we first examine the influence of a cased borehole on the fields induced by an LL3 in an otherwise homogeneous medium, then examine a log of the same tool in layered media consisting of a high resistivity anhydrite around the casing with a homogeneous formation and uncased borehole below.

Figure 3.13 shows the current paths around a casing shoe at DC and Figure 3.14 the same configuration at 35 Hz. We see a big difference: at 35 Hz the currents cannot pass through the casing shoe because of skin effect. In both cases, the source electrode is 50m below the casing shoe and the return electrode is at infinity.

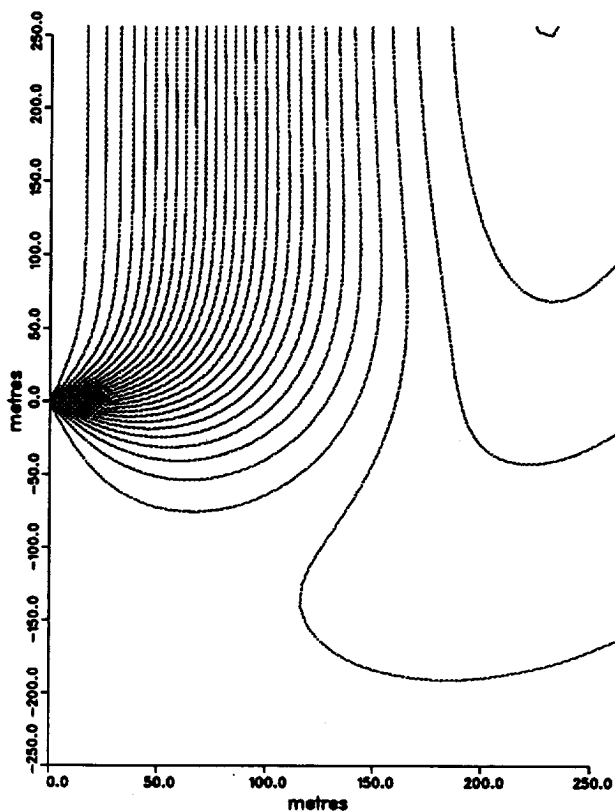


Figure 3.11: Current lines induced by a 35Hz electrode on a cable with bridge and armor in a 1 ohm-m formation. We show the current lines in just one azimuthal plane. The tool assembly consists of a 9.14m electrode with radius 45.72mm, an insulating bridge with radius 12.7mm and length 50m, and a conducting cable armor with conductivity $1.e-6$ ohm-m, interior radius 2.54mm and exterior radius 6.35mm. The current lines are virtually indistinguishable from those of Figure 3.9 indicating that at this contrast the cable armor is not a significant current return path.

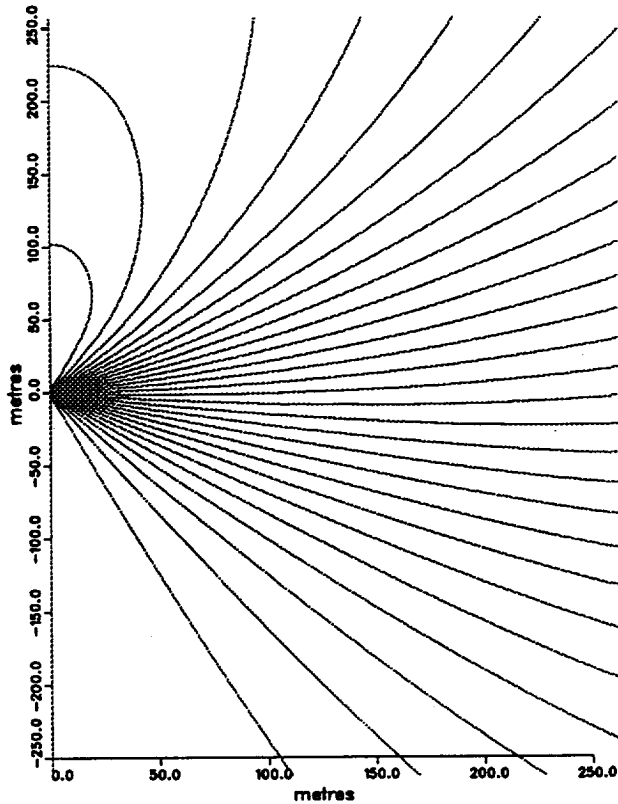


Figure 3.12: Current lines induced by a 35Hz electrode on a cable with bridle and armour in a 1.e4 ohm-m formation. We show the current lines in just one azimuthal plane. The tool assembly consists of a 9.14m electrode with radius 45.72mm, an insulating bridle with radius 12.7mm and length 50m, and a conducting cable armour with conductivity 1.e-6 ohm-m, interior radius 2.54mm and exterior radius 6.35mm. The current lines are clearly different from those of 3.9.

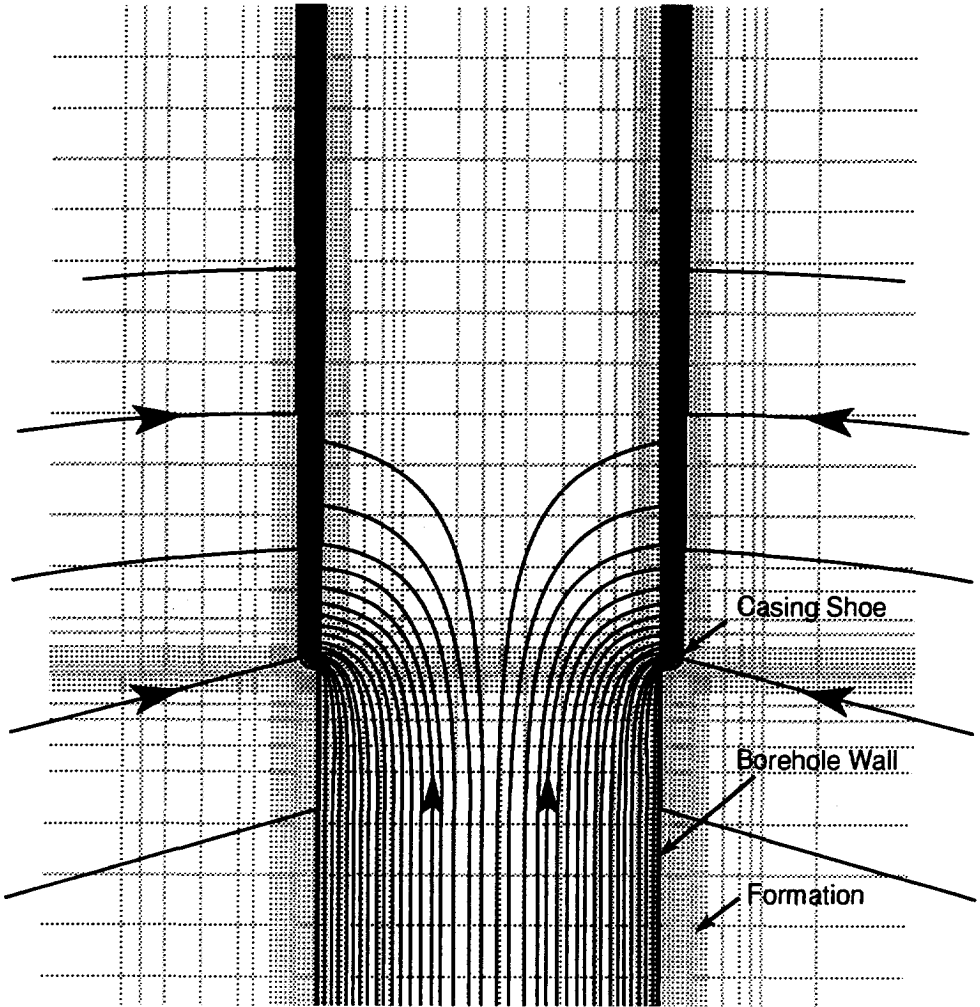


Figure 3.13: Current lines around a casing shoe with a DC current source far below the casing shoe. The casing acts as a good conductor and current will enter the casing from both the borehole and the formation. The casing resistivity is $2 \times 10^{-7} \Omega m$ with relative magnetic permeability 200. The interior radius of the casing is the borehole radius, which is 4.0 inches. The casing thickness is 0.3 inches. The formation is $10 \Omega m$ and the borehole is $0.1 \Omega m$.

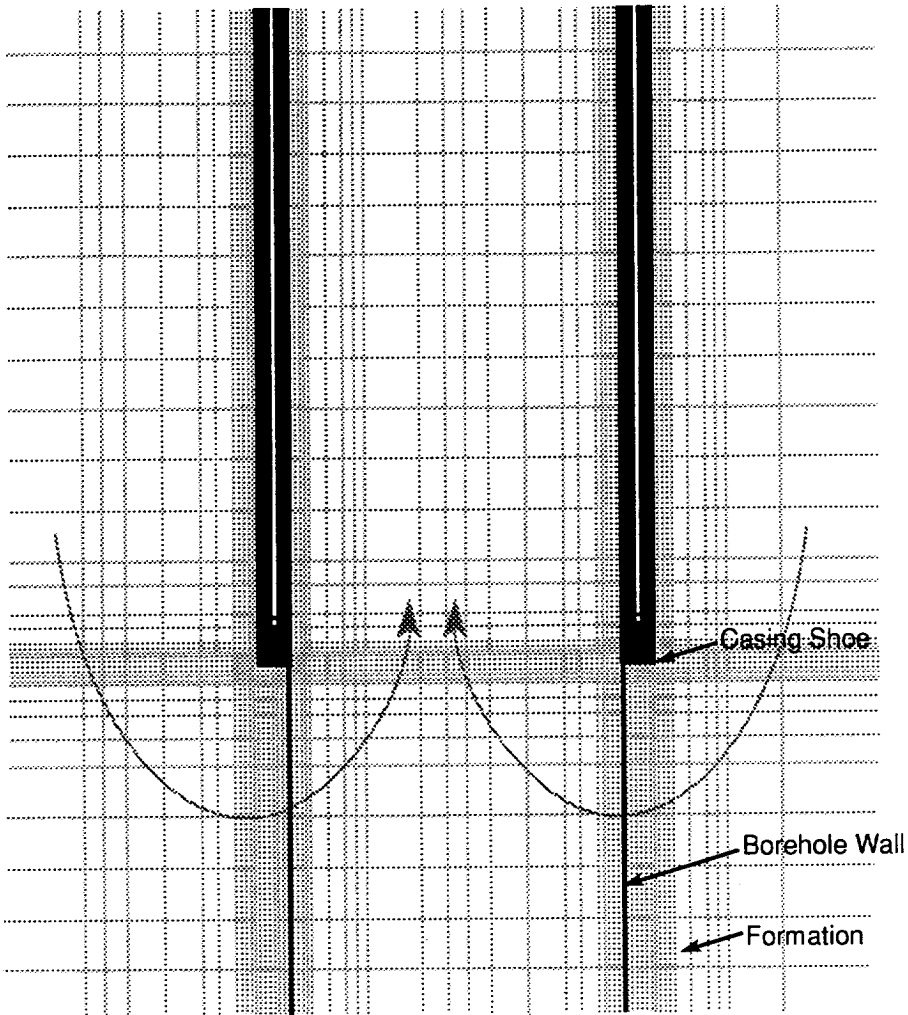


Figure 3.14: Current lines around a casing shoe with a 35Hz current source far below the casing shoe. Current cannot pass through the casing because of skin effect, instead current enters the exterior of the casing, travels down the casing shoe and back up the inside of the casing. The casing resistivity is $2 \times 10^{-7} \Omega m$ with relative magnetic permeability 200. The interior radius of the casing is the borehole radius, which is 4.0 inches. The casing thickness is 0.3 inches. The formation is $10 \Omega m$ and the borehole is $0.1 \Omega m$.

Casing 10m uphole of anhydrite layer. Freq = 35 Hz.

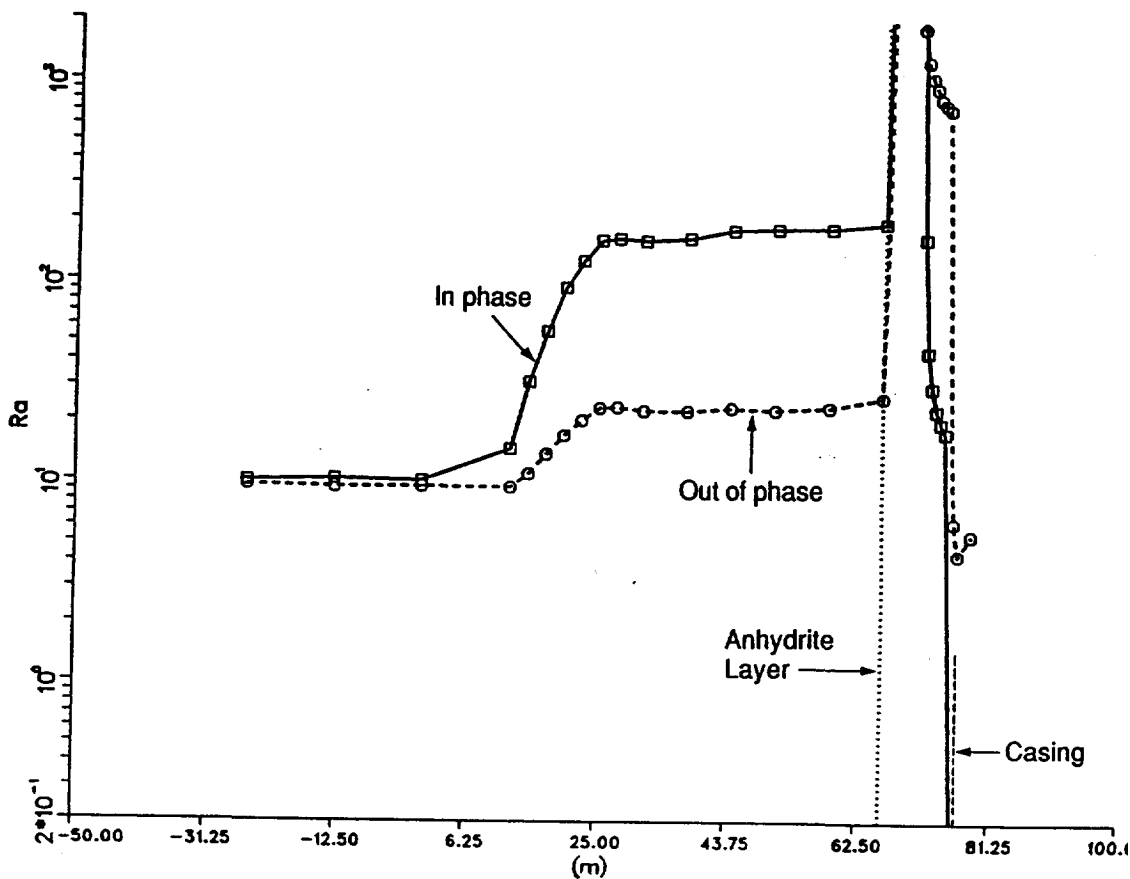


Figure 3.15: The Groningen effect. Simulated resistivity logs from an LL3 approaching a casing shoe. At 35 Hz there is a big kick in apparent resistivity once the bridge has entered the casing. The casing shoe is located 10m uphole of the anhydrite layer. The units on the x-axis are metres.

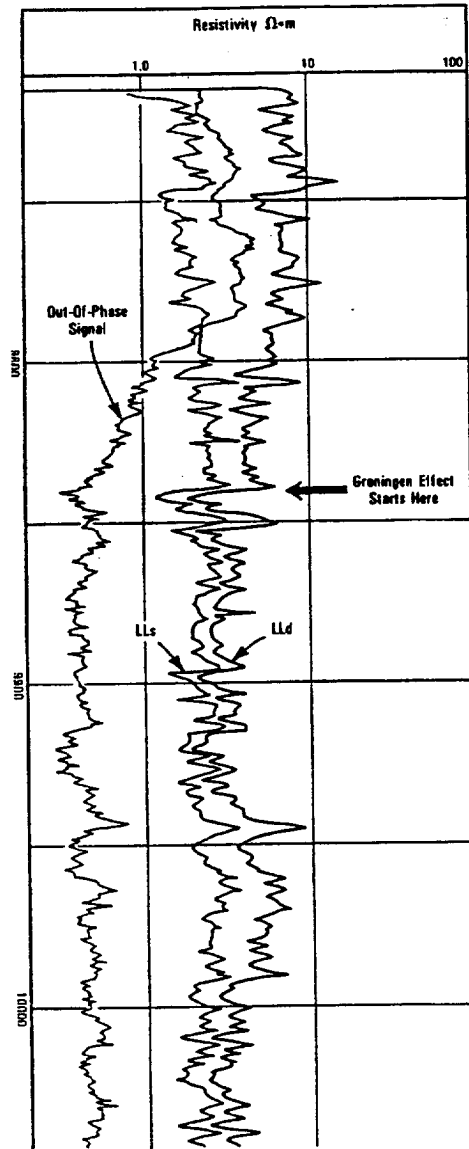


Figure 3.16: Resistivity logs from a 35Hz Dual Laterolog approaching a casing shoe. The Groningen effect appears as a big kick in the LLd out-of-phase component and an increased separation in LLd and LLs apparent resistivity as the bridge enters the casing.

The effect of this current shielding on a resistivity tool is that at 35Hz, the currents will effectively return to the bottom of the casing shoe at 35Hz, causing an increase in apparent resistivity when compared to the DC case. This is shown in the logs of Figure 3.15.

The features shown in Figure 3.15 have also been seen in the field. Figure 3.16, reproduced from [21], shows a typical example. The effect starts around 3794 feet, 196 feet below a highly resistive bed at 3598 feet, with a casing shoe 15 feet uphole of the bed boundary.

3.6 Conclusions

We have been able to model frequency effects on Laterolog configurations using a new finite element code and have been able to model the Groningen effect. The superconvergence developed for the Φ formulation in Chapter 3 extends to the H_ϕ formulation. The stiffness matrices resulting from the H_ϕ formulation are complex symmetric with the eigenvalues having positive real component bounded away from the origin. The stiffness matrices are readily inverted with the incomplete LU preconditioned biconjugate gradient algorithm.

Appendix 3.A Stiffness matrix expansions

This appendix gives explicit formulae for the stiffness matrices P and A as integrals over rectangular elements on a quasi-uniform grid with nodes $\rho_1, \dots, \rho_{N_\rho}$ and z_1, \dots, z_{N_z} . The basis functions are given explicitly as a tensor product of 1D local functions:

$$(3.27) \quad B_{ij}(\rho, z) = B_i^\rho(\rho) B_j^z(z)$$

where

$$(3.28) \quad B_i^\rho(\rho) = \begin{cases} (\rho - \rho_{i-1})/\Delta\rho_{i-1} & \text{if } \rho \in [\rho_{i-1}, \rho_i] \\ (\rho_{i+1} - \rho)/\Delta\rho_i & \text{if } \rho \in [\rho_i, \rho_{i+1}] \end{cases}$$

$$(3.29) \quad B_j^z(z) = \begin{cases} (z - z_{j-1})/\Delta z_{j-1} & \text{if } z \in [z_{j-1}, z_j] \\ (z_{j+1} - z)/\Delta z_j & \text{if } z \in [z_j, z_{j+1}] \end{cases}$$

with $\Delta\rho_i = \rho_{i+1} - \rho_i$ and $\Delta z_j = z_{j+1} - z_j$. We assume $\bar{\sigma} - i\omega\bar{\epsilon}$ and $i\omega\mu$ are constant within each mesh element so that

$$(3.30) \quad P_{ijpq} = P(\mathcal{B}_{ij}, \mathcal{B}_{pq}) = \sum_{I=1}^{N_\rho-1} \sum_{J=1}^{N_z-1} S_{ijpq}^{IJ}$$

where S_{ijpq}^{IJ} is the local 2D stiffness matrix over the IJ th rectangle:

$$(3.31) \quad \begin{aligned} S_{ijpq}^{IJ} = & \frac{1}{\sigma_z^{IJ} - i\omega\epsilon_z^{IJ}} \int_{\rho_I}^{\rho_{I+1}} \frac{\partial \mathcal{B}_i^\rho}{\partial \rho} \frac{\partial \mathcal{B}_p^\rho}{\partial \rho} \frac{d\rho}{\rho} \int_{z_J}^{z_{J+1}} \mathcal{B}_j^z \mathcal{B}_q^z \\ & + \frac{1}{\sigma_\rho^{IJ} - i\omega\epsilon_\rho^{IJ}} \int_{\rho_I}^{\rho_{I+1}} \mathcal{B}_i^\rho \mathcal{B}_p^\rho \frac{d\rho}{\rho} \int_{z_J}^{z_{J+1}} \frac{\partial \mathcal{B}_j^z}{\partial z} \frac{\partial \mathcal{B}_q^z}{\partial z} \\ & - i\omega\mu^{IJ} \int_{\rho_I}^{\rho_{I+1}} \mathcal{B}_i^\rho \mathcal{B}_p^\rho \frac{d\rho}{\rho} \int_{z_J}^{z_{J+1}} \mathcal{B}_j^z \mathcal{B}_q^z \end{aligned}$$

Clearly, S_{ijpq}^{IJ} is non-zero only when $|i - p| \leq 1$ and $|j - q| \leq 1$. In CWNLAT, the local stiffness matrices are stored as a 4×4 matrix for each element $[\rho_i, \rho_{i+1}] \times [z_j, z_{j+1}]$. CWNLAT uses a stencil formulation for the global stiffness matrix A as shown in Chapter 1 and stores A as a 3×3 matrix for each node (ρ_i, z_j) , $i = 1, \dots, N_\rho$, $j = 1, \dots, N_z$.

From the definitions of \mathcal{B}^ρ and \mathcal{B}^z , S_{ijpq}^{IJ} can be assembled from the integrals:

$$(3.32) \quad S_{ii}^\rho = \frac{1}{\Delta_{\rho_i}^2} \int_{\rho_i}^{\rho_{i+1}} \frac{1}{\rho} \frac{\partial}{\partial \rho} (\rho_{i+1} - \rho) \frac{\partial}{\partial \rho} (\rho_{i+1} - \rho) = \frac{\log(\rho_{i+1}/\rho_i)}{\Delta_{\rho_i}^2}$$

$$(3.33) \quad S_{i+1i}^\rho = S_{i+1i}^\rho = \frac{1}{\Delta_{\rho_i}^2} \int_{\rho_i}^{\rho_{i+1}} \frac{1}{\rho} \frac{\partial}{\partial \rho} (\rho - \rho_i) \frac{\partial}{\partial \rho} (\rho_{i+1} - \rho) = -\frac{\log(\rho_{i+1}/\rho_i)}{\Delta_{\rho_i}^2}$$

$$(3.34) \quad S_{i+1i+1}^\rho = \frac{1}{\Delta_{\rho_i}^2} \int_{\rho_i}^{\rho_{i+1}} \frac{1}{\rho} \frac{\partial}{\partial \rho} (\rho - \rho_i) \frac{\partial}{\partial \rho} (\rho - \rho_i) = \frac{\log(\rho_{i+1}/\rho_i)}{\Delta_{\rho_i}^2}$$

$$(3.35) \quad \mathbf{1}_{ii}^\rho = \frac{1}{\Delta_{\rho_i}^2} \int_{\rho_i}^{\rho_{i+1}} \frac{1}{\rho} (\rho_{i+1} - \rho)(\rho_{i+1} - \rho) = \frac{\rho_{i+1}^2 \log(\rho_{i+1}/\rho_i)}{\Delta_{\rho_i}^2} + \frac{\rho_i - 3\rho_{i+1}}{2\Delta_{\rho_i}}$$

$$(3.36) \quad \mathbf{1}_{i+1i}^\rho = \mathbf{1}_{i+1i}^\rho = \frac{1}{\Delta_{\rho_i}^2} \int_{\rho_i}^{\rho_{i+1}} \frac{1}{\rho} (\rho - \rho_i)(\rho_{i+1} - \rho) = -\frac{\rho_i \rho_{i+1} \log(\rho_{i+1}/\rho_i)}{\Delta_{\rho_i}^2} + \frac{\rho_{i+1} + \rho_i}{2\Delta_{\rho_i}}$$

$$(3.37) \quad \mathbf{1}_{i+1i+1}^\rho = \frac{1}{\Delta_{\rho_i}^2} \int_{\rho_i}^{\rho_{i+1}} \frac{1}{\rho} (\rho - \rho_i)(\rho - \rho_i) = \frac{\rho_i^2 \log(\rho_{i+1}/\rho_i)}{\Delta_{\rho_i}^2} + \frac{\rho_{i+1} - 3\rho_i}{2\Delta_{\rho_i}}$$

$$(3.38) \quad S_{jj}^z = \frac{1}{\Delta_{z_j}^2} \int_{z_j}^{z_{j+1}} \frac{\partial}{\partial z} (z_{j+1} - z) \frac{\partial}{\partial z} (z_{j+1} - z) = \frac{1}{\Delta_{z_j}}$$

(3.39)

$$S_{j+1j}^z = S_{jj+1}^z = \frac{1}{\Delta_{z_j}^2} \int_{z_j}^{z_{j+1}} \frac{\partial}{\partial z} (z_{j+1} - z) \frac{\partial}{\partial z} (z - z_j) = \frac{-1}{\Delta_{z_j}}$$

$$(3.40) \quad S_{j+1j+1}^z = \frac{1}{\Delta_{z_j}^2} \int_{z_j}^{z_{j+1}} \frac{\partial}{\partial z} (z - z_j) \frac{\partial}{\partial z} (z - z_j) = \frac{1}{\Delta_{z_j}}$$

$$(3.41) \quad \mathbf{1}_{jj}^z = \frac{1}{\Delta_{z_j}^2} \int_{z_j}^{z_{j+1}} (z_{j+1} - z)(z_{j+1} - z) = \frac{\Delta_{z_j}}{3}$$

$$(3.42) \quad \mathbf{1}_{j+1j}^z = \mathbf{1}_{jj+1}^z = \frac{1}{\Delta_{z_j}^2} \int_{z_j}^{z_{j+1}} (z_{j+1} - z)(z - z_j) = \frac{\Delta_{z_j}}{6}$$

$$(3.43) \quad \mathbf{1}_{j+1j+1}^z = \frac{1}{\Delta_{z_j}^2} \int_{z_j}^{z_{j+1}} (z - z_j)(z - z_j) = \frac{\Delta_{z_j}}{3}$$

S^ρ and S^z are termed 'local 1D stiffness matrices' and $\mathbf{1}^\rho$ and $\mathbf{1}^z$ 'local 1D mass matrices'. To solve Maxwell's equations in a flat 2D plane, one need only change the formulae for S_{ip}^ρ and $\mathbf{1}_{ip}^\rho$ to those of S_{ip}^z and $\mathbf{1}_{ip}^z$ respectively. This has also proven useful for debugging.

To compute A from P requires a boundary impedance term

$$\int_{\partial\Omega} \frac{Z_s}{\rho} B_{ij} B_{pq} dl$$

which can be evaluated from the 1D mass matrices

$$(3.44) \quad \int_{z_j}^{z_{j+1}} \frac{Z_s}{\rho} B_{ij} B_{pq} dl = \frac{Z_s}{\rho_i} \mathbf{1}_{jq}^z \delta_{ip} \quad \text{and} \quad \int_{\rho_i}^{\rho_{i+1}} \frac{Z_s}{\rho} B_{ij} B_{pq} dl = Z_s \mathbf{1}_{ip}^\rho \delta_{jq}$$

where δ denotes the Kröneckers delta function.

We use Gaussian quadrature to compute f_{ij} from equation (3.15b) unless M_ϕ consists of delta functions in which case $\langle B_{ij}, M_\phi \rangle_\Omega$ can be computed analytically.

Since $Z_s = -z'_s - i\omega z''_s$, $A = S + i\omega T$ with

$$(3.45) \quad S(u, v) = \int_{\Omega} \frac{\sigma}{(\sigma^2 + \omega^2 \epsilon^2) \rho} \left(\frac{\partial u}{\partial \rho} \frac{\partial v}{\partial \rho} + \frac{\partial u}{\partial z} \frac{\partial v}{\partial z} \right) + \oint_{\partial\Omega_\nu} \frac{z'_s}{\rho} uv$$

and

$$(3.46) \quad T(u, v) = \int_{\Omega} \frac{\epsilon}{(\sigma^2 + \omega^2 \epsilon^2) \rho} \left(\frac{\partial u}{\partial \rho} \frac{\partial v}{\partial \rho} + \frac{\partial u}{\partial z} \frac{\partial v}{\partial z} \right) - \int_{\Omega} \frac{\mu}{\rho} uv + \oint_{\partial \Omega_{\nu}} \frac{z_s''}{\rho} uv$$

so that S is positive semi-definite and T is indefinite. S is positive definite over $H_0^1(\Omega)$ by Poincaré's inequality.

Appendix 3.B Boundary Condition for Armoured Cable

We derive an effective boundary condition for a current carrying armoured cable. We model the cable as a conductor carrying an impressed current, I , inside the cable and separated from the cable armour by an perfect insulator. We set $\rho \in [a, b]$ for the cable armour with material properties σ , μ , ϵ . From Section 1.4.8 we know that locally the field variation in the armour is of the form

$$(3.47) \quad H_{\phi} = e^{ik_z z} [\alpha H_1^{(1)}(\gamma \rho) + \beta J_1(\gamma \rho)]$$

where $\gamma^2 + k_z^2 = k^2$ and k is the wavenumber inside the armour. We suppose the armour is sufficiently conductive that $\gamma \approx k$, i.e., $k_z = 0$. The boundary conditions on H_{ϕ} are

$$(3.48) \quad \alpha H_1^{(1)}(ka) + \beta J_1(ka) = I/(2\pi a) \quad \text{and} \quad \alpha H_1^{(1)}(kb) + \beta J_1(kb) = H_{\phi} \Big|_{\rho=b}.$$

The corresponding tangential electric field at $\rho = b$ is given by

$$(3.49) \quad E_z = \frac{k}{\sigma - i\omega\epsilon} \{(\alpha H_0^{(1)}(kb) + \beta J_0(kb))\}.$$

We solve for α and β in terms of I and $H_{\phi} \Big|_{\rho=b}$ and substitute into equation (3.49) to give

$$(3.50) \quad -E_z - Z_s H_{\phi} = t_{\phi} I$$

where

$$(3.51) \quad Z_s = -\frac{k}{\sigma - i\omega\epsilon} \frac{\begin{vmatrix} H_1^{(1)}(ka) & J_1(ka) \\ H_0^{(1)}(kb) & J_0(kb) \end{vmatrix}}{\begin{vmatrix} H_1^{(1)}(ka) & J_1(ka) \\ H_1^{(1)}(kb) & J_1(kb) \end{vmatrix}}$$

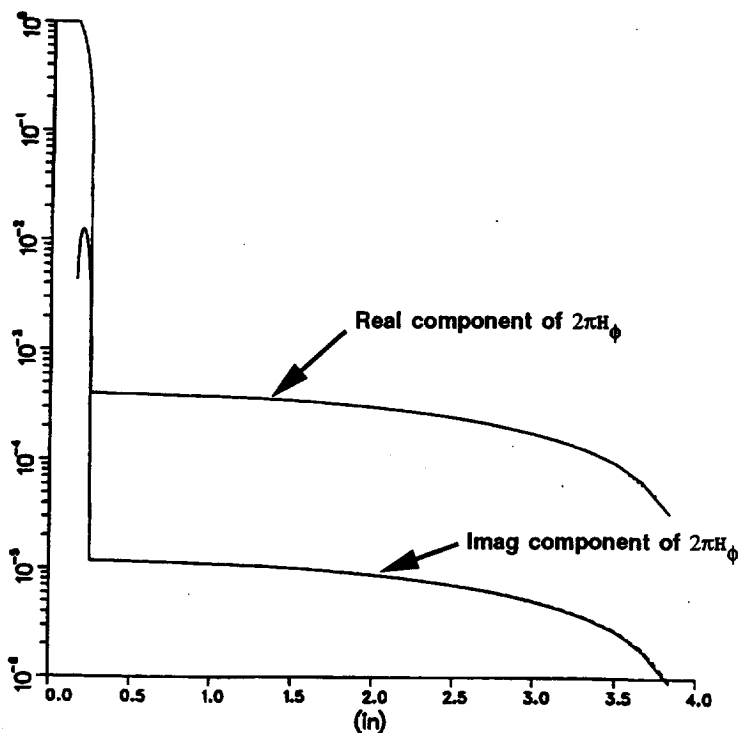


Figure 3.17: Real and imaginary components of $2\pi H_\phi$ across an armoured cable both computed three ways: shown solid, dotted and dashed. The solid curves is the analytic result, the dashed curves show the finite element results with the cable meshed and the dotted curves show the finite element result computed with inhomogeneous Neumann condition on the outer surface of the cable.

and

$$(3.52) \quad t_\phi = -i \frac{1}{\pi^2 ab} \frac{1}{\sigma - i\omega\epsilon} \begin{vmatrix} H_1^{(1)}(ka) & J_1(ka) \\ H_1^{(1)}(kb) & J_1(kb) \end{vmatrix}^{-1}.$$

For low frequencies the real components equal the DC values, $Z_s = -2\pi b/(\sigma_1\pi(b^2 - a^2))$ and $t_\phi = 1/(\sigma_1\pi(b^2 - a^2))$, while the imaginary components scale linearly with frequency.

Figure 3.17 shows the comparison between analytic and finite element methods. The first set of curves (solid) show the real and imaginary components of $2\pi\rho H_\phi$ crossing a cable armour with inner diameter 0.3" and outer diameter 0.5". The armour has relative magnetic permeability of 100 and conductivity of $10^6 S/m$. We have supposed an incident field in the formation such that the field at $R = 4''$ is zero. The second set of curves (dashed) show the finite element result with the cable armour meshed and the third set of curves (dotted) show the finite element result assuming the inhomogeneous Neumann condition along the outer surface of the cable. The curves overlay perfectly.

Appendix 3.C Linear resistance for coaxial currents

This appendix derives the formula $R_{coax} = \omega\mu/8$ for the linear resistance of the coaxial currents induced by an unshielded, long cable. The electric field due to a long cable carrying current I is given by, [20],

$$(3.53) \quad \mathbf{E} = -\hat{z} \frac{i\omega\mu}{4} I H_0^{(1)}(k\rho)$$

where $k^2 = i\omega\mu\sigma$. The power loss per unit length is given equivalently by either of the two expressions $\frac{1}{2} I^2 R_{coax}$ or $\frac{1}{2} \int \sigma |\mathbf{E}|^2$. Setting the two expressions equal gives the formula

$$(3.54) \quad R_{coax} = \sigma \left(\frac{\omega\mu}{4} \right)^2 2\pi \int_0^\infty \rho |H_0^{(1)}(k\rho)|^2 d\rho$$

and using

$$(3.55) \quad \int_0^\infty \rho |H_0^{(1)}(k\rho)|^2 d\rho = \frac{1}{\pi} \frac{1}{\omega\mu\sigma}$$

we arrive at $R_{coax} = \omega\mu/8$. The idea of obtaining R_{coax} by comparing two expressions for power loss was given in [17]. This last integral can be derived by using Kelvin functions, [39]:

$$(3.56) \quad \text{ber}(x) - i \text{bei}(x) = J_0(xe^{\pi i/4}) \quad \text{and} \quad \text{ker}(x) - i \text{kei}(x) = \frac{\pi i}{2} H_0^{(1)}(xe^{\pi i/4})$$

whence

$$(3.57) \quad \int_0^\infty \rho |H_0^{(1)}(k\rho)|^2 d\rho = \frac{4}{\pi^2} \int_0^\infty \rho (\text{ker}^2(\sqrt{\omega\mu\sigma}\rho) + \text{kei}^2(\sqrt{\omega\mu\sigma}\rho))$$

which can be integrated analytically (!) (e.g., [1] Equation (9.9.25)) to give

$$(3.58) \quad \frac{4}{\pi^2} \frac{1}{\omega \mu \sigma} [x(\ker(x)\ker'(x) - \ker(x)\ker'(x))]_0^\infty$$

For large x , $\ker(x)\ker'(x) - \ker(x)\ker'(x)$ decays as $e^{-x\sqrt{2}}$ (e.g., [1] Equation (9.10.32)) so it remains to evaluate the limit as $x \rightarrow 0$. For small enough x , we have

$$(3.59) \quad \ker(x) \sim -\log(x/2) \operatorname{ber}(x) + \pi/4 \operatorname{bei}(x) \quad \ker'(x) \sim -\log(x/2) \operatorname{bei}(x) - \pi/4 \operatorname{ber}(x)$$

and

$$(3.60) \quad \operatorname{ber}(x) \sim 1 \quad \operatorname{bei}(x) \sim x^2/4 \quad \ker'(x) \sim x \quad \ker'(x) \sim x/2$$

with the integral following from $x \ker(x)\ker'(x) \rightarrow \pi/4$ and $x \ker(x)\ker'(x) \rightarrow 0$.

References

- [1] Abramowitz, M. and I. A. Stegun, *Handbook of Mathematical Functions*, Dover, New York, 1972.
- [2] Allaud, L. and M. Martin, *Schlumberger, the History of a Technique*, Wiley, New York, 1977.
- [3] Anderson, B., "Induction sonde response in stratified media", *The Log Analyst*, **24**, no. 1, 1983, pp. 25-31.
- [4] Anderson, B., T. D. Barber, J. Singer, and T. Broussard, "ELMOD - putting electromagnetic modeling to work to improve resistivity log interpretation", in *Transactions of the 30th SPWLA Symposium*, Denver, CO, 1989. Paper M.
- [5] Axelsson, O. and V. A. Barker, *Finite Element Solution of Boundary Value Problems*, Academic Press, New York, 1984.
- [6] Chang, S. K. and B. Anderson, "Solution of induction logging by the finite element method", *Geophysics*, **49**, no. 11, 1984, pp. 1943-1958.
- [7] Chemali, R., S. Gianzero, and S. M. Su, "The effect of shale anisotropy on focused resistivity devices", in *Transactions of the 28th SPWLA Symposium*, London, UK, 1987. Paper H.

- [8] Chew, W. C., *Waves and Fields in Inhomogeneous Media*, Van Nostrand Reinhold, New York, 1990.
- [9] Chew, W. C., S. Barone, B. Anderson, and C. Hennessy, "Diffraction of axisymmetric waves in a borehole by bed boundary discontinuities", *Geophysics*, **49**, no. 10, 1984, pp. 1586–1595.
- [10] Chew, W. C., Z. Nie, Q.-H. Liu, and B. Anderson, "An efficient solution for the response of electrical well logging tools in a complex environment", *IEEE Trans. Geoscience and Remote Sensing*, **GE-29**, no. 2, 1991, pp. 308–313.
- [11] Coburn, M. E. and E. B. Nuckols, "Application of MWD resistivity logs to evaluation of formation invasion", in *Transactions of the 26th SPWLA Symposium*, Dallas, TX, 1985. Paper OO.
- [12] Davies, D. H., O. Faivre, M.-T. Gounot, B. Seeman, J. C. Trouiller, D. Benimeli, A. E. Ferreira, D. J. Pittman, J.-W. Smits, M. Randrianavony, B. Anderson, and J. R. Lovell, "Azimuthal Resistivity Imaging: A new generation Laterolog", in *SPE 67th Annual Technical Conference*, Washington, DC, 1992. Paper SPE 24676. Submitted to JPT.
- [13] Dewan, J. T., *Essentials of Modern Open-hole Log Interpretation*, PennWell, Tulsa, 1983.
- [14] Edmundson, H. and S. Gianzero, "The mathematics of resistivity and induction logging", *Schlumberger Technical Review*, **29**, no. 1, 1981, pp. 4–32. To be reprinted in *SPWLA Reprint Series on Resistivity Logging*, 1992.
- [15] Freund, R. W., "Conjugate gradient-type methods for linear systems with complex symmetric coefficient matrices", *SIAM J. Sci. Stat. Comput.*, **13**, no. 1, 1992, pp. 425–448.
- [16] Gianzero, S., R. Chemali, Y. Lin, S. Su, and M. Foster, "A new resistivity tool for measurements while drilling", in *26th SPWLA Symposium*, Dallas, TX, 1985. Paper A.
- [17] Habashy, T. M., *Notes on laterolog modelling*, 1990. Personal communication.
- [18] Howard, A. Q. and W. C. Chew, "Electromagnetic borehole fields in a layered, dipping bed environment with invasion", *Geophysics*, March 1992.
- [19] Jennings, A., "Influence of the eigenvalue spectrum on the convergence rate of the conjugate gradient method", *J. Inst. Math. Appl.*, **20**, 1977, pp. 61–72.
- [20] Kong, J. A., *Theory of Electromagnetic Waves*, John Wiley, New York, 1975.
- [21] Lacour-Gayet, P., "The Groningen effect . . . causes and a partial remedy", *Schlumberger Technical Review*, **29**, no. 1, 1981, pp. 37–47.

- [22] ———, *Method and apparatus for detecting an anomaly in a resistivity measurement of an earth formation*, 1982. US Patent 4,335,353.
- [23] Lovell, J. R., *Modelling frequency effects on Laterologs*, tech. rep., Schlumberger-Doll Research, Ridgefield, CT, 1990. Report EMG-90-34.
- [24] ———, “*Iterative methods for focussed Laterologs*”, in SIAM Conference on Mathematical and Computational Issues in the Geosciences, Houston, TX, 1993.
- [25] Lovell, J. R. and W. C. Chew, “*Effect of tool eccentricity on some electrical well logging tools*”, IEEE Trans. Geoscience Remote Sensing, **28**, no. 1, 1990, pp. 127–136.
- [26] Meijerink, J. A. and H. A. van der Vorst, “*An iterative solution method for linear systems of which the coefficient matrix is a symmetric M-matrix*”, Math. Comp., **31**, 1977, pp. 148–162.
- [27] Merchant, G. A. and S. G. Thadani, “*Finite electrode resistivity tool modelling*”, in Transactions of the 23rd SPWLA Symposium, Corpus Christi TX, 1982. Paper Q.
- [28] Moran, J. H. and R. Chemali, “*More on the Laterolog device*”, Geophysical Prospecting, **27**, no. 4, 1979, pp. 902–930.
- [29] Moran, J. H. and S. Gianzero, “*Effects of formation anisotropy on resistivity logging measurements*”, Geophysics, **44**, no. 7, 1979, pp. 1266 – 1286.
- [30] Nachtigal, N. M., S. C. Reddy, and L. N. Trefethen, *How fast are non-symmetric iterations?*, tech. rep., MIT, 1990. Numerical Analysis Report 90-2.
- [31] Peterson, A. F., C. F. Smith, and R. Mittra, “*Eigenvalues of the moment-method matrix and their effect on the convergence of the conjugate gradient algorithm*”, IEEE Trans. Antennas and Propagation, **36**, no. 8, 1988, pp. 1177–1179.
- [32] Ray, S. L. and A. F. Peterson, “*Error and convergence in numerical implementations of the conjugate gradient method*”, IEEE Trans. Antennas and Propagation, **36**, no. 12, 1988, pp. 1824–1827.
- [33] Schlumberger, C., M. Schlumberger, and E. G. Leonardon, “*Some observations concerning electrical measurements in anisotropic media and their interpretations*”, Trans. AIME, **110**, 1934, pp. 159 – 182.
- [34] Strang, G. and G. J. Fix, *An Analysis of the Finite Element Method*, Prentice-Hall, Inc., Englewood Cliffs, NJ, 1973.
- [35] Suau, J., P. Grimaldi, A. Poupon, and P. Souhaite, “*The Dual Laterolog R_{xo} tool*”, in SPE 47th Annual Technical Conference, San Antonio, TX, 1972. Paper SPE 4018.

- [36] Sumbar, E., F. E. Vermeulen, and F. S. Chute, "*Implementation of radiation boundary conditions in the finite element analysis of electromagnetic wave propagation*", IEEE Trans. Microwave Theory and Techniques, **39**, no. 2, 1991, pp. 267-273.
- [37] Titman, J., *Physics of Well Logging*, Dover, New York, 1984.
- [38] Todd, J., *A Survey of Numerical Analysis*, McGraw-Hill, 1962.
- [39] Watson, G. N., *A Treatise on the Theory of Bessel Functions*, Pergamon Press, New York, 1944. 2nd Ed.
- [40] Wilkinson, D. and P. S. Hammond, "*A perturbation method for mixed boundary-value problems in pressure transient testing*", Transport in Porous Media, **5**, 1990, pp. 609-636.
- [41] Woodehouse, R., "*The Laterolog Groningen phantom can cost you money*", in Transactions of the 19th SPWLA Symposium, 1978, pp. 1-17. Paper R.
- [42] Zemansky, P., "*Finite element modelling results*", Schlumberger Technical Review, **29**, no. 1, 1981, pp. 31-32.
- [43] Zienkiewicz, O., *The Finite Element Method*, McGraw Hill, 1977.

Contact Impedance Modelling and Verification

Abstract. This chapter examines different approaches to modelling electrodes subject to contact impedance and presents the results of some verification tests. Contact impedance is an electrochemical effect that can be represented as the limit of a thin layer of resistivity R_c and thickness d in front of a perfectly conducting electrode, where the limit is taken in such a way that the product $dR_c = Z_c$ remains constant. For DC problems, this limit can be represented by the boundary condition

$$\sigma \frac{\partial \Phi}{\partial \nu} = \frac{V - \Phi}{Z_c},$$

where V is the potential on the perfectly conducting electrode 'behind' the contact impedance layer, σ is the borehole conductivity in front of the layer and ν the unit normal pointing into the electrode. For non-DC problems, we cannot suppose that the electric field can be written in terms of a scalar potential Φ , but for both DC and CW problems in axisymmetric media, the electromagnetic field generated by TM tools such as Laterologs can be written purely in terms of H_ϕ . We show that for such configurations

$$E_z + Z_c \frac{\partial^2 H_\phi}{\partial z^2} = 0$$

is the natural representation of an electrode with contact impedance, Z_c , in an axisymmetric formation subject to time harmonic excitation. In an appendix, we detail CWNLAT and ALAT3D input files used to solve contact impedance problems and show excellent agreement between the two formulations.

4.1 Introduction

Contact impedances have typically been ignored when modelling Laterologs. Electrodes have been consistently taken as Dirichlet conditions in Φ , [7] or homogeneous Neumann conditions in H_ϕ , [1], [4]. For the newer tools with arrays of small electrodes, such as the FMI[†] and ARI[†], contact impedance becomes more important. In the SKYLINE finite element code, [2], contact impedance is modelled by placing thin insulating elements in front of the electrode. We propose a more mathematically rigorous approach where the insulating elements are replaced by effective boundary conditions which model the electrode physics. We shall

[†]Mark of Schlumberger

examine the boundary condition for contact impedance in a finite element context and discuss its implementation in terms of Φ and H_ϕ .

4.2 Contact impedance modelling

Consider a metallic electrode charged to a potential V on the boundary of a domain Ω filled with material with conductivity σ . The electrode will induce a potential field Φ satisfying Laplace's equation $\nabla \cdot \sigma \nabla \Phi = 0$ with $\Phi = V$ on the boundary. Contact impedance, Z_c (in Ωm^2), on the surface of the electrode changes the boundary equation $\Phi = V$ into the Robin boundary condition

$$(4.1) \quad \sigma \frac{\partial \Phi}{\partial \nu} = \frac{V - \Phi}{Z_c},$$

where ν is the outward pointing normal on $\partial\Omega$. If the boundary of Ω is decomposed into a sum of (connected) electrodes Γ_i separated from one another by insulators then the complete boundary condition on $\partial\Omega$ is

$$(4.2) \quad \sigma \frac{\partial \Phi}{\partial \nu} = \frac{V_i - \Phi}{Z_c} \quad \text{on } \Gamma_i,$$

$$(4.3) \quad \frac{\partial \Phi}{\partial \nu} = 0 \quad \text{on } \partial\Omega - \bigcup_i \Gamma_i,$$

which gives, by inspection, the well-defined elliptic system for Φ

$$(4.4) \quad \int_{\Omega} \sigma \nabla \Psi \cdot \nabla \Phi + \sum_i \int_{\Gamma_i} \frac{\Psi \Phi}{Z_c} = \sum_i \int_{\Gamma_i} \frac{\Psi V_i}{Z_c} \quad \forall \Psi \in H^1(\Omega),$$

where $H^1(\Omega)$ is the space of functions whose gradient has finite L^2 norm. If the V_i are not known *a priori* then we can add the equations

$$(4.5) \quad \int_{\Gamma_i} \frac{V_i - \Phi}{Z_c} = I_i$$

where I_i is the total outward flowing current on the i th electrode. (We are assuming for notational convenience that all of the electrodes have the same contact impedance.)

The above formulation is classical, e.g., [6]. In cylindrical coordinates, equation (4.4) becomes

$$(4.6) \quad \int_{\Omega} d\rho dz \rho \sigma \left[\frac{\partial \Psi}{\partial \rho} \frac{\partial \Phi}{\partial \rho} + \frac{\partial \Psi}{\partial z} \frac{\partial \Phi}{\partial z} \right] + \sum_i \int_{\Gamma_i} d\tau \rho \frac{\Psi \Phi}{Z_c} = \sum_i \int_{\Gamma_i} d\tau \rho \frac{\Psi V_i}{Z_c} \\ \forall \Psi \in H^1(\Omega),$$

where $d\tau = \tau_\rho d\rho + \tau_z dz$ and $\tau = \tau_\rho \hat{\rho} + \tau_z \hat{z}$ is the counterclockwise unit tangent vector.

We can also interpret the boundary condition for contact impedance as the limit of a shell whose thickness h tends to zero at the same time as the conductivity tends to zero in such a way that $h/\sigma \rightarrow Z_c$. (Note that this limit is dimensionally correct.)

The opposite limit where $\sigma \rightarrow \infty$ as $h \rightarrow 0$ in such a way that $\sigma h \rightarrow C_f$ provides a convenient representation for *fluid-filled fractures*: there is no discontinuity in potential crossing the fracture but non-zero current can pass along the inside of the fracture. With contact impedance, no current can travel parallel to the electrode surface but there is a potential drop across the layer. We shall return to fracture modelling in Chapter 5.

For example, in an axisymmetric configuration, consider a rectangular element $[\rho_1, \rho_2] \times [z_1, z_2]$ in the ρz plane, with bilinear approximation for Φ and Ψ so that

$$(4.7) \quad \Delta\rho \Delta z \Phi(\rho, z) = \Phi_1(\rho_2 - \rho)(z_2 - z) + \Phi_2(\rho - \rho_1)(z_2 - z) + \\ \Phi_3(\rho - \rho_1)(z - z_1) + \Phi_4(\rho_2 - \rho)(z - z_1),$$

and similarly for Ψ . We write $h = \Delta\rho = \rho_2 - \rho_1$, $\bar{\rho} = (\rho_1 + \rho_2)/2$ and $\Delta z = z_2 - z_1$ and examine the contribution of this element to the global stiffness matrix as $h \rightarrow 0$ and $h/\sigma \rightarrow Z_c$. We have that

$$(4.8) \quad \int_{\substack{[\rho_1, \rho_2] \times \\ [z_1, z_2]}} \sigma \nabla \Psi \cdot \nabla \Phi = \int_{\rho_1}^{\rho_2} \int_{z_1}^{z_2} \rho d\rho dz \sigma \left(\frac{\partial \Psi}{\partial \rho} \frac{\partial \Phi}{\partial \rho} + \frac{\partial \Psi}{\partial z} \frac{\partial \Phi}{\partial z} \right) \\ = (\Psi_2 - \Psi_1 \quad \Psi_3 - \Psi_4) \frac{\sigma \bar{\rho} \Delta z}{6 \Delta \rho} \begin{pmatrix} 2 & 1 \\ 1 & 2 \end{pmatrix} \begin{pmatrix} \Phi_2 - \Phi_1 \\ \Phi_3 - \Phi_4 \end{pmatrix} + \\ (\Psi_4 - \Psi_1 \quad \Psi_3 - \Psi_2) \frac{\sigma \Delta \rho}{6 \Delta z} \begin{pmatrix} \rho_2 + \bar{\rho} & \bar{\rho} \\ \bar{\rho} & \rho_1 + \bar{\rho} \end{pmatrix} \begin{pmatrix} \Phi_3 - \Phi_2 \\ \Phi_4 - \Phi_1 \end{pmatrix} \\ (4.9) \quad \rightarrow (\Psi_2 - \Psi_1 \quad \Psi_3 - \Psi_4) \frac{\bar{\rho} \Delta z}{6 Z_c} \begin{pmatrix} 2 & 1 \\ 1 & 2 \end{pmatrix} \begin{pmatrix} \Phi_2 - \Phi_1 \\ \Phi_3 - \Phi_4 \end{pmatrix}$$

as $\Delta\rho \rightarrow 0$. (For a fracture, it is the second matrix that would contribute to the stiffness matrix.) This result is equivalent to supposing a contact impedance on $\rho = \rho_2$ with $\Phi_1 = \Phi_4 = V$ and $\Psi_1 = \Psi_4 = 0$, for we have

$$(4.10) \quad \int_{\substack{\rho = \rho_2 \\ [z_1, z_2]}} \frac{\Psi(\Phi - V)}{Z_c} = \frac{\rho_2}{Z_c} \int_{z_1}^{z_2} dz \Psi(\Phi - V) = \frac{\rho_2 \Delta z}{6 Z_c} (\Psi_2 \quad \Psi_3) \begin{pmatrix} 2 & 1 \\ 1 & 2 \end{pmatrix} \begin{pmatrix} \Phi_2 - V \\ \Phi_3 - V \end{pmatrix}.$$

The same analogy holds true for arbitrary three dimensional geometries and is one of the advantages of the Φ formulation. In an axi-symmetric environment, an alternative choice of 'scalar potential' is the azimuthal component of magnetic field H_ϕ . Unlike Φ , H_ϕ this does not extend to a scalar potential in 3D but it does have the advantage of allowing frequency effects. Assuming axisymmetry and time harmonic excitation $e^{-i\omega t}$, Maxwell's equations for TM excitation:

$$(4.11a) \quad \nabla \times \mathbf{E} = i\omega\mu\hat{\phi}H_\phi,$$

$$(4.11b) \quad \nabla \times (\hat{\phi}H_\phi) = \sigma\mathbf{E} + \mathbf{J},$$

reduce to the second order scalar equation

$$(4.12) \quad \hat{\phi} \cdot \nabla \times \frac{1}{\sigma} \nabla \times (\hat{\phi}H_\phi) - i\omega\mu H_\phi = \hat{\phi} \cdot \nabla \times \mathbf{J}/\sigma$$

(here σ may be complex-valued). The question is how to generalize the boundary condition (4.1) on Γ_i . For example, if the electrode lies along a line of constant ρ , then differentiating equation (4.1) gives

$$(4.13) \quad \sigma \frac{\partial E_z}{\partial \nu} = \frac{E_z}{Z_c}$$

and then substituting

$$(4.14) \quad \sigma E_z = \frac{1}{\rho} \frac{\partial}{\partial \rho} (\rho H_\phi)$$

leads to

$$(4.15) \quad \frac{E_z}{Z_c} = \frac{\partial^2 H_\phi}{\partial z^2} + i\omega\mu\sigma H_\phi.$$

This boundary condition is *not* appropriate for modelling contact impedance. We shall demonstrate that the appropriate boundary condition is

$$(4.16) \quad \frac{E_z}{Z_c} = \frac{\partial^2 H_\phi}{\partial z^2}.$$

4.3 Contact impedance modelling with H_ϕ

One justification for equation (4.16) follows from a spectral analysis of the fields on the electrode. We suppose that σ is constant in Ω and write the fields in terms of their spectral $e^{ik_z z}$ components, as in Section 1.4.8. We write σ_c for the conductivity inside the impedance layer. We can suppose that inside the impedance layer, $a \leq \rho \leq b$

$$(4.17) \quad H_\phi = A[H_1^{(1)}(k_c \rho) - \frac{H_0^{(1)}(k_c a)}{J_0(k_c a)} J_1(k_c \rho)] e^{ik_z z}$$

$$(4.18) \quad E_z = A[H_0^{(1)}(k_c \rho) - \frac{H_0^{(1)}(k_c a)}{J_0(k_c a)} J_0(k_c \rho)] e^{ik_z z} \frac{k_c}{\sigma_c}$$

where $k_c^2 = i\omega\mu\sigma_c - k_z^2$, and in the formation $b \leq \rho$

$$(4.19) \quad H_\phi = [BH_1^{(1)}(k\rho) + CJ_1(k\rho)] e^{ik_z z}$$

$$(4.20) \quad E_z = [BH_0^{(1)}(k_c \rho) + CJ_0(k\rho)] e^{ik_z z} \frac{k}{\sigma}$$

where $k^2 = i\omega\mu\sigma - k_z^2$. The presence of the $J_{0,1}$ term indicates the possibility of sources are discontinuities in σ exterior to the $\rho = b$. The value for C will not be known a priori, we must find a boundary condition which is valid for arbitrary C .

We want to derive a formula for E_z/H_ϕ as $h \rightarrow 0$, where $b = a + h$ and $\sigma_c = h/Z_c$. E_z and H_ϕ are continuous at $\rho = b$ so regardless of the values of A , B and C

$$(4.21) \quad \frac{E_z}{H_\phi} = \frac{k_c Z_c}{h} \frac{H_0^{(1)}(k_c(a+h)) - \frac{H_0(k_c a)}{J_0(k_c a)} J_0(k_c(a+h))}{H_1^{(1)}(k_c(a+h)) - \frac{H_0(k_c a)}{J_0(k_c a)} J_1(k_c(a+h))}$$

for small h equals

$$(4.22) \quad \frac{E_z}{H_\phi} = \frac{k_c Z_c}{h} \frac{H_0^{(1)}(k_c(a+h)) - \frac{H_0(k_c a)}{J_0(k_c a)} J_0(k_c(a+h))}{H_1^{(1)}(k_c a) - \frac{H_0(k_c a)}{J_0(k_c a)} J_1(k_c a)}$$

which by l'Hôpital's rule becomes

$$(4.23) \quad \frac{E_z}{H_\phi} = -k_c^2 Z_c \frac{H_1^{(1)}(k_c a) - \frac{H_0(k_c a)}{J_0(k_c a)} J_1(k_c a)}{H_1^{(1)}(k_c a) - \frac{H_0(k_c a)}{J_0(k_c a)} J_1(k_c a)} = -k_c^2 Z_c = k_z^2 Z_c$$

which is *not* independent of k_z . Similarly, one can show that there is no expression of the form $(E_z - E_0)/(H_\phi - H_0)$ which is independent of k_z . Thus there is *no* first order boundary

condition on H_ϕ which will accurately model contact impedance. Equation (4.23) is, however, clearly just the spectral representation of (4.16) and so, regardless of the value of k_z , equation (4.16) correctly represents the physics of contact impedance on the electrode.

An alternative justification for equation (4.16) follows from a finite element formulation in the appropriate limit. If we take as fundamental unknown $u = 2\pi\rho H_\phi$ then Maxwell's equations on Ω (with perfectly conducting boundaries) reduce to

$$(4.24) \quad \int_{\Omega} d\rho dz \frac{1}{\sigma\rho} \left(\frac{\partial v}{\partial \rho} \frac{\partial u}{\partial \rho} + \frac{\partial v}{\partial z} \frac{\partial u}{\partial z} \right) - \int_{\Omega} d\rho dz \frac{i\omega\mu}{\rho} uv = 0 \quad \forall v \in H^1(\Omega).$$

Note the variable of integration is $d\rho dz$ not $\rho d\rho dz$. Physically, this is because the equations for H_ϕ correspond to integration about voltage loops in the ρz plane, whereas the equations for Φ correspond to integrals of current within cylindrical blocks.

We again consider a bilinear approximation of both u and v in the rectangle $[\rho_1, \rho_2] \times [z_1, z_2]$. In the limit as $h \rightarrow 0$ it is clear that the ω term will vanish, so we only need to consider the derivative terms. We obtain the local stiffness matrix

$$(4.25) \quad (v_2 - v_1 \quad v_3 - v_4) \frac{\Delta z}{6\bar{\rho}\sigma\Delta\rho} \begin{pmatrix} 2 & 1 \\ 1 & 2 \end{pmatrix} \begin{pmatrix} u_2 - u_1 \\ u_3 - u_4 \end{pmatrix} + \\ (v_4 - v_1 \quad v_3 - v_2) \frac{\Delta\rho}{6\bar{\rho}\sigma\Delta z} \begin{pmatrix} 2 & 1 \\ 1 & 2 \end{pmatrix} \begin{pmatrix} u_4 - u_1 \\ u_3 - u_2 \end{pmatrix}$$

which is a bit tricky in the limit because the denominator in the first term goes to zero, implying that we must also impose $u_2 = u_1 + O(h)$ and $v_2 = v_1 + O(h)$, etc. (We have also been a little sloppy in the integration of $1/\rho$ but this will certainly be ok as $h \rightarrow 0$.)

The condition that $u_2 \rightarrow u_1$, etc, follows physically from equation (4.14) that if $\sigma E_z \rightarrow 0$ then $\partial u / \partial \rho \rightarrow 0$, i.e, if there is no vertical component of current then the current flux through a loop of radius ρ_1 must be the same as through a loop of radius a .

We arrive at a stiffness matrix contribution of

$$(4.26) \quad (v_4 - v_1 \quad v_3 - v_2) \frac{Z_c}{6\bar{\rho}\Delta z} \begin{pmatrix} 2 & 1 \\ 1 & 2 \end{pmatrix} \begin{pmatrix} u_4 - u_1 \\ u_3 - u_2 \end{pmatrix}$$

which we write as a boundary contribution to the stiffness matrix by substituting $u_2 = u_1$, etc:

$$(4.27) \quad (v_4 - v_1 \quad v_4 - v_1) \frac{Z_c}{6\bar{\rho}\Delta z} \begin{pmatrix} 2 & 1 \\ 1 & 2 \end{pmatrix} \begin{pmatrix} u_4 - u_1 \\ u_4 - u_1 \end{pmatrix}$$

which simplifies to

$$(4.28) \quad (v_1 \quad v_4) \frac{Z_c}{\rho \Delta z} \begin{pmatrix} 1 & -1 \\ -1 & 1 \end{pmatrix} \begin{pmatrix} u_1 \\ u_4 \end{pmatrix}.$$

For an axisymmetric problem involving curved electrodes with tangent vector $\hat{\tau}$ and normal vector $\hat{\nu} = \hat{\phi} \times \hat{\tau}$, one can similarly show that contact impedance reduces to the differential equation

$$(4.29) \quad E_\tau + Z_c \frac{\partial^2 H_\phi}{\partial \tau^2} = 0$$

where we are using a non-standard meaning for the double derivative in polar coordinates:

$$(4.30) \quad \frac{\partial^2 H_\phi}{\partial \tau^2} = \left[\tau_\rho \frac{\partial}{\partial \rho} + \tau_z \frac{\partial}{\partial z} \right] \left(\tau_\rho \frac{1}{\rho} \frac{\partial(\rho H_\phi)}{\partial \rho} + \tau_z \frac{\partial H_\phi}{\partial z} \right).$$

Equation (4.29) is valid for arbitrary frequencies and does not require that σ be constant in front of the electrode.

The differential system for H_ϕ in Ω is thus equation (4.12) with equation (4.29) on the Γ_i and $H_\phi = \bar{u}/(2\pi\rho)$ on the insulating sections. We assume that we know the currents I_i from each electrode in which case we also know *a priori* the currents \bar{u} along the insulating sections of $\partial\Omega$. We shall assume for notational convenience that Ω is a rectangular domain with $\rho \geq a$ and the electrodes subject to contact impedance lie along $\rho = a$.

We multiply equation (4.12) by a test function ρh_ϕ and integrate (with respect to $d\rho dz$) over Ω to give the weak system

$$(4.31) \quad \int_\Omega d\rho dz \rho h_\phi \left(\frac{\partial}{\partial \rho} \frac{1}{\sigma \rho} \frac{\partial(\rho H_\phi)}{\partial \rho} + \frac{\partial}{\partial z} \frac{1}{\sigma \rho} \frac{\partial(\rho H_\phi)}{\partial z} + \frac{i\omega\mu}{\rho} \rho H_\phi \right) \\ \forall h_\phi \text{ such that } \rho h_\phi \in H^1(\Omega)$$

with the condition that $h_\phi = 0$ on $\partial\Omega - \bigcup_i \Gamma_i$ (where H_ϕ satisfies a Dirichlet constraint). Integrating by parts gives

$$(4.32) \quad \int_\Omega \frac{d\rho dz}{\sigma \rho} \left(\frac{\partial(\rho h_\phi)}{\partial \rho} \frac{\partial(\rho H_\phi)}{\partial \rho} + \frac{\partial(\rho h_\phi)}{\partial z} \frac{\partial(\rho H_\phi)}{\partial z} \right) - \int_\Omega d\rho dz \frac{i\omega\mu}{\rho} \rho h_\phi \rho H_\phi + \\ \int_{\partial\Omega} d\tau \frac{\rho h_\phi}{\sigma} \left(\nu_\rho \frac{1}{\rho} \frac{\partial(\rho H_\phi)}{\partial \rho} + \nu_z \frac{\partial H_\phi}{\partial z} \right) = 0$$

where $\hat{\nu} = \nu_\rho \hat{\rho} + \nu_z \hat{z} = \tau_z \hat{\rho} - \tau_\rho \hat{z}$. We recognize the boundary integral as

$$(4.33) \quad \int_{\partial\Omega} d\tau \frac{\rho h_\phi}{\sigma} \hat{\tau} \cdot \nabla \times (\hat{\phi} H_\phi) = \int_{\partial\Omega} d\tau \rho h_\phi E_\tau = \sum_i \int_{\Gamma_i} \rho h_\phi E_\tau$$

because h_ϕ is zero off the electrodes. Substituting equation (4.29) and writing $u = 2\pi\rho H_\phi$ and $v = 2\pi\rho h_\phi$ gives

$$(4.34) \quad \int_{\Omega} \frac{d\rho dz}{\sigma\rho} \nabla u \cdot \nabla v - \int_{\Omega} d\rho dz \frac{i\omega\mu}{\rho} uv + \sum_i \int_{\Gamma_i} d\tau v \frac{Z_c}{\rho} \frac{\partial^2 u}{\partial \tau^2} = 0$$

which we recognize as equation (4.24) with additional boundary terms. These boundary terms can be written in a symmetric fashion by observing that for $\rho = a$

$$(4.35) \quad \int_{\Gamma_i} d\tau v \frac{Z_c}{\rho} \frac{\partial^2 u}{\partial \tau^2} = - \int_{\Gamma_i} dz v \frac{Z_c}{\rho} \frac{\partial^2 u}{\partial z^2} = \int_{\Gamma_i} dz \frac{Z_c}{\rho} \frac{\partial u}{\partial z} \frac{\partial v}{\partial z}$$

because $v = 0$ on $\partial\Gamma_i$. (If two Γ_i were touching, the integration by parts would be trickier but the resulting weak formulation is still correct.)

To complete the chain of reasoning, we shall now suppose u and v to be linear on $[z_1, z_2] \subset \Gamma_i$ with $u(z) = u_4(z_2 - z) + u_1(z - z_1)$, etc., and examine the contribution of the boundary term to the stiffness matrix. We have

$$(4.36) \quad \int_{z_1}^{z_2} dz \frac{Z_c}{\rho} \frac{\partial u}{\partial z} \frac{\partial v}{\partial z} = \Delta z \frac{Z_c}{\rho} \frac{u_4 - u_1}{\Delta z} \frac{v_4 - v_1}{\Delta z}$$

which is equation (4.28).

To conclude, contact impedance Z_c on vertical electrodes Γ_i gives rise to the coercive system

$$(4.37) \quad \int_{\Omega} \frac{d\rho dz}{\sigma\rho} \left[\frac{\partial u}{\partial \rho} \frac{\partial v}{\partial \rho} + \frac{\partial u}{\partial z} \frac{\partial v}{\partial z} \right] - \int_{\Omega} d\rho dz \frac{i\omega\mu}{\rho} uv + \sum_i \int_{\Gamma_i} dz \frac{Z_c}{\rho} \frac{\partial u}{\partial z} \frac{\partial v}{\partial z} = 0 \quad \forall v \in H^1(\Omega)$$

with $u = \bar{u}$ and $v = 0$ on $\partial\Omega - \bigcup_i \Gamma_i$.

4.4 Verification

We have coded the potential formulation in 3D (ALAT3D) and the axisymmetric formulation for time harmonic excitation (CWNLAT). We shall compare the two codes in their domain of intersection, namely axisymmetric domains with zero frequency excitation.

An obvious test case for the contact impedance modelling is to ensure that the code can reproduce the correct answer for the cylindrically symmetric case of equations (4.17) and (4.19) for the case of an infinitely long electrode ($k_z = 0$). For this case, however, the contact impedance may only be a small perturbation and stronger tests are desirable. In general, contact impedance effects will be larger for small electrodes (large k_z) and low frequencies ω [3], [5].

We shall solve for the fields produced by arrays of finite length electrodes using the Φ formulation of equations (4.4) and (4.5) and the H_ϕ formulation of equation (4.37). In a numerical Galerkin formulation, the two solutions will necessarily provide upper and lower bounds for the true answer (which is not obtainable by analytic means).

For the verification results presented here we shall consider an array of electrodes of different sizes and impedances. The array is symmetric about $z = 0$ and Ω is the domain $a \leq \rho \leq R$, $0 \leq z \leq L$ for suitable a , R and L . Here a represents the tool radius and R and L suitable boundaries at "infinity" where the field distribution can be assumed known (e.g., zero). The first tool we consider has radius 1.8 and electrodes

#	z_1	z_2	Impedance
E1	0.0	1.0	$Z_c = 3 \times 10^{-2}$
E2	2.0	3.0	$Z_c = 3 \times 10^{-2}$
E3	4.0	60.0	$Z_c = 3 \times 10^{-3}$

with a current return (i.e., zero potential) at $L = 1000$ (all dimensions are in inches). Sections of the tool which are not electrodes are perfect insulators. We place the tool in 4" radius borehole filled with a 0.1 Ωm mud. Assuming that each electrode in turn fires unit current then measuring the potentials at each electrode gives rise to a 3×3 transfer impedance matrix, Z .

For an extreme test case, we can suppose a 'no-flow' boundary condition at $R = 4$ (i.e., that the formation is infinitely resistive). The matrix from the Φ formulation

$$(4.38) \quad Z = \begin{pmatrix} 97.42648 & 92.96011 & 92.56337 \\ 92.96011 & 97.18669 & 92.56337 \\ 92.56338 & 92.56338 & 92.56337 \end{pmatrix}$$

agrees closely with the matrix from the H_ϕ formulation

$$(4.39) \quad Z = \begin{pmatrix} 97.42926 & 92.96208 & 92.56518 \\ 92.96208 & 97.18991 & 92.56518 \\ 92.56518 & 92.56518 & 92.56518 \end{pmatrix}.$$

Alternatively, rather than using equation (4.5), we can suppose that each of the electrodes is in turn excited to unit voltage and solve equation (4.4) for Φ and compute the total currents emitted, which gives the matrix

$$(4.40) \quad Y = \begin{pmatrix} 0.2071 & -0.0178 & -0.1893 \\ -0.0178 & 0.2178 & -0.2001 \\ -0.1893 & -0.2001 & 0.4002 \end{pmatrix}$$

which is in excellent agreement to the inverse of Z , namely

$$(4.41) \quad Z^{-1} = \begin{pmatrix} 0.2070 & -0.0178 & -0.1893 \\ -0.0178 & 0.2178 & -0.2000 \\ -0.1893 & -0.2000 & 0.4001 \end{pmatrix}.$$

For a second tool configuration, we subdivide the long electrode E_3 into three pieces, E_3, E_4, E_5 , with the centre section E_4 having a very low contact impedance and we also lower the contact impedance of E_1 .

#	z_1	z_2	Impedance
E1	0.0	1.0	$Z_c = 1 \times 10^{-5}$
E2	2.0	3.0	$Z_c = 3 \times 10^{-2}$
E3	4.0	5.0	$Z_c = 3 \times 10^{-3}$
E4	6.0	7.0	$Z_c = 1 \times 10^{-5}$
E5	8.0	60.0	$Z_c = 3 \times 10^{-3}$

The ALAT3D and CWNLAT input files for both configurations are given in Appendix 4.A.

Having a small Z_c allows us to test for any degradation in convergence for Φ , because as is clear from equations (4.4) and (4.6) there may be overflow problems for small enough Z_c . The stiffness matrix for H_ϕ does not become singular as $Z_c \rightarrow 0$, however.

Again supposing the formation to be infinitely resistive we get

$$(4.42) \quad Z = \begin{pmatrix} 93.67669 & 93.34482 & 93.13902 & 92.94752 & 92.56518 \\ 93.34481 & 97.57388 & 93.14523 & 92.94783 & 92.56518 \\ 93.13902 & 93.14524 & 93.67528 & 92.95377 & 92.56518 \\ 92.94752 & 92.94783 & 92.95377 & 93.06466 & 92.56518 \\ 92.56518 & 92.56518 & 92.56518 & 92.56518 & 92.56518 \end{pmatrix}$$

from the H_ϕ formulation and

$$(4.43) \quad Z = \begin{pmatrix} 93.67136 & 93.34255 & 93.13659 & 92.94512 & 92.56338 \\ 93.34255 & 97.57022 & 93.14283 & 92.94543 & 92.56338 \\ 93.13659 & 93.14283 & 93.67185 & 92.95140 & 92.56338 \\ 92.94512 & 92.94543 & 92.95140 & 93.06246 & 92.56338 \\ 92.56338 & 92.56338 & 92.56338 & 92.56337 & 92.56338 \end{pmatrix}$$

from the Φ formulation using equation (4.4).

With voltage excitation instead of current excitation and solving for Φ we obtained

$$(4.44) \quad Y = \begin{pmatrix} 1.4529 & -0.1228 & -0.4548 & -0.6637 & -0.2116 \\ -0.1228 & 0.2270 & -0.0374 & -0.0508 & -0.0161 \\ -0.4548 & -0.0374 & 1.4084 & -0.7185 & -0.1977 \\ -0.6637 & -0.0508 & -0.7185 & 3.1088 & -1.6759 \\ -0.2116 & -0.0161 & -0.1977 & -1.6758 & 2.1120 \end{pmatrix}$$

which again compares well to the inverse of Z , namely

$$(4.45) \quad Z^{-1} = \begin{pmatrix} 1.4529 & -0.1228 & -0.4548 & -0.6637 & -0.2116 \\ -0.1228 & 0.2270 & -0.0374 & -0.0508 & -0.0160 \\ -0.4548 & -0.0374 & 1.4084 & -0.7185 & -0.1977 \\ -0.6637 & -0.0508 & -0.7185 & 3.1088 & -1.6759 \\ -0.2116 & -0.0160 & -0.1977 & -1.6758 & 2.1120 \end{pmatrix}.$$

For a 'practical' tool configuration, denoted AZI5, we shall suppose that no current flows from $E1$ and $E4$, that $E3$ and $E5$ are held to the same potential (unknown *a priori*) and that $E1$ and $E4$ are both held to unit potential. This gives 5 equations in 5 unknowns leading to a well defined system. We define the apparent resistance to be V_{E1}/I_{E2} . This can be computed in terms of the Z matrix as

$$(4.46) \quad \frac{V_1}{I_2} = \frac{\begin{vmatrix} Z_{12} & Z_{13} & Z_{15} \\ Z_{42} & Z_{43} & Z_{45} \\ Z_{32} - Z_{52} & Z_{33} - Z_{53} & Z_{35} - Z_{55} \end{vmatrix}}{\begin{vmatrix} Z_{43} - Z_{13} & Z_{45} - Z_{15} \\ Z_{33} - Z_{53} & Z_{35} - Z_{55} \end{vmatrix}}$$

or else in terms of the Y matrix as

$$(4.47) \quad \frac{V_1}{I_2} = \frac{\begin{vmatrix} Y_{12} & Y_{11} + Y_{14} & Y_{13} + Y_{15} \\ Y_{22} & 0 & Y_{23} + Y_{25} \\ Y_{42} & Y_{41} + Y_{44} & Y_{43} + Y_{45} \end{vmatrix}}{\begin{vmatrix} Y_{12} & Y_{13} + Y_{15} \\ Y_{42} & Y_{43} + Y_{45} \end{vmatrix}}.$$

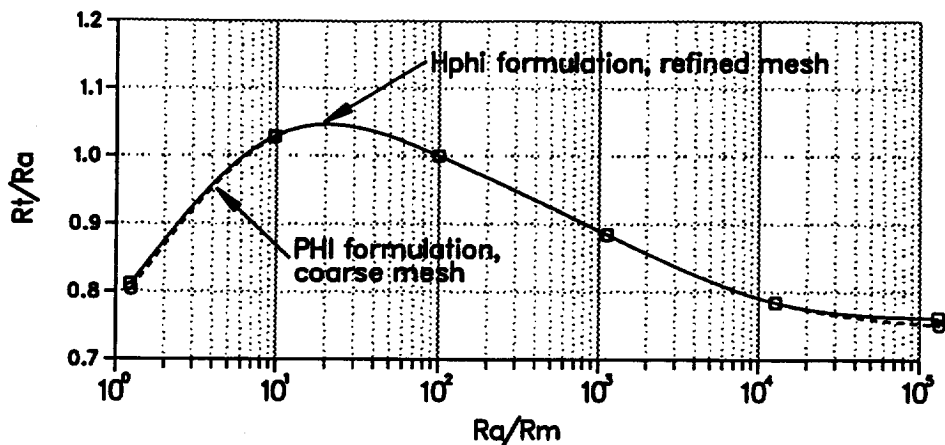


Figure 4.1: Borehole correction chart for the AZ15 configuration. R_a denotes the apparent resistivity, R_m the mud resistivity and R_t the true formation resistivity.

For the previous example, we obtain that in an infinitely resistive formation, $I_2 = 0$ and so the apparent resistivity is also infinite. For more general formations, we will obtain a (finite valued) apparent resistivity by scaling the apparent resistance V_1/I_2 by some constant (in this case $K = 0.171 m$) so that in a $10\Omega m$ formation (with conductive borehole) the apparent resistivity is also $10\Omega m$.

Using the two different formulations in H_ϕ and Φ , Figure 4.1 shows the apparent resistivity, R_a , computed numerically as a function of the formation resistivity, R_t . For clarity, we have computed the Φ -result on a coarser mesh with a uniform zone in a neighbourhood of the borehole surrounded by a non-uniform triangulation in the remainder of the formation. It can be seen that for most contrasts, the mesh is sufficiently fine and excellent agreement is obtained. When there is no contrast between R_t and R_m , then the zone of uniform triangulation needs to be extended further into the formation whereas when the contrast is extremely high the mesh near the borehole wall needs refining.

As discussed in Chapter 2, the drilling process can allow mud to enter the formation and change the value of R_t . A schematic diagram is given in Figure 4.2. We assume that the shoulder beds are impermeable and not invaded by the mud fluid and that the bed of interest has been subject to a piston-like invasion, so that its resistivity takes on a step profile with value R_{xo} for ρ less than some radius and R_t in the remainder of the bed. The effect of changing radius of invasion is shown in Figure 4.3 where we have $R_t = 1000$, $R_m = 0.1$, $R_{xo} = 10$. We also compare the result for the H_ϕ and Φ formulations on two different meshes

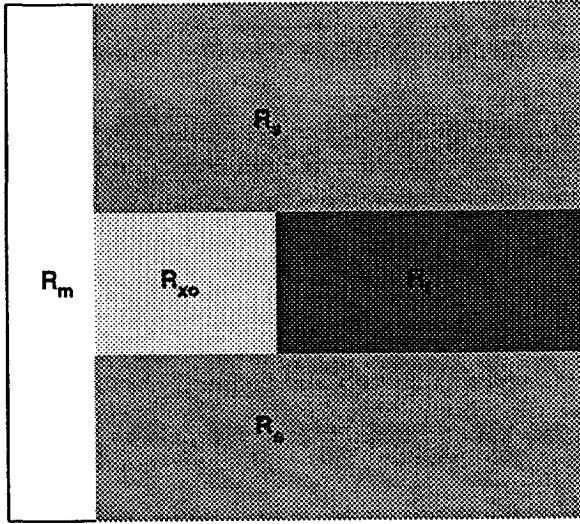


Figure 4.2: Schematic interpretation of an invaded bed assuming a step profile of invasion. R_t is the bed resistivity, R_{xo} is the resistivity of the invaded zone, R_m is the mud resistivity and R_s the resistivity of the shoulder beds.

to show the effect of mesh diameter.

To test the 3D code in non-axisymmetric situations, we built a finite element code to solve for z -invariant potential fields in circular wedges with constant conductivity. Assuming a product mesh $\{\rho_1, \dots, \rho_n\} \times \{\phi_1, \dots, \phi_m\}$, we chose tensor product basis functions

$$(4.48) \quad B_{ij}(\rho, \phi) = B_i^\rho(\rho) B_j^\phi(\phi)$$

where

$$(4.49) \quad B_i^\rho(\rho) = \begin{cases} \frac{\rho - \rho_{i-1}}{\Delta \rho_{i-1}} & \rho \in [\rho_i, \rho_{i-1}], \\ \frac{\rho_{i+1} - \rho}{\Delta \rho_i} & \rho \in [\rho_{i+1}, \rho_i], \\ 0 & \text{elsewhere,} \end{cases} \quad B_j^\phi(\phi) = \begin{cases} \frac{\phi - \phi_{j-1}}{\Delta \phi_{j-1}} & \phi \in [\phi_{j-1}, \phi_j], \\ \frac{\phi_{j+1} - \phi}{\Delta \phi_j} & \phi \in [\phi_j, \phi_{j+1}], \\ 0 & \text{elsewhere,} \end{cases}$$

and $\Delta \rho_i = \rho_{i+1} - \rho_i$, $\Delta \phi_j = \phi_{j+1} - \phi_j$.

The global stiffness matrix can be built as a tensor product of the one dimensional stiffness and mass matrices in ϕ and ρ .

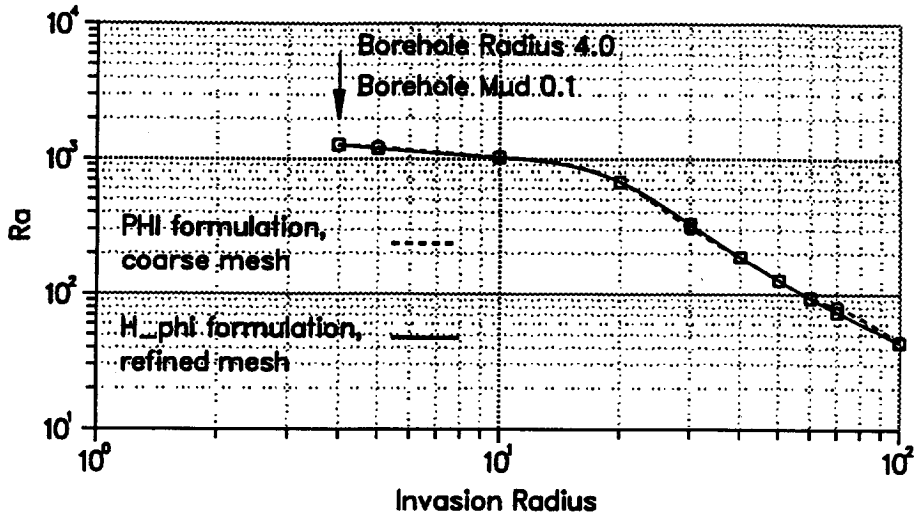


Figure 4.3: Invasion modelling for the AZ15 configuration. $R_t = 1000\Omega m$, $R_{x_o} = 10\Omega m$ and $R_m = 0.1\Omega m$. All linear dimensions are in inches. R_a denotes the apparent resistivity, R_m the mud resistivity, R_{x_o} is the resistivity of the invaded zone and R_t the true formation resistivity.

The components of the local stiffness and mass matrices in ϕ are given by

(4.50)

$$A_{ij}^{\rho} = \int \frac{\partial B_i^{\rho}}{\partial \rho} \frac{\partial B_j^{\rho}}{\partial \rho} \rho d\rho; \quad \leftarrow \quad \begin{cases} \int_{\rho_i}^{\rho_{i+1}} \frac{\partial B_i^{\rho}}{\partial \rho} \frac{\partial B_i^{\rho}}{\partial \rho} \rho d\rho & = \frac{\rho_{i+1} + \rho_i}{2\Delta\rho_i} \\ \int_{\rho_i}^{\rho_{i+1}} \frac{\partial B_i^{\rho}}{\partial \rho} \frac{\partial B_{i+1}^{\rho}}{\partial \rho} \rho d\rho & = -\frac{\rho_{i+1} + \rho_i}{2\Delta\rho_i} \\ \int_{\rho_i}^{\rho_{i+1}} \frac{\partial B_{i+1}^{\rho}}{\partial \rho} \frac{\partial B_{i+1}^{\rho}}{\partial \rho} \rho d\rho & = \frac{\rho_{i+1} + \rho_i}{2\Delta\rho_i} \end{cases}$$

(4.51)

$$M_{ij}^{\rho} = \int B_i^{\rho} B_j^{\rho} \frac{d\rho}{\rho}; \quad \leftarrow \quad \begin{cases} \int_{\rho_i}^{\rho_{i+1}} B_i^{\rho} B_i^{\rho} \frac{d\rho}{\rho} & = \frac{\rho_{i+1}^2}{\Delta\rho_i^2} \log \frac{\rho_{i+1}}{\rho_i} + \frac{\rho_i - 3\rho_{i+1}}{2\Delta\rho_i} \\ \int_{\rho_i}^{\rho_{i+1}} B_i^{\rho} B_{i+1}^{\rho} \frac{d\rho}{\rho} & = -\frac{\rho_{i+1}\rho_i}{\Delta\rho_i^2} \log \frac{\rho_{i+1}}{\rho_i} + \frac{\rho_i + \rho_{i+1}}{2\Delta\rho_i} \\ \int_{\rho_i}^{\rho_{i+1}} B_{i+1}^{\rho} B_{i+1}^{\rho} \frac{d\rho}{\rho} & = \frac{\rho_i^2}{\Delta\rho_i^2} \log \frac{\rho_{i+1}}{\rho_i} + \frac{\rho_{i+1} - 3\rho_i}{2\Delta\rho_i} \end{cases}$$

and the components of the local stiffness and mass matrices in ρ are given by

(4.52)

$$A_{ij}^{\phi} = \int \frac{\partial B_i^{\phi}}{\partial \phi} \frac{\partial B_j^{\phi}}{\partial \phi} d\phi; \quad \leftarrow \quad \begin{cases} \int_{\phi_i}^{\phi_{i+1}} \frac{\partial B_i^{\phi}}{\partial \phi} \frac{\partial B_i^{\phi}}{\partial \phi} d\phi & = 1/\Delta\phi_i \\ \int_{\phi_i}^{\phi_{i+1}} \frac{\partial B_i^{\phi}}{\partial \phi} \frac{\partial B_{i+1}^{\phi}}{\partial \phi} d\phi & = -1/\Delta\phi_i \\ \int_{\phi_i}^{\phi_{i+1}} \frac{\partial B_{i+1}^{\phi}}{\partial \phi} \frac{\partial B_{i+1}^{\phi}}{\partial \phi} d\phi & = 1/\Delta\phi_i \end{cases}$$

(4.53)

$$M_{ij}^{\phi} = \int B_i^{\phi} B_j^{\phi} d\phi; \quad \leftarrow \quad \begin{cases} \int_{\phi_i}^{\phi_{i+1}} B_i^{\phi} B_i^{\phi} d\phi & = \Delta\phi_i/3 \\ \int_{\phi_i}^{\phi_{i+1}} B_i^{\phi} B_{i+1}^{\phi} d\phi & = \Delta\phi_i/6, \\ \int_{\phi_i}^{\phi_{i+1}} B_{i+1}^{\phi} B_{i+1}^{\phi} d\phi & = \Delta\phi_i/3 \end{cases}$$

because

(4.54)

$$\begin{aligned} \int \nabla B_{ij} \cdot \nabla B_{pq} &= \int \frac{\partial B_i^{\rho}}{\partial \rho} \frac{\partial B_p^{\rho}}{\partial \rho} B_j^{\phi} B_q^{\phi} \rho d\rho d\phi + \int \frac{\partial B_j^{\phi}}{\partial \phi} \frac{\partial B_q^{\phi}}{\partial \phi} B_i^{\rho} B_p^{\rho} \frac{d\rho d\phi}{\rho} \\ &= A_{ip}^{\rho} M_{jq}^{\phi} + M_{ip}^{\rho} A_{jq}^{\phi} \end{aligned}$$

and

(4.55)

$$\oint_{\rho=\rho_1} B_{ij} B_{pq} \rho d\phi = \rho_1 M_{jq}^{\phi} \delta_{i1} \delta_{p1}.$$

which can be substituted into equation (4.4).

Given the setup of Figure 4.4, We examine the potential along the tool surface for $Z_c = 0$ and $Z_c = 3 \times 10^{-2} \Omega m^2$ and for $R_t = 0$ and $R_t = \infty$. When $R_t = 0$ the formation is perfectly conducting and we suppose that $I_1 = 1$ and $I_2 = 0$ with the current returning to the borehole wall. When $R_t = \infty$, we suppose that $I_1 = -I_2 = 1$. In the former case, the voltage along the mandrel is always positive and we present the data on a logarithmic scale to demonstrate the agreement over a large dynamic range, in the latter case the voltage is skew symmetric and we present the data on a linear scale.

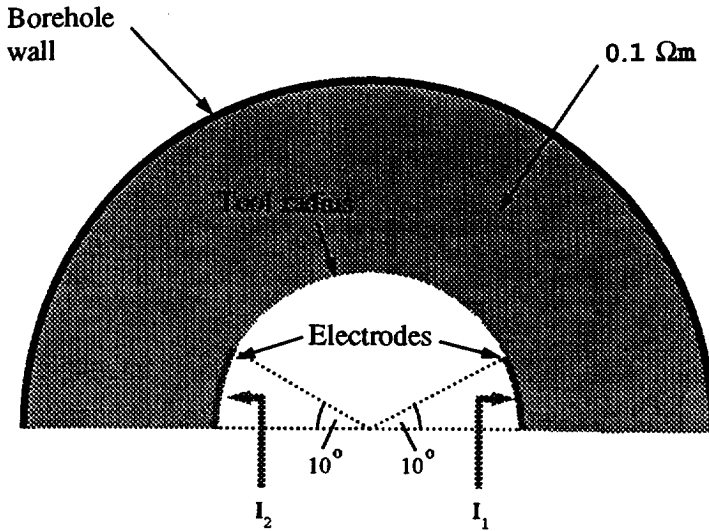


Figure 4.4: Nonaxisymmetric test configuration. The electrodes lie on the surface of the tool mandrel. Here, we suppose the borehole wall is either a perfect insulator, or a perfect conductor.

Comparing Figure 4.5 to Figure 4.6 we see that the presence of contact impedance does not significantly affect excellent agreement between the codes. We can also see that the greatest effect of the contact impedance is the change in value of V_1 which increases by an order of magnitude. The potential distribution along the mandrel is actually rather independent of Z_c , save that the electrodes themselves become equipotentials when $Z_c = 0$. Also note that it is only the current carrying electrode that demonstrates a dependence on Z_c , even though the same boundary condition is being used for both V_1 and V_2 . In all cases, we see that the greatest discrepancy between the two codes occurs near the edge of the electrodes, which is due to the different meshing strategies.

4.5 Conclusions

We have developed a formulation for contact impedance that is valid for non-zero frequencies as well as at DC. When cast in terms of H_ϕ , the boundary condition requires a second order tangential derivative in H_ϕ . The validity of this formulation was confirmed by showing that finite element and spectral methods gave rise to the same expression. When the boundary term is written as a weak condition it adds to the coercivity of the stiffness matrix in H_ϕ . Moreover,

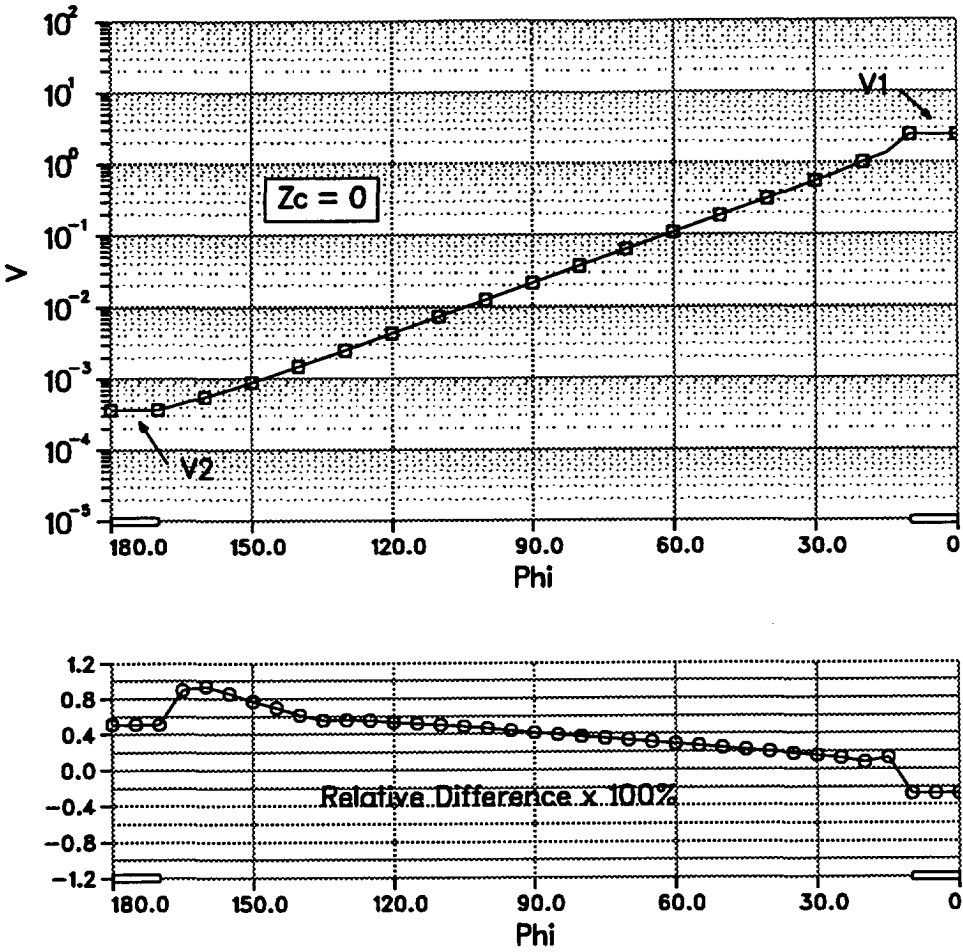


Figure 4.5: Surface potential $V = V(\phi)$ as a function of the azimuthal angle ϕ for $I_1 = 1$ and $I_2 = 0$ and $R_t = 0$. Tool radius = 1.8". Borehole radius = 3.0". $Z_c = 0 \Omega m^2$. Error is relative to the 2D data.

as the contact impedance tends to zero, there is no singularity in the stiffness matrix, unlike the case for the DC formulation in terms of Φ . Lastly, we have demonstrated excellent agreement between 2D and 3D finite element codes for configurations involving large impedance drops over current carrying electrodes.

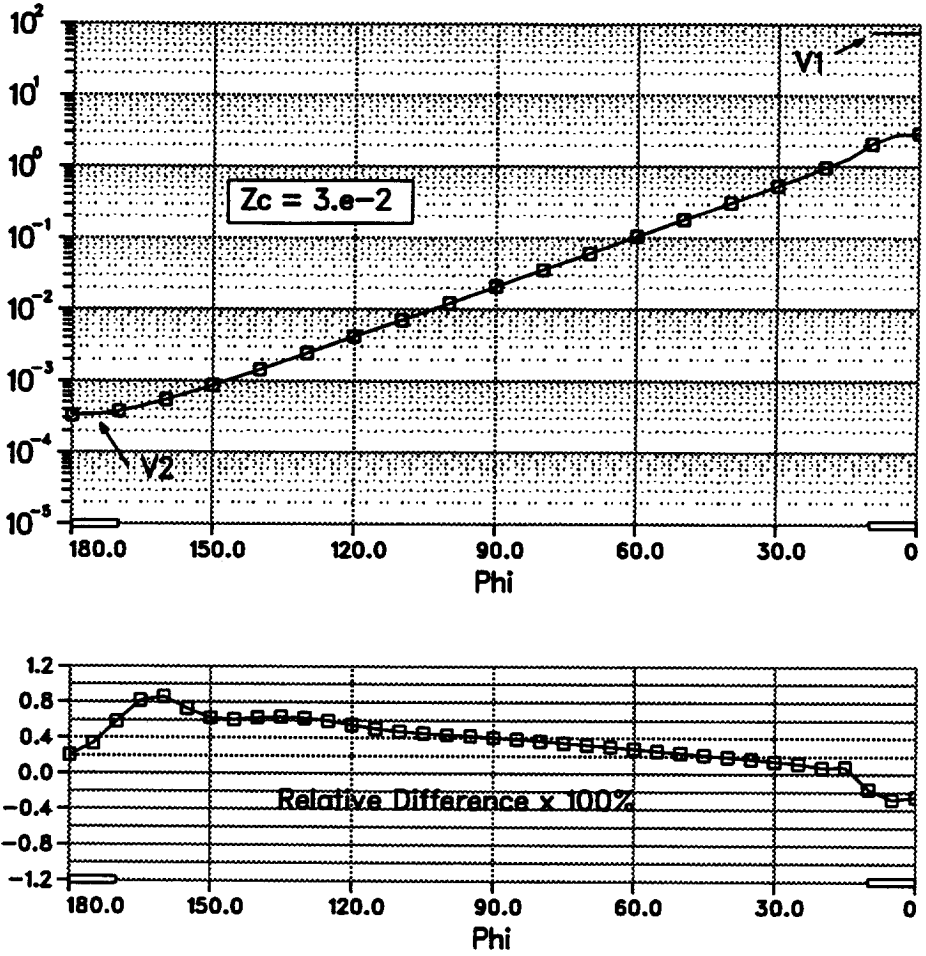


Figure 4.6: Surface potential $V = V(\phi)$ as a function of the azimuthal angle ϕ for $I_1 = 1$ and $I_2 = 0$ and $R_t = 0$. Tool radius = 1.8". Borehole radius = 3.0". $Z_c = 3 \times 10^{-2} \Omega m^2$. 3D results shown solid, 2D results dashed. Error is relative to the 2D data.

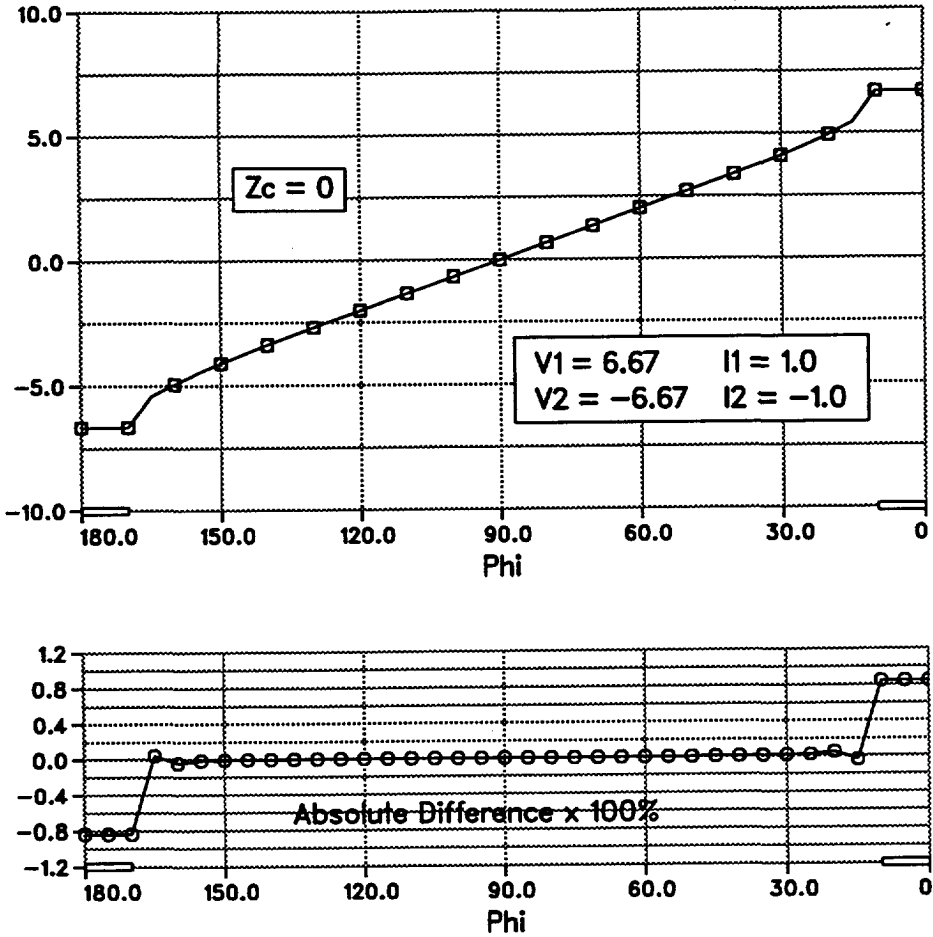


Figure 4.7: Surface potential $V = V(\phi)$ as a function of the azimuthal angle ϕ for $I_1 = 1$ and $I_2 = -1$ and $R_t = \infty$. Tool radius = 1.8". Borehole radius = 3.0". $Z_c = 0 \Omega m^2$. 3D results shown solid, 2D results dashed.

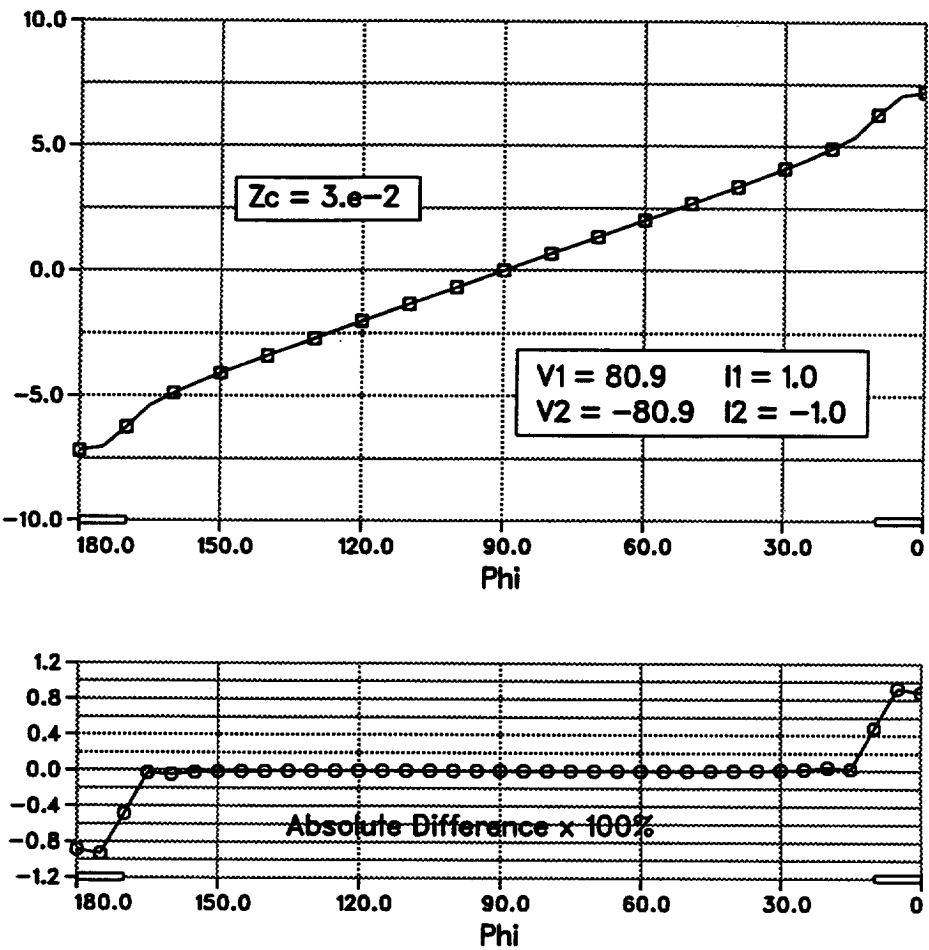


Figure 4.8: Surface potential $V = V(\phi)$ as a function of the azimuthal angle ϕ for $I_1 = 1$ and $I_2 = -1$ and $R_1 = \infty$. Tool radius = 1.8". Borehole radius = 3.0". $Z_c = 3 \times 10^{-2} \Omega m^2$. 3D results shown solid, 2D results dashed.

Appendix 4.A CWNLAT and ALAT3D sample input files

CWNLAT input file for 3-electrode configuration and infinite resistivity formation. Current sources, H_ϕ formulation. Result given in equation (4.39)

```
#CWNLAT input for azimuthal test #1.
#3 electrodes with non-zero contact impedance
Quiet
5

###
# Tool description - 3 electrodes on sonde, symmetry across Z=0
###

electrodes
1 1.8 0.0 1.8 1.0
2 1.8 2.0 1.8 3.0
3 1.8 4.0 1.8 60.0
4 1.8 1000 3.0 1000
5 3.0 1000 4.0 1000

known current - CWNLAT will loop over 3 missing sections
(0.,0.) 1.8 0.00 1000 0
(0.,0.) 4.0 0 4.0 1000

scont
(3.e-2,0.) 1
(3.e-2,0.) 2
(3.e-3,0.) 3

###
# Formation description
###
blocks of constant resistivity [rmin,zmin,rmax,zmax]
#borehole
1 1.8 0. 4.0 1000.
#rock is assumed infinitely resistive

list of resistivities [RES, MU, EPS]
```

```

1  0.1    1. 1.
2  100    1. 1.

###
#  Mesh
###
Z
#ZSONDE -- tool coordinates DO need to be here!
0 0.1 0.5 0.9 1.0 1.5 2.0 2.1 2.5 2.9 3.0 3.5 4.0 4.1
4.5 5.0 5.5 6.0 6.5 7.0 7.5 8.0 8.5 9.0 10.0 11.0 15.0 20 25
30 35 40 44 48 52 56 58 59 59.9
60 61 62 66 70 75 80 90 100 150 200 300 400 550 750 900 950
990 999 1000

RHO values
1.8 1.82 1.84 1.86 1.92 1.96 2.1 2.2 2.3 2.4 2.6 2.8 3.0
3.3 3.6 3.8 4.0

Mesh -- i.e., refine the mesh by this factor
6
###
#  Miscellaneous
###
potential reference
3.0 1000.

ueps (convergence criterion for conjugate gradient)
1.e-9

output
0 t1.cwn_dat

```

ALAT3D input file for 3-electrode configuration and infinitely resistive formation. Current sources excitation. Result given in equation (4.38)

#ALAT3D input file for 3 electrode tool

MODULEF meshes and ALAT3D output files
t1.mod

4.A. SAMPLE INPUT FILES

141

t1.sd
t1.dip_dat

LIST OF MATERIALS (#, RES, INVRES each on a separate line)

Region ONE is ALWAYS the borehole fluid

1 0.1 0.1
2 100. 100.

BOREHOLETOOL (Bx,By,Tool,Ecc). Restrictions: Ecc=0 and Bx = By

4.0 4.0 1.8

DOMAINS (x1,z1,x2,z2) - borehole value takes priority

2 -5000 0 5000 5000

INVASION (either 1 or 2 radii with an optional 3rd parameter)

10. 10.

Z -- tool coordinates are NOT added to this list.

#ZSONDE -- tool coordinates DO need to be here!

0 0.1 0.5 0.9 1.0 1.5 2.0 2.1 2.5 2.9 3.0 3.5 4.0 4.1
4.5 5.0 5.5 6.0 6.5 7.0 7.5
8.0 8.5 9.0 10.0 11.0 15.0 20 25 30 35 40 44 48 52 56 58 59 59.9
60 61 62 66 70 75 80 90 100 150 200 300 400 550 750 900 950
990 999 1000

X/RHO values -- there are no elements beyond RHO=4.0

1.8 1.82 1.84 1.86 1.92 1.96 2.1 2.2 2.3 2.4 2.6 2.8 3.0
3.3 3.6 3.8 4.0

ELECTRODES (REF, THETA1, R1, Z1, THETA2, R2, Z2)

1 180 1.8 0 0 1.8 1.0
2 180 1.8 2.0 0 1.8 3.0
3 180 1.8 4.0 0 1.8 60.

NULL POTENTIAL (cannot lie outside formation...)

180 1.8 1000 0 4 1000

Azimuthal mesh -- if only one value given then its axisymmetric

0

Surface Impedances on current electrodes

```
1 3.e-2
2 3.e-2
3 3.e-3
```

Precision -- double precision required on the VAX

```
2
```

REFINE -- refines only the RHO/Z mesh, not in THETA.

```
4
```

GAUSS/CG

```
0 1.E-10
```

Window: Cuts beyond this radius are NOT added to the mesh

```
50.0
```

qzone - exterior to 50000 use resistivity 0.1

#Inside qzone=4.0 use a quasi-uniform mesh

```
4.0 50000 0.1
```

For this problem, the ALAT3D code converged in 75 iterations per excitation using point ILU preconditioning. If we solved the same problem but assuming a 5 degree wedge instead of azimuthal symmetry, then the number of iterations did not change *provided* we chose lexicographic ordering with the ϕ variables first. If we numbered the ρ, z plane first, the number of iterations for this problem was greater than 10,000. For coarse meshes, the convergence rate for the azimuthally symmetric problem was essentially the same as for the 5-degree wedge regardless of which lexicographic ordering was chosen, however. It is only for fairly fine meshes that node ordering dominates the iteration count. Note that listing the ϕ nodes first also minimizes the bandwidth but as we are using sparse storage schemes this is not really pertinent.

For the azimuthally symmetric problem, if the contact impedance is set to 10^{-6} on each electrode, the iteration count did not change, indicating that the ILU preconditioning was able to handle contrasts of 10^6 on electrode surfaces. The transfer impedance matrix was

$$(4.56) \quad Z = \begin{pmatrix} 93.0388 & 92.7111 & 92.4447 \\ 92.7111 & 92.8175 & 93.4447 \\ 92.4447 & 93.4447 & 93.4447 \end{pmatrix}$$

confirming that contact impedance has the greatest effect on the smallest electrodes.

CWNLAT input file for 5-electrode configuration and infinite resistivity formation. Current sources, H_ϕ formulation. Result given in equation (4.42)

#CWNLAT input for azimuthal test #2.

#5 electrodes with non-zero contact impedance

Quiet

5

###

Tool description - 5 electrodes on sonde, symmetry across Z=0

###

electrodes

1	1.8	0.0	1.8	1.0
2	1.8	2.0	1.8	3.0
3	1.8	4.0	1.8	5.0
4	1.8	6.0	1.8	7.0
5	1.8	8.0	1.8	60.0
6	1.8	1000	3.0	1000
7	3.0	1000	4.0	1000

known current - CWNLAT will loop over missing sections

(0.,0.)	1.8	0.00	1000	0
(0.,0.)	4.0	0	4.0	1000

scont

(1.e-5,0.)	1
(3.e-2,0.)	2
(3.e-3,0.)	3
(1.e-5,0.)	4
(3.e-3,0.)	5

###

Formation description

###

blocks of constant resistivity [rmin,zmin,rmax,zmax]

#borehole

1 1.8 0. 4.0 1000.

#rock is assumed infinitely resistive

list of resistivities [RES, MU, EPS]

```
1 0.1 1. 1.
2 100 1. 1.
```

###

Mesh

###

Z

#ZSONDE -- tool coordinates DO need to be here!

0 0.1 0.5 0.9 1.0 1.5 2.0 2.1 2.5 2.9 3.0 3.5 4.0 4.1

4.5 4.9 5.0 5.1 5.5 5.9

6.0 6.1 6.5 6.9 7.0 7.1 7.5 7.9

8.0 8.1 8.5 9.0 10.0 11.0 15.0 20 25

30 35 40 44 48 52 56 58 59 59.9

60 61 62 66 70 75 80 90 100 150 200 300 400 550 750 900 950

990 999 1000

RHO values

1.8 1.82 1.84 1.86 1.92 1.96 2.1 2.2 2.3 2.4 2.6 2.8 3.0

3.3 3.6 3.8 4.0

Mesh -- i.e., refine the mesh by this factor

6

###

Miscellaneous

###

potential reference

3.0 1000.

ueps (convergence criterion for conjugate gradient)

1.e-9

output

0 t2.cwn_dat

ALAT3D input file for 5-electrode configuration and infinitely resistive formation. Current source excitation, Φ formulation.

#ALAT3D input file for 5 electrode tool

MODULEF meshes and ALAT3D output

t2.mod

t2.sd

t2.dip_dat

LIST OF MATERIALS (#, RES, INVRES each on a separate line)

Region ONE is ALWAYS the borehole fluid

1 0.1 0.1

2 100. 100.

BOREHOLETOOL (Bx,By,Tool,Ecc). Restrictions: Ecc=0 and Bx = By

4.0 4.0 1.8

DOMAINS (x1,z1,x2,z2) - borehole value takes priority

2 -5000 0 5000 5000

INVASION (either 1 or 2 radii with an optional 3rd parameter)

10. 10.

Z -- tool coordinates are NOT added to this list.

#ZSONDE -- tool coordinates DO need to be here!

0 0.1 0.5 0.9 1.0 1.5 2.0 2.1 2.5 2.9 3.0 3.5 4.0 4.1

4.5 4.9 5.0 5.1 5.5 5.9 6.0 6.1 6.5 6.9 7.0 7.1 7.5 7.9

8.0 8.1 8.5 9.0 10.0 11.0 15.0 20 25 30 35 40 44 48 52 56 58 59

59.9 60 61 62 66 70 75 80 90 100 150 200 300 400 550 750 900

950 990 999 1000

X/RHO values -- there are no elements beyond RHO=4.0

1.8 1.82 1.84 1.86 1.92 1.96 2.1 2.2 2.3 2.4 2.6 2.8 3.0

3.3 3.6 3.8 4.0

ELECTRODES (REF, THETA1, R1, Z1, THETA2, R2, Z2)

1 180 1.8 0 0 1.8 1.0

2 180 1.8 2.0 0 1.8 3.0

3 180 1.8 4.0 0 1.8 5.0

```

4 180    1.8  6.0   0  1.8 7.0
5 180    1.8  8.0   0  1.8 60.

```

```

NULL POTENTIAL (cannot lie outside formation...)
180 1.8 1000   0 4 1000

```

```

Azimuthal mesh -- if only one value given then its axisymmetric
0

```

```

Surface Impedances
#current electrodes
1 1.e-5
2 3.e-2
3 3.e-3
4 1.e-5
5 3.e-3

```

```

Precision -- double precision required on the VAX
2
REFINE -- refines only the RHO/Z mesh, not in THETA.
4
GAUSS/CG
0 1.E-10

```

```

Window: Cuts beyond this radius are NOT added to the mesh
50.0

```

```

qzone - exterior to 50000 use resistivity 0.1
#Inside qzone=4.0 use a quasi-uniform mesh
4.0 50000 0.1

```

In fact, the above input files can be improved by noting that two of the electrodes do not emit current. They can be replaced by the keyword "COURT-CIRCUIT" or "CONNECTIONS" in ALAT3D. (ALAT3D only looks at the first letter of each keyword!) Also the upper *E*3 and *E*5 electrodes are always held at the same potential so we can give them the *same* reference number. The resulting computation is 60% faster.

ALAT3D input file for 5-electrode configuration and infinitely resistive formation using 'connections.' Current source excitation, Φ formulation.

#ALAT3D input file for 5 electrode tool (+CONNECT)

MODULEF meshes and ALAT3D output

t3.mod

t3.sd

t3.dip_dat

LIST OF MATERIALS (#, RES, INVRES each on a separate line)

Region ONE is ALWAYS the borehole fluid

1 0.1 0.1

2 100. 100.

BOREHOLETOOL (Bx,By,Tool,Ecc). Restrictions: Ecc=0 and Bx = By

4.0 4.0 1.8

DOMAINS (x1,z1,x2,z2) - borehole value takes priority

2 -5000 0 5000 5000

INVASION (either 1 or 2 radii with an optional 3rd parameter)

10. 10.

Z -- tool coordinates are NOT added to this list.

#ZSONDE -- tool coordinates DO need to be here!

0 0.1 0.5 0.9 1.0 1.5 2.0 2.1 2.5 2.9 3.0 3.5 4.0 4.1

4.5 4.9 5.0 5.1 5.5 5.9 6.0 6.1 6.5 6.9 7.0 7.1 7.5 7.9

8.0 8.1 8.5 9.0 10.0 11.0 15.0 20 25 30 35 40 44 48 52 56 58 59

59.9 60 61 62 66 70 75 80 90 100 150 200 300 400 550 750 900

950 990 999 1000

X/RHO values

1.8 1.82 1.84 1.86 1.92 1.96 2.1 2.2 2.3 2.4 2.6 2.8 3.0

3.3 3.6 3.8 4.0

ELECTRODES (REF, THETA1, R1, Z1, THETA2, R2, Z2)

1 180 1.8 2.0 0 1.8 3.0

2 180 1.8 4.0 0 1.8 5.0

2 180 1.8 8.0 0 1.8 60.

Connect -- i.e., set the net electrode current to zero.

```
3 180    1.8  0      0  1.8 1.0
4 180    1.8  6.0    0  1.8 7.0
```

NULL POTENTIAL

```
180 1.8 1000    0 1000 1000
```

Azimuthal mesh

```
0
```

Surface Impedances

```
4 1.e-5
1 3.e-2
2 3.e-3
3 1.e-5
```

Precision -- double precision recommended on the VAX

```
2
```

REFINE -- refines only the RHO/Z mesh, not in THETA.

```
2
```

GAUSS/CG

```
0 1.E-10
```

Window: Cuts beyond this radius are NOT added to the mesh

```
50.0
```

qzone - exterior to 50000 use resistivity 0.1

```
50.0 50000 0.1
```

The resulting transfer impedance matrix will necessary have 'blanks' in it for the lines corresponding to current excitation from the short-circuits. These 'blanks' are flagged as "-99999.99" by ALAT3D. For the above input file, we obtained the transfer impedance matrix

$$(4.57) \quad \begin{pmatrix} 97.26731 & 92.56338 & 93.04290 & 92.74260 \\ 92.56338 & 92.56338 & 92.56338 & 92.56338 \\ 93.04290 & 92.56338 & -99999.99 & -99999.99 \\ 92.74260 & 92.56338 & -99999.99 & -99999.99 \end{pmatrix}.$$

References

- [1] Chaba, A., *Os efeitos Delaware e Groningen: Um estudo quantitativo por elementos finitos*, Master's thesis, Universidade Federal do Pará, Belém, Brazil, 1993.
- [2] Gounot, M.-T., *The SKYLINE finite element code*, 1983. Personal communication.
- [3] Lorenz, W. J. and F. Mansfield, "Determination of corrosion rates by electrochemical DC and AC methods", *Corrosion Science*, **21**, no. 9, 1981, pp. 647-672.
- [4] Lovell, J. R., *Modelling frequency effects on Laterologs*, tech. rep., Schlumberger-Doll Research, Ridgefield, CT, 1990. Report EMG-90-34.
- [5] Macdonald, D. D., "Theoretical analysis of electrochemical impedance", in *Corrosion 87*, NACE, Houston, TX, 1987. Paper 479.
- [6] Perronet, A., *The club MODULEF: a library of subroutines for finite element analysis*, in *Computing Methods in Applied Sciences and Engineering*, vol. 704 of *Lecture Notes in Mathematics*, Springer-Verlag, Berlin, 1979, pp. 127-153.
- [7] Zemansky, P., "Finite element modelling results", *Schlumberger Technical Review*, **29**, no. 1, 1981, pp. 31-32.

Hierarchical Formulations and 3D Mesh Discretization

Abstract.

The ALAT3D finite element code has been developed to solve for resistivity tools operating at (or near) DC in complicated three-dimensional formations. The basis functions used are conformal with bed boundaries regardless of the deviation of the borehole. In particular, ALAT3D is appropriate for solving for modelling TM resistivity tools in horizontal wells. To avoid mesh distortion at high dip angles, the basis functions used are a direct sum of R1 elements on a quasi-uniform mesh of pentahedra combined with additional tetrahedral patches which overlay the bed boundaries. To construct these patches requires a recursive algorithm to subdivide pentahedra or hexahedra into tetrahedra in such a way that the tetrahedra are aligned against the bed boundaries. To ensure continuity of the potential field, the tetrahedral basis functions are required to be zero on the boundary of each patch. The resulting formulation is akin to that of a domain decomposition solver with two domains: a uniform mesh of pentahedra and the tetrahedral mesh of patches. The solution method uses approximate solvers on the two subdomains which are combined as preconditioners to a conjugate gradient algorithm over the whole domains. The approximate solvers which are currently implemented in ALAT3D are based on incomplete LU factorization but more sophisticated hierarchical and multilevel techniques could also be implemented.

5.1 Introduction

In the previous chapters, we have mostly concentrated on azimuthally symmetric formulations. For many important applications, however, a full 3D geometry is required. Finite element solutions to the full 3D vector Maxwell equations such as [3] are very slow. For low frequency tools, it is often preferable to solve an approximate 3D scalar problem. For TM excitation, the appropriate formulation is Laplace's equation $\nabla \cdot \sigma \nabla \Phi = 0$ where Φ is the electric scalar potential satisfying $\mathbf{E} = -\nabla \Phi$. 3D finite element equations for Φ were presented in earlier chapters. In this chapter, we shall concentrate on the choice of interpolation spaces and corresponding meshes.

A natural meshing strategy for 3D borehole resistivity problems is to construct a mesh in ρ, z and then rotate that mesh in ϕ . If the ρ, z mesh consists of triangles then the 3D mesh will consist of triangular prisms, rectangles in ρ, z become hexahedra in 3D. We refer to such discretizations as product formulations and they have many advantages normally associated with finite difference codes such as vectorization, amenability to structured matrix inversion techniques and a modularity that lends itself to simple coding.

Having decided upon a mesh strategy, one must consider local interpolation strategies. There are two 'natural' formulae: the first is linear in the cylindrical coordinate system and the second is linear in the Cartesian system. Essentially, the former corresponds to elements which are conformal with the cylindrical geometry of the tool and borehole, the latter implies a polygonal approximation. In section 5.2 we compare these two approaches as they apply to laterolog modelling in heterogeneous media.

The resulting stiffness matrix can be inverted to solve for potential distributions and the resulting procedure is useful for modelling modern imaging tools such as the azimuthal resistivity imager, ARI[†], provided the tool is centred. In section 5.3 we show how small changes to the formalism allow for eccentricity and give some examples. Even allowing for eccentricity, however, the meshes will not, in general, be conformal to bed boundaries and fractures because these, presumably, will have some deviation relative to the borehole. Indeed, a major modelling issue for the azimuthal laterolog is to predict the response of the tool in horizontal or highly deviated wells. In section 5.4 we show how to use hierarchical techniques to create interpolation spaces whose basis functions can be conformal to arbitrary bed boundaries without significantly departing from the product structure built in the first section. This requires an understanding of how to decompose of a mesh of pentahedra into tetrahedra and the details of this are given in section 5.5.

In section 5.6 we show how the same hierarchical formulation can also be applied to modelling the response of the resistivity tools crossing inclined fluid-filled fractures.

5.2 Tensor product discretization

We consider finite element solutions to the problem of non-axisymmetric 3D sources in a 2D axisymmetric formation, such as found when solving for the ARI[†] centred within a non-deviated borehole. Although the source excitation is complicated, the formation takes on a simple Cartesian product form where by the 'product' of two geometric domains Ω_1 and Ω_2 , written $\Omega_1 \times \Omega_2$, we mean the set of pairs (x_1, x_2) with x_i in their respective domains.

[†]Mark of Schlumberger

For a simple example, a solid cylinder is the product of a circular disk (the cross section) with an interval $[z_1, z_2]$ (the cylinder axis). Given triangulations \mathcal{T}_i on Ω_i there is a natural triangulation on $\Omega_1 \times \Omega_2$ with elements $T_1 \times T_2$ for $T_i \in \mathcal{T}_i$. For example, if \mathcal{T}_1 consists of triangles covering the ρ, z plane $\rho \geq a$, and \mathcal{T}_2 consists of line segments along the ϕ axis, then $\mathcal{T}_1 \times \mathcal{T}_2$ is a mesh of pentahedral prisms aligned with the axis of symmetry. In this section, we compare and contrast finite element formulations based on this product mesh and on the corresponding tensor product of interpolation spaces.

Recall from Chapter 1 that the tensor product of two vector spaces V and W with bases v_1, \dots, v_n and w_1, \dots, w_m is the nm dimensional space $V \otimes W$ with basis vectors $v_i \otimes w_j$ where some appropriate physical definition is given to $v_i \otimes w_j$. $V \otimes W$ has the mathematical property that any bilinear function defined on $V \times W$ decomposes as the composition of the map $(v, w) \mapsto v \otimes w$ followed by a linear map from $V \otimes W$ to \mathbb{R} . We shall see that if V and W are approximation spaces based on triangulations \mathcal{T}_1 on Ω_1 and \mathcal{T}_2 on Ω_2 , respectively, then $V \otimes W$ is the natural approximation space for the product space $\Omega_1 \times \Omega_2$.

5.2.1 Isoparametric elements

Given an azimuthally symmetric domain meshed with pentahedral elements, it is appropriate to consider Laplace's equation in cylindrical coordinates. The potential field Φ satisfies

$$(5.1) \quad \frac{1}{\rho^2} \frac{\partial}{\partial \phi} \sigma \frac{\partial \Phi}{\partial \phi} + \frac{1}{\rho} \frac{\partial}{\partial \rho} \sigma \rho \frac{\partial \Phi}{\partial \rho} + \frac{\partial}{\partial z} \sigma \frac{\partial \Phi}{\partial z} = 0,$$

where σ is the conductivity in the (bounded, polygonal) domain Ω under consideration. We suppose that σ is piecewise constant so that $\Phi \in H^1(\Omega)$, i.e., Φ lies in the space of functions whose gradient has finite L^2 energy. We interpret equation (5.1) in the weak (or distributional) sense:

$$(5.2) \quad \int_{\Omega} d\phi d\rho dz \Psi \left[\frac{\partial}{\partial \phi} \sigma \frac{\partial \Phi}{\partial \phi} + \frac{\partial}{\partial \rho} \sigma \rho \frac{\partial \Phi}{\partial \rho} + \frac{\partial}{\partial z} \sigma \frac{\partial \Phi}{\partial z} \right] = 0,$$

for all $\Psi \in H_0^1(\Omega)$. We suppose that Φ is held at zero potential over part of the boundary $\partial\Omega_0$ and write $H_0^1(\Omega)$ for the space of functions in $H^1(\Omega)$ which vanish on $\partial\Omega_0$, so that Φ and Ψ are both in $H_0^1(\Omega)$. We suppose the remainder of the domain to be covered in insulating sections surrounding N electrodes Γ_k across which current can flow. The boundary condition on the insulating sections is $\partial\Phi/\partial\nu = 0$ where ν is the outward pointing normal. The boundary condition on Γ_k is

$$(5.3) \quad \sigma \frac{\partial \Phi}{\partial \nu} = \frac{V_k - \Phi}{Z_c},$$

where Z_c is the electrode contact impedance and V_k the applied voltage. We also interpret these boundary conditions in the weak sense, so that for all Ψ in $H_0^1(\Omega)$

$$(5.4) \quad \int_{\partial\Omega} \sigma \Psi \frac{\partial \Phi}{\partial \nu} = \sum_{k=1}^N \int_{\Gamma_k} \Psi \frac{V_k - \Phi}{Z_c}.$$

We will assume all of the electrodes to lie on a cylindrical mandrel of radius $\rho = a$ and to be composed of 'square' patches $\phi \in [\phi_{k_1}, \phi_{k_2}]$, $z \in [z_{k_1}, z_{k_2}]$. So that equation (5.4) can also be written

$$(5.5) \quad \int_{\partial\Omega} \sigma \Psi \frac{\partial \Phi}{\partial \nu} = \sum_{k=1}^N \int_{\phi_{k_1}}^{\phi_{k_2}} a d\phi \int_{z_{k_1}}^{z_{k_2}} dz \Psi \frac{V_k - \Phi}{Z_c},$$

and for notational convenience we assume Z_c to be the same for each electrode. If we apply integration by parts to equation (5.2) and substitute equation (5.4) we obtain

$$(5.6) \quad \int_{\Omega} d\phi d\rho dz \sigma \rho \left[\frac{1}{\rho^2} \frac{\partial \Psi}{\partial \phi} \frac{\partial \Phi}{\partial \phi} + \frac{\partial \Psi}{\partial \rho} \frac{\partial \Phi}{\partial \rho} + \frac{\partial \Psi}{\partial z} \frac{\partial \Phi}{\partial z} \right] = \sum_{k=1}^N \int_{\Gamma_k} \Psi \frac{V_k - \Phi}{Z_c} \quad \forall \Psi \in H_0^1(\Omega).$$

Given a triangular mesh in the ρ, z domain with nodes (ρ_i, z_i) , $i = 1, \dots, N$ and a sequence of azimuthal nodes ϕ_j , $j = 1, \dots, M$, we discretize equation (5.6) by projecting Φ (and Ψ) onto the space $V_h^\phi \otimes V_h^{\rho z}$ generated by basis functions

$$(5.7) \quad B_{ij}(\phi, \rho, z) = B_j^\phi(\phi) B_i^{\rho z}(\rho, z),$$

where we exclude basis functions which are nonzero on $\partial\Omega_0$. Here

$$(5.8) \quad B_j^\phi(\phi) = \begin{cases} \frac{\phi - \phi_{j-1}}{\phi_j - \phi_{j-1}} & \phi \in [\phi_{j-1}, \phi_j], \\ \frac{\phi_{j+1} - \phi}{\phi_{j+1} - \phi_j} & \phi \in [\phi_j, \phi_{j+1}], \\ 0 & \text{otherwise.} \end{cases}$$

are the basis functions for the space V_h^ϕ and the $B_i^{\rho z}$ span the space $V_h^{\rho z}$ where $B_i^{\rho z}(\rho, z)$ are the piecewise linear functions introduced in Chapter 2: If a triangle Δ_I has node numbers n_r ,

$r = 1, 2, 3$ and coordinates (ρ_r, z_r) then within Δ_I

$$(5.9a) \quad B_{n_1}^{\rho z}(\rho, z) = \frac{(z_2 - z_3)(\rho - \rho_3) - (\rho_2 - \rho_3)(z - z_3)}{(z_2 - z_3)(\rho_1 - \rho_3) - (\rho_2 - \rho_3)(z_1 - z_3)},$$

$$(5.9b) \quad B_{n_2}^{\rho z}(\rho, z) = \frac{(z_3 - z_1)(\rho - \rho_1) - (\rho_3 - \rho_1)(z - z_1)}{(z_3 - z_1)(\rho_2 - \rho_1) - (\rho_3 - \rho_1)(z_2 - z_1)},$$

$$(5.9c) \quad B_{n_3}^{\rho z}(\rho, z) = \frac{(z_1 - z_2)(\rho - \rho_2) - (\rho_1 - \rho_2)(z - z_2)}{(z_1 - z_2)(\rho_3 - \rho_2) - (\rho_1 - \rho_2)(z_3 - z_2)}.$$

If the B_j^ϕ span the vector space V_h^ϕ and the $B_i^{\rho z}$ span the space $V_h^{\rho z}$ then the B_{ij} span the space $V_h^\phi \otimes V_h^{\rho z}$. If we write

$$(5.10) \quad \Phi(\phi, \rho, z) = \sum_{pq} \Phi_{pq} B_{pq}(\phi, \rho, z) \quad \text{and} \quad \Psi(\phi, \rho, z) = B_{ij}(\phi, \rho, z),$$

then equation (5.6) takes the form of the discrete system of equations

$$(5.11) \quad \sum_{pq} A_{ijpq} \Phi_{pq} = V_{ij} \quad \forall i, j$$

where

$$(5.12) \quad A_{ijpq} = \int_{\Omega} d\phi d\rho dz \sigma \rho \left[\frac{1}{\rho^2} \frac{\partial B_{pq}}{\partial \phi} \frac{\partial B_{ij}}{\partial \phi} + \frac{\partial B_{pq}}{\partial \rho} \frac{\partial B_{ij}}{\partial \rho} + \frac{\partial B_{pq}}{\partial z} \frac{\partial B_{ij}}{\partial z} \right] + \sum_{k=1}^N \int_{\Gamma_k} \frac{B_{pq} B_{ij}}{Z_c}$$

and

$$(5.13) \quad V_{ij} = \sum_{k=1}^N \int_{\Gamma_k} \frac{B_{ij} V_k}{Z_c}.$$

If we assume the triangular mesh to consist of elements Δ_I , $I = 1, \dots, N_\Delta$, then the 3D domain is composed of $(M - 1)N_\Delta$ pentahedra. The elements are curved with respect to the cylindrical coordinate system and are referred to as *isoparametric*, [31]. We suppose that σ (and Z_c) are constant within each pentahedron so that the integrals of equation (5.12) (and (5.13)) can be evaluated by summing the contributions from individual pentahedra:

$$(5.14) \quad \int_{\Omega} d\phi d\rho dz \sigma \rho \left[\frac{\partial B_{pq}}{\partial \rho} \frac{\partial B_{ij}}{\partial \rho} + \frac{\partial B_{pq}}{\partial z} \frac{\partial B_{ij}}{\partial z} \right] = \sum_{I=1, J=1}^{N_\Delta, M-1} \sigma_{IJ} M_{qj}^\phi \Big|_J A_{pi}^{\rho z} \Big|_I,$$

$$(5.15) \quad \int_{\Omega} d\phi d\rho dz \frac{\sigma}{\rho} \frac{\partial B_{pq}}{\partial \phi} \frac{\partial B_{ij}}{\partial \phi} = \sum_{I=1, J=1}^{N_{\Delta}, M-1} \sigma_{IJ} A_{qj}^{\phi} \Big|_J M_{pi}^{\rho z} \Big|_I,$$

and

$$(5.16) \quad \int_{\Gamma_k} a d\phi dz \frac{B_{pq} B_{ij}}{Z_c} = \sum_{I, J} \frac{a}{Z_c} M_{qj}^{\phi} \Big|_J M_{pi}^z \Big|_I,$$

where

$$(5.17) \quad M_{qj}^{\phi} \Big|_J = \int_{\phi_{J-1}}^{\phi_J} d\phi B_q^{\phi} B_j^{\phi},$$

$$(5.18) \quad A_{qj}^{\phi} \Big|_J = \int_{\phi_{J-1}}^{\phi_J} \frac{\partial B_q^{\phi}}{\partial \phi} \frac{\partial B_j^{\phi}}{\partial \phi},$$

are the local mass and stiffness matrices in ϕ and

$$(5.19) \quad M_{pi}^{\rho z} \Big|_I = \int_{\Delta_I} \frac{d\rho dz}{\rho} B_p^{\rho z} B_i^{\rho z},$$

$$(5.20) \quad A_{pi}^{\rho z} \Big|_I = \int_{\Delta_I} d\rho dz \rho \left[\frac{\partial B_p^{\rho z}}{\partial \rho} \frac{\partial B_i^{\rho z}}{\partial \rho} + \frac{\partial B_p^{\rho z}}{\partial z} \frac{\partial B_i^{\rho z}}{\partial z} \right],$$

$$(5.21) \quad M_{pi}^z \Big|_I = \int_{\Delta_I \cap \partial\Omega} dz B_p^{\rho z} B_i^{\rho z} = \int_{z_I}^{z_{I+1}} dz B_p^{\rho z} B_i^{\rho z}.$$

are the corresponding matrices in ρz . Note that we are assuming that those electrodes which are subject to contact impedance lie on a cylinder with constant ρ so we do not need a matrix $M_{pi}^{\rho} \Big|_I$.

As the basis functions are only non-zero over local domains, most of the above integrals are zero. For example if Δ_I has nodes $\{n_1, n_2, n_3\}$ then $A_{pi}^{\rho z} \Big|_I = 0$ if $\{p, i\} \not\subseteq \{n_1, n_2, n_3\}$ and $A_{pi}^{\rho z} \Big|_I$ thus constitutes a 3×3 local stiffness matrix $\hat{A}_{rs}^{\rho z} = A_{n_r n_s}^{\rho z} \Big|_I$ for $r, s = 1, 2, 3$. We also define the local mass matrix as $\hat{M}_{rs}^{\rho z} = M_{n_r n_s}^{\rho z} \Big|_I$. Similarly $M_{qj}^{\phi} \Big|_J$, $M_{pi}^z \Big|_J$ and $A_{qj}^{\phi} \Big|_J$ reduce to 2×2 local matrices \hat{A}^{ϕ} , \hat{M}^{ϕ} and \hat{M}^z .

Explicitly, we find that

(5.22)

$$\hat{M}^z = \Delta z \begin{pmatrix} 1/3 & 1/6 \\ 1/6 & 1/3 \end{pmatrix},$$

(5.23)

$$\hat{A}^\phi = \frac{1}{\Delta\phi} \begin{pmatrix} 1 \\ -1 \end{pmatrix} (1 \quad -1),$$

(5.24)

$$\begin{aligned} \hat{A}^{\rho z} = \frac{\bar{\rho}}{4\Delta} \left[\begin{pmatrix} z_2 - z_3 \\ z_3 - z_1 \\ z_1 - z_2 \end{pmatrix} (z_2 - z_3 \quad z_3 - z_1 \quad z_1 - z_2) \right. \\ \left. + \begin{pmatrix} \rho_2 - \rho_3 \\ \rho_3 - \rho_1 \\ \rho_1 - \rho_2 \end{pmatrix} (\rho_2 - \rho_3 \quad \rho_3 - \rho_1 \quad \rho_1 - \rho_2) \right], \end{aligned}$$

(5.25)

$$\hat{M}^\phi = \Delta\phi \begin{pmatrix} 1/3 & 1/6 \\ 1/6 & 1/2 \end{pmatrix},$$

(5.26)

$$\hat{M}^{\rho z} \approx \frac{\Delta}{\bar{\rho}} \begin{pmatrix} 1/3 \\ 1/3 \\ 1/3 \end{pmatrix} (1/3 \quad 1/3 \quad 1/3),$$

where Δ is the area of Δ_I , $\bar{\rho} = (\rho_1 + \rho_2 + \rho_3)/3$, $\Delta\phi = \phi_{J+1} - \phi_J$, $\Delta z = z_{I+1} - z_I$ and $\hat{M}^{\rho z}$ has been evaluated numerically by assuming one Gauss point at the barycentre of Δ_I . Symbolically, the 3D stiffness matrix has been decomposed as $\hat{M}^\phi \otimes \hat{A}^{\rho z} + \hat{A}^\phi \otimes \hat{M}^{\rho z}$.

The derivation of equations (5.24) and (5.26) is standard (e.g., [25]) but is repeated here for the reader's convenience. As we are dealing with just one triangle, we can write B_r instead of $B_{n_r}^{\rho z}$ and we see from (5.9) that the B_r are actually the composition of two functions $F_I^{-1} : \Delta_I \rightarrow \hat{\Delta}$ followed by $\hat{B}_r : \hat{\Delta} \rightarrow \mathbb{R}$ where $\hat{\Delta}$ is the 'standard triangle' $\{(\hat{x}, \hat{y}) : 0 \leq \hat{x} \leq 1 - \hat{y}, 0 \leq \hat{y} \leq 1\}$,

$$(5.27) \quad \hat{B}_1(\hat{x}, \hat{y}) = 1 - \hat{x} - \hat{y}, \quad \hat{B}_2(\hat{x}, \hat{y}) = \hat{x}, \quad \hat{B}_3(\hat{x}, \hat{y}) = \hat{y},$$

and $F_I : \hat{\Delta} \rightarrow \Delta_I$ is the affine map

$$(5.28) \quad \begin{pmatrix} \rho \\ z \end{pmatrix} = F_I(\hat{x}, \hat{y}) = \sum_{r=1}^3 \begin{pmatrix} \rho_r \\ z_r \end{pmatrix} \hat{B}_r(\hat{x}, \hat{y}).$$

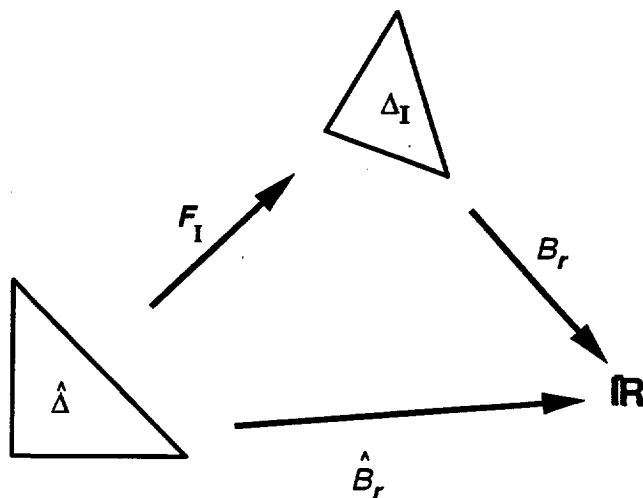


Figure 5.1: Linear functions on Δ_I are the composition of F_I^{-1} with the map \hat{B}_r .

The configuration is shown in Figure 5.1. F_I and \hat{B}_r are P1 affine maps. The \hat{B}_r are also termed barycentric coordinates and constitute the local basis functions relative to the (\hat{x}, \hat{y}) coordinates.

The integrals over Δ_I are transformed to integrals over $\hat{\Delta}$ according to the usual formula

$$(5.29) \quad \hat{A}_{rs}^{\rho z} = \int_{\Delta_I} d\rho dz \nabla B_r \cdot \nabla B_s = \int_{\hat{\Delta}} d\hat{x} d\hat{y} |DF_I| \nabla B_r \cdot \nabla B_s$$

where the Jacobian $|DF_I|$ is the determinant of

$$(5.30) \quad DF_I = \begin{pmatrix} \rho_2 - \rho_1 & \rho_3 - \rho_1 \\ z_2 - z_1 & z_3 - z_1 \end{pmatrix},$$

and $DB = (\nabla B_1, \nabla B_2, \nabla B_3)^t$ is obtained from the chain rule

$$(5.31) \quad DB(\rho, z) = D\hat{B} DF_{\hat{\Delta}}^{-1} = \begin{pmatrix} -1 & -1 \\ 1 & 0 \\ 0 & 1 \end{pmatrix} \begin{pmatrix} \rho_2 - \rho_1 & \rho_3 - \rho_1 \\ z_2 - z_1 & z_3 - z_1 \end{pmatrix}^{-1}$$

$$(5.32) \quad = \frac{1}{2\Delta} \begin{pmatrix} -1 & -1 \\ 1 & 0 \\ 0 & 1 \end{pmatrix} \begin{pmatrix} z_3 - z_1 & \rho_1 - \rho_3 \\ z_1 - z_2 & \rho_2 - \rho_1 \end{pmatrix}.$$

Noting that DB is constant across $\hat{\Delta}$ we can remove $DB^t DB$ from the integral to obtain

(5.33)

$$\hat{A}^{\rho z} = 2\Delta DB^t DB \int_{\hat{\Delta}} \rho d\hat{x} d\hat{y}$$

(5.34)

$$= 2\Delta DB^t DB \int_0^1 dy \int_0^{1-y} [\rho_1 + (\rho_2 - \rho_1)x + (\rho_3 - \rho_1)y]$$

(5.35)

$$= 2\Delta DB^t DB \left[\frac{\rho_1}{2} + \frac{\rho_2 - \rho_1}{6} + \frac{\rho_3 - \rho_1}{6} \right],$$

which is equation (5.24).

Equation (5.26) follows in the same way by first transforming the domain of integration in (5.19) to $\hat{\Delta}$

$$(5.36) \quad \hat{M}^{\rho z} = 2\Delta \int_0^1 d\hat{y} \int_0^{1-\hat{y}} d\hat{x} \frac{1}{\rho_1 + (\rho_2 - \rho_1)\hat{x} + (\rho_3 - \rho_1)\hat{y}} \\ (1 - \hat{x} - \hat{y} \quad \hat{x} \quad \hat{y})^t (1 - \hat{x} - \hat{y} \quad \hat{x} \quad \hat{y}),$$

but then rather than pursue a tedious analytic formula, we use Gaussian quadrature with weights w_p and stations (x_p, y_p)

$$(5.37) \quad \hat{M}^{\rho z} = 2\Delta \sum_p w_p \frac{1}{\rho_1 + (\rho_2 - \rho_1)x_p + (\rho_3 - \rho_1)y_p} \\ (1 - x_p - y_p \quad x_p \quad y_p)^t (1 - x_p - y_p \quad x_p \quad y_p).$$

Tables of Gaussian quadratures for the triangle are listed in [26] and for equation (5.26) we took the simplest, namely $x_p = y_p = 1/3$, $w_p = 1/2$. [25] shows that the numerical error caused by evaluating the mass matrix $\hat{M}^{\rho z}$ with only one Gauss point will not cause a degradation in the accuracy of Φ_{pq} (analogous to 'mass lumping' in time-domain modelling).

5.2.2 Cartesian elements

An alternative approach is to *not* take into account the cylindrical geometry but to think of the pentahedra as having straight edges, essentially replacing the cylindrical borehole and mandrel with a polygonal one. Each element, Π , whose triangular faces have Cartesian coordinates (x_r, y_r, z_r) and $(x_{r+3}, y_{r+3}, z_{r+3})$, $r = 1, 2, 3$, is the image of the function $F_{\Pi} : \hat{\Pi} \rightarrow \Pi$,

$$(5.38) \quad F_{\Pi}(\hat{x}, \hat{y}, \hat{z}) = \sum_{r=1}^3 \begin{pmatrix} (1 - \hat{z})x_r + \hat{z}x_{r+3} \\ (1 - \hat{z})y_r + \hat{z}y_{r+3} \\ z_r \end{pmatrix} \hat{B}_r(\hat{x}, \hat{y}).$$

where $\hat{\Pi}$ is the 'standard pentahedron' $\hat{\Delta} \times [0, 1]$ and $\mathbf{x}_r = \rho_r \cos \phi_j$, $\mathbf{x}_{r+3} = \rho_r \cos \phi_{j+1}$, etc., defines the mapping from cylindrical to Cartesian coordinates. We refer to such non-isoparametric elements as Cartesian or *polygonal*. We define the local basis functions on the pentahedron as F_{Π}^{-1} composed with a R-linear map from the standard pentahedron. If we assume a node numbering n_{11}, n_{21}, n_{31} and n_{12}, n_{22}, n_{32} for the triangular faces of Π , then

(5.39)

$$\Phi(x, y, z)|_{\Pi} = \sum_{p=1, q=1}^{3,2} \Phi_{n_{pq}} B_{pq}(x, y, z) = \sum_{r=1}^3 [\Phi_{n_{r1}}(1 - \hat{z}) + \Phi_{n_{r2}} \hat{z}] \hat{B}_r(\hat{x}, \hat{y}),$$

where $F_{\Pi}(\hat{x}, \hat{y}, \hat{z}) = (x, y, z)$ and the \hat{B} were defined in equation (5.27). The global stiffness matrix can again be reduced to a sum over the pentahedra, in this case of 6×6 matrices

$$(5.40) \quad \hat{A}^{xyz} = \int_{\Pi} dx dy dz \nabla B_{ij} \cdot \nabla B_{pq}$$

$$(5.41) \quad = \int_{\hat{\Pi}} d\hat{x} d\hat{y} d\hat{z} |DF_{\Pi}| DB^t DB,$$

where

$$(5.42) \quad DB = D\hat{B}DF_{\Pi}^{-1} \quad \text{and} \quad DF_{\Pi} = \left(\frac{\partial F_{\Pi}}{\partial \hat{x}}, \frac{\partial F_{\Pi}}{\partial \hat{y}}, \frac{\partial F_{\Pi}}{\partial \hat{z}} \right).$$

The resulting integrals are even more tedious to evaluate analytically than those of equation (5.36) because the Jacobian of F_{Π} is *not* constant

(5.43)

$$DF_{\Pi}(\hat{x}, \hat{y}, \hat{z}) = \begin{pmatrix} x_1 & x_2 & x_3 & x_4 & x_5 & x_6 \\ y_1 & y_2 & y_3 & y_4 & y_5 & y_6 \\ z_1 & z_2 & z_3 & z_1 & z_2 & z_3 \end{pmatrix} \begin{pmatrix} \hat{z} - 1 & \hat{z} - 1 & \hat{x} + \hat{y} - 1 \\ 1 - \hat{z} & 0 & -\hat{x} \\ 0 & 1 - \hat{z} & -\hat{y} \\ -\hat{z} & -\hat{z} & 1 - \hat{x} + \hat{y} \\ \hat{z} & 0 & \hat{x} \\ 0 & \hat{z} & \hat{y} \end{pmatrix},$$

and

$$(5.44) \quad DB = \begin{pmatrix} \hat{z} - 1 & \hat{z} - 1 & \hat{x} + \hat{y} - 1 \\ 1 - \hat{z} & 0 & -\hat{x} \\ 0 & 1 - \hat{z} & -\hat{y} \\ -\hat{z} & -\hat{z} & 1 - \hat{x} + \hat{y} \\ \hat{z} & 0 & \hat{x} \\ 0 & \hat{z} & \hat{y} \end{pmatrix} DF_{\Pi}^{-1}.$$

Instead we use Gaussian quadrature appropriate for the standard pentahedron. Tables of station points and weights are again available from [26]. In all of our calculations, we used a 21 point formula.¹ For small enough $\Delta\phi$, the difference between the isoparametric and polygonal formulations will be quite small and this has also been observed experimentally.

5.3 Eccentricity

In the previous section, we showed how the stiffness matrix for a centred tool could be built as a tensor product $A^\phi \otimes M^{\rho z} + M^\phi \otimes A^{\rho z}$ where, in some sense, the M matrices are the identity operators and the A matrices are the stiffness matrices in the component spaces. This formulation lends itself to isoparametric elements and we also showed how build directly a stiffness matrix using polygonal elements. Borehole and shoulder effects on centred tools are amenable to this formulation but effects on eccentric tools are not. In this section, we discuss eccentricity modelling.

Eccentricity modelling is important for azimuthally sensitive tools such as the Azimuthal Resistivity Imager, ARI[†], and the Resistivity at the Bit, RAB[†], used in LWD because eccentricity will put some of the measurement electrodes closer to the borehole wall than other electrodes, and hence induce a higher apparent resistivity. This could mask any true azimuthal variation in formation conductivity, [6], [20], [24]. For simple geometries, one can derive analytic solutions for the response of an eccentric tool: e.g., [12] solves for an eccentric point source in a borehole, [18] solves for an eccentric point source in a cylindrically layered medium, [19] solves for eccentric coils on an infinite mandrel in a cylindrically layered medium, and [11] solves for an eccentric sonde with finite-length sources in a formation with borehole. For more complicated configurations, we shall see that finite element methods are much simpler.

Indeed, for the polygonal approximation of the previous section, eccentricity is particularly straightforward to take into account. We assume an eccentricity ϵ along the x -axis such that the tool remains some finite distance away from the borehole wall. Let $\eta(\rho)$ be the linear function which is 1 at $\rho = a$ and 0 at $\rho = b$, where a is the mandrel radius and b the borehole wall. I.e., if $\rho = \sum_{r=1}^3 \rho_r \hat{B}_r(\hat{x}, \hat{y})$ then

$$(5.45) \quad \eta(\rho) = \frac{b - \rho}{b - a} = \frac{b}{b - a} - \frac{1}{b - a} \sum_{r=1}^3 \rho_r \hat{B}_r(\hat{x}, \hat{y}).$$

¹This computation is relatively slow. It would be faster if we could cast A^{xyz} as a tensor product.

[†]Mark of Schlumberger

Then the following function will map standard pentahedra onto a deformed mesh which is conformal with the eccentered (polygonal) mandrel.

(5.46)

$$F_{\Pi}^{\epsilon}(\hat{x}, \hat{y}, \hat{z}) = \sum_{r=1}^3 \begin{pmatrix} \rho_r [(1 - \hat{z}) \cos \phi_j + \hat{z} \cos \phi_{j+1}] \\ \rho_r [(1 - \hat{z}) \sin \phi_j + \hat{z} \sin \phi_{j+1}] \\ z_r \end{pmatrix} \hat{B}_r(\hat{x}, \hat{y}) + \begin{pmatrix} \epsilon \eta(\rho) \\ 0 \\ 0 \end{pmatrix},$$

In practice, we shall choose b to be one mesh radius less than the borehole radius so that the formation is always surrounded by an undeformed "collar" – this will prove convenient when we add fractures.

The only thing we have to watch out for is that the function F_{Π}^{ϵ} does not produce degenerate pentahedra. But if we consider a quadrilateral in the ρ, ϕ plane $\phi \in [\phi_1, \phi_2]$, $\rho \in [\rho_1, \rho_2]$ then because $a + \epsilon < b$ (otherwise the tool is touching the borehole) $|\eta(\rho_2) - \eta(\rho_1)| < \rho_2 - \rho_1$. From this one can deduce that there cannot exist α and β such that simultaneously $\rho_1 \sin(\alpha) = \rho_2 \sin(\beta)$ and $\rho_1 \cos(\alpha) + \eta(\rho_1) = \rho_2 \cos(\beta) + \eta(\rho_2)$, i.e., the image of the *isoparametric* quadrilateral under F_{Π}^{ϵ} is never degenerate. The proof is straightforward. If such an α and β exist, then we must be able to find a β such that

$$(5.47) \quad \rho_1 \cos \alpha + \eta_1 = \sqrt{\rho_1^2 - \rho_2^2 \sin^2 \beta} + \eta_1 = \rho_2 \cos \beta + \eta_2$$

so that

$$(5.48) \quad \rho_1^2 = \rho_2^2 + 2(\eta_2 - \eta_1)\rho_2 \cos \beta + (\eta_2 - \eta_1)^2$$

which implies that

$$(5.49) \quad \rho_1 \geq \rho_2 - |\eta_2 - \eta_1|$$

which contradicts our hypothesis on $\eta(\rho)$. For some non-linear choices of η , degenerate cases can be constructed, however.

Similarly, if the polygonal angles in the mesh are less than $\pi/2$ then the image of the straight-line quadrilateral is never degenerate. For example, if we consider the case of just one azimuthal node at $\pi/2$ then in Figure 5.2 we see that a degenerate element will be created if the line from X to the node on the tool to Y is convex. If the eccentricity is less than that ϵ_0 which corresponds to a straight line from X to Y then no degenerate elements will be created. If the line from X to Y is straight then we must have that $a = b - \epsilon_0$ so that $\epsilon_0 = b - a$, i.e., the eccentricity has pushed the tool to touch the borehole wall. For smaller eccentricities, even for a $\pi/2$ azimuthal separation the quadrilaterals will not be degenerate. Clearly, as the azimuthal

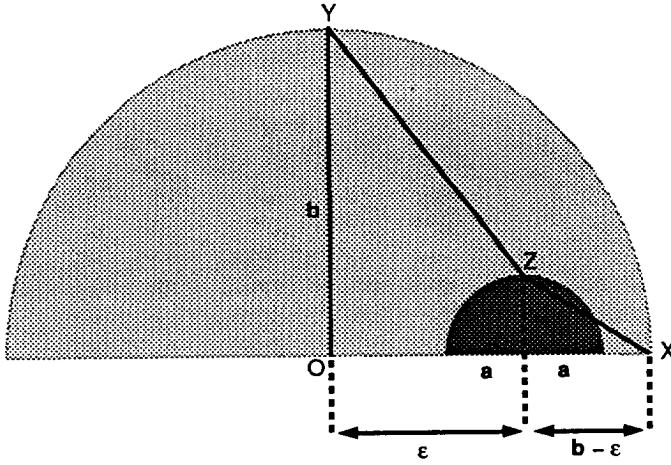


Figure 5.2: Eccentered tool with radius a in a borehole with radius b . An invalid mesh will be created if the node Z lies outside the triangle OXY , but this can only happen if $a \geq b - \epsilon$, i.e., if the tool is touching the borehole wall.

separation between the nodes decreases there is even less possibility for degeneracy. Thus for the Cartesian case, the only change in the code necessary is replacing DF_{Π} in (5.41) and (5.43) with DF_{Π}^{ϵ} . Essentially, in (5.43) we just add $\epsilon\eta(\rho)$ to the x_i . An alternative approach used by the SKYLINE finite element code, [13] is to subdivide each distorted pentahedron (and hence every pentahedron) into tetrahedra in which case analytic formulae can be used throughout the domain.

For the isoparametric elements, things are slightly more complicated because the Jacobian is no longer separable in terms of ϕ and ρ so the local stiffness matrices lose their tensor product structure, and in addition must be evaluated numerically. An explicit formula for F_{Π}^{ϵ} follows from equation (5.46)

$$(5.50) \quad F_{\Pi}^{\epsilon}(\hat{x}, \hat{y}, \hat{z}) = \sum_{r=1}^3 \begin{pmatrix} \rho_r \cos((1 - \hat{z})\phi_j + \hat{z}\phi_{j+1}) \\ \rho_r \sin((1 - \hat{z})\phi_j + \hat{z}\phi_{j+1}) \\ z_r \end{pmatrix} B_r(\hat{x}, \hat{y}) + \begin{pmatrix} \epsilon\eta(\rho) \\ 0 \\ 0 \end{pmatrix}$$

so that

$$(5.51) \quad \left. \frac{\partial F_{\Pi}^{\epsilon}}{\partial \hat{x}, \hat{y}} \right|_{(\hat{x}, \hat{y}, \hat{z})} = \sum_{r=1}^3 \begin{pmatrix} \rho_r [\cos((1 - \hat{z})\phi_j + \hat{z}\phi_{j+1}) - \epsilon/(b - a)] \\ \rho_r \sin((1 - \hat{z})\phi_j + \hat{z}\phi_{j+1}) \\ z_r \end{pmatrix} \left. \frac{\partial B_r}{\partial \hat{x}, \hat{y}} \right|_{(\hat{x}, \hat{y})},$$

and

$$(5.52) \quad \left. \frac{\partial F_{\Pi}^{\epsilon}}{\partial \hat{z}} \right|_{(\hat{x}, \hat{y}, \hat{z})} = \sum_{r=1}^3 \begin{pmatrix} -\rho_r \sin((1 - \hat{z})\phi_j + \hat{z}\phi_{j+1}) \\ \rho_r \cos((1 - \hat{z})\phi_j + \hat{z}\phi_{j+1}) \\ 1 \end{pmatrix} B_r(\hat{x}, \hat{y}).$$

We use the same 21 point Gaussian quadrature routine as for the Cartesian case.

5.4 Bed boundaries²

Given a pentahedral mesh, one can always arrive at a mesh which is conformal with an arbitrary inclined plane by suitably subdividing the pentahedra into tetrahedra. Such subdivisions are appropriate when solving for the tool response in a heterogeneous formation through which the borehole has been drilled at a non-perpendicular angle, [22]. Unfortunately, if one pentahedra is subdivided then all of its neighbours must also be subdivided and continuing this way we see that *all* the pentahedra in the mesh must be subdivided, regardless of the location of the interface. As tetrahedral decompositions tend to be less accurate than pentahedral this causes a degradation in accuracy. Moreover, the subdivision tends to introduce an orientation to the mesh which further degrades the accuracy. One approach, valid for dip angles less than, say, 45 degrees is to shear the mesh and not introduce new nodes. This is the approach taken by the SKYLINE finite element code and, in effect, is also the method we have chosen to model eccentricity. This method becomes increasingly unstable for high dip angles and will not give a valid mesh for horizontal bed boundaries parallel to the horizontal borehole.

The approach considered in this section is to subdivide pentahedra but to choose a non-standard interpolation scheme. Specifically, let $V_h^{\phi} \otimes V_h^{\rho z}$ denote the space of basis functions for the pentahedral mesh and let V_h^{Δ} denote the space of basis functions for the tetrahedral mesh which is conformal to all the dipping bed boundaries. Let W_h^{Δ} be the subspace of V_h^{Δ} containing only those nodes which are *not* also nodes of $V_h^{\phi} \otimes V_h^{\rho z}$. Then, by construction,

$$(5.53) \quad W_h^{\Delta} \cap V_h^{\phi} \otimes V_h^{\rho z} = 0$$

so that $W_h^{\Delta} \cup V_h^{\phi} \otimes V_h^{\rho z}$ is actually a direct sum $W_h^{\Delta} \oplus V_h^{\phi} \otimes V_h^{\rho z} = W_h^{\Delta} \oplus V_h^{\Pi}$, say. This is the basis set that we use for the finite element modelling. Clearly, the only pentahedra that need to be subdivided are those through which bed boundaries pass and in the absence of a bed

²Presented at [17].

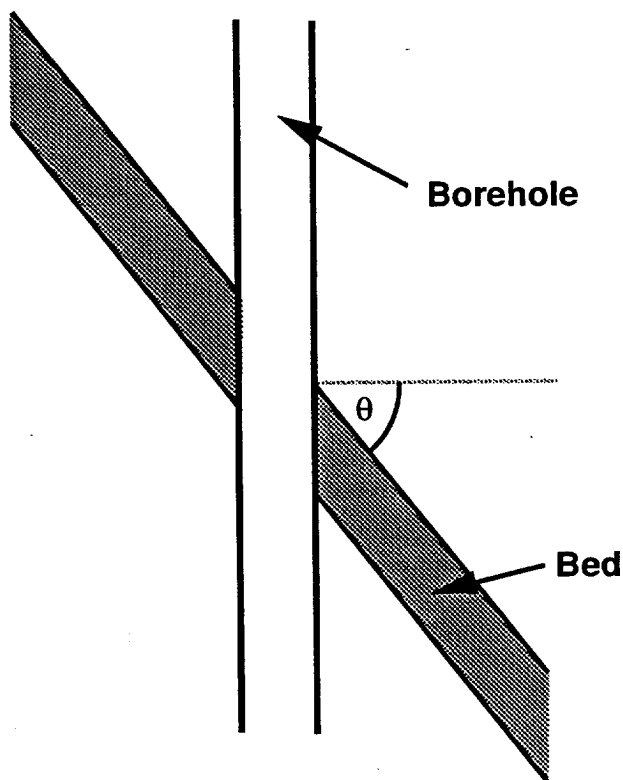


Figure 5.3: The dip angle θ of a bed is taken to be the relative angle to the horizontal plane, so that a dip angle of zero corresponds to an azimuthally symmetric geometry and a dip angle of 90 degrees corresponds to a horizontal borehole parallel to the layering.

boundary the finite element code retains its product structure. Suppose that the finite element matrix corresponding to this direct sum is written

$$(5.54) \quad \begin{pmatrix} A_{11} & A_{12} \\ A_{21} & A_{22} \end{pmatrix}$$

where A_{11} is the original stiffness matrix on the pentahedral mesh and A_{22} is a stiffness matrix for Laplace's equation on a 3D volume which surrounds the bed boundaries. The boundary conditions for the latter case being homogeneous Dirichlet conditions. $A_{21} = A_{12}^T$ represents the coupling term between the two vector space summands (although the basis functions split as a direct sum, the operator does *not*). We refer to the nodes of A_{22} as the overlay nodes and, assuming that bed boundaries do not intersect one another then A_{22} actually corresponds to the disjoint sum of 2D Poisson's equations along the bed boundary. The forcing term is the extent to which the original basis functions in V_h^Π fail to take into account the charge accumulation along the bed boundary. In particular, note that for many cases involving weak contrasts, the overlay solution will just cause a small perturbation to the solution on the pentahedral mesh.

We term this decomposition a *hierarchical formulation* because clearly $W_h^\Delta \subset W_h^\Delta \oplus V_h^\Pi$ and $V_h^\Pi \subset W_h^\Delta \oplus V_h^\Pi$. In general, any sequence of bases is called hierarchical if one basis set is a subset of the next. For a simple example consider the basis consisting of the two functions defined on $[0, 1]$ shown in the top of Figure 5.4. The lower half of Figure 5.4 shows two choices of basis for a vector space defined on a mesh V_h which is half the diameter of the original mesh. The upper set of basis functions is denoted B_{2h} . Figure 5.4a shows a non-hierarchical basis, whereas Figure 5.4b shows a hierarchical scheme. In the latter case, the basis vectors of B_{2h} are also basis vectors of B_h . Hierarchical bases in FEM offer many of the advantages found in nested dissection or substructuring and their use can also drastically improve the stiffness matrix condition number [30]. Such bases also offer intriguing connections with multigrid, [29], and with the (different) aggregation methods of Chatelin & Miranker [4], Chew [5], and Douglas [7]. There is also currently interest in the hierarchical properties of wavelet bases (e.g., [21]).

For this analogy in 1D, we can suppose that we have 'pentahedral' nodes at $x = 0$ and $x = 1$ and that we wish to discretize the problem $d/dx(\sigma du/dx) = 0$ where $\sigma = 1$ for $x < 1/2$ and $\sigma = \tau$ for $x > 1/2$. The basis functions are

$$(5.55) \quad B_1 = x \quad B_2 = 1 - x$$

and for a unique solution let's suppose that we have $u(0) = 1$ and $u(1) = 0$.

The local stiffness matrix for this 'element' is

$$(5.56) \quad \int_0^1 \sigma \frac{dB_i}{dx} \frac{dB_j}{dx} = \int_0^{1/2} \frac{dB_i}{dx} \frac{dB_j}{dx} + \tau \int_{1/2}^1 \frac{dB_i}{dx} \frac{dB_j}{dx}$$

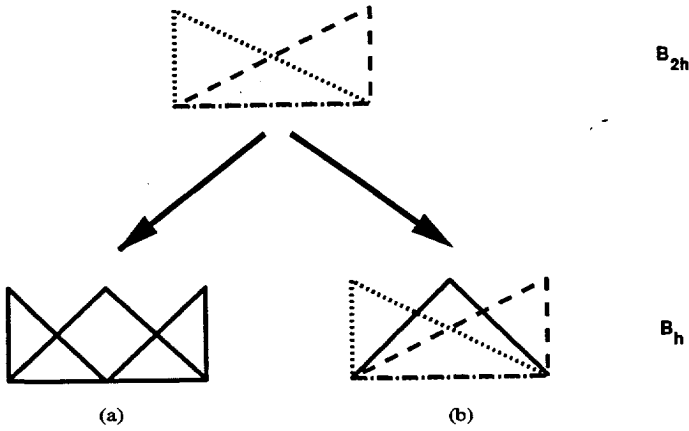


Figure 5.4: 2-level hierarchical bases on $[0, 1]$. In case (b), the two basis functions of B_{2h} are also basis functions of B_h .

$$(5.57) \quad = \frac{1}{2} \begin{pmatrix} 1 & -1 \\ -1 & 1 \end{pmatrix} + \tau \frac{1}{2} \begin{pmatrix} 1 & -1 \\ -1 & 1 \end{pmatrix}$$

and imposing the Dirichlet condition at $x = 0$ gives the matrix

$$(5.58) \quad \begin{pmatrix} 1 & 0 \\ 0 & 1 \end{pmatrix} \begin{pmatrix} u_1 \\ u_2 \end{pmatrix} = \begin{pmatrix} 1 \\ 0 \end{pmatrix},$$

with solution $u(x) = 1 - x$.

Now we add a 'tetrahedral' node at $x = 1/2$. It's basis function is

$$(5.59) \quad B_3(x) = \begin{cases} 2x & x \in [0, 1/2], \\ 2 - 2x & x \in [1/2, 1]. \end{cases}$$

We now obtain the stiffness matrix

$$(5.60) \quad \begin{pmatrix} (1+\tau)/2 & -(1+\tau)/2 & 1-\tau \\ -(1+\tau)/2 & (1+\tau)/2 & \tau-1 \\ 1-\tau & \tau-1 & 2+2\tau \end{pmatrix},$$

which becomes

$$(5.61) \quad \begin{pmatrix} 1 & 0 & 0 \\ 0 & 1 & 0 \\ 0 & 0 & 2+2\tau \end{pmatrix} \begin{pmatrix} u_1 \\ u_2 \\ u_3 \end{pmatrix} = \begin{pmatrix} 1 \\ 0 \\ \tau-1 \end{pmatrix},$$

after the imposition of Dirichlet constraints. The solution is $u_1 = 1$, $u_2 = 0$, $u_3 = (\tau - 1)/(2\tau + 2)$ which, coincidentally, is the true solution. In particular, notice that as $\tau \rightarrow 1$ then the contribution from the 'tetrahedral' node is not needed and $u_3 \rightarrow 0$. For this example $u_3 \rightarrow 0$ because the true solution lay in the space generated by B_1 and B_2 , more generally, the presence of the u_3 node will be akin to a mesh refinement at the bed boundary. Also notice that in the computation of the stiffness matrix for the pentahedral nodes we *do* take into account the change in conductivity in the computation of A_{11} .

For a more complicated example of nested bases, consider Laplace's equation with Dirichlet boundary conditions

$$(5.62) \quad \nabla \cdot \sigma \nabla u = 0, \quad u = f \text{ on } \partial\Omega,$$

discretized using the two meshes shown in Figure 5.5. We suppose that σ is constant above and below the diagonal interface, Γ , shown in Figure 5.5b. The set of piecewise bilinear basis functions used in Figure 5.5a will be denoted B_1 . The basis functions used in Figure 5.5b will be the linear elements on triangles given in equation (5.9) and denoted B_2 . We suppose that we do not want to use the triangular basis functions over the whole domain, but instead choose $B_1 \cup \tilde{B}_2$ where \tilde{B}_2 denotes those triangular basis functions which are *zero* at any node of B_1 . In this way, we gain the ability to model sharp changes in the field across the interface without changing the basis functions away from the interface. Suppose that V_i is the space of functions generated by B_i , then we want to write the scalar field u as $u_1 + u_2$ with $u_i \in V_i$. This decomposition would not normally be unique. We enforce uniqueness by insisting that $u_2 = 0$ on all of the nodes of B_1 . u_2 is thus only non-zero on the area shown shaded in Figures 5.5a and 5.5b, which we denote Ω_2 . The non-zero nodes of u_2 lie only along the 1D interface, Γ .³

At the boundaries of the domain, we suppose that $f \in V_1$ so that we can set $u_2 = 0$ everywhere on the boundary $\partial\Omega_2$. We write V_1^0 for the space of piecewise bilinear functions in V_1 which are *zero* on the boundary $\partial\Omega$. We thus obtain a well-defined Galerkin scheme by choosing test functions $v_1 \in V_1^0$ and $v_2 \in V_2$ such that

$$(5.63) \quad \int_{\Omega} \sigma \nabla v_1 \cdot \nabla (u_1 + u_2) = 0 \quad \text{and} \quad \int_{\Omega} \sigma \nabla v_2 \cdot \nabla (u_1 + u_2) = 0$$

for all v_1 and v_2 , with $u_1 = f$ on $\partial\Omega$ and $u_2 = 0$ on $\partial\Omega_2$. This obviously corresponds to a

³In purely formal terms, we can think of u_2 being the restriction to Γ of a function in $H^1(\Omega)$ with $u_2|_{\partial\Omega} = 0$, so that $u_2 \in H_0^{1/2}(\Gamma)$. We have chosen a decomposition $H^1(\Omega) = \bar{H}^1(\Omega) \oplus H_0^{1/2}(\Gamma)$ where $\bar{H}^1(\Omega)$ is that space of functions u with $\langle u, v \rangle_{\Gamma} = 0$ for all $v \in H_0^{1/2}(\Gamma)$. I.e., we have specifically removed from $H^1(\Omega)$ those functions which have discontinuous normal derivative across Γ and put those functions into $H_0^{1/2}(\Gamma)$ instead. The FEM discretization inherits the decomposition of these function spaces.

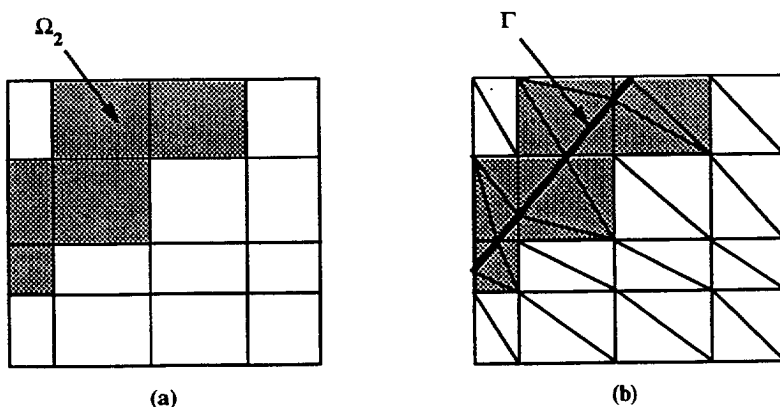


Figure 5.5: Meshes on $[0, 1]^2$. Γ denotes the interface between two different material constants and it is required that nodes on Γ be incorporated into the finite element solution.

stiffness matrix with block structure

$$(5.64) \quad \begin{pmatrix} A_{11} & A_{12} \\ A_{12}^t & A_{22} \end{pmatrix}.$$

A_{11} denotes the discretized Laplace equation using piecewise bilinear functions over Ω and A_{22} represents the discretized Laplace equation using piecewise linear functions over Ω_2 . A_{11}^{-1} produces a function whose normal derivative is continuous across Γ , so that the normal current is discontinuous and leads to a charge build up. u_2 is the extra contribution needed to make the normal current continuous again. The coupling matrix A_{12} will take on a similar form to that from Figure 5.4b. One can think of the solid triangle being a basis function in \tilde{B}_2 and the basis functions $B_{2h} \subset B_h$ are the B_1 .

This example was a little contrived because on $\partial\Omega_2$, u_2 is linear and so could match perfectly against a bilinear function defined on the rectangles. A simple strategy would have been to remove the bilinear basis functions from Ω_2 and have a well-defined finite element scheme with triangles inside Ω_2 and rectangles outside.

This strategy is *not* possible in 3D. An intersecting plane will result in a mesh of tetrahedra on Ω_2 and give rise to piecewise linear functions defined on the triangles of the boundary $\partial\Omega_2$. These would *not* match up against the bilinear elements on the square faces of $\partial(\Omega - \Omega_2)$. In effect, $u_1 + u_2$ would not be continuous. The only ways to enforce continuity are either (i) extend Ω_2 to encompass the whole domain or (ii) set $u_2 = 0$ on $\partial\Omega_2$. The first case, that of

extending Ω_2 to the entire domain requires a tetrahedral mesh everywhere, which was what we had tried to avoid. In the second case, we see that $u_1 + u_2$ is continuous precisely because the zero function is equally well defined as bilinear on a square mesh or linear on a triangular mesh.

Our strategy for 3D meshing is thus to rotate a 2D mesh of triangles to form a mesh of pentahedra. The stiffness matrix A_{11} will be block tridiagonal. Each bed boundary defines an intersecting plane which cuts through the domain. We convert each intersected pentahedra into a sum of tetrahedra, but we *only* subdivide those pentahedra which are actually intersected. We write Ω_2 for the sum of tetrahedra. We solve for $u_1 + u_2$ where u_2 is defined on the mesh of tetrahedra and, for continuity, u_2 is zero on $\partial\Omega_2$. A_{22} represents Laplace's equation on the tetrahedra. A_{11} represents the differential equation relative to the original discretization scheme.⁴

Because the stiffness matrix has retained a rich structure, many iterative and direct inverse methods suggest themselves. We shall give examples based on conjugate gradient with suitable preconditioners based on the incomplete LU factorization of Chapter 2.

We have found that the positivity of LU depends strongly on the node numbering chosen. In particular, if we choose a 'natural' ordering, with the overlay nodes listed after the pentahedral nodes then the convergence was almost invariably poor. Nor did choosing a profile minimizing scheme such as reverse Cuthill-McKee help [2].⁵ The problem is that we are trying 'point-oriented' preconditioners. We are ignoring the block structure of A and that is a mistake.

A better preconditioner is to write $A_{11} = L_{11}U_{11} + C_{11}$ and $A_{22} = L_{22}U_{22} + C_{22}$ so that

$$(5.65) \quad \begin{pmatrix} A_{11} & A_{12} \\ A_{12}^t & A_{22} \end{pmatrix} = \begin{pmatrix} L_{11} & 0 \\ 0 & L_{22} \end{pmatrix} \begin{pmatrix} U_{11} & 0 \\ 0 & U_{22} \end{pmatrix} + \begin{pmatrix} C_{11} & A_{12} \\ A_{12}^t & C_{22} \end{pmatrix}$$

We call this preconditioner a "block ILU" preconditioner. Although the defect matrix, C , is now bigger than it was for point ILU, the number of iterations will be greatly decreased, even if $L_{11}U_{11}$ or $L_{22}U_{22}$ are not positive definite. A comparison of the two preconditioners is shown in Figure 3. This example involved a Dual Laterolog[†] in a $0.01\Omega m$ borehole with one semi-infinite bed of resistivity $1\Omega m$ beneath another of resistivity $100\Omega m$. The interface was inclined by 80 degrees. We compare point-ILU preconditioning with block ILU preconditioning. The former required 4300 iterations and the latter only 740. For this problem, there were 3329 nodes in each of 32 ρz planes and an additional 7629 tetrahedral

⁴ A_{11} could also correspond to a finite difference discretization.

⁵ Moreover, an RCM numbering will destroy the structure of A that we have been trying to maintain!

[†] Mark of Schlumberger

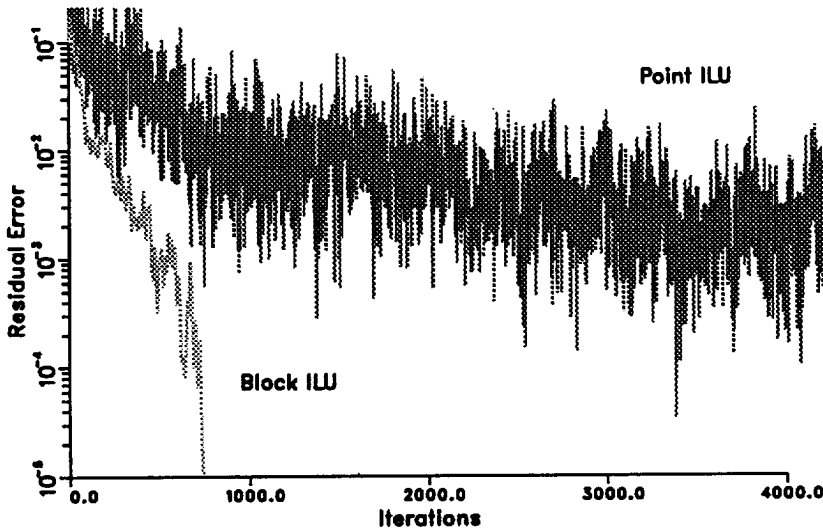


Figure 5.6: Point versus Block ILU Preconditioning.

nodes, making a total of 114157 unknowns. For this example, if we chose to *not* add the additional basis functions on the tetrahedra, the number of iterations fell to 720 and the accuracy degraded by 8%.

Also notice that in the computation of the stiffness matrix for the pentahedral nodes we *do* take into account the change in conductivity in the computation of A_{11} .

This last point raises a question when computing the integrals over Π . Because of the interface, Π will be given as a sum of tetrahedra. We can either perform a numerical integration within the tetrahedra or else stick with the original 21 point Gaussian integration over Π and assign conductivity according to which tetrahedron the Gauss point lies. In practice, the difference between the two is small. We chose the latter for the somewhat biased reasoning that if the conductivity either side of the interface is the same then it will have absolutely no effect on A_{11} , essentially by construction. The presence of the overlay nodes will change the answer a little, however, essentially as if we had refined along the bed boundary.

The block ILU preconditioner presented above can also be viewed as a type of domain decomposition preconditioner with inexact solvers, [8]. The two ‘domains’ are, respectively, the nodes on the pentahedral mesh and the nodes on the tetrahedral overlay patch. The inexact

solvers are the incomplete LU factorizations over the two domains. As the domains overlap completely, we can expect the convergence rate to be essentially the same as the convergence rate for the pentahedral mesh with no overlap.

5.5 Decomposition of pentahedra

We have seen that in order to incorporate a dipping interface, we must subdivide pentahedra into tetrahedra which are aligned on that interface. To do so we first label those pentahedra according to whether or not they intersect the interface and then those pentahedra are each subdivided into three tetrahedra. This latter step is a little non-trivial. There are two ways to subdivide a rectangular face into triangles and so eight possible ways of subdividing the faces of the pentahedra. Six of these correspond to valid tetrahedral subdivisions and two do not. Two possible valid subdivisions are shown in Figure 5.7. The subdivision of one pentahedron affects the subdivision of its neighbours because the subdivision of each rectangular face must match up (otherwise the mesh of tetrahedra would not constitute a valid finite element space and the basis functions would be discontinuous). The two configurations shown in Figure 5.8 do *not* correspond to a tetrahedral subdivision. So, as each pentahedron face is being subdivided, one must make a choice of the two possible subdivisions, and then check that this choice does not lead to a conflict once the whole mesh has been subdivided. If it does lead to a conflict that instead choose the other subdivision. Written recursively with the correct recursively defined data structures, the algorithm is in fact, fairly straightforward. An outline of the program is given below.

We suppose that we are given a list of rectangular faces, with each pentahedra the union of three rectangular faces. Each rectangular face also knows which pentahedra it belongs to. For convenience, we arrange the pentahedra in a linked list so that if p is a pentahedron then $p \rightarrow n$ is the next pentahedron in the list. $p = \text{NULL}$ indicates the end of the list. Each rectangle r is assigned an integer $r \rightarrow o$ which when 1 or -1 determines which diagonal to choose for the tetrahedral subdivision.

Then when the subroutine `subdivide_pent()` below returns `TRUE` a valid subdivision will have been applied to each of the pentahedra. We have not tried to prove that `subdivide_pent()` cannot return `FALSE` but this has never been observed. The following algorithm is written in a pseudo-C notation.

```
typedef struct {float x,y,z;} POINT;
typedef struct {POINT *i, *j, *k, *l; PENT *p1, *p2; int o;} RECT;
typedef struct {RECT *i, *j, *k; PENT *n;} PENT;
```

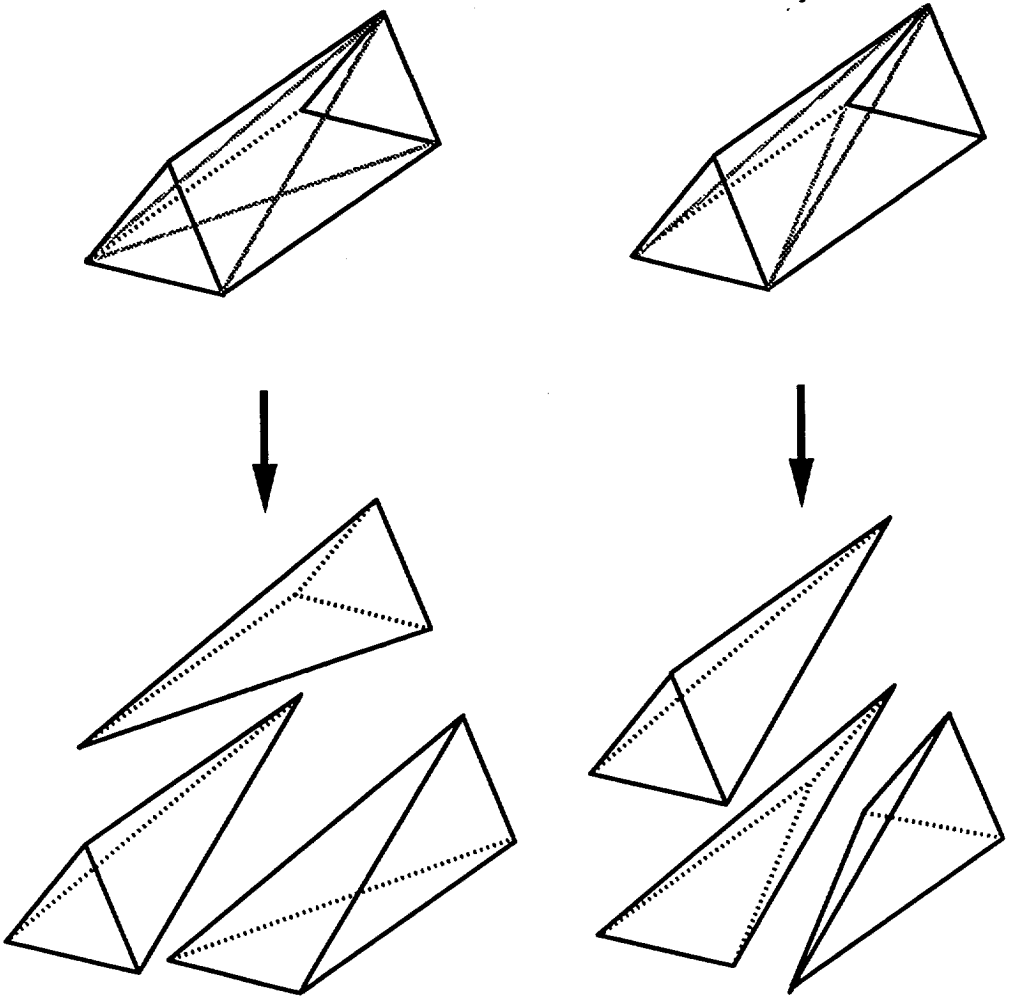


Figure 5.7: Two possible decompositions of a pentahedra into three tetrahedra.

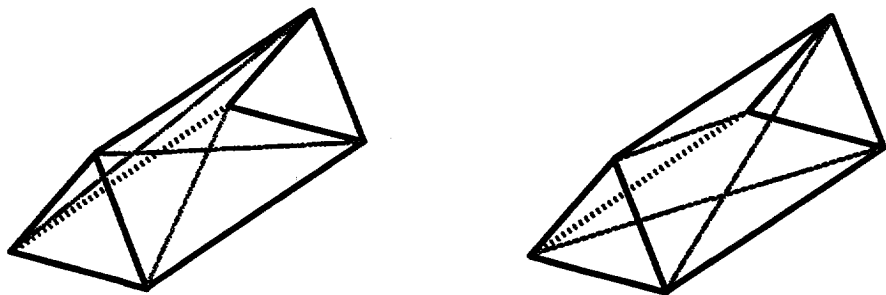


Figure 5.8: Invalid decomposition of a pentahedra into three tetrahedra.

```

subdivide_pent(p)
PENT *p;
{
    if (p == NULL) return (TRUE);
    if (orient_pent(p) == FALSE) return(FALSE);
    return(subdivide_pent(p->n));
}

orient_pent(p)
PENT *p;
{
    if (p->i->o == 0) if (orient_face(p->i) = FALSE) return(FALSE);
    if (p->j->o == 0) if (orient_face(p->j) = FALSE) return(FALSE);
    if (p->k->o == 0) if (orient_face(p->k) = FALSE) return(FALSE);
    return (pent_ok(p));
}

orient_face(f)
FACE *f;
{
    f->o = 1;
    if (orient_pent(f->p1) && orient_pent(f->p2)) return(TRUE);
    f->o = -1;
    if (orient_pent(f->p1) && orient_pent(f->p2)) return(TRUE);
    f->o = 0;
    return(FAIL);
}

```

```
pent_ok(p)
PENT *p;
{
    All of the faces have been assigned orientations.
    If orientations correspond to a tetrahedral subdivision:
        return(TRUE);
    else
        return(FALSE);
}
```

The test for `pent_ok` is actually quite simple. As is clear from Figures 5.7 and 5.8, in a valid subdivision there will be one node which is connected to two diagonals, in an invalid subdivision the diagonals will cycle around.

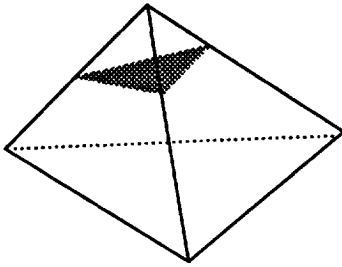
In fact, the problem of subdividing a mesh from pentahedra into tetrahedra is a little simpler for our case because the pentahedra are obtained by rotation from a 2D mesh. One need only find orientations of the lines in the 2D triangles such that no triangle is a closed cycle and then from these orientations one can easily determine valid subdivisions of the pentahedral mesh. The structure of the above algorithm is still the same.

Once one has obtained a mesh of tetrahedra, adding the interface results in the possible cases shown in Figure 5.9. In each case, the subdivision results in a combination of pentahedra and tetrahedra. In Figure 5.9a there is one tetrahedron and one pentahedron, Figure 5.9c has two pentahedra and Figure 5.9d has two tetrahedra. Figure 5.9b gives rise to a tetrahedron and a rectangular pyramid which must be subsequently divided into two tetrahedra. We then convert this mix of tetrahedra and pentahedra into a mesh of tetrahedra using essentially the same algorithm as given above. Once one has obtained a mesh of tetrahedra aligned with a given interface then an additional interface can be added (e.g., if one wants to model intersecting fractures).

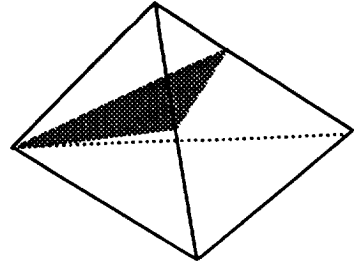
5.6 Fractures

For a slightly different application of the hierarchical formulation, we consider fracture modelling.

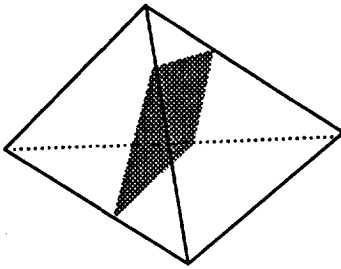
Understanding the response of electrical tools in fractures is essential to providing valid interpretation products. Fractures are important as they provide conduits for drilling mud



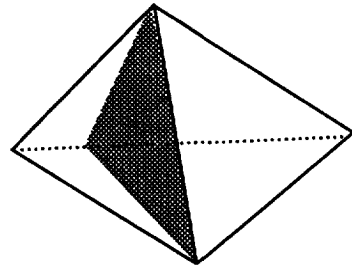
(a)



(b)



(c)



(d)

Figure 5.9: Addition of a planar interface to a tetrahedron results in four possible combinations of tetrahedra and pentahedra. Case (b) gives rise to a rectangular pyramid which must be subdivided into two tetrahedra.

during exploration and for possible hydrocarbon during production, [15], [16]. A knowledge of the fracture system is also useful for stimulation and "fracking," [28].

The essential physics is that the presence of fractures filled with conductive fluid allows electrical current to flow more deeply into the formation along current paths that would not be possible in the absence of the fracture, [24]. Conversely, fractures filled with highly resistive mud block current paths. For example, vertical fractures filled with oil-based mud are known to complicate Induction and CDR responses, [1].

Despite the large scale changes brought about by the fracture, at the scale of the fracture the physics is still that of Maxwell's equations, or, Laplace's equation at DC. In particular, the assumption is that the resistance normal to the fracture is *zero* implying that the potential is continuous across (and along) the fracture. Current can flow along the fracture, however, so the boundary condition is that

$$(5.66) \quad \sigma \frac{\partial u}{\partial \nu} \Big|_{-}^{+} = d \nabla_{\perp} \cdot \sigma_f \nabla_{\perp} u,$$

where u is the potential, ∇_{\perp} the (2D) transverse derivative along the fracture, d is the fracture thickness and σ and σ_f are the formation and fracture conductivities, respectively. The configuration is shown in Figure 5.10.

5.6.1 Finite element formulation

The boundary condition (5.66) fits naturally into our finite element framework. Suppose that we have a system of basis functions spanning a linear space V_h which is conformal with the fracture plane then we would like to find the solution u_h in V_h which satisfies the weak system of equations

$$(5.67) \quad \langle v_h, \nabla \cdot \sigma \nabla u_h \rangle = 0 \quad \forall v_h \in V_h$$

and

$$(5.68) \quad \langle v_h, \sigma \frac{\partial u}{\partial \nu} \Big|_{-}^{+} \rangle = \langle v_h, d \nabla_{\perp} \cdot \sigma_f \nabla_{\perp} u \rangle_F \quad \forall v_h.$$

where the subscript F denotes integration along the surface of the fracture. Additional boundary conditions will apply to u_h and v_h on the boundary of the domain as discussed in earlier chapters – here we shall suppose perfectly conducting electrodes on an otherwise insulating boundary.

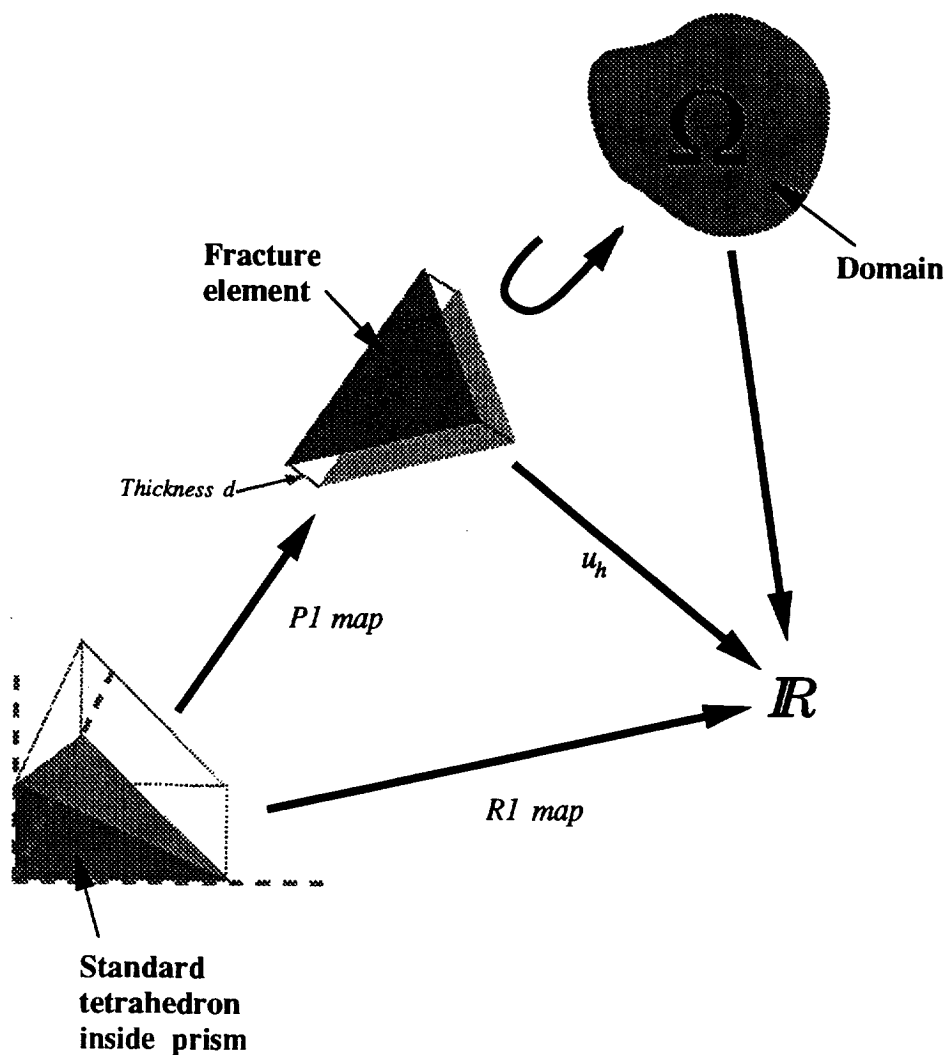


Figure 5.10: Subparametric thick fracture element in \mathbb{R}^3 . The fracture is viewed as a prism of thickness d inside the domain Ω and filled with fluid of conductivity σ_f . This prism is the image of the 'standard prism' under a $P1$ map. The finite element approximation, u_h , is defined to be the inverse of this $P1$ map followed by an $R1$ map from the 'standard prism.' In the limit as $d \rightarrow 0$, u_h is continuous across the fracture, but current can also propagate within the fracture element.

Applying integration by parts we obtain that

$$(5.69) \quad \int_{\Omega} \sigma \nabla u_h \cdot \nabla v_h + \oint_F d\sigma_f \nabla_{\perp} u_h \cdot \nabla_{\perp} v_h = 0 \quad \forall v_h \in H_0^1(\Omega).$$

with v_h zero on the perfectly conducting electrodes (where u_h is known a priori).

5.6.2 Local stiffness matrices

Explicit expressions involving transverse derivatives are most simply derived by assuming that the fracture element has some finite thickness d and is the image of a standard prism under a linear (P1) map. Recall that the most general 'first order' map on a prism takes the R-linear form

$$(5.70) \quad R(\hat{x}, \hat{y}, \hat{z}) = R_1(1 - \hat{x} - \hat{y})(1 - \hat{z}) + R_2\hat{x}(1 - \hat{z}) + R_3\hat{y}(1 - \hat{z}) + R_4(1 - \hat{x} - \hat{y})\hat{z} + R_5\hat{x}\hat{z} + R_6\hat{y}\hat{z},$$

whereas the P1 'first order' map on the tetrahedron takes the form

$$(5.71) \quad P(\hat{x}, \hat{y}, \hat{z}) = P_1(1 - \hat{x} - \hat{y} - \hat{z}) + P_2\hat{x} + P_3\hat{y} + P_4\hat{z}.$$

The local element u_h is given by the composition shown in Figure 5.10 where now the P_i are nodal coordinates in R^3 . We suppose that the nodes within the fractures are ordered so that 1, 2 and 3 lie on the lower triangle and $i + 3$ is above i . The map P is clearly determined by the coordinates of nodes 1, 2, 3 and 4 and is invertible for non-zero d . The map u_h is thus well defined from \mathbb{R}^3 to \mathbb{R} (actually more general than we need: we only need u_h to be defined on an open set containing the prism in Ω). We can compute the derivative of u_h by the chain rule, with derivatives of P and R written by inspection.

$$(5.72) \quad \nabla P = \begin{pmatrix} x_2 - x_1 & y_2 - y_1 & z_2 - z_1 \\ x_3 - x_1 & y_3 - y_1 & z_3 - z_1 \\ x_4 - x_1 & y_4 - y_1 & z_4 - z_1 \end{pmatrix}$$

and similarly for ∇R . In particular, note that ∇P can be computed explicitly in terms of d and the nodal coordinates of the lower triangle. Suppose that $\mathbf{n}/|\mathbf{n}|$ is the unit normal to the triangle containing nodes 1, 2, 3 so that

$$(5.73) \quad \mathbf{n} = \begin{vmatrix} \mathbf{i} & \mathbf{j} & \mathbf{k} \\ x_2 - x_1 & y_2 - y_1 & z_2 - z_1 \\ x_3 - x_1 & y_3 - y_1 & z_3 - z_1 \end{vmatrix}$$

and

$$(5.74) \quad \begin{pmatrix} x_4 \\ y_4 \\ z_4 \end{pmatrix} \begin{pmatrix} x_1 \\ y_1 \\ z_1 \end{pmatrix} + \frac{d\mathbf{n}}{\mathbf{n}}$$

so ∇P (and its inverse) can be computed.

5.7 Implementation details

The above formulation of hierarchical bases has been coded in the ALAT3D package. The code requires about 10000 lines of FORTRAN to perform the construction and inversion of the stiffness matrix and the postprocessing to compute tool responses. The subroutine to subdivide a mesh of pentahedra into tetrahedra with given planes intersecting the mesh was coded in a separate 3000 line C program called COUPXX. The ALAT3D package, in fact, allows the user a choice of how to interpolate the fields across interfaces. The most accurate is to choose the interpolation space of the form $W^\Delta \oplus V^\phi \otimes V^{\rho z}$ as described above, but the user can also force the field to have *zero* projection onto the space W^Δ . In this case, the element integrals are evaluated as

$$\int_{\Omega} \sigma \nabla B_{ij} \cdot \nabla B_{pq} = \sum_{\Delta} \sigma_{\Delta} \int_{\Delta} \nabla B_{ij} \cdot \nabla B_{pq}$$

with 21 point Gaussian quadrature for the element integrals over tetrahedra. This ensures that contribution from a pentahedra containing, say, a small sliver from a highly conductive bed will be correctly accounted for.

A third possibility is to *not* subdivide pentahedra at all with

$$\int_{\Omega} \sigma \nabla B_{ij} \cdot \nabla B_{pq} = \sum_{\Pi} \int_{\Delta} \sigma_{\Pi} \nabla B_{ij} \cdot \nabla B_{pq}$$

and σ_{Π} now evaluated at the Gauss points within the pentahedron (for this numerical integration we used a 15 point quadrature). The advantage of this method is that one does not need to call COUPXX to perform the element subdivisions, the disadvantage is that very thin beds or fractures could completely miss the Gauss points. In effect, this last method converts the true bed profile into an approximate 'step' profile. Experience has shown that the most efficient scheme is to subdivide pentahedra crossing bed boundaries only if they lie within a sphere around the source electrodes, where the potential beyond the sphere is small enough that assuming a step profile will not significantly degrade the response. Within the sphere, uses the

full $W^\Delta \oplus V^\phi \otimes V^{\rho z}$ interpolation space. A typical example involving the azimuthal laterolog requires about 5000 nodes in the ρz plane and 100 nodes in the ϕ plane. The total storage required is then about 40,000,000 words of memory. Double precision is used throughout ALAT3D so this corresponds to about 20,000,000 storage locations for the stiffness matrix and potential fields. On a DEC Alpha workstation the solution is obtained in about 15 cpu minutes per electrode excitation – as discussed in Chapter 2, for a focussed resistivity device we have to solve for each excitation independently and apply the focussing conditions to the resulting transfer impedance matrix. The Azimuthal Resistivity Imager requires 16 such excitations per tool position.

Node numbering is an important issue for preconditioned conjugate gradient schemes, e.g., see [9], [10]. We found that for 3D Laterolog problems, one should list the nodes as (ϕ_1, ρ_1, z_1) , (ϕ_2, ρ_1, z_1) , \dots , (ϕ_n, ρ_1, z_1) , (ϕ_1, ρ_2, z_2) , etc. The stiffness matrix over pentahedra is thus *not* block tridiagonal. We use an RS/CS sparse storage scheme as described in Chapter 2. The cost of performing the ILU decomposition is negligible compared to the cost of the 200–400 iterations of conjugate gradient (per electrode excitation). Another approach would be to allow fill-in in ϕ when computing the ILU factorization so that at each iteration the ϕ nodes are solved exactly. The conjugate gradient routine could then be viewed as an acceleration of line-relaxation, [14], [27]. This would ensure rapid communication between the azimuthal planes and, in particular, an azimuthally symmetric result would be obtained in the same number of iterations as for the 2D problem on the ρz mesh (of course, each iteration would be more expensive).

The triangular mesh in ρz is simply obtained by deleting nodes from a rectangular mesh in ρ, z whenever the aspect ratio of the rectangles is worse than $3 :: 1$. The user enters a list of nodes in ρ and z at run-time. The program COETHYN constructs the triangular mesh, with the option of using additional adaptive refinement as described in Section 2.5.

ALAT3D also allows an interpolation space of the form $W^\Delta \oplus V^z \otimes V^{\rho\phi}$, where now the pentahedral mesh is created by taking the tensor product of a 2D triangular mesh in the $\rho\phi$ plane with a 1D mesh in z . In this case, the Modulef finite element package is used to create the triangular mesh in the ρ, ϕ plane, [23]. For applications involving horizontal wells, such a mesh can require fewer unknowns. Moreover, for horizontal wells, the 2D mesh in $\rho\phi$ can always incorporate the bedding planes so there are no additional W^Δ nodes and σ is constant within each pentahedron.

When computing a log over many tool positions, the potential field from one tool position will be a good initial guess for the potential field at the next. Our design of hierarchical bases lends itself well to this formalism, because there is no need for interpolation between different meshes. The only basis functions which change with tool position lie in W^Δ where *zero* is often a good initial guess. The picture on the cover shows the initial error when

we use the previous tool position. The error is concentrated along those elements whose conductivity changed when the tool moved, namely the green and yellow diagonal region. For the 3D geometries we have considered, using the previous tool position combined with a line relaxation sweep gave a very good initial error, but the asymptotic convergence rate did not change. As we have discussed, focussing constraints often require the subtraction of very similar numbers in the transfer impedance matrix. This in turn requires great accuracy in the conjugate gradient iteration and the asymptotic convergence rate can dominate the computation time. To truly take advantage of the field from a previous tool position one needs to embed the constraints into the conjugate gradient routine as discussed in Chapter 2.

5.8 Conclusions

In conclusion, we have developed a robust method of adding basis functions which are conformal with sharp changes in material properties. If appropriate block preconditioners are chosen then these additional functions do not cause any significant increase in the number of iterations required for convergence. A physical understanding of the finite element and mesh discretization process has led to better preconditioning and more accurate and robust solutions. In particular, by *not* subdividing pentahedra into tetrahedra on most of the domain, we can retain many advantages of finite difference algorithms on structured meshes (e.g., block relaxation and hierarchical formulations). The only way to avoid this subdivision, however, is to not use a full set of tetrahedral basis functions near bed interfaces. Instead we limit the tetrahedral basis to those functions which are zero along all pentahedral faces. The resulting matrix has the structure of a direct sum $W^\Delta \oplus V^\phi \otimes V^{\rho z}$ and we have shown how to tailor the ILU decomposition to invert the corresponding stiffness matrices.

References

- [1] Anderson, B., S. Bonner, M. G. Luling, and R. Rosthal, "Response of 2-MHz LWD resistivity and wireline induction tools in dipping beds and laminated formations", *The Log Analyst*, 33, no. 5, 1992, pp. 461–475.
- [2] Axelsson, O. and V. A. Barker, *Finite Element Solution of Boundary Value Problems*, Academic Press, New York, 1984.
- [3] Boyes, W. E., D. R. Lynch, K. D. Paulsen, and G. N. Minerbo, "Nodal-based finite-element modeling of Maxwell's equations", *IEEE Trans. Antennas and Propagation*, 40, no. 6, 1992, pp. 642–651.

- [4] Chatelin, F. and W. L. Miranker, "Acceleration by aggregation successive approximation methods", *Linear Algebra and Applications*, **43**, 1982, pp. 17 – 47.
- [5] Chew, W. C. and C. C. Lu, "NEPAL – the use of Huygen's equivalence principle for solving the volume integral equation of scattering", in *Ninth Annual Review of Progress in Applied Computational Electromagnetics*, Monterey, CA, 1993.
- [6] Davies, D. H., O. Faivre, M.-T. Gounot, B. Seeman, J. C. Trouiller, D. Benimeli, A. E. Ferreira, D. J. Pittman, J.-W. Smits, M. Randrianavony, B. Anderson, and J. R. Lovell, "Azimuthal Resistivity Imaging: A new generation Laterolog", in *SPE 67th Annual Technical Conference*, Washington, DC, 1992. Paper SPE 24676. Submitted to JPT.
- [7] Douglas, C., "A multilevel solver for boundary value problems", *IEEE Trans. Electronics*, **32**, 1985, pp. 1987 – 1991.
- [8] Dryja, M. and O. B. Widlund, *Some Domain Decomposition Algorithms for Elliptic Problems*, in *Iterative Methods for Large Linear Systems*, Academic Press, San Diego, 1990, ch. 16, pp. 273–291.
- [9] Duff, I. S. and G. A. Meurant, "The effect of ordering on preconditioned conjugate gradients", *BIT*, **29**, 1989, pp. 635–657.
- [10] Dutto, L. C., "The effect of ordering on preconditioned GMRES algorithm for solving the compressible Navier-Stokes equations", *Int. J. Num. Eng.*, **36**, 1993, pp. 457–497.
- [11] Gianzero, S., S. Y. Lin, R. Chemali, and W. Dossey, "The effect of sonde eccentricity on resistivity tools: An exact theoretical model", in *Transactions of the 26th SPWLA Symposium*, Dallas, TX, 1985. Paper GG.
- [12] Gianzero, S. C. and R. Rau, "The effect of sonde position in the hole on responses of resistivity logging tools", *Geophysics*, **42**, no. 3, 1977, p. 652.
- [13] Gounot, M.-T., *The SKYLINE finite element code*, 1983. Personal communication.
- [14] Hackbusch, W., *Multigrid Methods and Applications*, Springer-Verlag, Berlin, 1985.
- [15] Hornby, B. E. and S. M. Luthi, *An integrated interpretation of fracture apertures computed from electrical borehole scans and reflected Stoneley waves*, in *Geological Applications of Wireline Logs II*, 65, The Geological Society, Bath, UK, 1992, pp. 185–198.
- [16] Kostek, S. and C. J. Randall, "Borehole acoustic wave propagation in the presence of fractures: A finite difference approach", in *Transactions of the 61st SEG Symposium*, Houston TX, 1991.

- [17] Lovell, J. R., "*Hierarchical basis functions for 3D finite element methods*", in Ninth Annual Review of Progress in Applied Computational Electromagnetics, Monterey, CA, 1993.
- [18] Lovell, J. R. and W. C. Chew, "*Response of a point source in a multicylindrical layered medium*", IEEE Trans. Geoscience Remote Sensing, **25**, no. 6, 1987, pp. 850–858.
- [19] ———, "*Effect of tool eccentricity on some electrical well logging tools*", IEEE Trans. Geoscience Remote Sensing, **28**, no. 1, 1990, pp. 127–136.
- [20] Luthi, S. M. and P. Souhaite, "*Fracture apertures from electrical borehole scans*", Geophysics, **55**, 1990, pp. 821–833.
- [21] Mallat, S. G., "*Multiresolution approximations and wavelet orthonormal bases of $L^2(\mathbb{R})$* ", Trans. Amer. Math. Soc., **315**, no. 1, 1989, pp. 69–87.
- [22] Monheit, S. and G. Gustavson, "*Influence of dip angle and eccentricity on borehole penetration*", Izvestiya, Borehole Geophysics, **69**, no. 1, 1989, pp. 181–210.
- [23] Perronet, A., *The club MODULEF: a library of subroutines for finite element analysis*, in Computing Methods in Applied Sciences and Engineering, vol. 704 of Lecture Notes in Mathematics, Springer-Verlag, Berlin, 1979, pp. 127–153.
- [24] Sibbit, A. M. and O. Faivre, "*The Dual Laterolog response in fractured rocks*", in Transactions of the 26th SPWLA Symposium, Dallas, TX, 1985. Paper T.
- [25] Strang, G. and G. J. Fix, *An Analysis of the Finite Element Method*, Prentice-Hall, Inc., Englewood Cliffs, NJ, 1973.
- [26] Stroud, A. H., *Approximate Calculation of Multiple Integrals*, Prentice-Hall, Englewood Cliffs, NJ, 1971.
- [27] Varga, R. S., *Matrix Iterative Analysis*, Prentice Hall, New York, 1962.
- [28] Wilkinson, D. and P. S. Hammond, "*A perturbation method for mixed boundary-value problems in pressure transient testing*", Transport in Porous Media, **5**, 1990, pp. 609–636.
- [29] Xu, J., "*Iterative methods by space decomposition and subspace correction*", SIAM Review, **34**, no. 4, 1992, pp. 581–613.
- [30] Yserentant, H., "*On the multilevel splitting of finite element spaces*", Numer. Math, **49**, 1986, pp. 379–412.
- [31] Zienkiewicz, O., *The Finite Element Method*, McGraw Hill, 1977.

Conclusions and Future Research

Abstract. Finite element methods for complicated heterogeneous formations have been developed in earlier chapters. Future research will concentrate on faster inversion techniques which take advantage of the structure built into the finite element stiffness matrices

6.1 Overview

Finite element methods for resistivity logging tools in complicated heterogeneous formations have been developed in earlier chapters. In particular, in 3D, the basis functions will lie in an approximation space of the form $V_h = V^{\rho z} \otimes V^\phi \oplus V^\Delta$ which we have termed a hierarchical decomposition because of the natural inclusions $V^{\rho z} \otimes V^\phi \hookrightarrow V_h$ and $V^\Delta \hookrightarrow V_h$. The corresponding stiffness matrices take on a highly structured form

$$(6.1) \quad \begin{pmatrix} A_{11} & A_{12} \\ A_{21} & A_{22} \end{pmatrix}$$

where A_{11} is block tridiagonal because of the tensor product structure on the pentahedral mesh. We refer to such a matrix as block Laplacian because both A_{11} and A_{22} represent discretizations of Laplace's equation. The solution technique we have proposed in Chapter 5 was to use a block ILU preconditioner to accelerate a conjugate gradient iteration.

We have also examined ILU preconditioners in Chapter 3, where they were used with success to invert the complex symmetric matrices arising from a finite element decomposition for H_ϕ valid for arbitrary frequencies ω . We also saw in Chapter 4 how the more complicated boundary condition for contact impedance can be brought into the H_ϕ framework.

Preconditioning alleviates ill-conditioning brought about by non-zero frequencies, high contrasts in material properties and the large variation in scale between the mesh diameter h and the size of the total domain Ω .

The main problem with the block ILU preconditioner in 3D is that it is relatively expensive per

iteration and does not rapidly propagate data through the mesh. A more promising approach is to use a hierarchical scheme in ϕ to replace the discretization $V\phi$ into a hierarchical scheme so that the basis functions are stacked according to Figure 5.4. The Laplace operator discretized according to this basis function will have $O(1)$ condition number so the block triangular stiffness matrix over the pentahedral mesh should have condition number no worse than that of the Laplace operator discretized over the triangular mesh in ρz . The downside will be that the stiffness matrix will have roughly twice as many non-zero entries and will not have a structure well suited to (point) LU preconditioning. Simple smoothing methods such as Gauss-Seidel should be powerful however, especially if incorporated into an alternating direction scheme. In effect, the resulting algorithm would be equivalent to using multigrid with line relaxation along the azimuthal direction and ILU-preconditioned conjugate gradient in the ρz plane.

In Chapter 2, we showed that focussing can cause a loss of symmetry in the stiffness matrix and future research will examine ways in which non-symmetric iterative methods can be used to derive a robust iterative scheme which does not require solving for each electrode excitation independently. For example, we have seen that GMRES applied to the Schur complement, as developed in Chapter 2, can require N full matrix inversions, where N is the number of focussing constraints. Preliminary research indicates that the Bi-Conjugate gradient method applied directly to the non-symmetric stiffness matrix gives a solution in approximately the same amount of time as 2-3 electrode excitations. With a suitable (non-symmetric) preconditioner, this iteration count might be further improved.

There is also a natural decomposition of the stiffness matrix into blocks corresponding to domains of constant material properties. Domain decomposition techniques can be used to take advantage of this structure and provide a framework which can take advantage of parallel MIMD architectures.¹

In conclusion, the thrust of this thesis has been to build relatively well conditioned stiffness matrices which retain a significant amount of internal structure and to show how simple preconditioners can be extended to complex symmetric matrices (2D) and block Laplacian matrices (3D). Future research will concentrate on faster inversion techniques which take advantage of this structure and which can extend the methods to rapid solutions of the full Maxwell equations in three-dimensional geometries.

¹MIMD is an acronym for Multiple Instruction Multiple Data. Early so-called 'parallel' machines such as the CM2 could, in fact, only operate the same operation on all components of an array. Much more interesting is the possibility of allowing the code to act differently on different pieces of data, this is the essence of MIMD. A typical MIMD example would have different cpu's solving the differential equation in different domains. Another would be to evaluate a spectral integral by giving a separate wavenumber to each cpu and accumulating their computation of the integrand.

Glossary of Codes

The following codes have been referred to in the text:

LATER A 2D finite element code which solves for Φ in an azimuthally symmetric medium. The mesh is a quasi-uniform rectangular mesh in the ρz plane. The code was written by Ecole des Mines, Paris, under contract by Schlumberger in 1975.

SKYLINE A 2D finite element code which solves for Φ in a 3D geometry consisting of cylindrical wedges. This configuration can be sheared to account for dip and the tool can be eccentered within the borehole. The code was written by Ecole des Mines, Paris, under contract by Schlumberger in 1980 and extensively modified and improved by Marie-Therese Gounot at Schlumberger Etudes et Production, Paris.

CWNLAT A 2D finite element package which can solve for a variety of scalar potentials including H_ϕ or Φ in an azimuthally symmetric medium and H_z or Φ in the xy plane. The code was written in 1989 by John R. Lovell at Schlumberger-Doll Research, Ridgefield, CT and subsequently modified to allow for a variety of boundary conditions as described in Chapters 3 and 4. Sample input files for CWNLAT are given in Chapter 4.

ALAT3D A 3D finite element code which solves for Φ in a more or less arbitrary geometry. The basis functions used are R -linear on pentahedra with the option of adding additional tetrahedral nodes on interfaces between bed boundaries. Dipping beds are *not* simulated by shearing the mesh and the code is as accurate at 90 degree dip as at 0 degree dip. Both ALAT3D and CWNLAT share the same keyword driven user-friendly interface. ALAT3D was written in 1992-1993 by John R. Lovell at Schlumberger-Doll Research, Ridgefield, CT. Sample input files for ALAT3D are given in Chapter 4.

FEMIND A 2D finite element code designed to solve for induction tools in axisymmetric formations. The code uses a block-Gaussian elimination to efficiently solve for multiple tool positions and was written in 1980 by Barbara Anderson and Steve Chang at Schlumberger-Doll Research, Ridgefield, CT.

TWODEPEP A commercial finite element package developed by Granville Sewell which uses finite element techniques with adaptive mesh refinement to solve 2D partial differential equations.

Glossary of Tools

The following Schlumberger logging tools have been referred to in the text:

ARI[†] Azimuthal Resistivity Imager has been designed as an upgrade to the Dual Laterolog (DLL)[†]. In addition to the DLL electrodes, additional azimuthal sensors have been added which generate a quantitative resistivity image. The ARI also incorporates an advanced postprocessing system which minimizes the Groningen effect, the modelling of which was performed with the CWNLAT code of Chapter 3.

DLL[†] Dual Laterolog consisting of a shallow resistivity measurement (LLs)[†] and a deep measurement (LLd)[†] both of which modes operate simultaneously. The focussed current patterns of the two modes of the DLL are shown in Figure 1.2.

LL3[†] Early Laterolog consisting of a current measure electrode surrounded by two large guard electrodes. The three electrodes are maintained at the same potential. The corresponding log is similar to that of the LLd but is subject to more severe shoulder effects. As both the LLd and LL3 have reference potential 'N' at the end of a long bridle then the two logs are equally susceptible to Groningen effect.

FMI[†] Formation Micro Imager measures the resistivity in front of an array of buttons and thereby obtains a resistivity image. Four pads are used to maximize coverage of the borehole wall.

ES[†] A four electrode array run in either Lateral or Normal configurations. Current leaves electrode *A* and returns to electrode *B* and the voltage difference between electrodes *M* and *N* is measured.

DIT[†] Dual Induction Tool consists of an array of two three-coil induction tools. Each such system consists of a transmitter and receiver coil with the direct signal from transmitter to receiver subtracted by measuring the signal at a third 'bucking' coil. One such combination gives a deep resistivity measurement (ILD)[†] and the other a more shallow measurement (ILM[†]).

[†]Mark of Schlumberger

Samenvatting

Bij de opsporing van aardolie en aardgas spelen weerstandsmetingen in boorgaten, meestal in samenhang met metingen van andere grootheden zoals de porositeit van de formatie, een belangrijke rol. Het bepalen van relevante parameters van de formatie uit weerstandsmetingen is een gecompliceerd, niet-lineair probleem, waarbij veelal aanvullende geologische informatie nodig is. Het is daarbij van belang dat de gebruikte meetinstrumenten (tools) zonder misleidende artefacten zo nauwkeurig mogelijke meetwaarden verstrekken. Dat maakt zowel bij het ontwerp van nieuwe meetinstrumenten als bij de interpretatie van metingen van bestaande instrumenten, goed fysisch inzicht noodzakelijk. Daartoe is er duidelijk behoefte aan modelleringsalgorithmen die het mogelijk maken om de responsie van een meetinstrument in een gecompliceerde twee- of driedimensionale meetomgeving, b.v. in een boorgat, te bepalen.

De meting van elektrische weerstand, massadichtheid en porositeit van het gesteente in een formatie kan worden verricht tijdens het boren van een boorgat in die formatie dan wel na het boren door een meetsonde in het boorgat te laten zakken. Beide meetsituaties hebben voor- en nadelen. De laatste methode bekend onder de naam "wireline logging" heeft als voordeel dat complexe metingen kunnen worden verricht door sensoren die niet zijn blootgesteld aan de barre omstandigheden tijdens het boren. De meetdata kunnen met relatief hoge transmissiesnelheid via een gewapende kabel naar het aardoppervlak worden verzonden. "Logging while drilling" (LWD) heeft als groot voordeel dat de metingen niet worden beïnvloed door de diffusie van de boorvloeistof (mud) in de steenformatie. Nadeel is dat de transmissiesnelheid van de telemetrie zeer laag is. De meetdata worden naar het aardoppervlak verzonden via pulsen in de boorvloeistofstroom.

Voor zowel "wireline logging" als "logging while drilling" kunnen de weerstandsmetingen worden onderscheiden in die van het "Laterolog"-type en die van het "Induction"-type. In een rotationeel symmetrische boorgatomgeving zullen instrumenten van het Laterolog-type elektrische stromen genereren die in azimuthale vlakken vloeien. Instrumenten van het Induction-type daarentegen genereren stromen die om het boorgat circuleren. Laterologmetingen zijn dikwijls moeilijk te interpreteren omdat de responsie op een zeer niet-lineaire wijze van de conductiviteit van de formatielagen kan afhangen. Inversie van de responsie van een Induction-meting is nagenoeg lineair. Daarom is het modelleren van meetinstrumenten van het Laterolog-type vanuit rekentechnisch standpunt een grotere uitdaging. In het bijzonder omdat de inversie meestal via een iteratief proces van voorwaartse modelleringsmethoden plaats vindt. Bij het modelleren van instrumenten van beide types wordt uitgegaan van de lineaire veldvergelijkingen van Maxwell.

Het voorwaartse modelleren van de Laterolog wordt bijna altijd uitgevoerd met behulp van eindige-elementenpakketten. Deze pakketten vereisen inversie van grote, ijle matrices. In dit

proefschrift zijn nieuwe pakketten ontwikkeld waarbij moderne methoden worden gebruikt om de matrixinversie te versnellen. Bovendien wordt inzicht in de fysica van het probleem gebruikt om de toegepaste numerieke technieken verder te verfijnen.

In een rotationeel symmetrische boorgatconfiguratie is de beste manier om de Laterolog te modelleren om het eindige-elementenschema te formuleren in termen van de azimuthale component van de magnetische veldsterkte, H_ϕ . Dit in plaats van de klassieke wijze van formuleren met behulp van de scalaire elektrische potentiaal Φ . Met deze H_ϕ -formulering kunnen frequentie-effecten zoals het Groningen-effect - een anomale indicatie van koolwaterstoffen onder formatielagen met grote weerstand - worden gemodelleerd. Bovendien zal de H_ϕ -formulering in tegenstelling tot de formulering in termen van de elektrische potentiaal, geen numerieke singulariteiten vertonen als de contactimpedantie van de elektroden steeds kleiner wordt.

In volledig driedimensionale configuraties, b.v. in het geval van boorgaten in formaties met sterk hellende lagen of voor horizontale boorgaten, is de H_ϕ -formulering niet geschikt. Noch is dan een volledige, vectoriële elektromagnetische formulering praktisch haalbaar, zodat een formulering in termen van de elektrische scalaire potentiaal resteert. Voor de numerieke implementatie daarvan is een ruimtelijke discretisatie nodig die aansluit aan de sterk hellende lagen of aan eventueel aanwezige scheuren in de formatie. Zo'n discretisatie moet zodanig worden uitgevoerd dat structuur behouden moet blijven om het oplossen van het resulterende stelsel vergelijkingen met moderne iteratieve methoden mogelijk te maken. Decompositie van de benaderingsruimte is daarbij direct gerelateerd aan de vermazing en de discretisatiestrategie terwijl het bovendien inzicht verleent in mogelijke preconditioneringstechnieken voor de toegepaste geconjungeerde gradiëntenmethode.

Recentelijk is veel vooruitgang geboekt bij het ontwikkelen van preconditioneringstechnieken waarmee de convergentie van eindige-elementenmethoden kunnen worden versneld. Incomplete LU factorisatie blijkt daarbij bijzonder aantrekkelijk te zijn voor laagfrequente problemen in configuraties met verliezen. Rekentijden van $O(N^{5/4})$ in tweedimensionale en van $O(N^{7/6})$ in driedimensionale problemen, waarbij N het aantal onbekenden is, zijn daarbij gerealiseerd.

Een probleem daarbij is dat N nog steeds zeer groot kan worden: in de orde van enkele honderdduizenden voor typische driedimensionale problemen. Een belangrijk aspect daarbij is de toepassing van hiërarchische vermazingstechnieken. Hierbij worden gecompliceerde elektroden en formatiegeometrieën met zo'n min mogelijk aantal knooppunten gemodelleerd. De oplossing die daartoe wordt voorgesteld is om patches van tetraëdische vermazing over een uniforme vermazing met pentahedra en hexahedra te leggen. De grove vermazing met tetrahedra moet daarbij nog steeds voldoende fijn zijn om nauwkeurige berekeningen van spanningen op en stromen door elektroden te kunnen uitvoeren. Details van deze hiërarchische

vermazingstechnieken voor twee- en driedimensionale problemen worden bediscussieerd.

Combinatie van bovengenoemde hierarchische vermazing met gepreconditioneerde en superconvergente berekening hebben geresulteerd in een aantal geavanceerde numerieke pakketten die zijn gebruikt om een aantal tot voor kort onoplosbare problemen te modelleren in zowel twee- als driedimensionale configuraties in "wireline logging" en in "logging while drilling."

Biographical Sketch

John Richard Lovell was born in Cardiff, Wales on February 27th, 1959. He read mathematics at Jesus College, Oxford and received a B. A. (Hons) degree in 1980. He then left the UK to pursue a Ph. D. in algebraic topology at Cornell University, Ithaca, NY but, despite an initial burst of momentum resulting in a Master's degree one year later, in 1983 he succumbed to the charms of nearby Wells College, Aurora, NY and took a leave of absence from Cornell to teach undergraduate Mathematics and Statistics. In 1984, astonished by the presence of real milk at the Schlumberger coffee stations, he felt he had little choice but to join the Electromagnetics Department as Associate Research Scientist. Here, under the guidance of Weng Cho Chew and Tarek Habashy, he learnt of the beautiful synthesis of complex analysis, numerical mathematics and electromagnetic theory that constitutes spectral methods in layered media. His research on induction and dielectric sensors in such geometries led to co-authorship of four refereed papers, [3], [4], [5], [6] and more than forty internal reports and conference presentations.

In 1987, he received an M. A. from Oxford and in 1989 was promoted to Research Scientist. His research on finite element methods for tools operating at low frequencies resulted in the finite element packages CWNLAT (1989) and ALAT3D (1992). This work was influential in the design and interpretation of a Wireless Telemetry System, the Azimuthal Resistivity Imager, [2], and the Resistivity at the Bit measurement while drilling. With the encouragement and supervision of Prof.dr.ir Hans Blok and Schlumberger managers Dr Kambiz Safinya and Dr Mike Oristaglio, this research ultimately led to the present Ph.D. thesis.

In 1990, he was elected to the Electromagnetics Academy, MIT and in 1992 was invited by Petrobras to teach a graduate level course in resistivity modelling at the Federal University of Pará, Belém, Brazil. The course was attended by fifteen graduate students and visiting professors and resulted in supervision of the Master's thesis, [1].

His current research interests lie in the application of finite elements, special functions and numerical analysis to the computation of electromagnetic fields, with special emphasis on a synthesis of modern iterative techniques such as domain decomposition and multigrid with classical numerical EM methods such as method of moments and mode matching.

His main social activity outside of Schlumberger is running through the swamps and fields around Ridgefield in pursuit of a bedraggled 'Hare' carrying flour and beer – a world-wide phenomenon known as Hashing. In addition, he has also found time to learn how to dance to alternative "new-wave" music under the gentle tutelage of Rebecca Dalebout, for which he will be eternally grateful. His other main pursuits are the study of the Japanese language and windsurfing.

References

- [1] Chaba, A., *Os efeitos Delaware e Groningen: Um estudo quantitativo por elementos finitos*, Master's thesis, Universidade Federal do Pará, Belém, Brazil, 1993.
- [2] Davies, D. H., O. Faivre, M.-T. Gounot, B. Seeman, J. C. Trouiller, D. Benimeli, A. E. Ferreira, D. J. Pittman, J.-W. Smits, M. Randrianavony, B. Anderson, and J. R. Lovell, "Azimuthal resistivity imaging: A new generation Laterolog", in SPE 67th Annual Technical Conference, Washington, DC, 1992. Paper SPE 24676. Submitted to JPT.
- [3] Lovell, J. R. and W. C. Chew, "Response of a point source in a multicylindrical layered medium", IEEE Trans. Geoscience Remote Sensing, **25**, no. 6, 1987, pp. 850-858.
- [4] ———, "Effect of tool eccentricity on some electrical well logging tools", IEEE Trans. Geoscience Remote Sensing, **28**, no. 1, 1990, pp. 127-136.
- [5] Lovell, J. R. and T. M. Habashy, "An induction gradiometer for conductivity contrast detection: Theoretical modelling", Radio Science, **25**, no. 4, 1990, pp. 357-371.
- [6] Lovell, J. R. and B. E. Hornby, "Borehole coupling at sonic frequencies", Geophysics, **57**, no. 7, 1990, pp. 806-814.

Index

- H -formulation, 30
- $H^r(\Omega)$, 12
- $H^{1/2}(\partial\Omega)$, 14
- $H^{curl}(\Omega)$, 18, 27, 28, 31
- $H_0^r(\Omega)$, 13
- $H_0^{curl}(\Omega)$, 27
- $H^{-r}(\Omega)$, 13
- $H^{-1/2}(\partial\Omega)$, 14
- Φ -formulation, 30
- ALAT3D, 119, 126, 139–148, 180, 181
- Apparent resistivity, 2, 6, 42, 48, 55, 57, 79, 80, 87, 92, 101, 130, 161
- Azimuthal Resistivity Imager, ARI, 152, 161, 181, 189
- Bandwidth, 19, 142
- Barycentre, 157
- Bessel function, 35
- Biconjugate gradient, 62, 81, 98
- Bilinear form $\langle \cdot, \cdot \rangle$, 8
- Bridle, 80
- Cartesian product, \times , 7, 152
- Coercive, 8, 34
- Completeness, 12, 13
- Contact impedance, 60, 84, 120–124
- CWNLAT, 81, 84, 97, 98, 109, 119, 126, 139–148
- Defective matrices, 64
- Direct sum, \oplus , 11, 15, 16, 52, 54, 164, 166, 180, 181
- Domain decomposition, 171
- Dual Induction Tool, DIT, 2, 6, 43, 44, 189
- Dual Laterolog, DLL, 48, 189
- Dyads, 11
- Eccentricity, 81, 161–164
- Electric charge density, 22
- Fill-in, 20, 65, 181
- Focussing, 2, 40, 45, 56–60, 80
- Formation Micro Imager, FMI, 119, 189
- Fractional Sobolev spaces, 12, 14, 168
- Fractures, 121, 162, 175, 177–180
- Galerkin formulation, 16, 23, 49, 67, 127, 168
- Galvanic sources, 41
- Gauss-Seidel relaxation, 62, 70, 186
- Gaussian elimination, 19, 20, 57, 70
- Gaussian quadrature, 9, 110, 157, 159, 161, 164, 171, 180
- GMRES, 71, 72
- Groningen effect, 6, 80, 106, 107, 189
- Hankel function, 34
- Hermitian matrix, 61
- Horizontal boreholes, 40, 152, 181
- Inductive sources, 41
- Isoparametric elements, 155, 160
- Kelvin functions, 113
- Kernel, 10, 16, 59

- Krylov spaces, 65, 96
- Lagrange multiplier, 16, 59
- Laterolog tool, 2, 80
- Line relaxation, 181
- LL3, 48, 101, 189
- Logging while drilling, LWD, 40, 80, 87
- LWD, 161
- Method of moments, 16, 98
- MIMD parallel computers, 186
- Node numbering, 54, 142, 160, 170, 181
- Normal equations, 65
- P1 linear map, 51, 53, 67, 158, 179
- Perfect conductor, 24
- Perfect insulator, 24, 82, 84, 101, 111
- Positive definite, 61
- Preconditioning, 21, 62, 64–66, 81, 96, 170
- Profile storage scheme, 19
- Q1 linear map, 51
- R1 linear map, 179
- Reaction, 26
- Reciprocal systems, 26
- Richardson extrapolation, 93
- RS/CS storage scheme, 21, 181
- Shoulder effect, 2, 48, 161, 189
- Sobolev embedding theorem, 14
- Solenoids, 41, 43
- Sommerfeld contour, 35, 44
- Sparse matrices, 19
- Staggered mesh, 56
- Steepest descent, 62
- Stencil, 21, 109
- Stiffness matrix, 16, 52, 92
- Superconvergence, 55, 57, 81, 91–93
- Tensor product, \otimes , 1, 11, 21, 153
- Tornado charts, 80
- Toroids, 41, 45, 87
- Transfer impedance matrix, 57, 70, 127–129, 142, 148, 182
- Vertical electric dipole (VED), 47
- Vertical magnetic dipole (VMD), 43, 45
- Weak formulation, 7, 15, 23, 27, 51, 90, 125, 153